The Mapping and Modelling of Spiral Structure in the Milky Way :

The Potential of the Interstellar Medium

Lee James Summers, BSc(Hons), MSc(R).

A Thesis submitted by Lee James Summers to the University of Exeter for the degree of Doctor of Philosophy in Physics, March, 2012.

I certify that all material in this thesis which is not my own work has been identified and that no material has previously been submitted and approved for the award of a degree by this or any other University.

Signed: . . . . . .
Lee James Summers

Date: . . . . . .

Abstract

GENTLEMEN, -

It was in 1864 that the first clues as to the nature of the space between stars were first identified in literature. These spaces became known as the interstellar medium. Any study of star formation must include an understanding of this interstellar medium (ISM) and its various component parts. Molecular clouds, dense regions of the ISM, are the sites where all known star formation is thought to occur. Hence, whenever an area containing young stars reside, it is assumed that one will also find a molecular cloud. Knowledge of these stellar birthplaces assist not only in models of stellar evolution, star formation potential, rate and efficiency - but also the ISM gives indications as to Galactic structure and the dynamics therein.

Within this thesis I begin with an introduction and historical background of the field before detailing the research which was conducted. Firstly, I discuss a new model describing the spatial and kinematic structure of the Milky Way's spiral potentials; the Perseus arm, the Outer arm and the outer Scutum-Centaurus arm and also the kinematics of the streaming motions of the gas within them. Material associated with each of these arms is then extracted.

Using the models and spiral arm maps derived, I present spatially convolved maps of each spiral arm region (Perseus, Outer and Scutum-Centaurus) at a constant linear scale. By minimising the biases inherent with angular observations of our Galaxy, this presents the data as an analogue of - and as such directly comparable to - extragalactic observations of spiral structure. Finally I present a series of analyses performed on the data and models; derivation of large-scale properties of the spiral arms (i.e. identification of where the arm is unconfused with fore- and back-ground emission, scale height, velocity dispersions, arm mass); dynamical analyses of the models; molecular cloud decomposition of the constant-linear-scale-maps. The findings are then compared with those in the Galactic and extra-galactic literature.

I am, Gentlemen,
Yours Faithfully,
L. J. Summers

(Abstract in the style of: Christiansen & Hindman (1952), the first detection of Galactic HI)


arm
Perseus
Outer
Galactic
spiral
molecular
fit
km
model
kpc
cloud
mass
HI
material
distance
emission
velocity
data
shows
structure
arms
regions
line
gas
clouds
constant
region
one
Galaxy
outer
form
within
resolution
used
Spiral
seen
observations
kinematic
Arm
also
ISM
cluster
clusters
Though
first
curve
found
distances
CO
rotation
presented
CRM
work
two
possible
pc
density
stars
size
parameters
shock
due
formation
since
Milky
scale
atomic
Table
map
using
may
component
centre
NGC
Sct-Cen
observed
spatial
defined
linear

Contents

Declaration & Derived Works

I, Lee James Summers, declare that the work presented within this doctoral thesis was carried out in accordance with the regulations of the University of Exeter. This work is original - except where indicated by special reference in the text - and no part of the dissertation has been submitted for any other degree at any other University, be that overseas or in the United Kingdom, except where indicated below:

Chapters 1 and 2 have elements adapted within it from a progressional Literature Review and report submitted during the first year of my PhD.

Chapters 2 has elements adapted within from the ExFCRAO collaboration's data release paper;

- **The Exeter-FCRAO CO Survey of the Northern Galactic Plane**, Brunt C. M., Heyer, M., Mottram, J., Douglas, K., & Summers L. J. *in prep*

Chapters 3, 4 and 5 are adapted from three papers which are a product of this thesis work;

- **The Spiral Structure of the Outer Milky Way in Position, Velocity and Composition I : The Perseus Spiral Arm** Summers L. J. & Brunt C. M., *(Submitted, MNRAS)*
- **The Spiral Structure of the Outer Milky Way in Position, Velocity and Composition II : The Outer & outer Sct-Cen Spiral Arms** Summers L. J. & Brunt C. M., *written, presubmission* (awaiting acceptance of Paper I)
- **The Spiral Structure of the Outer Milky Way in Position, Velocity and Composition III : The Gaseous Composition of the Outer Galaxy** Summers L. J. & Brunt C. M., *in prep*

The models presented within this work have also been used by the Planck consortium's **3D GALAXY project**, but I am unable to present its findings here. In addition to the publications indicated above, areas of this work also appear in a number of conference proceedings. Finally, any views expressed in this thesis are those of the author and in no way represent those of the University of Exeter.

Acknowledgements

I would take time to acknowledge the innumerable trees whom - without thought for their own wellbeing - have selflessly given their lives so that the multiple copies of this document could be printed for the various stages of submission, rest in peace my friends. Maintaining the horticultural theme, I would also like to mention *Lazarus*, my adopted Bonsai tree, who sadly did not receive the care he so deserved during the final stages of my PhD - and as such did not survive.

Moving to a more serious tone,

There have been so many people I have interacted with over the course of my PhD, so many contributions to the life I've lead for 36 months in so many ways - not just academically - thank you all. But in particular, I would like to acknowledge; my thesis advisor, Dr Chris Brunt, who has been more than understanding in addition to providing invaluable guidance over the past three years; to my uncle, Professor David Edwards, for his comments and suggestions; to Dr Joe Mottram whose guidance on all things Python made programming and scripting things just that bit more bearable.

As we approach sentimentality with brooding sense of guarded caution, I would like to thank my family - my Mum, Dad and Sister - whom have been supportive of me and my worrisome rants for, not only the past 3, but 26 years (minus a bit for my Sister).

Finally, for those whom are reading this as a start to their research careers, I leave you with this inestimable piece of advice:

"*If you're going to live in Starcross* ($+50^\circ 37' 36.5''$, $-3^\circ 26' 59.56''$) *buy a car*"

This work makes use of the Exeter-FCRAO Carbon Monoxide Northern Galactic Plane Survey, Brunt et al. (in prep); the CfA composite ^{12}CO Survey, Dame et al. (2001); The Canadian Galactic Plane Survey, Taylor et al. (2003); The VLA Galactic Plane Survey, Stil et al. (2006); The Leiden, Argentine, Bonn HI Survey, P. M. W. Kalberla et al. (2005).

Lee James Summers
University of Exeter, U.K.
2012

List of Figures

List of Tables

List of Symbols

Symbol	Units	Notes
$\mathcal{A}_{\text{annulus}}$	pc or degrees	2D area of annulus around a cluster
$\mathcal{M}_{\text{H}_2}$	$\text{M}_\odot$	Total Hydrogen mass
$\|\mathbf{B}\|$	Gauss	Magnetic field strength
A_{arm}	km s^{-1} kpc^{-1}	Oort's Constant A based on fit to arm
A_v	magnitudes	Extinction coefficient
b	degrees or radians	Galactic Latitude
B_{arm}	km s^{-1} kpc^{-1}	Oort's Constant B based on fit to arm
d_{helio}	pc or kpc	Heliocentric distance
d_{per}	pc or kpc	Perseus arm heliocentric distance
$\Delta\phi_{sp}$	degrees or radians	Difference between the pitch and shock angles
Δv	km s^{-1}	Spectral velcity channel width
ΔV_{LSR}^{shock}	km s^{-1}	Russeil et al. (2007) deviation from circular motion
Δv_{arm}	km s^{-1}	Velocty w.r.t $v_{arm}(\ell)$ - Arm Centric Velocity
ΔL	pc or kpc	Target linear resolution of the CRM maps
C^{18}O	-	Carbon Monoxide isotope
ℓ	degrees or radians	Galactic Longitude
ϵ	degrees or radians	The angle needed to project v_{arm} along the line of sight
η_{eff}	$\frac{1}{0.66}$	Efficiency correction factor for the ExFCRAO
HI	-	Atomic Hydrogen
H_2	-	Molecular Hydrogen
λ	-	Wavelength
LSR	-	Local standard of rest
M_{arm}^{atomic}	$\text{M}_\odot$	Mass of atomic gas within an arm
$M_{arm}^{molec.}$	$\text{M}_\odot$	Mass of molecular gas within an arm
$\text{M}_\odot$	1.98×10^{30} Kg	Solar mass in Kg
m_{H_2}	$2\times1.67\times10^{-27}$ Kg	Mass of a Hydrogen molecule

cont...

– cont.

Symbol	Units	Notes
n_{tot}	cm^{-3}	Number density of particles
Ω_0	km s^{-1} kpc^{-1}	The ratio of $\frac{v_0}{R_0}$
ϕ_{pitch}	radians or degrees	Spiral arm pitch angle
ϕ_{shock}	degrees or radians	The angle at which material is shocked in a spiral arm
R	pc or kpc	Galactic radius
R_{arm}	pc or kpc	Spiral arm R
R_c	pc or kpc	Co-rotation radius
R_{warp}	pc or kpc	Galactic radius where the warp begins to contribute
R_0	pc or kpc	Distance from the Solar position to the GC
σ_{vel_z}	km s^{-1}	Transverse velocity dispersion
$\sigma_{vel_z}^{atomic}$	km s^{-1}	Transverse velocity dispersion of the atomic gas
$\sigma_{vel_z}^{molec.}$	km s^{-1}	Transverse velocity dispersion of the molecular gas
σ_{vel}	km s^{-1}	Spectral velocity dispersion
σ_{vel}^{atomic}	km s^{-1}	Spectral velocity dispersion of the atomic gas
$\sigma_{vel}^{molec.}$	km s^{-1}	Spectral velocity dispersion of the molecular gas
T_A^*	K	Antenna tempertaure
^{13}CO	-	Carbon Monoxide isotope
θ	radians	Galactocentric longitude
Θ_*	km s^{-1}	Rotational velocity (BB93 rotation curve)
Θ_0	km s^{-1}	Solar Rotational velocity (BB93 rotation curve)
θ_{eff}	degrees	Effective angular resolution for target ΔL
$\theta_{fwhm_{pix}}$	pixels	Number of pixels corresponding to N×θ_{eff}
Ω_p	km s^{-1}	Pattern speed of the spiral structure
θ_{res}	degrees	Angular resolution of input data
$\Theta(R)$	pc or kpc	Non-flat rotation curve
T_{mb}	K.kms^{-1}	main beam, efficiency corrected T_A^*
^{12}CO	-	Carbon Monoxide isotope
v_0	km s^{-1}	Constant Solar rotational velocity (SB model)
$v_0(R)$	km s^{-1}	Variable Solar rotational velocity (SB model)
v_a and v_b	km s^{-1}	Fitting parameters for Variable Shock Model
v_{arm}	km s^{-1}	Rotation velocity of a spiral arm
v_{outer}	km s^{-1}	Outer arm velocity w.r.t LSR
v_{per}	km s^{-1}	Perseus arm velocity w.r.t LSR
v_{prime}	km s^{-1}	Spiral arm best-fit shock velocity gradient
v_R	km s^{-1}	Radial spiral arm velocity residual
$v_{sct-cen}$	km s^{-1}	outer Sct-Cen arm velocity w.r.t LSR
v_{shock}	km s^{-1}	Spiral arm best-fit shock velocity
v_θ	km s^{-1}	Azimuthal spiral arm velocity residual

cont...

– cont.

Symbol	Units	Notes
v_{LSR}	km s^{-1}	Velocity with respect to the LSR
X	pc or kpc	Spiral arm azimuth, $\ell(180°)\equiv X(0$ kpc $)\equiv\theta(\frac{\pi}{2})$
$X_{X_1}^{X_2}$	kpc	X selection between $X = X_1$ and $X = X_2$
$\mathrm{X_{CO}}$	$\frac{1}{\mathrm{K.kms^{-1}}}$	X-factor, conversion of CO column to H_2
Z	pc or kpc	Linear displacement from the b=0°plane
Z_{arm}	pc or kpc	Displacement to the midplane of the spiral arm, $Z_{midplane}$
Z_{FWHM}	pc or kpc	Scale height of the arm
$Z_{FWHM}^{molec.}$	pc or kpc	Scale height of the molecular arm
Z_{FWHM}^{thick}(HI)	pc or kpc	Scale height of the thick atomic arm component
$Z_{FWHM}^{thick}(H_2)$	pc or kpc	Scale height of the thick molecular arm component
Z_{FWHM}^{thin}(HI)	pc or kpc	Scale height of the thin atomic arm component
$Z_{FWHM}^{thin}(H_2)$	pc or kpc	Scale height of the thin molecular arm component
$Z_{midplane}$	pc or kpc	Z position of the arm midplane w.r.t. Z_0 (Galactic plane)

CHAPTER 1

Introduction & Historical Background

"If we knew what we were doing, it wouldn't be called research."
Albert Einstein, 1879-1955

1.1 The Nature of the Interstellar Medium

The existence of material within the interstellar medium (ISM) has not always been detected, nor inferred, from analysis of observations. Though these *voids* were first postulated by Sir John Herschel (1864), son of the great Sir William Herschel, it would be some time before the true nature of the ISM was to be fully understood. It was not until the advent of newer and more accurate observing techniques in the late 19^{th} and early 20^{th} centuries, that these empty expanses between stars were beginning to be filled with new spectroscopic information.

1.1.1 Dark Marks on a Light Sky : The Void Problem

The ISM has a density lower than any vacuum attainable in the laboratory, it is because of this that it was difficult for early instruments to detect the material within it. As a result, the first indications of the presence of an ISM was due to dark voids which appeared on optical photographic plates, as can be seen Figure 1.1. Intrigued by these voids, astronomers set about trying to classify these *vacant lanes* in the heavens. One of the most famous quotes on the subject, by E. E. Barnard, states;

> "I have elsewhere at various times called attention to the connection of nebulosities with some vacant regions on the sky... The extraordinary vacant lanes amongst the Milky Way...suggest that they are not only devoid of stars, but are darker than the immediate sky."
> Taken from *On a nebulous groundwork in the constellation Taurus.*, E. E. Barnard (1907)

The main concerns with the initial findings were that these, comparatively void, regions of space were actually *darker* than the adjacent space. Barnard initially postulated that these regions

Lee J Summers

Image Copyrighted.
Original source image can be found:

θ-Oph - Barnard (1906)
Taurus - Barnard (1907)

Third Party Copyright Marker

Figure 1.1: Photographic plate showing the obscuration of light in the region of [Left] Taurus, Barnard (1907). [Right] θ-Ophiuci, taken from Barnard (1906) (first discussed in Barnard (1899))

could be due to dead nebulous material; reasoning that, when a nebula dies, it becomes invisible and absorbs all light passing through it (Verschuur 1988). From a cosmological stand-point this is the first recorded - and published - inference to a situation in which the Universe is thought to contain material which astronomers' current instrumentation cannot detect. The most recent incarnation of *undetectable matter*, is theorised via application of the virial theorem to galaxy clusters, was termed *Dark Matter* by the Swiss astrophysicist Fritz Zwicky (1937) and is still is not fully understood.

Barnard was by no means the only astronomer confronted with these *unexplained* dark patches on the sky (Kapteyn 1909a,b; Slipher 1912). A series of papers by Kapteyn identified that studying the real distribution of stars on the sky is difficult since contemporaries were uncertain about the attenuation of the light between the source and observer. Kapteyn amalgamated the *absorption* of light and the *scattering* of light along the line of sight and considered the effects of each phenomena on the observed flux one would expect to receive in an instrument's detector. It was thought that possible sources of this absorption were two-fold; first, there could be intervening *meteoric matter* blocking the line of sight to the source and hence the light is attenuated by an amount proportional to the amount of *stuff* along that sight path. The second, assumes a transparent universe and the density of stars gradually decreasing as one moves out from the sun. The latter explanation was deemed to be problematic since it would assume that the sun was in a special location in the Galaxy (i.e. coincident with the location of maximum density), which violates the later derived relative densities obeying the *Cosmological Principle*. This Cosmological Principle is an astronomical interpretation of the *Copernican Principle*, postulated by Lemaître (1927) (english

translation, Lemaître 1931), which states - we occupy no special nor unique position in space. The assumption that the attenuation of light is merely apparent and is due to the absorption of light, this makes the observed reduction in flux along arbitrary lines of sight understandable. This was an important step in beginning to understand the nature of the ISM. Kapteyn (1909a) focussed on explaining what the author termed *general absorption*, however, in the conclusions to the paper, Kapteyn identifies that possible *gas-absorption* which were producing *spaces-lines* or *space-bands* would be important. The bands detected in these interstellar regions were producing spectra as unique as the stars being observed. However, due to the restrictions of the observing equipment which was available at the time, in summation, Kapteyn states:

> "As, however, I have no evidence as to the real occurrence of such lines or bands, no more need be said at the moment"
> Taken from *On the absorption of light in space*, J. C. Kapteyn (1909a)

A sometimes overlooked work in the form of Slipher (1912), whose observations of the nebulosity within the Pleiades, found that the light from the nebula was giving - what was considered to be - a stellar spectrum. When taken out of context, these observations seemed to suggest a stellar origin to the spectra. The question was whether these nebulae shine due to their own emission or by reflection of light from the neighbouring stars. Were the light observed was due to reflected starlight, the implication would be that the background stars are all of the same spectral type to be able to produce the coherent spectrum. The observation plates gave no indication as to the source of these spectral traces being due to the scattered light from nearby Sirius. Slipher suggested that the nebulae observations were central stars being enveloped by fragmentary and disintegrated matter, the first inference that the observed spectra from these nebulae were not of stellar origin. The following year, Barnard (1913) revisited the possibility of these observations were indicative of *Black Holes* - in the sense of the absence of light rather than the more recent Hawking & Penrose (1970) sense of the term. It is in Barnard (1913) that the first suggestion that the dark voids are not, in fact, voids at all but rather a result of there being large masses obscuring the light from the source. Still other astronomers began to take interest in the void problem in the form of Shaw (1914), making the point that there was the possibility that the voids were due to interstellar masses on the small scale. Though Shaw (1914) still maintained the probable cause of the larger scale voids are due to there just being no stars in those regions. It was now that Barnard's voids were starting to be accepted as actual features in the interstellar regions rather than observational inaccuracies or anomalies yielding further studies to be conducted.

1.1.2 The Interstellar SchISM

Early studies of the diffuse ISM contained present Eddington (1926a,b), were shocked to discover the presence of matter within it - as stated previously, since the mean density of the ISM is very low. With the advent of high resolution spectroscopy in the early 1930s, the true nature of this diffuse medium was beginning to be understood. The first of these next generation spectrographs was housed at the Mount Wilson Observatory. From the spectroscopic analysis of the sky which was

conducted, astronomers were able to ascertain the existence of interstellar molecules; something which excited - though some may say perturbed - early astronomers.

> "I write about molecules with great diffidence, having not yet rid myself of the tradition that 'atoms are physics, but molecules are chemistry'..."
> Taken from *Interstellar Matter*, Sir A. S. Eddington (1937)

Until the 1930s, most of the matter discovered in the diffuse ISM were ionised atomic forms. It was known that ionised matter of similar charge repel one another, therefore the probability of these atoms combining into molecular forms was deemed unlikely (Barnard 1899, 1906; Eddington 1937) and was eventually dubbed *The Water Problem*. It was commented that the presence of dark markings on image plates could not all be due to the effect of large opaque masses obscuring the light from background sources (Barnard 1899, 1906, 1919a,b). Though it was *possible* that at least *some* of these obscurations were the result of real, extended, features. Absorption lines in the spectra of stars had already been observed (Heger 1922), but there were occasions where there were anomalous absorptions present within the spectra. Identified as anomalous Sodium and Calcium lines, there source was uncertain (Hartmann 1904a,b). It wasn't until a letter to *Pacific & American Physical Society*, Merrill (1934) presented a new series of absorption lines which were in the observed stellar spectra of the newly commissioned MWO. These new lines were in addition to the stationary Fraunhofer lines, in the observed Ca^+ and Na spectra, discovered by Joseph von Fraunhofer (1814). These new lines consisted of;

- **Stellar Lines**, due to gases in the observed star's own atmosphere.
- **Terrestrial Lines**, due interactions with Earth's own atmosphere.
- **Detached lines**, these lines were caused somewhere between the source and the observer.

Merrill (1934) had discovered four additional lines within these observed spectra, but could not identify their origin. Thus causing the contemporary view - that these absorptions were due solely to atomic material - to be challenged. A year after publication of Merrill (1934), Russell (1935) suggested the source of these addition lines were molecular compounds residing along the line-of-sight, Swings (1937) suggested that this were more likely to be the case since the absorption lines were not as sharp as the atomic counterparts and that, *"the fuzzy character of these* [molecular] *lines, adds weight to the* [Merrill (1934)] *hypothesis"* (Swings 1937). The *fuzzy* nature of these lines is effectively a resolution effect since these individual lines are closely spaced and correspond to energy-level transitions. Each line represents an increment of energy due to the change in the rotational state of the molecule - if these lines are unresolved, then the bands appear to be continuous.

There was great debate as to the origin of Merrill's lines, with Swings & Rosenfeld (1937) and Saha (1937) being the main contributors. One of the main ideas to emerge - in adjunct to the discussion of the source of these bands - was the potential importance of the intensity of the UV field and the photodisassociative effect it would have on the molecules. The main indication of the presence of the UV field was that most of the material which was being detected and observed was

in its atomic form - as previously stated. There were concerns that the interstellar environment was not conducive to the production - nor maintenance - of material in molecular form. Even though in the summary of Merrill (1934), the widening of the observed lines forces one to question the atomic origin of these lines. The work of Swings & Rosenfeld (1937) estimated the abundances of these newly observed interstellar molecules. They postulated that the compounds detected were diatomic - for example; H_2, OH, NH, CN CO, O_2 *etc*. These new compounds were found to be less abundant than the already established abundances of Ca^+ and Na which were determined by Dunham (1937); Douglas & Herzberg (1941); McKellar (1941). It was concluded that the space between stars was not as empty as once thought.

1.2 The Relative Densities of the ISM

> "Perhaps [it is] my inclination that... in as much as the gas responsible for the mysterious light was *common air*, it is fitting that the mysterious dark obscuring masses in the Galaxy would turn out to be *common clouds*."
> Taken from *Interstellar Matter*, Sir A. S. Eddington (1937)

The ISM is best thought of as a continuous field of compounds with areas of relatively higher and lower density, see Figure 1.2, with *clouds* and *clumps* being enhancements within this density field. Having established in the previous years that the *stuff between stars* was actually real material, composed of *gaseous material* (molecular, atomic and ionic) and *dust* (graphitic, graphenic (Ivanovskaya et al. 2010), silicate and metallic), astronomers set about trying to detect and track the densities and contents of this medium. Dust is mixed in with all but the hottest phases of the ISM and is a source of interstellar extinction, gas phase depletion and also are sites which provide chemistry pathways for dust grain catalysis. Dust grains vary in size from a few microns to being almost macromolecular (50-100 atoms). The grains can interact with light with the total, and wavelength dependant, extinction being due to absorption and scattering - dust clouds can been seen in the reflection of starlight from dusty clouds. We are also able to determine the shapes of the dust grains, since the light which passes through non-spherical dust grains gets polarised - which is detectable. In addition to the polarisation of light, we are also able to detect emission from the grains themselves in the form of thermal continuum emission, in the mid-to-far infrared due to the local radiation field, and also thermal continuum emission in the near-to-mid infrared.

Beginning with the discovery of interstellar Ti^+ by Dunham (1937) which was confirmed in Saha (1937) and added to the known Calcium and Sodium lines, the possibility of new interstellar tracers began to be a reality. Such is the nature of the ISM, the continuous density distribution makes it difficult for any pragmatic and objective classification scheme to be devised, since the density boundaries are a little blurred. In addition to this, any cloud decomposition can be dependant on the clump-finding algorithm used to analyse it, e.g. `GAUSSCLUMPS` (Stutzki & Guesten 1990); `CLUMPFIND` (Williams et al. 1994); `CLOUDPROPS` (Rosolowsky & Leroy 2006) - see Chapter 5.

Table 1.1 presents characteristics of some arbitrarily defined cloud classifications to show the relative parameters for the varying densities of structure, Snow & McCall (2006). To truly

Lee J Summers

Image Copyrighted.
Original source image can be found:

http://www.esa.int/SPECIALS/Planck/
SEMF2FRZ5BG_1.html

Third Party Copyright Marker

Figure 1.2: A false-colour image of the whole sky as seen by Planck. The dust throughout the Galaxy is shown in blue-scale. In the background, the yellow features show the Cosmic Microwave Background. CREDIT: ESA, Planck LFI and HFI Consortia (2010)

Table 1.1: Physical Attributes of Galactic Molecular Clouds. Table data adapted from Stahler & Palla (2004)

Cloud Type	A_v (mag)	n_{tot} (cm^{-3})	Size (pc)	Temperature (K)	Mass ($M_\odot$)	Example
Diffuse	1	500	3	50	50	ζ Ophiuchi
Giant Molecular	2	100	50	15	10^5	Orion
Dark						
Complex	5	500	10	10-25	10^4	Taurus-Auriga
Individual	10	10^3	2	10	30	B1
Dense	10	10^4	10^{-1}	10	10	TMC-1/B335

Lee J Summers

Figure 1.3: Galactic Plane emission of decreasing wavelength (decreasing from top to bottom). **Radio Continuum** (408MHz) *Bonn, Jodrell Bank & Parkes*; **Atomic Hydrogen** (21cm) *Leien-Dwingeloo, Maryland-Parkes*; **Radio Continuum** (2.4→2.7 GHz) *Bonn & Parkes*; **Molecular Hydrogen** (115GHz) *Columbia-GISS*; **Infrared** (12, 60, 100μm) *IRAS*; **Near Infrared** (1.25, 2.2, 3.5 μm) *COBE/DIRBE*; **Optical** *Lausten et al. Photomosaic*; **X-Ray** (0.25, 0.75, 1.5 keV) *ROSAT/PSPC*; **Gamma-Rays** (>100MeV) *CGRO/EGRET*. IMAGE CREDIT: NASA (2010)

appreciate the richness and diversity of emission from the ISM, remembering though originally thought to be devoid of material, the multi wavelength map of the Milky Way's Galactic plane in Figure 1.3 shows the variety of emission which is detectable within the Galaxy. The various types of tracer and their uses when observing the ISM is discussed later in the Chapter. However, before moving on to the history of cloud finding and classification, let us first consider how the ISM is structured and how one would expect to find large scale structure within it.

1.2.1 Colder, Warmer, Hotter : The Multi-Phase ISM

The One Phase Medium & One Dimensional Collisions

Models of the ISM, as with most models, have been through many iterations. The first, and most simple, interpretation is a one-phase model of the ISM, Ledoux (1951); Kaplan (1966); Spitzer (1968a); Stone (1970a). The concept of a one-phase model is that the ISM consists of homogeneous isothermal layers about a central density region. Observations of atomic hydrogen (HI) in the Galaxy found that there was no offset between the absorption and emission lines observed from a particular cloud, Hagen, Lilley, & McClain (1955); Muller (1957). The absorption lines for a given cloud appeared to contain significantly higher velocity structure compared to both the absorption immediately surrounding the cloud and also the cloud's own emission spectra. This offset was considered to be due to differences in the resolution of the obtained data. It wasn't until the works of Shuter & Verschuur (1964) that the offset was speculated to be due to the presence of a warmer inter-cloud medium. Early attempts to model the one-phase medium by Ledoux (1951) found that the one-phase model obeyed the Jeans' criterion for gravitational collapse of the *cloud*. Ledoux found in the analysis of the model that it allowed for the *nebulous* matter to condense in such a way that it propagates a gravitational instability which would lead to the formation of smaller, more compact, *nebulae*. This was revisited again, with the advent of the multi-phase medium model, as part of a series of papers by Stone (1970a), who investigated the one versus two dimensional approach to modelling cloud interactions. Using hydrodynamical models of the interactions taking place between two homogeneous interstellar masses, Stone (1970a) made assumptions regarding the internal mechanical and thermal dynamics. The issues with these one-phase models begin to present themselves post-interaction. When two masses of gas collide, there is a relatively severe compression of the material at the event-horizon, however; due to the one dimensional approximation of the model, the expansion is only in one dimension. This causes the gas, in its compressed state, to be more stable than in its diffuse state, which is unphysical. Also, post-event, shocked re-expansion of the gas does not recover the initial cloud conditions and the collisions become unrealistic (Stone 1970a,b).

The Two Phase Medium & Two Dimensional Models

It was clear that the one-phase medium was not predicting the observations. Because of this, a new interpretation of the ISM was prompted by many authors; Shuter & Verschuur (1964); Spitzer (1968b); Field, Goldsmith, & Habing (1969); Spitzer & Scott (1969); Kaplan (1977); Joshi & Tarafdar (1977); Tarafdar (1978); Monaco (2002, 2003). The ISM was found to have a wide range of thermal and density regions, these regions were amalgamated into semi-descrete phases for ease of explanation. This new two-phase interpretation (Field et al. 1969) of the ISM took into account the discrepancies with the relative differences between the velocity structure of an observed set of absorption and their related emission lines. The two-phase medium consists of the Cold Neutral Medium (CNM), usually Galactic HI or the diffuse clouds (see later), and a warmer rarefied phase identified as the Warm Inter-cloud Medium (WIM). These two phases, in pressure equilibrium, exist due to the medium being heated via interaction with cosmic radiation.

Lee J Summers

Image Copyrighted.
Original source image can be found:

Figure 5, Cox (2005)

Third Party Copyright Marker

Figure 1.4: The Two-Phase ISM, thermal pressure vs density plot (Cox 2005, adapted from Figure 5). The *red-blue-green* continuous curve is the function. red is the warm component (T $\approx 10^4$K), green is the cold component (T $\approx 10^2$K), blue is the thermally unstable regime. The dashed aqua extension to the function shows the effect of increased heating ($\approx 10\times$) on the system. The black-dashed line is the mid-plane pressure, orange-dashed line is the magnetic component of pressure.

Though this understanding of the structure was a step in the right direction, this interpretation was by no means perfect - it favours cold clouds surrounded by a warmer inter-cloud medium. The absence of a *Hot* phase leads to an estimated supernova rate which is not sustainable, McKee & Ostriker (1977). The two-phase approximation is still used in modern physics, where models are used to investigate the large-scale (rather than clumpy) nature of the ISM in the segregation of two main constituents; the cold clouds and warmer inter-cloud regions. From the derived density, one can infer the electron density and the level, and rate, of ionisation within the region of the ISM at that specific density. These are then used to form a function of thermal balance between the cooling and heating of the *cloud*, this is then used to infer a thermal pressure function; Parravano, Hollenbach, & McKee (2003). This allows one to build a function which examines the probability of material fragmentation and cloud formation, which can show the densities and temperatures (both thermal and pressure) of the cloud. It can also show that the inter-cloud gas is in thermal equilibrium, i.e. the phase segregation, see Figure 1.4. In Figure 1.4 the gas in the unstable region, gas above the curve is too hot for its density and thus cools to a more stable regime. Cooling moves material to the right of the parameter space, to higher density, this takes it further from the stable curve, which causes it to cool faster until the stable branch is reached once more. Gas below the curve has excess heating which, at constant thermal pressure, moves horizontally to the left of the parameter space to a more stable region of the curve. There are a number of *surprises* which arise from the two-phase model;

Lee J Summers

Image Copyrighted.
Original source image can be found:

Figure 10, Aller (1991)

Third Party Copyright Marker

Figure 1.5: A schematic diagram of the Three-Phase ISM, based on the model set out by McKee & Ostriker (1977) and adapted from Figure 10. in Aller (1991).

- Thermal pressure in diffuse HI has little dynamical effect. In quiescent regions, the thermal pressure is less than the magnetic pressure. Therefore the flows are on dimensional and as such the transitions between layers are longer than the expected timescales.
- Zero thermal pressure is allowed at low densities. - There is no physical need for thermal pressure
- Over a wide range of HI densities, the limited equilibrium region makes thermal pressure looks more important than it truly is.
- In quiescent regions, the magnetic field should vary inversely with the local density.
- The forbidden zone represents a slow transition between stable components.
- If cold clouds exists, when heating occurs, the photoelectric heating provides a feedback loop for an upper limit of a given pressure.

The Three and Five Phase Medium

The key assumption with the two-phase model was that the phases of the the ISM were in approximate equilibrium. This is true to the cold gas, but not so much for the warm gas. In an attempt overcome the issues over ionisation within the CNM, various modifications to the two-phase model were suggested. The existence of a *hot* region of the ISM, postulated to be due to

supernovae, was identified and investigated in Cox & Smith (1974); McKee (1990); McKee & Ostriker (1977) - see Figure 1.5 for a diagrammatic representation of the model.

Observations published by McKee & Ostriker (1977) gave rise to discrepancies which, when compared to the two-phase theory, could not be adequately explained. Exemplified in that the height structure of a two-phase ISM would be different than what we observe, McKee (1990). The overall structure of the ISM is governed by the formation and ejection of stars and stellar material from within it. From observational data, we infer that the neutral and ionised components of the ISM extend out of the Galactic plane by not a negligible amount. If one were to consider the weight (pressure) of this gas bearing down on the Galaxy, the turbulence required to maintain this scale height is more than can be provided by the CNM and WIM alone. The importance of supernovae in the overall structure of the ISM, and by inference the Galaxy, was identified previously. It is the random supernovae which generate the three-phase medium - in which hot, low density gas surround warm and cold gaseous structures, see Figure 1.5. Background X-ray observations by Williamson, Sanders, Kraushaar, McCammon, Borken, & Bunner (1974); Burstein, Borken, Kraushaar, & Sanders (1977), supplemented by UV observations using O(VI) ions (Rogerson, York, Drake, Jenkins, Morton, & Spitzer 1973; Jenkins & Meloy 1974) implied that there was an additional, as yet unseen, *hot* component to the ISM which was yielding these interesting results. Jenkins & Meloy (1974), when observing the absorption spectra of O(VI), found that measured radial velocities of these lines were not corresponding to the surrounding stellar velocities. They argue that because of this difference between the observed lines and the stellar velocities, the source of the O(VI) absorption *must* be from some interstellar matter rather than being of stellar origin. From this they infer that a new phase of the ISM, a hot phase, which would still be in in equipartition of pressure with the *normal* two-phase medium would not only be responsible for this offset in observed radial velocity, but also be the cause of the soft X-ray flux which was being observed in the diffuse background. The soft X-rays mentioned previously had already been, at least, semi-identified by Williamson et al. (1974) as indicative of a hot third phase of the ISM. Taking observations of three different lines of site in the southern sky, they observed these regions in the X-ray. It was found, all three regions were identified as having low neutral Hydrogen column densities, but the emission suggested that there was a hot component of gas, of order $T \simeq 10^5 \rightarrow 10^6$ K. Burstein et al. (1977) took further Galactic observations in three different soft X-ray flux bands; 100-188eV, 150-284eV and 500-850eV and attempted to fit the emission to known ISM sources. It was found that the X-ray flux could not be well fit to mono-thermal gas, instead the data were best fit to a three-phase medium, with the hot component being able to accommodate both the O(VI) absorption and the soft X-ray emission.

Though the three-phase medium is well accepted as a fairly accurate interpretation of the structure of the ISM, there are debates as to whether there is an even colder component in the form of *Dark Clouds* (Lindsay, Bok, & Shapley 1937; Bok 1938; Bergin & Tafalla 2007). Thought to be a short lived by-product of star formation and are discussed later. There are two schools of thought with regards to including these very small regions of cold dense gas, whether the are small enough to be negligible considering the overall characteristics of the diffuse ISM - or they are a phase in there own right, in which case it would be more accurate to describe the ISM as a

four-stage medium (Cox 2005). Still other works suggest that there may even be a *five* phase ISM (Mihalas & Binney 1981, Section 3-11, page 180). The five-phase-medium is summarised below;

- **Molecular Clouds, H_2**. This phase has a density $>10^9$ m^{-3} and a temperature range of T$\approx$ 10 $\rightarrow$ 20 K. Molecular clouds comprise of $\approx$30% of the ISM, by mass but 0.05% by volume.

- **Cold Neutral Medium, HI absorption**. The CNM HIis distributed in sheets and filaments, this phase has a density $\approx 10^8$ m^{-3} and a temperature range of T$\approx$ 80 $\rightarrow$ 100 K. By volume, the CNM is approximately 1-4% of the ISM and is traced int he UV and optical bands.

- **Warm Neutral (intercloud) Medium, HI emission**. The WNM is located on the edges of photodissociated regions and the boundaries of H II regions and molecular clouds, this phase has a density $\approx 10^5$ m^{-3} and a temperature range of T$\approx$ 8000 K. By volume, the WNM is approximately 30% of the ISM and is traced int he UV and optical bands.

- **Warm Ionised Medium, H II emission**. The WIM is due to ionisation by OB stars and is evidence of shocks and collisions high above the Galactic Plane, this phase has a density $\approx 10^6$ m^{-3} and a temperature range of T$\approx$ 6000 $\rightarrow$ 12000 K. By volume, the WIM is approximately 25% of the ISM and is traced in Hα emission (λ = 6563Å).

- **Hot Ionised Medium, X-Ray and OIV absorption**. The HIM has a vertical scale height of $\approx$ 3 kpc and is sometimes called the hot corona of the Galaxy. The hot gas is buoyant and appears as bubbles and fountains high above the disc of teh Galaxy. The HIM phase has a density $<10^4$ m^{-3}. The medium is traced is two different radiative regimes; the *hotter* gas is traced by diffuse X-Rays of $T_{hot} > 10^6$ K; the *cooler* gas is traced in the far-UV (OIV, NV and CIV) for gas $T_{cool} \approx 10^5$ K.

1.2.2 The Hierarchy of the ISM

So often in system dynamics, one makes assumptions as to the initial conditions of a system. In a theoretical world of smooth, spherical particles undertaking perfectly elastic collisions, it is important to remember that there is a vast variation in cloud structures, sub-structures and types which are attempted to be classified through observations. Though, in general, any cloud classification system is a somewhat arbitrary since the controlling parameters, such as mass and size, are not entirely objectively obtained since - as mentioned previously and discussed later in Chapter 5 - the clump-finding algorithm used has an effect on the cloud sample and parameters defined. Having referred earlier to Table 1.1, this shows one such cloud classification scheme. Instead of attempting to define a new classification system here, to give an overview of the diverse possible regimes of the ISM, the system presented in Snow & McCall (2006) will be used. This system, instead of classifying a large-scale amount of material, describes the local conditions within an individual *parcel of gas*.

Lee J Summers

Image Copyrighted.
Original source image can be found:

Figure 1, Snow & McCall (2006)

Third Party Copyright Marker

Figure 1.6: Cloud classification regimes as defined by $\frac{n(X)}{n_H}$, local number density of species X relative to the number density of H and N_H. Taken from Snow & McCall (2006), adapted from the photodissociation model of the diffuse ISM, Neufeld, Wolfire, & Schilke (2005)

Table 1.2: Physical Attributes of Diffuse Galactic Clouds. Table data adapted from Snow & McCall (2006)

	Diffuse Atomic Cloud (DAC)	Diffuse Molecular Cloud (DMC)	Translucent Cloud (TC)
Molecular Gas Fraction Classification	$f_n(H_2)<0.1$	$f_n(H_2)>0.1$, $f_n(CO)<0.9$	$f_n(C^+)<0.5$, $f_n(CO)<0.9$
A_v (min)	0	~0.2	$\sim 1 \rightarrow 2$
Typical n_{H_2} (cm^{-3})	$10 \rightarrow 100$	$100 \rightarrow 500$	$500 \rightarrow 5000$
Observational Techniques	Optical, 21cm	Optical absorption, mm absorption spectra	Optical absorption mm absorption and emission

Diffuse Clouds

The first classification of cloud to be explored is the diffuse cloud regime. With their near unity extinction, background and constituent radiation can be easily observed (and was indeed done so, see section 1.1) with the absorption lines giving information as to not only the constituent material but also the chemical reactions occurring within these clouds. There are two further distinctions

Lee J Summers

Image Copyrighted.
Original source image can be found:

http://www.nasa.gov/mission_pages/WISE/multimedia/
gallery/pia13455.html

Third Party Copyright Marker

Figure 1.7: ζ Ophiuchi clouds complex representing the Diffuse Cloud regime. Image Credit: NASA/JPL-Caltech/UCLA

within this category, the diffuse atomic cloud (DAC) and the diffuse molecular cloud (DMC). This distinction into the atomic and molecular phases of the diffuse medium, though not always made (Burgh et al. 2007), allows for a more complete description of the cloud's state within the ISM. As the name suggests, the DACs are present the regions of the ISM which are exposed to the harshest UV fields and are, as such, mostly photodissociated by strong UV fields (Saha 1937), resulting in a relatively sparse environment. Photodissociation can be split into two regimes, as defined in van Dishoeck & Visser (2011), by *small* and *large* molecular photodissociation, see section 1.3.1.

The DACs tend to mainly consist of atomic Hydrogen (HI). For reference, species with ionisation potentials less than that of Hydrogen are found in their ionic forms in these regions. The *over density* of HI causes a significant number of free electrons to exist within the clouds. As has been mentioned, the main tracer of the DACs is the 21-cm HI line first observed Galactically by Ewen & Purcell (1951); Christiansen & Hindman (1952), we will discuss this further later. The comparative scarcity of molecular matter within the DACs implies that there is an absence of chemistry, Dickey & Lockman (1990), but there is also a suggestion that this may not be the case in the form of *diffuse interstellar bands*, DiBs . DiBs were first observed in Heger (1922) and give rise to unidentified absorption in the spectra of background stars and objects, Herbig (1995). Their interstellar origin was not initially understood due to the limitations of the observing equipment available. It was not until the works of Merrill (1934) and Merrill & Humason (1938), later corroborated by Beals & Blanchet (1938), that the nature of these lines were identified as interstellar rather than being due to the target source. The DiBs detected, over a decade previously, were identified as interstellar because the velocity variations which occur in spectroscopic binaries were

not present in the DiB observations (Beals & Blanchet 1938). More recent work; Herbig (1975); Tulej, Kirkwood, Pachkov, & Maier (1998); Galazutdinov, Musaev, Krełowski, & Walker (2000), have increased the number of detected DiBs and improved the understanding of their possible sources. Initially it was thought that since the flux detected from the DiBs was proportional to the amount of reddening, when observing the background sources, the dust grains in the foreground were thought to be the source of the absorptions (Merrill & Humason 1938). It was because the existence of gas-phase molecules and the reactions thereof were not fully known nor understood hence this solid state solution to the problem. The source of the DiBs are now thought to be neutral or ionised Polycyclic Aromatic Hydrocarbons (PAHs), first found by Donn (1968). For a reference, a survey of PAHs in the interstellar medium and the effect they have on the DiBs is published by Salama et al. (1999), but is beyond the scope of this work so will not be discussed further.

Having discussed the *diffuse atomic* regime at length, we now shift our attention to the diffuse molecular clouds (DMCs). It is important to understand the importance of gas-phase species within the cloud and there are also grains of dust which account for, the canonically accepted, 1% of the cloud's total mass. The dust grains, which will be described later, provide a mechanism by which the chemistry of the cloud by enabling adsorption to the grain surface, absorption and re-emission of background photons. The presence of dust allows attenuation of the interstellar radiation field and facilitates the presence of molecules. In addition to this, the Hydrogen self-shields and thus the fraction of molecular Hydrogen is increased it also means that this protection allows gas-phase molecule reactions to occur, either through ion-neutral reactions or by dust-grain adherence (both of which are discussed later). However, the level of attenuation is not sufficient to shield the Carbon Monoxide (CO, see later) causing the Carbon to remain in its ionised form. As has been mentioned previously, a majority of the information determined about the clouds is via the absorption spectra; the main observational bands being the optical (CO, CH and CN), the near-infrared (CO and H_2^{3+}) and at mm-wavelengths (HCO^+, OH and C_2H). It is also important to note that the molecular Hydrogen exists within an atomic envelope and as such the column of Hydrogen determined will include a certain amount of the atomic component, this will yield a Hydrogen fraction significantly higher than the Hydrogen fraction at the cloud's core (Stahler & Palla 2004).

Maintaining the current nomenclature for this final diffuse cloud regime, see Table 1.2. Increasing the A_v increases the shielding effect of the cloud, reducing the photo-dissociative effect on the Carbon, which is turn allows the transcendence from the ionised, C^+, to the molecular form, CO. Chemical reactions within the Translucent Cloud (TC) regime differ from the DMC and even more so from the DAC, the reduction in the number of free electrons in the cloud and the radiation field and an increase in the number of C^+ ions allow for the gas-phase reaction of C→ CO, van Dishoeck & Black (1988). As time progresses from $t_0 \rightarrow t_0 + \delta t$, one may argue that as δt increases, it may be possible to trace a pseudo-evolutionary track along these cloud types from DAC → DMC → TC. This assumption is based on the concept that each cloud type describes relies on its predecessor to exist. In total, the diffuse clouds represent a small fraction of the overall cloud structure and gas content of the Galaxy and are not sources of significant, if any,

star formation; McKee (1989); Blitz (1997); Stahler & Palla (2004); Snow & McCall (2006).

Giant Molecular Clouds

Giant Molecular Clouds (GMCs), present a completely different dynamical chemical environment than the cloud sub-types previous discussed. A GMC is an aggregation of atomic HI and molecular H_2 gas clouds which, some believe, can exist for prolonged lengths of time through a equipartition of pressures, Stahler & Palla (2004). Though others, such as Elmegreen (1990a,b); Ballesteros-Paredes et al. (1999); Klessen et al. (2004); Ballesteros-Paredes (2006); Elmegreen (2011); Klessen (2011); Glover & Clark (2012), believe that GMC formation is a far more aggressive process due to random collisions, gravitational instabilities, angular momentum considerations, magnetic field influences and turbulent motions due to turbulent initial conditions (Mestel & Paris 1984; Crutcher 1999; Glover & Mac Low 2007; Girichidis et al. 2011; Imara & Blitz 2011; Vázquez-Semadeni et al. 2011). The thermal motion of the cold gas core is regulated by the warmer, more diffuse, envelope (similar to the DMCs). This environment leads to a situation in which star formation can commence. Star formation then occurs through the gravitational condensation of matter onto areas of more dense gas. GMCs are essentially a compound structure which are created through the aggregation of smaller *clumps* of gas into a larger structure. Similar to Galaxies leading to Groups which can lead to Clusters and so on. Though it is better to think of the GMC as an area of continuous gas where the clumps are areas of relatively high density than when compared to the inter-clump medium, Andersson et al. (1991); Evans et al. (1999); Snow & McCall (2006); Vázquez-Semadeni et al. (2011). Though as is always the way in subjective classification of large-scale structure; does one split or does one clump? Depending whether one is a *clumper* or a *splitter* will have ramifications on how one interprets the density fluctuations through out the parent cloud and as such any catalogue of cloud-like features derived (Brunt et al. 2003; Heyer et al. 2008). The effect of *clumping* or *splitting* and also the resolution dependance of derived cloud parameters are presented in Chapter 5.

From recent interpretations of observations (Stahler & Palla 2004; Heitsch et al. 2005; Elmegreen 2000; Efremov 2011; Elmegreen 2011; Klessen 2011) and simulations (Dobbs et al. 2006, 2010; Dobbs 2010), it is possible to deduce that the clustering (hence forming the GMC) occurs as gas flows into potential wells along the spiral arms of the Galaxy. Molecular clumps form within the GMC through condensation, this is a self protecting process by which the condensation of atomic to molecular matter leads to shielding from the UV radiation, thus causing the photodissociation of the products which, in turn, assist in the production more more molecular matter. The space between *clumps* is occupied by the *inter-clump medium*, ICM, which is of lower density, as previously mentioned, than that of the clumps. Through the detection of $^{13}C^{16}O$ absorption lines, it is possible to deduce that some fraction of the ICM is molecular, with the remainder being atomic in nature, detected through the 21-cm line (Blitz & Williams 1999). The atomic gas envelopes of the GMCs, in linear size, are significantly larger than the complexes which they surround. On average a GMC envelope can extend for several times the linear size of the cloud, Weinreb et al. (1963).

It is still a controversial matter as to whether the individual velocity dispersions of clumps

Lee J Summers

Image Copyrighted.
Original source image can be found:

http://www.spitzer.caltech.edu

Third Party Copyright Marker

Figure 1.8: The W5 molecular cloud complex. Image Credit : NASA/JPL-Caltech, Spitzer Space Telescope, http://www.spitzer.caltech.edu

within a cloud is random with no systematically significant motion to a common point of collapse (Stark & Brand 1989; Walsh et al. 2002; Stark & Lee 2006; Tasker & Tan 2009). If this were true then it would imply that a GMC complex structure is in equilibrium until destroyed by the stars which it spawns. However, it is commonly thought that the clouds are in equipartition of the thermal, kinetic, gravitational and magnetic pressures. It is this *balance* of these pressure which maintain the GMC structure. Using the Virial Theorem, one may assume that a balanced cloud may be in a state of pseudo-Virial Equilibrium, or Energy-Equipartition (Ballesteros-Paredes 2006), hence the following can be considered to be true;

$$2T + 2U + W + M = 0 \tag{1.1}$$

Where T is the total kinetic energy of the bulk motion, U is the energy contained in the random thermal motion, W is the gravitational potential energy and M is the energy associated with the magnetic field. Though the equation appears to be showing all the pressures/energies are equatable to one-another. This is an incorrect assumption. Consider, instead, a spheroidal shell encompassing the 'complete' cloud, this equation describes the equipartition of net flow of energy through the surface of the shell. The expression gives the impression that the clouds are somewhat docile and in equilibrium. However, authors such as; Blitz & Shu (1980), Ballesteros-Paredes et al. (1999), Elmegreen (2000), Ballesteros-Paredes (2006) and Ballesteros-Paredes et al. (2008) believe the clouds to be more dynamic and energetic than transient. With the clouds having short formation times, and having a rapid evolutionary sequences due to the high velocity HI streams within the cloud causing disruption and density fluctuations within the complex (Ballesteros-Paredes et al.

1999). Also, the equilibrate and virial consideration of the clouds' nature and the description of their formation and existence is questioned (Ballesteros-Paredes 2006). The internal magnetic field of the complex is estimated by the Zeeman splitting of the OH and 21-cm spectra lines(Stahler & Palla 2004), it is noted that the internal magnetic field of the complex acts orthogonally to that of the |**B**| in the Galactic plane (Gómez & Cox 2004; Vázquez-Semadeni et al. 2011). The direction of the interior magnetic field is determined through the measurement of the polarisation of background light as it passes through the GMC complex. Any well ordered field in a self-gravitating cloud would cause matter to stream along the field lines until a planar structure for the complex is reached. Planar flattening does not appear to occur in current observational samples of GMCs and hence the interior field is thought to be smooth in nature. Internal field distortion arises from Magnetohydrodynamic waves, these MHD waves assist in the prevention of flattening of the GMC, Stahler & Palla (2004). The main source of complex support arises from the internal kinetic energy of the component clumps, which are determined through the broadening of the CO spectral line.

Dark Clouds

Dark Clouds represent the coolest and most dense regions of the ISM; Lindsay, Bok, & Shapley (1937); Bok (1938); Bergin & Tafalla (2007). This species of Galactic Molecular Cloud falls into two distinct classifications: individual and complex systems of dark cloud. Stahler & Palla (2004) state that the clumps within GMCs could be described as essentially being individual Dark Clouds, with the largest of these clumps have been found to be of the order $10^3 M_\odot$. However, larger Dark Clouds of similar density, but with mass of order $10^4 M_\odot$, exist and are referred to as Dark Cloud Complexes. Dark clouds are named such due to their high column densities ($n_{H_{2_{peak}}} \geq 10^{23} cm^{-2}$) and opacities ($A_{v_{peak}} = 100$), (Du & Yang 2008; van der Wiel & Shipman 2008). This causes the Dark Clouds to appear as dark extinctive features on an otherwise radiatively bright background, similar to the first observations of atomic and molecular clouds (Bok 1938).

Dark Cloud Complexes account for a significant fraction of star formation in Galactic clouds. However, unlike previous cloud types the Dark Cloud complexes do not form OB associations (usually synonymous with larger, more massive, stellar formation systems). The most commonly studied form of Dark Cloud Complex is the infra-red incarnation of the type - the IRDC. Since the extinction of infra-red radiation is significantly lower than that for the optical regime, the distances to which the IRDCs can be observed is greater, hence a lager sample of data is available. With observational data being more readily available for the IR regime - due to the comprehensive sky coverage mainly due to large area IR surveys such as 2MASS, Skrutskie et al. (2006), and the *Spitzer Space Telescope*'s Galactic Legacy Infra-red Mid-plane Survey Extraordinaire (GLIMPSE; Benjamin et al. (2003)) - extinction mapping has begun to combine the number density of stars with the associated colour information (Cambrésy et al. 2002).

The earliest investigations into these optically thick, so called, "Dark Regions", "Dark Nebulae" or "Dark Clouds" were conducted by Bok (1938); Bok & Reilly (1947); Lynds (1962) and later by Feitzinger & Stuewe (1984). However, many IRDCs were omitted from the final catalogues because the searching for these clouds was conducted by eye and hence many remained

excluded from the data. The IRDC subclass were discovered by the Midcourse Space Experiment (MSX), Egan et al. (1998), as dark foreground extinctive features on the otherwise radiatively bright mid-infrared background. Typical size and mass scales for the IRDCs are $\sim$ 5pc and $10^3 - 10^4 M_\odot$. The temperature of emission for the complexes is $\sim$ 25 K causing them to generally emit at $8.6 \rightarrow 10.6 \mu$m. This low temperature implies there is a lack of massive star formation which is usually associated with the more dense cloud morphologies. Conversely, the conditions described make them exemplary candidates for the sites of early stages of star formation, Simon et al. (2006).

The shape of the IRDCs can be either compact (core-like) or filamentary in nature (similar in morphology to that of galaxy cluster aggregations). It has been found, through observation of the clouds, that the distribution of the IRDCs peaks towards sites of star formation, the spiral arm tangents and the 5 kpc Galactic molecular ring. Though Du & Yang (2008) suggests this distribution may be nothing more than an amplified selection effect and states a larger, more uniform survey, would be required to ascertain whether this pattern is true. van der Wiel & Shipman (2008) suggests that it has not yet been established whether, or not, all IRDCs harbour active star formation or just starless cores. The IRDCs represent the densest condensations of molecular material ($10^3 \rightarrow 10^6$ cm^{-3}). The elongated morphology of the IRDCs may be the result of the contraction of larger, less dense, gas clouds, which collapse down, via conservation of angular momentum, to naturally flattened structures (Churchwell et al. 2009). These cold (T<20 K) and dense ($< 10^5$ cm^{-3}) regions were found, from the earliest observations to be the sites of star formation (Carey et al. 1998; Pillai et al. 2006; Kauffmann & Pillai 2010; Benaglia 2011; Beuther 2011) . The work by Bergin & Tafalla (2007) suggests that these Dark Clouds represent the most accessible sites where solar mass stars can be born and are the precursors to stellar cluster environments - which by inference of the concepts proposed in Blitz & Williams (1999), should be the sites of future massive star formation (Churchwell et al. 2009; Vasyunina et al. 2009; Kauffmann & Pillai 2010; Benaglia 2011). Though the structure of these IRDCs are useful in understanding other aspects of the Galaxy; the non-planar nature of some IRDCs can be indicative of differential Galactic rotation, but the distortion out of the plane is not explained by this. The non-planar distortions of the IRDCs could be indicative of a turbulent ISM with the non-smooth boundaries of the IRDCs also implicating the presence of this turbulence.

Though research into the nature (and possible nurture) of the formation and maintenance of Dark Clouds & Complexes is ongoing, several questions remain unanswered; Is there an evolutionary path within the class? Are they part of some larger evolutionary sequence, of which we only have a snap-shot? Some schools of thought believe that the Dark Clouds are in fact evolutionary stepping stones, an intermediate species, linking the GMCs with the Dense Cores (and Bok Globules). Implying there is a, currently misunderstood, mechanism linking all three cloud classes. Du & Yang (2008) goes on to state that we may only truly understand the links, if any, between these classes via more detailed mapping of the sources using a variety of tracers, only then may these issues be clarified.

Dense Molecular Clouds

The final cloud type to be discussed is the Dense Molecular Cloud. Within this classification there are two further sub-classes; the Dense Cores, dense compact dense molecular regions which are within some larger molecular complex structure; and the Bok Globule, named for the astronomer whom first observed these objects Bok & Reilly (1947). The extrinsic difference between the Dense Cores and the Bok Globules is; where the Dense Cores are embedded in a larger cloud structure, the Bok Globules are not. So, Bok Globules may be considered as isolated cores, giving information that would otherwise be unavailable in an embedded core observation (Bok 1977). The molecular line characteristics of these cores will not be discussed in detail here, however, for completeness it is noted that the different molecular line transitions require varying levels of hydrogen density, n_{H_2}, to allow the transition excitation to occur. Dense Cores which have not yet formed stars are said to be pre-steller or starless cores (Benson & Myers 1989), these are considered to be the earliest form (in terms of formation chronology) of this cloud-type. These pre-stellar cores are characterised by a distinct lack of any point IR source at the centre of the cloud, Tafalla (2008), though this could be due to current limits in millimetre and sub-millimetre sensitivity and resolution. Starless cores tend to reflect a somewhat uniform density of $10^5 \rightarrow 10^6 \mathrm{cm}^{-3}$ for the central region, 5000< $\frac{R}{[\mathrm{AU}]}$ <10000. Outside this central area, the density drops off as a power law at larger distances. As the Dense Cores evolve; self-gravitational collapse through local fluctuations in the distribution of matter causes an increase in the central point density. Eventually this over density will reach a limit where, the point density causes gravitational instability in the core, Tafalla (2008). This gravitational instability causes the core to condense and collapse. Dense Cores are sites of major star formation; the condensation, through rotational collapse, of the Dense Core matter forms stars. This collapse causes the magnetic field lines interior to the core to become parallel to the gas motion. This occurs to a set limit where the magnetic pressure generated by the compression of field lines equals that of the self-gravitating, which impedes any further collapse.

Shifting our attention from the embedded cores to that of, the previously mentioned, Bok Globules. With the exception of their relative isolation exterior to larger cloud complexes, the Bok Globules are essentially the same, in terms of physical attributes, to that of the embedded Dense Cores. The catalogue of Bok globules, published by Clemens & Barvainis (1988), contained 248 small, isolated, centrally opaque molecular clouds with angular sizes less that 10' (though of varying linear size) - see Figure 1.9 for the positional extents and locations of the clouds within the Galaxy. Using these objects as a basis, they then compared the the locations of the clouds to the 1985 *IRAS* point source catalogue and found that 346 were, or were probably, associated with 149 of the catalogued clouds. Clemens & Barvainis (1988) concluded that for the 149 clouds, the lack of stellar foreground emission and the fact that these candidates subtended the smallest angles within the catalogue as a whole - linear equivalent of all being <1.5 pc, that these clouds represented the most simple form of dark clouds in the Galaxy - Bok Globules. Clemens & Barvainis (1988) also investigated the ellipticity of these small clouds and deduced a mean E($\frac{a}{b}$)=2, implying that the standard set of spherical models may not be applicable when describing the evolution of these objects. This catalogue of associated objects was subsequently supplemented in

the southern sky by the works of Bourke et al. (1995a,b), who studied 169 globules - 76 of which were found to have *IRAS* sources probably associated with them.

Lee J Summers

Image Copyrighted.
Original source image can be found:

Figure 3, Clemens & Barvainis (1988)

Third Party Copyright Marker

Figure 1.9: Adapted from Figure 3 in Clemens & Barvainis (1988) showing the Galactic distribution of clouds surveyed. The star forming regions of Ophiuchus, Taurus and Orion are indicated showing that a majority of the clouds surveyed resides exterior to these regions. The *catalogued* and *uncatalogued* points refer to works prior to the Clemens & Barvainis (1988) work.

Their sparse surroundings and simple appearance make Bok Globules ideal candidates for high resolution mapping of Dense Cores. Bok Globules tend to consist of a core, mass of the order $10M_{\odot}$, which is then surrounded by an envelope of gas approximately twice the mass of the BG-core (Clemens & Barvainis 1988). At the centre of the Bok Globule, so far only IR stars of low luminosity have been detected. A typical example of this is *object 5335*, near the peak density of its core, lies a far infra-red star of luminosity $3L_{\odot}$, Stahler & Palla (2004). Thus far, research into Bok Globules have only yielded detections of low IR luminosity stars at the centre of Bok Globules and Dense Cores alike. This forces one to postulate on where more massive stars are formed. How, for example, are massive stars formed if, even in the most dense regions, stars of relatively low luminosity/mass are *born*? Bok Globules could be the solution to this problem. One may consider Bok Globules to be the remnants of such a birth, the cores of once large cloud complexes which have long been dispersed by both radiative and stellar pressure or the formed stars it once contained (Benson & Myers 1989; Stahler & Palla 2004; Simon et al. 2006). However, this is problematic to observe directly; since high mass stars tend to disperse their parent clouds over a time scale significantly shorter than that of the stellar lifetime, it is difficult to observe the birth of such O and B stars, but relatively easy to observe their formation's destructive consequences.

Other works such as Huard et al. (1999, 2000); Launhardt et al. (2000), suggest that within Bok Globules there are multiple epochs of star formation which allow stars of varying ages to exist

Table 1.3: Tracer compounds used in the study of the ISM: T_0, equivalent temperature; n_{crit}, critical density of the main isotopologue; A_{ul} , probability per time of spontaneous decay from its upper to its lower state. Data Table adapted from Stahler & Palla (2004)

Molecule	Relative Abundance	Transition Type	Detected λ	T_0 (K)	n_{crit} cm^{-3}	A_{ul} (s^{-1})	Tracer of
H_2	1	vibrational	2.1μm	6600	$7.8x10^7$	$8.5x10^{-7}$	Shock
CO	$8x10^{-5}$	rotational	2.6 mm	5.5	$3.0x10^3$	$7.5x10^{-8}$	Low Density
OH	$3x10^{-7}$	Λ-doubling	18cm	0.08	$1.4x10^0$	$7.2x10^{-11}$	Magnetic Field
NH_3	$2x10^{-8}$	inversion	1.3cm	1.1	$1.9x10^4$	$1.7x10^{-7}$	Temperature
H_2CO	$2x10^{-8}$	rotational	2.1mm	6.9	$1.3x10^6$	$5.3x10^{-5}$	High Density
CS	$1x10^{-8}$	rotational	3.1mm	4.6	$4.2x10^5$	$1.7x10^{-5}$	High Density
HCO^+	$8x10^{-9}$	rotational	3.4mm	4.3	$1.3x10^5$	$5.5x10^{-5}$	Ionisation
			1.3mm	1.1	$1.4x10^3$	$1.9x10^{-9}$	Maser Emission
H_2O	$7x10^{-8}$	rotational					
			527μ m	27.3	$1.7x10^7$	$3.5x10^{-3}$	Warm Gas Probe

within a relatively confined volume. With Huard et al. (1999) finding stars of various evolutionary ages within the same globule - a mix of class 0 protostars and class I and class II pre-main sequence stars - and Launhardt et al. (2000) finding that, through observations of star-forming cores in the globules, there exists hierarchical stellar systems or binaries instead of single stellar objects. Launhardt et al. (2000) suggest that a cause of these multiple stellar systems is due to multiple condensations of molecular material within each globule. Though it should be noted that presence of a binary system does not automatically imply such a state (Sterzik et al. 2003). In summary, the Bok Globules provide astronomers with a unique opportunity to observe the conditions of very dense condensations of the ISM in relative isolation, giving valuable information as to the conditions and physics within embedded structures.

1.3 Chemical and Physical Mechanisms within the ISM

Knowing there is an aggregation of *stuff* in a clumpy state in space is all well and good but this does not give any understanding as to its composition. The next step is how to analyse these clouds to better understand their nature. Probably the most simple piece of information of interest to astronomers studying the ISM is; *how much stuff is in this thing I'm observing?*, or to put it another way: *how massive is the cloud?*

Referring to Table 1.3, it can be seen that molecular Hydrogen is dominant by mass, therefore it is reasonable to assume that to a significant degree, the total mass of the molecular cloud. The problem with trying to detect Hydrogen in its molecular form is that the molecule is axi-symmetic, it doesn't have a dipole moment and, therefore, is not easily excited. Astronomers circumvent this problem by looking for and detecting tracer molecules. These tracer molecules whose measurable properties, in terms of abundances or emission give astronomers information as to a cloud's properties. For example, when determining the molecular hydrogen content of the

Lee J Summers

Image Copyrighted.
Original source image can be found:

Figure 1, van Dishoeck & Visser (2011)

Third Party Copyright Marker

Figure 1.10: Photodissociation processes for diatomic - and small polyatomic - molecules and the corresponding cross-section. **AB** is a molecule whose products are **A** and **B**; and D_e is the energy of an incident photon. Figure adapted from van Dishoeck & Visser (2011), based on the work of van Dishoeck & Black (1988)

cloud, essentially a cloud's mass, astronomers use carbon monoxide to trace the hydrogen content - since the CO formation is thought to be proportional to the H_2 and as such more CO implies more H_2. To begin to understand how these molecules form, it would be best to start with and understanding of the chemistry within the clouds to outline the mechanisms involved.

1.3.1 The Photodissociation of Molecules

A process which has been mentioned previously, *photodissociation* is the primary method of dissipation of gaseous molecular species in regions of the ISM which are exposed to strong UV radiation field, this generally occurring in the diffuse and translucent cloud regimes (as discussed in section 1.2.2). The photodissociation rate for a given region of ISM is dependant on the cross-section (i.e. the likelihood of interaction) of the process involving the molecule, the strength of the incident radiation and also the position of the molecule within the UV field and cloud.

Figure 1.10 shows a summary of the three photo-dissociative processes in the case of diatomic and small polyatomtic molecules. Briefly discussing Figure 1.10 from top down, the first process is *direct photodissociation*. Direct photodissociation is where a single molecule (AB) absorbs an incident photon of energy, D_e and is excited from the ground to a higher electronic state. This process has typical reaction rates for this process are $A_{21} \simeq \frac{10^9}{\text{second}}$ and with $t_{\text{photo}} \simeq \frac{10^{13}}{\text{second}}$. Due to the slow spontaneous return to the ground state, this almost always results in a successful reaction forming two separate products (A+B, in Figure 1.10). The ease with which these reac-

tions can occur and the difficult with which the electrons would return to the ground state causes the cross-section of this process to be dependant on the wavelength of the incident UV-photon peaking at D_e.

Not all photodissociation occurs with molecules existing in their ground state, *pre-dissociation* occurs in the regime where the incident photon interacts with an electron shell in an excited bound state. Generally these bound-state electrons have a negative potential energy and as such are required to interact non-radiatively with one another. The pre-dissociation rate is usually comparable to, or greater than, the rate for spontaneous emission and as such is the dominant process. However, in the situation where the excited bound state is not pre-dissociated it is still possible for *spontaneous radiative dissociation* to occur. Spontaneous radiative dissociation involves the emission of continuum energy photons. Since any given molecule has a number of possible excited states, when exposed to a UV field it is possible (at least statistically speaking) for all three methods of photodissociation to occur, but in reality only a maximum of two of these pathways occur in the interstellar environment, van Dishoeck & Visser (2011).

1.3.2 Molecular Cloud Chemistry

One of the main reasons for why early studies of the ISM found it so difficult to believe there to be interstellar molecules was that they did not really understand how such molecules could exist in such a sparse medium. Within even the most quiescent clouds, there exists some degree of dynamical perturbation due to the processes occurring in the cloud's interior. Most of the reactions tend to be occur via ion-molecule interactions; where an ion and a stable molecular form - through the slight polarisation of its neutral atom, thus causing an instantaneous-induced dipole electrostatic attraction. Ion-neutral and ion-molecule were identified by Herbst & Klemperer (1973); D'Hendecourt, Allamandola, Baas, & Greenberg (1982).

$$\alpha^{\pm} + \beta \rightarrow \gamma^{\pm} + \delta \tag{1.2}$$

Note : if $\alpha = \delta$ and $\beta = \gamma$ then the reaction is merely *Charge Exchange*

The ion-molecule reaction pathway allows reactions, within even the coolest clouds, in regions where the temperature is too low for the neutral-neutral reaction pathway to overcome its associated potential barrier ($\frac{\delta E}{k_b}$ = 1000K). During the early 1970s (Herbst & Klemperer 1973), the ion-molecule pathway had been accepted as a possible route to overcome the potential barrier. It was found that the effective cross-section of the reaction, due to the long-range nature of the electrostatic attractive force, was greatly increased when compared to that of the cross-section of a solely collisional reaction mechanism. Even at Dark and Dense Cloud temperatures, the reactions can proceed with enough pace to account for the observed abundances of the isotopologues for various species. Though these regions are cold and dense, the molecules within them acquire energy by heating via incident cosmic-rays (Stahler & Palla 2004). Though the expression in equation 1.2 shows that reactions involving negative ions are possible, they are less frequent than those involving a positive species. The only difference with negative reactions are that there is a free electron as one of the products. The free electrons created by negative-ion interaction destroys

the positive ionic species within the clouds. Often, auto-ionisation occurs with the species just re-emitting the electron into the intra-cloud medium. However, if the reacting species spits before auto ionisation occurs;

$$\alpha^{+} + e^{-} \rightarrow \beta + \gamma \tag{1.3}$$

Thus, two neutral molecules will be the product of the reaction. Most of the processes detailed in this chapter occur via the reaction mechanisms above. The exception being H_2 which forms using the surface of the clouds dust grains as a catalyst surface on which to adhere (Hollenbach & Salpeter (1971); Gould & Salpeter (1963); Gould et al. (1963)).

1.3.3 The Detection of Atomic Hydrogen

The most simple and abundant atom in the Universe, first observed in by Christiansen & Hindman (1952) though predicted by van de Hulst in 1945, the 21-cm HI line has been used for studies of the atomic gas component of not only the Milky Way's ISM but also that of other galaxies. Using the Galaxy as a template for observation, the distribution of HI within the Galaxy is fairly widespread, see Figure 1.11. However, this widespread distribution was, and is, useful for determining the Galactic rotation curve. The HI emission will be doppler shifted at by varying amounts at different positions through the Galactic disc. The traditional view of HI was that the atomic gas surrounded the molecular content as a protective envelope. The atomic gas envelope which surrounds the molecular clouds is significantly more extended compared to molecular core which it surrounds. The source of these envelopes may be the remnants of the atomic clouds which condensed to form the molecular component or it may be it photo-dissociated material from the molecular cloud, (Blitz & Williams 1999). Atomic Hydrogen is also useful in tracking the spiral arms of the Galaxy and can be used to refine velocity models, see later. From the image in Figure 1.11, it can be seen that the observations of the HI can be a little *messy* at times with the circular artefacts obvious in the inner-Galaxy and also the *fingers of God* effect pointing towards the Solar position - see Section 1.5.2.

1.3.4 Formation of Molecular Hydrogen

Dust Grain Catalysis

As has been mentioned previously, the lack of a dipole moment on the H_2 molecule makes it very difficult to detect. When it was first discussed in Gould & Salpeter (1963), though the interstellar H_2 was unable to be detected at that time, the presence of it within the ISM was suspected. Radio observations of Galactic structure had shown that the spiral arms of the Galaxy are filled with neutral atomic Hydrogen, however there were elements of higher density *invisible* mass within the HI clouds. It was suggested that the atomic Hydrogen would be able to combine and form H_2 via a mechanism referred to as *dust grain catalysis*. The adsorption of the Hydrogen molecules provide a reaction surface (in the first instance an ideal lattice), by reducing the effective binding energy of the individual Hydrogen atoms allowing them to bind to one-another (Gould et al. 1963). On

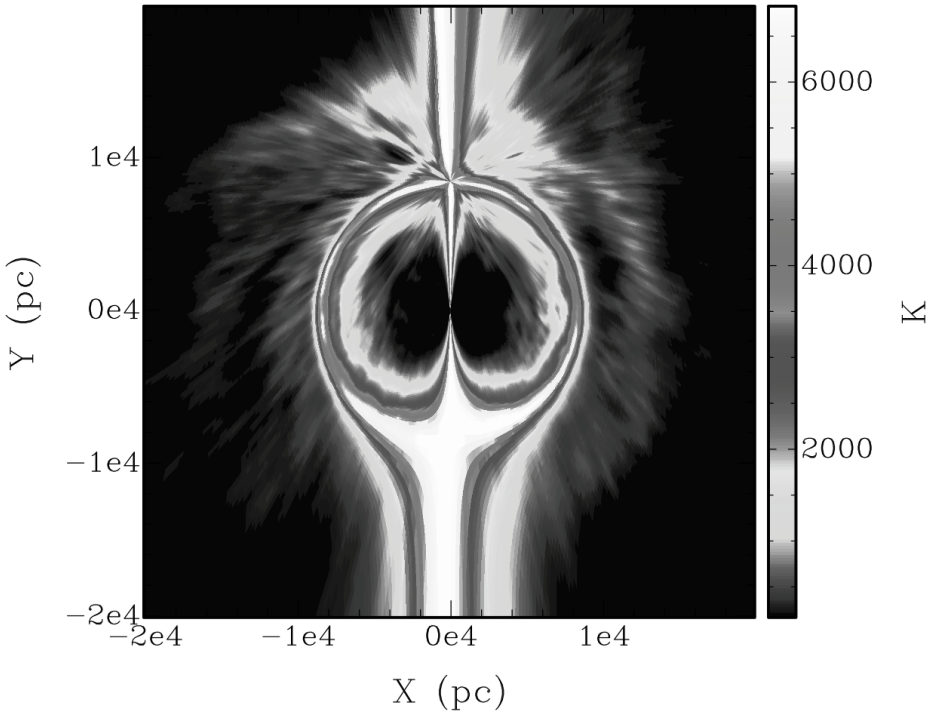

Figure 1.11: The raw, uncorrected, summed temperature map showing the Galactic distribution of Atomic Hydrogen (HI), as viewed through the b=0^o plane. The Galactic centre is at (0,0) and, by extension, the Solar position is at (0, 8500). The velocity compression in the centre and anti-centre regions are shown in the excess in emission in these regions. Though the exact mapping of emission from (ℓ, b, v_{LSR}) to (X,Y) is difficult since the exact contribution of angle to space is troublesome to map.

the surfaces of the dust grains, see Figure 1.12, the H atoms are able to recombine. The atoms are physisorbed and chemisorbed, the with mobility of the atoms across the surface being governed by the quantum mechanical tunnelling, Cazaux & Tielens (2004, 2010), though the exact mechanism through which the atoms combine is somewhat dependant on the composition of the dust grain. Depending on whether the grain has an ice-based mantle surrounding a carbon or silicon based core; Govers, Mattera, & Scoles (1980). The main issue with the modelling of this mechanism is that since, at least in the astrophysical context, the dust grains generally exist in environments where there is relatively little shielding, it is therefore assumed that the dust on to which the H atoms combine will not have an ice-based mantle. Hence, most more recent models concentrate on dust which is graphitic (Pirronello et al. 1997a), graphenic (Ivanovskaya et al. 2010) or silicate (Pirronello et al. 1997b) in nature without an ice-based mantle surface on which to adsorb.

Consider two Hydrogen atoms, H_α and H_β; The first incident atom, H_α, is attracted to the dust grain by a van der Waals attraction (physisorption) and adsorbs to the dust grain's surface. So as to exist at the lowest possible energy, H_α quantum mechanically tunnels to find a defect in the structural lattice. Once at this defect, the H_α atom forms a stronger bond with the structure using its unpaired electron. The difference in binding energy strength between the van der Waals and the ionic lattice bond is; $\frac{E_{IB}}{E_{vdW}} = 2.5$. Within a time interval, given by t_{coll} (equation 2.3),

Lee J Summers

Figure 1.12: Hydrogen Forming on dust grain surfaces. Left: Axisymmetric molecular Hydrogen, Right: dust grain surface reactions (Image Credit: Gianfranco Vidali, Syracuse University, 1999).

a second atom, H_β, attracted to H_α, finds a binding site near to H_α and the two atoms combine. Post-combination the molecular hydrogen created does not have an unpaired set of electrons and is therefore only weakly bonded to the granular surface, hence, through the mechanisms stated above, the H_2 returns to the gas-phase. However, some argue that a cloud lifetime of 1-2 Myr is too short to account for the formation of the *required* volume of H_2. An approximate H_2 formation rate is described in Hollenbach & McKee (1979); Mac Low & Glover (2012),

$$t_{\text{formation}} \simeq \frac{10^9 \text{yr}}{\text{n}} \tag{1.4}$$

With the full derivation in Appendix A, n is the number density in cm^{-3}, suggesting, for a cloud averaged density of $\overline{n}$ $\sim$100cm^{-3} conversion of atomic to molecular Hydrogen takes longer than the lifetime of a transient cloud; approximately 10 Myr, Blitz & Shu (1980). This approximation, however, does not take into account turbulent conditions within the clouds from internal dispersive motions, Glover & Mac Low (2007).

Though this is an elegant solution to the formation of H_2 in the ISM, there are still discrepancies as to the efficiency of this process. By I mean that it does not account for all the inferred molecular Hydrogen inhabiting the ISM. The removal of the perfect lattice and the introduction of a "defective" lattice in Hollenbach & Salpeter (1971) allowed this process to occur at lower grain temperatures. This mechanism is efficient at temperatures <20K and a plausible explanation of formation. Even at higher temperatures, of hundreds of kelvin, Cazaux & Tielens (2004, 2010) found that the atoms can be strongly or weakly bound to the grain surface and can move from one site to another through quantum mechanical tunnelling according to their mass and the tempera-

ture of the grain. More recent works on the intermediate temperature regime of the ISM, Thrower et al. (2011), postulate that molecular Hydrogen may also form via neutral super-hydrogenated polyaromatic hydrocarbons as catalysts, which provide the adsorption sites, through a mechanism similar to the grain-based pathway already described.

Gas Phase Reactions

In addition to the reaction on dust grain surfaces mentioned previously, at higher pressures, densities and temperatures it is possible for H_2 to form in an environment completely devoid of dust, occurring completely in the gas-phase. The regime is analogous to the conditions early in the existence of the Galaxy. In these more extreme conditions there are two reaction coupled pathways by which the Hydrogen can form;

$$H + e^- \rightarrow H^- + h\nu \Rightarrow H^- + H \rightarrow H_2 + e^- \tag{1.5}$$

Where $h\nu$ denotes a photon. The ambient photons created allow the production of H_2 through;

$$H + H^+ \rightarrow H_2^+ + h\nu \Rightarrow H_2^+ + H \rightarrow H_2 + H^+ \tag{1.6}$$

The above reactions are valid for the early Universe, before the condensation of dust, due to the limited supply of free ions, the number of molecules created by this path would be small. It is noteworthy, however, that at sufficiently high temperatures the following reaction takes place which could have been responsible for the first formed molecular clouds, Glover & Mac Low (2011);

$$H + H + H \rightarrow H_2 + H \Rightarrow H_2 + H + H \rightarrow 2H_2 \tag{1.7}$$

The depletion of H_2 occurs via the photodissociation of the molecule by UV photons produced by O and B type stars, see section 1.2.2. Because of this photodissociation, it is not possible for there to exist a cloud of pure molecular Hydrogen. H_2 becomes self-shielding through the creation of an atomic envelope around the H_2, which protects the interior Hydrogen from the photodissociatative effect of the photons by cutting down the penetrating radiation.

1.3.5 Formation & Detection of Carbon Monoxide

The first detection of interstellar Carbon Monoxide (CO) was conducted by Wilson, Jefferts, & Penzias (1970). The observations of nine sources towards the Orion nebula detected sharp emission at 2.6mm (T=5.5 K and $\Delta E_{1\rightarrow 0} = 4.8 \times 10^{-4}$eV), which they attributed to CO, the original detection profile can be seen in Figure 1.13. From the Figure it is easy to see why these observations were so exciting, not only is the emission sharply peaked with respect to any background noise.

Unlike H_2, CO *does* have a permanent dipole moment which causes strong emission through the radio frequencies. The asymmetry of the molecule allows, when excited, to be rotationally stimulated and the changing electric field produced by the dipole emits radiation at radio wave-

Lee J Summers

Image Copyrighted.
Original source image can be found:

Figures 1 & 2, Wilson et al. (1970)

Third Party Copyright Marker

Figure 1.13: Left: The spectrum of CO in the Orion Nebula made with the NARAO receiver. The central frequency being 115, 267.2 MHz. Right: Distribution in Right Ascension of the peak antenna temperature. Both plots taken from Wilson et al. (1970)

lengths (2.6mm). CO, and its various isotopologues thereof, is considered to be the primary tracer of molecular gas in both intra- and extra-galactic astronomy. The isotopologue which is easiest to detect, according to Stahler & Palla (2004) is $^{12}C^{16}O$, with $^{13}C^{16}O$, $^{12}C^{18}O$ and $^{12}C^{17}O$ also proving useful as a pobe of differing densities (Goldsmith et al. 1997). The low critical density of CO allows it to be used to probe the lower density regions of clouds rather than dense cores. The reason for this being that within the cores themselves, the radiation of the detectable J= 1→ 0 transition is completely absorbed by optically thick core medium. It is for this reason that the other CO isomers are used since they are not optically thick in these regions. The CO is excited to the J=1 state by the collisional excitation of CO with H_2. The consequence of the collision is dependent on the ambient density of the medium. If the CO-H_2 collision occurs in an area of low ambient density, then the transition of the CO, J= 0→ 1 is immediately followed by the emission of a photon, resulting from the CO not having any other molecules with whom to transfer its energy . When the ambient density is high, then the CO can pass its energy to a H_2 molecule, which results in no photon emission, Stahler & Palla (2004). The lowest rotational levels of the CO energies and progressively occupied as the cloud density increases (Goldsmith et al. 1997).

The next most abundant compound after molecular Hydrogen, CO is created through gas-phase reactions in the ISM. The species has a comparatively high binding energy (11.1 eV) thus protecting it from additional destructive reactions, auto-ionisation *etc*. Due to the self-shielding effect of CO, it aggregates in a similar manner to that of H_2 (but remains dissociated to a greater depth), hence it allows CO to be an accurate tracer of the Hydrogen mass of the cloud.

One possible pathway of CO formation is through gas-phase reactions involving CH^+, CH

and OH; (Oppenheimer & Dalgarno 1975; van Dishoeck & Black 1988).

$$CH^+ + O \rightarrow CO + H^+ \rightarrow CO^+ + H \tag{1.8}$$

$$CO^+ + H \rightarrow CO + H^+ \tag{1.9}$$

$$CH + O \rightarrow CO + H \tag{1.10}$$

As with the H_2, the actual amount of CO can be miscalculated. In very warm - low density - regions, the CO suffers from photodissociation from UV photons and as such becomes undetectable by these methods and as such the amount of CO can be underestimated. Conversely; more dense - cooler - regions, also suffer from CO depletion through *Gas-Phase Freeze-Out*, Bergin & Tafalla (2007). This is where the CO molecules freeze onto the surfaces of the dust grains within the cloud itself - removing that molecule from the gas phase and hence from being a possible reactant. This was found to dominate in clouds with densities higher than $\sim 3\text{x}10^{-4}\text{cm}^{-3}$, Bacmann et al. (2002).

1.3.6 Converting a CO Detection to a Column of H_2: The X_{CO} Factor

As has been previously covered at length, molecular clouds are mass dominated by molecular Hydrogen and it was discussed how the lack of a dipole moment on the axisymmetric Hydrogen molecule makes it difficult to detect. It is known that the CO and H_2 form at proportionate abundances. Therefore, if one knows the column density of the CO, one may infer the column density of the Hydrogen nuclei. However, using the ratio of the $\frac{N(CO)}{N(HI)+N(H_2)}$ to calculate this, owing to differences in the values $\frac{N(CO)}{N(HI)+N(H_2)}$ used, causes the masses of clouds determined by this method were subject to a large uncertainty, Liszt (1982). This was mainly to do with the abundance of the $\frac{CO}{H_2}$ varying with most lines of sight and also what value an individual astronomer preferred - usually based on the extinction along the line-of-sight. The X_{CO} was initially determined by the optical absorption along the line of sight and then applied to the column as necessary. It was realised that this method was the best way to diagnose the masses of the molecular clouds, but the subjective nature of the conversion constant was concerning. It wasn't until the work of Liszt (1982) that an attempt was made to homogenise the $\frac{N(CO)}{N(HI)+N(H_2)}$ *constant*. I use the word *constant* with reservation, since it is not in the truest sense of the word 'constant', as we shall see shortly.

The work presented in Liszt (1982) found, by observing clouds along many different lines of sight, that the integrated intensity of ^{12}CO at the 2.6mm wavelength varied very little with the conditions inferred within the cloud. He found there to be a fairly uniform ratio of ;

$$X_{CO} = \frac{N(H)}{\int T_A^* dv} = 1.0 \pm 0.5 \times 10^{21} (\text{K.kms}^{-1})^{-1} \tag{1.11}$$

This is by no means is a solution to solve all the problems of cloud analysis, it is best to consider it more a 'mystical' rather than a 'magic bullet' solution. More recent works on modelling X_{CO} have found that the initial findings - that it is invariant with environment - is not entirely true. Subsequent works have found that X_{CO} can vary with local density (by extension,

UV field strength) and metallically, see Figure 1.14.

Lee J Summers

Image Copyrighted.
Original source image can be found:

Figure 1, Glover & MacLow (2010)

Third Party Copyright Marker

Figure 1.14: Variation of modelled X_{CO} with environment, specifically local density. The dotted lines in the left plot show the values from equation 1.12, whereas the dashed line shows a constant $(1.8\pm0.3)\times10^{20}$. Plots adapted from Glover & Mac Low (2010, 2011).

X_{CO} parameters modelled in Glover & Mac Low (2011)

$$X_{CO_{est}}[A_v < 3.3] = \frac{N(H)}{\int T_A^* dv} \simeq \left(\frac{A_v}{3.3}\right)^{3.3} \times (2.4 \times 10^{20})\left[\frac{1}{K.km\ s^{-1}}\right] \tag{1.12}$$

$$X_{CO_{est}}[A_v > 3.3] = \frac{N(H)}{\int T_A^* dv} \simeq (2.4 \times 10^{20})\left[\frac{1}{K.km\ s^{-1}}\right]$$

From the plots in Figure 1.14, one can see that there is a change in estimated value for X_{CO} at varying metallically and density. The left panel in Figure 1.14 shows that, for extinctions of $A_v < 3.3$, X_{CO} depends on the A_v where as at higher densities: the value of X_{CO} is more consistent with the value obtained by Dame et al. (2001), which was determined observationally within the Milky Way. Glover & Mac Low (2010) notes that though there is *some* variation of X_{CO} with metallicity, for a given extinction (in these simulations at least) the variation of is very little, so too is the dependence of X_{CO} upon it. Glover & Mac Low (2011) suggest that previous works which have suggested a strong correlation between metallicity and X_{CO} (Obreschkow & Rawlings 2009), do so because of the dependance of metallicity and observed visual extinction for a fixed cloud size and density - rather than by a direct correlation between these factors. The second plot in Figure 1.14 shows that the presence, or not, of the UV field has little effect on the observed X_{CO} value at $[A_v > 3.3]$, but at $[A_v < 3.3]$ the simulations suggest that the photodissociation of the ^{12}CO at these lower A_v can explain why we observe the Milky Way value of X_{CO} to be

approximately (1.8± 0.3) $\times 10^{20}$ ($K^{-1}.km^{-1}.s$), shown as the horizontal dashed line. For this work, the observationally derived value of X_{CO} by Dame et al. (2001) will be used.

1.3.7 Measuring Cloud Mass

As already discussed earlier, the lack of a dipole moment in H_2 makes it difficult to detect observationally. Because of this, astronomers use a tracer molecule which forms in a predictably proportionate manner, carbon monoxide - CO. CO forms through gas-phase reactions and aggregates in a similar way to that of molecular Hydrogen, through atomic self-shielding, thus making it an excellent tracer (Oppenheimer & Dalgarno 1975; van Dishoeck & Black 1988). The CO molecule *does* have a strong dipole moment which strongly emits in the radio wave band (2.6mm). It is the J=1→0 of the ^{12}CO which we observe to infer the presence of the H_2. However, CO is only a good tracer of low density environments, above the density limit, the photon emitted as a result of the decent of the electron from the 1 to 0 J-state is reabsorbed before it can be fully emitted, thus making the area optically thick. It is the low density limit which will be observed here, with the rotational levels of CO being progressively occupied with increasing density.

For the purposes of this work, the isotope of ^{12}CO will be used to measure the Hydrogen and hence cloud mass. The method used to equate the CO mass to that of Hydrogen is a simple conversion using X_{CO} and X_{HI}. Each of the clusters will have a position in parameter space of (l,b,V_{LSR}), centering the integration of material at this value of V_{LSR}. To calculate the mass of a cloud, taking the case where we assume a cylindrical volume ($\ell_0 \pm \delta\ell, b_0 \pm \delta b, v_0 \pm \delta v$) CO intensity map, centred on (ℓ_0, b_0, v_0) over integrated over a velocity interval $\pm\delta v$;

$$W = \int_{r=0}^{r} \int_{-\delta v}^{+\delta v} T(\ell_0, b_0, v_0)\ dv\ dA \tag{1.13}$$

Where; W is the total integrated CO intensity of emission of the volume centred on (ℓ_0, b_0, v_0). Once a value for W is obtained it can be related to the column density of observed molecule, N_{col}, by the relation:

$$N_{col} = W.X \tag{1.14}$$

Where X_{CO} =1.99x10^{20}cm^{-2} for a CO→H_2 conversion and X_{HI} =1.821x10^{18}cm^{-2} for HI mass calculation. The value of X is independent of the properties of the molecular cloud (e.g. metallicity), Obreschkow & Rawlings (2009). The mass of molecular Hydrogen is obtained via;

$$\mathcal{M}_{H_2} = N_{col}.\mathcal{A}_{annulus}.m_{H_2} \tag{1.15}$$

Where, $\mathcal{M}_{H_2}$= Hydrogen Mass
$\mathcal{A}_{annulus}$= Area of Annulus
and
m_{H_2}= Molecular Hydrogen Mass

It is this procedure which will be used when converting the temperature to the equivalent mass of a region within a survey. Though here it has been assumed that the total intensity is

calculated over a uniform cylindrical volume, it can be extended for any shape or dimension of cloud.

1.4 Star Formation Mechanisms

1.4.1 General Overview of Low Mass Star Formation

Low mass star formation, supported by many observations, occurs through the gravitational condensation of matter within a cloud into areas of, eventually, significantly higher density. Local over densities within the molecular clouds cause minor fluctuations in the gravitational potential of the cloud, thus causing minor potential wells. These potential wells allows the flow of gas into them, thereby increasing the local density, which increases the potential and hence attracts more matter. Molecular clouds tend to produce OB associations which are the source of the cloud's destruction. The stellar winds produced by the young stellar populations and the associated heating of the cloud causes the atomic and molecular surrounding gas to disperse. As the molecular cloud grows older the internal structure evolves into having smaller *clumps* of smaller diameter and larger *bubbles*, i.e., the more dense regions reduce hence increasing the areas of lower density through the creation of stellar populations. An example of this is the gravoturbulent fragmentation of the molecular cloud, Klessen et al. (2004). This where the stellar clusters form through the supersonic turbulence within the gas which is constituent to the cloud. It is the turbulence which causes the fluctuations in density, which is exacerbated in areas of higher density thus promoting local collapse through gravitational instability in these areas. This collapse of molecular material to young stellar objects usually occurs over time scales of $\approx 10^7$ years, see section 1.3.4.

Though the above is a highly abridged explanation of low mass star formation, the upper mass limit of stars which my form in such a manner is approximately 8 $M_\odot$. For more massive stars, one must explore a different regime of formation. For low mass stars, the accretion of material on to the protostellar core stops well before hydrogen burning commences, whereas for the high mass stars - they start hydrogen burning and develop radiation-driven winds as they continue to evolve onto the main sequence to hotter, more luminous, states (Blitz & Williams 1999). The final disruption of the birth-cloud occurs just as the high mass stars form winds, outflows and UV radiation fields. When the remnant molecular cloud has been dissipated, the result is a cluster - or association - of OB stars cospatial with a population of lower-mass stars. Though it is noteworthy to point out that recent works imply that the cluster environment isn't actually required to form stars, Bressert et al. (2011).

In recent literature, there have been three theoretical pathways to forming massive stars. All these pathways may be possible depending on the initial conditions of formation and also the environmental conditions within the clouds themselves i.e. levels of turbulence and threshold pressure on the ISM envelope (Zinnecker & Yorke 2007). The three main competing theories of high mass star formation (HMSF), though not directly related to this work but are summarised here, are: *monolithic collapse & disk accretion*, *competitive accretion & runaway growth* and *stellar collisions & mergers*. Though stellar collisions and mergers has been somewhat disproven as a viable pathway for high mass formation, it is included for completeness.

1.4.2 High Mass Star Formation Mechanisms

Stellar Collision & Mergers

The first mechanism by which high mass stars can be thought to form is via *Stellar Collision & Mergers*. The formulation of this theory, i.e., the formation of large-massive stars by smaller ones colliding, was to combat two contemporary problems with HMSF modelling. It was thought that the radiation pressure on the dust within the molecular clouds, where the stars would eventually form, would be too large, thus not allowing for a conducive environment which stars would be able to form. With the advent of Monolithic collapse, this problem was negated, see later. The second issue with forming massive stars was that the number density of high-mass stars within clusters was too large and there was doubt as to whether there would be a sufficiently large enough gas cloud which could collapse to form these densities - in both number and mass - of star. Though there are mechanisms which explain the presence and how these stars would form , it is still possible for the build-up of high mass stars. Though, to its detriment, this process can only happen in the situation where there is already a relatively large number of high and intermediate stellar objects; which is problematic. This implies that stellar mergers are rare and only account for the most massive stars in the most dense clusters, if at all (Zinnecker & Yorke 2007)

Lee J Summers

Figure 1.15: Diagrammatic representation of the Monolithic Collapse, adapted from Figure 11 Zinnecker & Yorke (2007): The inner accretion disk around a close massive accreting binary pair: inward radial flow is allowed in the equatorial plane. A polar cavity is evacuated by a combination of radiation and the stellar wind. The disk is self-shielded from the intense EUV field by an ionisation front separating H II and HI gas; and from the FUV field interior to the $\frac{\mathrm{HI}}{\mathrm{H_2}}$ interface by dust, molecular hydrogen, and CO. Relative sizes of the regions are not to scale

Monolithic Collapse

Monolithic collapse, Yorke & Sonnhalter (2002); McKee & Tan (2003), applies to the collapse of isolated massive molecular cores, see Figure 1.15. They numerically calculated the collapse of a slowly rotating, non magnetic clump of varying mass using a frequency dependant radiation hydrodynamic code. Though, within the code, the simulation produces high mass 'stars' it is important to understand the inner most regions of the simulations cannot be resolved. It is unclear whether this lack of central resolution - or at least the ability to understand what is occurring at the centre of the simulation - means that the central regions could contain either: a dense central cluster or a single large central object. This causes difficulties when controlling the mass loss form the central objects. The assumption is that the material accretes on to a single object which only allows an upper bound on the mass of stars to form to be formed by this mechanism. In principle, high mass stars could be formed via this process, but the number of assumptions and unknowns involved in the simulation makes it difficult to draw conclusive results of the type and properties of the stars which would form.

The turbulent core model (McKee & Tan 2002, 2003; McKee & Ostriker 2007) of high-mass star formation assumes that stars form in turbulent, gravitationally bound cores, where thermal pressure dominates the region. The clump, and proto-stellar cores within it, are all centrally concentrated so that the pressure and the density both exhibit a power-law dependancy with the radius of the clump. The infall rate of the stellar material onto the clump is governed by the surface density of the proto-stellar core - it is noteworthy to mention that the core's surface density is comparable to that of the clump in which is is situated. Observations of massive stars in the Galaxy suggested that these stars only form in regions of high surface density, which the McKee & Tan (2002) model predicts, in conjunction with the clusters containing massive stars and the globular clusters with high column densities of material. The model predicts a timescale of approximately 10^5 yr for a massive star to form, which is consistent with observation.

Competitive Accretion

The final mechanism by which high mass stars may form, to be considered here, is the process dubbed *Competitive Accretion*; Bate (1997); Bonnell et al. (1997); Bonnell & Bate (2006). The main difference between *Monolithic Collapse* and *Competitive Accretion* is that the former assumes that all the mass which is going to be constituent to the stars is 'clumped' before collapse begins. Whereas in the latter, the mass continues to be accreted on to the core throughout formation. The basic principles of the model is that the type of star formed is dependant on where it is in the simulation and how quickly it gets to a stage where it's more massive when compared to the stellar material around it. Basically, the environmental influences on a patch of material is just as important to its evolution; i.e., the better placed the material is within the simulation the more easily the simulation is promote growth of that material. The simulations were the first 3D representation of the HMSF process, it uses a Smoothed Particle Hydrodynamical code and a motion caption of the simulation can be seen in Figure 1.16. The resolution of the Bate-Bonnell code is a significant improvement over the monolithic collapse model in that the code can distin-

Lee J Summers

Image Copyrighted.
Original source image can be found:

http://www.phy.syr.edu/research/astro/

Third Party Copyright Marker

Figure 1.16: Stills from a movie showing 3D SPH simulated competitive accretive collapse of a 10K, 0.8pc, 500$M_{\odot}$ cloud. The time scale spans ~0.29Myr, increasing in time from the left-to-right/top-to-bottom. Image Source: Matthew Bate, University of Exeter. (Bate 2009, 2011)

guish the type of stellar product. This mechanism goes someway to explain why the presence of massive stars is so rare; in that for a star to be *massive* it would have had to have been at the top of the hierarchy at each accretion stage. There were some concerns within the community that the model was too heavily dependant on the simulations starting with a cloud which were gravitationally bound too strongly instead of relying on the turbulent conditions within the clouds. However, more recent simulation by Bonnell & Bate (2006) and Bate (2009, 2011), show that there is not an issue with the large-scale versus local-scale collapse of a cloud. Since the younger proto-stars could be carried via flows within the cloud to regions which have yet to induce collapse.

1.5 The Milky Way in the Cosmos

In it's most literal translation, the term *Cosmos* derives from the Greek meaning *Order*, the literary antithesis of chaos. As popular author, Douglas Adams once wrote; *"Space is big, really big..."*, and is such the way with any large, complex structure, the classification and understanding grows in proportion to our ability to understand it. As early as the second century A.D., Claudius Ptolemaeus espoused the Ptolemaic model (see Figure 1.17) of the Universe (later known as the geocentric model) in an attempt to place Earth in the sky relative to the bodies which move on the sky through the study of stars, planets and the wider Galaxy (from the Greek, *Galaxias*, meaning Milky; from which we get its name, The Milky Way). Moving away now from the relative locality of the solar system to look at the morphological classification of galaxies.

Lee J Summers

Image Copyrighted.
Original source image can be found:

[Left]:
http://galileo.rice.edu/images/things/ptolematic_universe.gif
[Right]:
Churchwell et al. (2009)

Third Party Copyright Marker

Figure 1.17: [Left:]The ancient Ptolemaic interpretation of the COSMOS from Petrus Apianus' *Cosmorgraphia*, Apianus (1539). The Ptolemaic order of spheres, from inner-most (Earth) to outer; Moon [Lunar], Mercury [Mercurii], Venus [Veneris], Sun [Solis], Mars [Martis], Jupiter [Iovis], Saturn [Saturni], Fixed Constellations, Sphere of he Prime Mover. Image taken from Edward Grant *"Celestial Orbs in the Latin Middle Ages"* (Jun. 1987). [Right:] Modern schematic view of the Galaxy through the b=0^o plane, inspired by *GLIMPSE* observations of the Galactic plane; implying the Milky Way is a Sb-type spiral galaxy. Image Credit: NASA/JPL-Caltech/R. Hurt (SSC-Caltech)

1.5.1 Galaxy Morphology & Classification

The era of early modern astronomy, Section 1.1.2, was dominated by optical wavelength detections, such were the instruments which were available. In the catalogue of Deep Sky Objects, William Herschel (1782), the physical nature of extra-galactic sources had yet to be fully understood or determined. It was not until Third Earl of Rosse, William Parsons, in 1845 whilst analysing observations of M51 was spiral structure - or indeed *any* morphological structure - even postulated upon (Bailey et al. 2005). Rosse, like Herschel before him, referred to these objects as *island universes* and *extra-Galactic Nebulae*. However, with Herschel's contemporary understanding of the etymology of the word universe meaning 'the entirety of existence', it fell in to disuse and was instead replaced by 'galaxy'. The discipline of what would become galaxy morphology remained relatively un-persued until the groundbreaking work by Edwin Hubble (1926, 1936). An example of how vast the array of possible morphological types and observable structures of galaxies within our universe can be seen in Figure 1.18.

Lee J Summers

Figure 1.18: A selection of extragalatic false-colour images showing the diversity of galaxy morphologies. (Image Credit: Jamie Symonds/NASA).

Hubble's famous contribution to the field is the 'Hubble Sequence', remaining, to this day, a somewhat standard basis and measurement of studying galaxies. The sequence, shown in Figure 1.19, maps Hubble's contemporary belief that the evolution of galaxies progressed from smooth Elliptical (E-type) galaxies through to Spiral (S-type) galaxies which are dominated with a central bar (Sb-type). Over time, as more and more extragalactic observations were made, a larger sample became available and the additional classes of Irregulars and, more recently, the intermediate Spiral classes were added to the sequence. However, now it is understood that the evolutionary sequence of Elliptical to Spiral class galaxies is not entirely accurate. The different morphological

types are thought to evolve from the different initial conditions of the gas cloud from which the galaxy is formed. The angular momentum of this host gas cloud is thought to play a key role and is the basis of the ATLAS^{3D} interpretation of structural evolution (Cappellari et al. 2011). Galactic scale clouds with a relatively low initial angular momentum is unable to spin down, so may collapse into a pure Elliptical type galaxy. Whereas a cloud with relatively high angular momentum can spin and collapse down into a disc, the non-rigid body rotation of the galactic disc causes density fluctuations in the plane which manifest as local potential over-densities; i.e., spiral arms and thus form a pure Spiral type galaxy. Though this explains the *thoroughbred* galaxy types of Elliptical and Spiral classes, the host of irregulars and intermediate spirals are not as easy to explain from first principles. These intermediate galaxy sub-classes perhaps forming an transitional evolutionary regime between the Elliptical and Spiral class. More recent work by the ATLAS^{3D} consortium has suggested that instead of a *tuning fork*, the shape being more like a *Comb* with the x-axis being proportional to the angular momentum of a galaxy and the y-axis being indicative to the number of evident spiral features, see Figure 1.20.

Since the initial work of Hubble, the classification of galaxy types has become a significantly larger and more complicated scheme, though still based on observables; size, brightness, bulge-to-disc ratios, bulge-to-enveople sizes (in luminosity), disc symmetry and shape (e.g. asymmetry, rings, bar, number of arms), surface brightness, colour and dust content (though the final two parameters can be related). It is interesting that even with the ever growing number of statistics that the Hubble sequence still provides a guide to the evolution and behaviour of galaxies. de Vaucouleurs (1959); van den Bergh (1960a); van den Bergh (1960b); Sandage (1961); Sandage (1986). Later works by Ferrini & Galli (1988) show that many properties dependant on the stage of evolution of an observed galaxy is easily tracked accross the sequence via (B-V) colour and the $\frac{Bulge}{Disc}$ ratio. These quantity vary monotonically across the Hubble sequence with late-type spirals being bluer and having smaller $\frac{Bulge}{Disc}$ ratios than the early type spirals; Driver et al. (2006); Kelvin et al. (2010).

Elliptical Class Galaxies

This class of galaxy are defined by their apparent 2-dimensional ellipticity on the sky with designation E(n), where n is defined as the ellipticity; n=$10 \times \left(1 - \frac{b}{a}\right)$, where b and a are the semi-major and minor axes of the observed galaxy respectively. E(0) are circular in their appearance and conversely, the E(7) class being flattened. Though the n parameter does not give any information as to the third dimension's shape and extent, it is thought that the most luminous E-type galaxies are tri-axial. The major fraction of stars in these galaxies are Population II stars and as such elliptical galaxies tend to be redder a symptom of being dominated by an older, redder, stellar populous. During this phase of the stars' lifetime, the low and intermediate mass become very luminous and thus *outshine* their younger, equal mass, counterparts. In most case the Population II stars are in the red-giant phase of their evolution and reside in the red-giant or assymtotic-giant branches of the Hertzsprung-Russell diagram.

Lee J Summers

Figure 1.19: The Figure songs the 75 Spitzer Infra-red Nearby Galaxy Survey (SINGS) galaxies arranged in a tuning fork based on their optical morphology. The colour images of each galaxy were created from the SINGS IRAC 3.6μm (blue), IRAC 8.0μm (green), and MIPS 24μm (red) images. IMAGE CREDIT: Karl Gordon, kgordon@stsci.edu.

Lee J Summers

Figure 1.20: Comparison between the classic tuning-fork classification scheme (left) by Hubble (1936) and the new comb diagram (right) proposed by the ATLAS^{3D} team, Cappellari et al. (2011)

Spiral Class Galaxies

Spiral type galaxies, as the name suggests, exhibit spiral structure. In general, S-type galaxies are composed of two major components; the spiral arms and the central bulge. the degree to which the arms are wound and also the extent of the bulge are the sources of the classification for the morphological type. Spirals are further sub-divided by the presence of a bar through the central bulge or not, with 'S' denoted normal spirals and 'SB' denoting barred-spirals in the nomenclature. In conjunction with the bulge classification, the degree to which the spiral arms are wound around the galaxy is also taken into account, with 'a' being tightly wound and with 'd' being very loosely wound. So, Sa class galaxies have no central bar and who's arms are tightly wound where a SBd type has a barred centre with very loosely bound spiral arms. As one would expect, the differing environments of bulge and arms give rise to different stellar populations. The spiral arms contain younger Population I, P(I), stars which have a wide range of metalicities (relatively high by comparison) and are bluer than the P(II) stars in the ellipticals. Though it is important to understand that as the stars move through the spiral arms and head towards the galactic centre, this causes an age-spread in the stellar types. This means that the P(I) stars in the galactic disc are slightly older than the PI stars still traversing the spiral arms, Driver (2004). There also theoretically exists a third classification of stellar type, the Population III stars which are considered to be metal free, but they have yet to be observed and as such are probably at quite a high redshift and are not present in the local Universe, Fosbury et al. (2003).

The generation and maintenance of spiral structure - and its associated potential - within S-type galaxies will be discussed later with the Milky Way specifically. Beginning with a brief summary of this key structural feature: A simplified description of the arms is that they can be approximated by a logarithmic spiral; Russeil et al. (2007); Hou et al. (2009); Summers & Brunt (submitted,i) in their spatial distribution in the plane of a galaxy. The arms manifest as a rotating uniform potential, in density (Roberts 1972) orbiting the central part of the bulge with constant angular velocity. As the stars move through the spiral arms, the stellar system is modified by the gravitational effect of the higher density. The relatively high densities of the ISM in these arm regions are what facilitates the formation of bright blue, in the optical bands, young, P(I) stars; making the spiral arms, of extra-galactic sources, comparatively easy to observe.

Lenticular Class Galaxies

Similar to spiral galaxies in their disc-like initial structure, the lenticular galaxy class is thought to provide a morphological stepping stone between the elliptical and spiral morphologies. However, unlike spiral class galaxies, lenticular galaxies exhibit no (or very depleted) spiral structure with the galaxy having used up or lost, via interaction, its ISM. As a result of this, it is thought that very little star formation occurs within lenticular galaxies; Buta, Corwin, & Odewahn (2007). Though observations of older S-type galaxies have found that if a spiral galaxy uses up $\approx$90% of its interstellar atomic hydrogen, then it can no longer maintain its level of star formation, Roberts & Haynes (1994). As a consequence of this, the galaxy would quickly lose its spiral arms, with the main stellar populations being P(II) and older P(I) stars. It is this 'duality of states', in both

structure and constituents, which preposes the hypothesis that lenticular galaxies provide an intermediary galaxy class. Though, at least in morphological theory, this galaxy class appears defined - in practice the lenticular class is usually based on S-type designations so finding properly defined 'lenticular galaxies' is difficult and as such this class is usually referred to as intermediate-spirals.

Lee J Summers

Figure 1.21: The Whirlpool galaxy, Messier 51(M51, NGC 5194), exhibiting grand design spiral structure. Image taken from *http://messier.seds.org/m/m051.html*, accessed on 11th May 2011.

Irregular Class Galaxies

As the name suggest; the Irregular galaxy class (Irr) do not generally fall into any distinct category. By their very nature they are *irregular* and do not have corresponding features to either elliptical nor spiral morphology. Irregular galaxies comprise ≈3% of observed galaxies, being of low luminosity and as such making them difficult to detect. It is thought that it is possible that the Irr-type galaxies are formed through gravitational interactions between the *pure* galaxy classes of spiral and elliptical. There are two main sub-classes of irregular in the Hubble classification Irr-I, galaxies which present *some* structure but not enough to accurately place it on the sequence, and Irr-II, irregular galaxies which present a lack of any systematic structure that can place it in the sequence at all; de Vaucouleurs (1959).

There is a third class of irregular galaxy which has been observed, the dwarf-Irregular (dI or dIrrs) is thought to be the local analogue of the multitude of faint blue galaxies which tend to populate deep field galaxy surveys, Ellis (1997). Although the original Hubble classification placed most, if not all, Irregular galaxies, in a single morphological class, it is now more common to make another distinction between normal Irregular galaxies and Peculiar Galaxies, Graham & Guzmán (2003); Guzmán et al. (2003). Peculiar galaxies are galaxies unusual properties and

structure evolve due to: some being active galaxies with violent internal processes taking place, others may be normal galaxies but with certain features being obscured by dust or other absorption features, whereas others may be due to tidal interactions between colliding galaxies, Summers (2008).

1.5.2 The Fingers of God Effect

From the XY projection of Galactic HI in Figure 1.11 - and also present in distribution of H_2 and H II regions presented in Figure 1.24 - it can be seen that, at times, the observations of the HI can be difficult to interpret. With the circular artefacts caused by the tangent-points and the kinematic ambiguities in the inner-Galaxy (discussed later) and the *fingers of God* (foG) effect pointing towards the Solar position. The latter being the Galactic based analog of the effect seen in the Redshift distortion of galaxies - is present across the parameter space, thus making an accurate picture of the Galaxy's structure is difficult to determine. Though there are those who incorrectly assume that the foG effect is indicative of a privileged observational locale - i.e. Galactocentric universe (Harnett 2008) - the source of the distance-spread is due to the random dispersions in the velocities of the individual components about the central mean - be that central mean determined for the centre of a galaxy cluster or a Galactic cloud.

Beginning with the extragalactic description of this phenomena using data acquired by the CfA Redshift Survey (Huchra et al. 1983) - see Figure 1.22. When plotting the observed galaxies in Redshift-position, they appear to stream along a line-of-slight to the observer and are radially elongated. At a suitably near Redshift, Universal expansion - or the recessional velocity - is much larger than the local peculiar velocities of the individual galaxies. This should cause the Hubble flow to be 'smooth' (Lynden-Bell 1986) and as such the Redshift/velocity of the galaxies can be used as a surrogate for distance - in a similar way to kinematically determined distances in the Galaxy - via,

$$D = \frac{v_{obs}}{H_0} \tag{1.16}$$

Where, D is the distance to the observed galaxy, v_{obs} is its observed velocity and H_0 is the chosen value of the Hubble constant - the rate of recession of distant astronomical objects per unit distance away, H_0=73.8 ±2.5 km s^{-1} Mpc^{-1} (Riess et al. 2011). However, as can be seen in Figure 1.22, there are thin filaments of galaxies in Redshift parameter space which are pointing back to the observer. We are not privileged observers in the Universe, so the effect must either be kinematic or geometric (in terms of the cluster/galaxy shapes) in origin. The work of Bahcall et al. (1986) investigated the kinematic and geometric contributions to the elongation of the observations within the parameter space. They concluded that though there is at least some contribution to the elongation - possibly due to shell-like or cell based clustering of galaxies - the main contribution is from the kinematics. The kinematic contribution is due to the random dispersions in the peculiar velocities of the galaxies within a cluster - i.e. deviations from the pure Hubble flow - causing the galaxies to be radially elongated. Since this effect is kinematically, and not a spatially, induced there is no effect on the observed angular position. On the significantly larger scale, however,

Figure 1.22: The presence of Redshift elongation in extragalactic observations. Data taken from the SAO CfA Redshift Survey, Huchra et al. (1983).

Figure 1.23: Distribution of galaxies in the 2-degree field Galaxy Redshift Survey (2dfGRS, Colless 1999) after correction for deviations from the Hubble flow.

there is also a second Redshift-space distortion which is more difficult to quantify, the Kaiser Effect - Kaiser (1987). The Kaiser effect is more applicable to over-dense galaxy clusters and is due to the coherent, linear, variation in velocities of galaxies and they undergo infall to the cluster's central mass. Though the exact mechanics of this is beyond the scope of this thesis and is merely included for completeness, the non-Hubble peculiar velocities can be compensated for, to a degree, by comparing the elongation of the two-point correlation function and the flattening of the power spectrum of the clusters to their expected values - see Figure 1.23.

Though on Galactic scales the change in Redshift is negligible, the same basic principles apply when transforming the observed velocity of a region of emission to a distance. The conversion of the $\ell - v_{LSR}$ data within the LAB HI survey to the Galactocentric XY projection involves transforming the v_{LSR} into a distance and is shown in Figure 1.11. Kinematic distance estimates and the implications and contributions of spiral potentials on this calculation are discussed later in this Chapter, for now only the foG effect is described. A detected cloud is going to have a measured v_{LSR} , but it would naive to assume that this velocity would be applicable to all points within the cloud. The emission is subject to velocity dispersions, as were the galaxies when compared to their cluster centres, therefore when the Galactic emission is converted from velocity to distance, the data are radially elongated. Here, however, instead of the velocities being deviations from the Hubble flow, the dispersive velocities are those deviating from the expected rotation curve for the Galaxy - be that rising, falling or flat.

1.5.3 The Milky Way - A Spiral Galaxy?

Having discussed the various morphological types of galaxy identified from redshift 0→15 (ish), surely it should be relatively straight forward to classify our own Galaxy, the Milky Way. Unfortunately this is not the case. The main issue with classifying the Milky Way is that we are resident within it. When looking at galaxies such as M51 - see Figure 1.21 - it is relatively easy to identify it as a Spiral, since one is able to observe the whole structure at once. As was shown in Figure 1.11, when viewed from within a galaxy, the distribution of gas in the plane can be difficult to disentangle, with very little - if any - spiral structure being apparent in observations. The main issue with intrinsic Galaxy observations is that most of the methods by which spectral data are obtained is heavily dependant on the location that the observations are take - the foG effect described above. Exemplified in Figure 1.24, it is clear that most of the Giant Molecular Cloud (GMC) and HII emission can be seen to be emanating from the solar position which, when taken at face value, would imply that we occupy a special place in the Galaxy. This is not the case as discussed earlier. Work by Combes (1991) endeavoured to place an observer within the galaxy, M51 in an attempt to recover the spiral structure we observe through Galactic methods of observation when applied to this extra-galactic source with quite evident spiral structure.

It has been mentioned previously that spiral arms are home to the vast fraction of the molecular cloud content of a galaxy, since these molecular clouds are traced fairly well by CO. Most large-scale CO surveys aim to map the molecular content (hence spiral structure) of the Milky Way, with the data being obtained in Galactic longitude-latitude-velocity (*lbv*), the difficulty arises when trying to recover the spatial structure of the observations from the spectra. The usual way of deter-

Lee J Summers

Image Copyrighted.
Original source image can be found:

[adapted from] Figures 3 & 4, Hou et al. (2009)

Third Party Copyright Marker

Figure 1.24: The right panel shows an example of the Fingers of God Effect, adapted from Hou et al. (2009). The colour distribution of both HII and GMCs in the Galaxy, colour brightness is proportional to its contribution to structure. The left panel shows watermarked HI data is overlaid on the GMC and HII region distribution, taken from Levine et al. (2006)

Lee J Summers

Image Copyrighted.
Original source image can be found:

Figure 5, Combes (1991)

Third Party Copyright Marker

Figure 1.25: The left panel shows the projection of molecular clouds within M51 in the *x*-*y* plane, simulated from infra-red and near infra-red pictures. The right panel shows a view through the b=0^{o} plane as derived by an observer planed at the (0.0 kpc ,-7.0 kpc) position. Figure and caption adapted from Combes (1991)

mining the distance-velocity conversion is to use rotation curves and map the velocity to a distance as defined by the rotation curve, we go into this in greater detail later. Assuming a constant value of $\frac{d(V_{rad})}{d(R_{gal})} \simeq 12.0 kms^{-1}pc^{-1}$ across most of the Galactic disc, Combes (1991) attempted to recover the spiral structure of M51 via methods comparable to the way we observe molecular clouds and complexes within our own Galaxy. That is, using kinematic determination of the distances to the various complexes, though initially, this appears to be a sound method, there are issues. The main contributing factor to the kinematic distances are the rotation curves and velocity models used to determine these distances. As can be seen in Figure 1.25, when fitting the observed velocity to assumed circular rotation, the presence of non-circular motions within a galaxy causes difficulties in recovering the spiral structure. It can be concluded that just because clear spiral potentials are not visible in neither Figure 1.11 nor Figure 1.24, that does not necessarily mean that there is no spiral structure present within the Milky Way. However, we are able to identify possible spiral structure from the ℓbv_{LSR} maps, an example is show in Figure 1.26, taken from Dame, Hartmann, & Thaddeus (2001) CO observations of the Galactic plane. It is evidence such as this which implies the presence of non-circular motions within the Milky Way, Roberts (1972).

It is important to note at this juncture that we observe this non-circular motion in velocity and not, at least directly, in space. So even though we observe these multi-valued functions in velocity it may not translate into distance - see Figures 1.27 and 1.28 in section 1.5.5 .

1.5.4 Milky Way Spatial Spiral Structure

We know the Milky Way has evidence of spiral arms (Russeil 2003; Russeil et al. 2007; Vallée 2008; Hou et al. 2009; Reid et al. 2009); but understanding this structure and how materials flow through it is important in understanding, not only the large scale dynamics, but also the smaller intra-arm regions where star formation is thought to occur. Within the Milky Way, like most spiral galaxies, the main sites of star formation reside within spiral arms - therefore being able to isolate these regions for further study is vital in understanding them. Though it is generally accepted that the Milky Way has four main spiral arms, the properties of these arms – for example, pitch angle, shock strength and levels of symmetry – vary not only between arms but also self-consistently with azimuth (Foster & Cooper 2010). There are many models, interpretations and measurements of spiral arm dynamics in the literature; Hou et al. (2009); Reid et al. (2009); Vallée (2008) (Table 1 therein); Russeil (2003); to name a recent selection. The pitch angle, derived from the spatial models of the Milky Way's spiral arms, is found to be approximately constant $\simeq 13°$- though this could be a symptom of the limitation of using linear logarithmic forms to fit to the spatial structure of the arm. Other works that fit more complex spatial functions (Seigar & James 1998) find that the pitch angle of spiral arms can change along their length. One such work is Hou et al. (2009) whom fit a polynomial logarithmic form to Galactic GMCs and H II regions the derivative of which describes the varying pitch angle with Galactocentric radius, R. A varying pitch angle implies that the distribution of spiral arms becomes non-uniform, in that the *tightness* of the logarithmic spiral varies with R and the arm becomes 'unwound' - implying a a possible lack of symmetry of spiral arms.

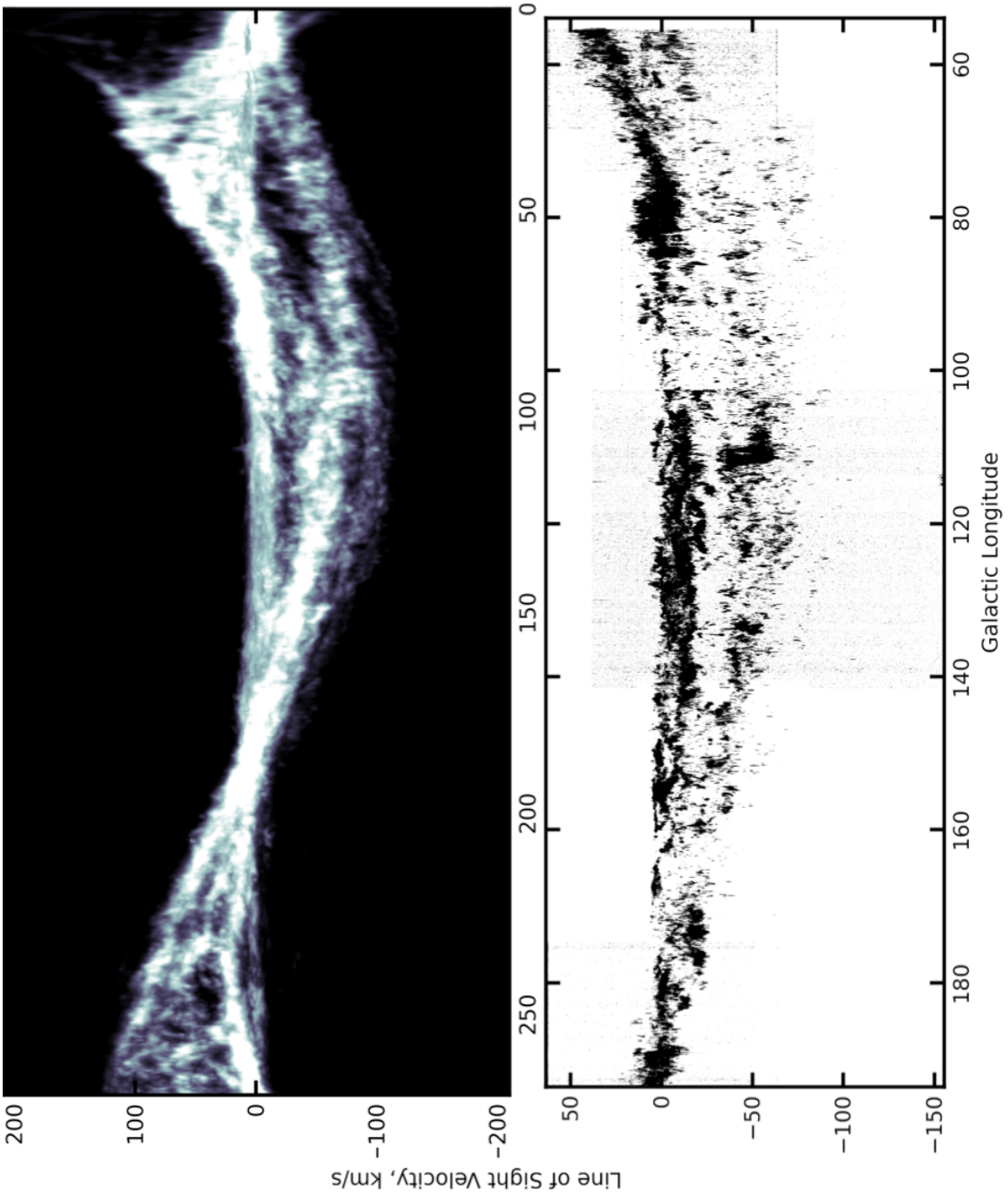

Figure 1.26: Longitude velocity map of HI [top], taken from LAB HI survey, and ^{12}CO [bottom], taken from the ExFCRAO survey, showing the presence of kinematic spiral structure in the longitude-velocity plane. The HI shows the large scale distribution of spiral structure, whereas the ^{12}CO traces the sub-structure of the kinematic arms.

1.5.5 Milky Way Kinematic Spiral Structure

Here I describe the features of the spiral arms' kinematic structure rather that the wider rotation curve as a whole. Discussion about the chosen galactic rotation curve and the testing of the IAU and Reid et al. (2009) standard solar constants can be seen in Chapter 3.

Shifting from the spatial to the kinematic structure, though the two are related, of the Milky Way - in the regions of the Galaxy where spiral potentials exist, a *velocity anomaly* (Foster & Cooper 2010) can be seen in the orbital velocity of material and objects through the Galaxy. For the Milky Way this is observed as a small negative shift in angular velocity of material in the region of the arm, Brand & Blitz (1993). This is observed, for the Perseus arm - the nearest large scale structure to the solar position (see later), at Galactocentric radii of between 9 and 11 kpc, depending on the line of sight - causing the distance-velocity relation to be multi-valued and another 'near-far-furthest' uncertainty is introduced, Summers & Brunt (in prep). There is evidence of spiral structure in ^{12}CO and HI, see ℓ-v_{LSR} ^{12}CO diagram - Figure 1.26. In these spectral line surveys, data are taken in terms of position-velocity coordinates, therefore to transform the observed velocity into an actual linear distance from the observer one needs to convert the observed velocity to a *kinematic distance*. This is facilitated via one's chosen rotation curve, which means that the determined distance can vary greatly depending on the chosen rotation curve. Though all measurements are subject to an uncertainty - as is their nature - the uncertainties on kinematically determined distances are larger than those on measured distance methods (such as trigonometric parallaxes). It is important to note at this juncture that kinematically determined distances can be corrected for the non-circular component of velocity in the regions of spiral arms, see Reid et al. (2009), but the accuracy with which these corrections compensate for the non-circular motion varies - see Chapter 3. I will take a moment to discuss the two regimes of kinematic distance uncertainty below.

Inner-Galaxy Distance Ambiguity

For ease of explanation, let us split the Galaxy into two spatial regimes. The first being; the inner Galaxy, where values of R (the Galactocentric radius) is less than R_0 (the solar distance from the Galactic centre) and the second being the outer Galaxy, where the reverse is true (i.e. where R>R_0). Taking Figure 1.27 as cartoon of what the main problem with inner Galaxy observations is, for a given velocity along a single line of sight, it is possible for that velocity to correspond to a *near* and *far* distance giving rise to the problem. This means, within a spectral line survey a pixel of emission at the near distance corresponds to less mass (proportional to $\frac{1}{d^2}$, where d is the distance from the observer to the emission) than if that pixel of emission were considered to be at the far distance. This can lead to under (or over) estimation of cloud sizes and masses which can introduce inaccuracies to any sample of gas. It can also introduce problems in that the emission is just placed incorrectly in the Galactic map meaning the overall spatial distribution of gas can be misleading. Admittedly, this effect can be reduced by including other observations in the analysis, for example trying to match up emission to objects with measured parallaxes or photometrically determined distances, though not all emission is, or can be, associated with a measurable object.

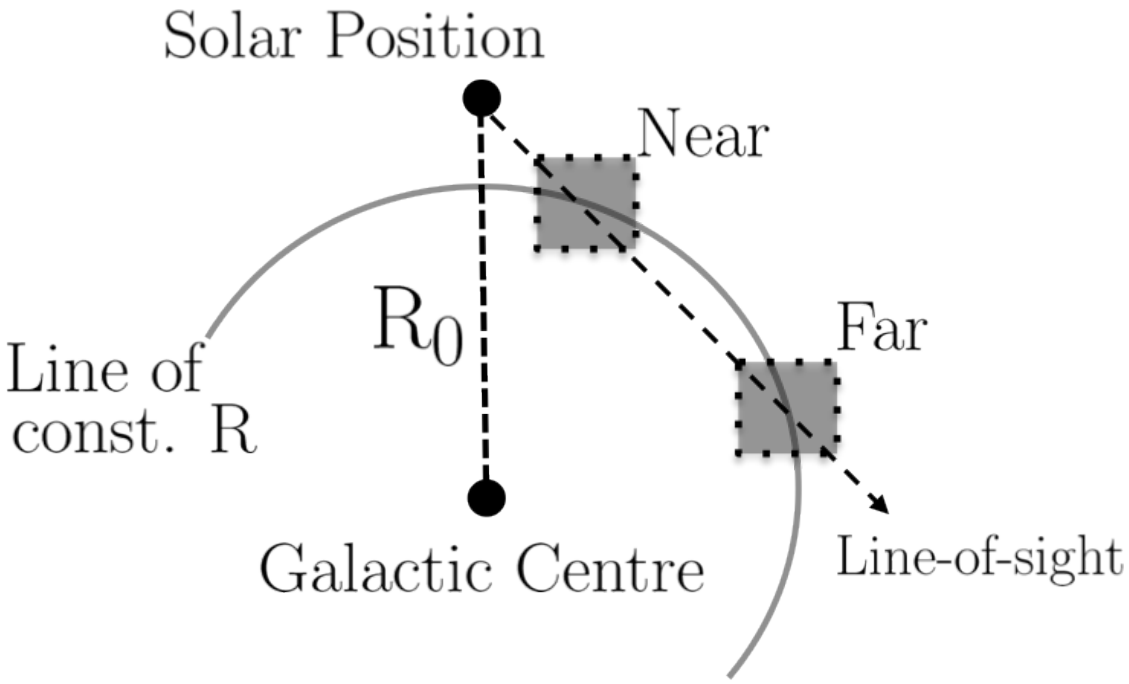

Figure 1.27: Inner-Galaxy distance ambiguity for kinematically based distance determinations, exemplifying the near-far distance ambiguity.

Outer-Galaxy Distance Ambiguity

Shifting our attention from the inner to the outer-Galaxy. The distance ambiguity described above is not an issue for outbound observations, since one would expect a monotonic relation between observed velocity and distance. However, one must consider the presence of shocked motions in the regions of the spiral arms, an example of which can is shown in Figure 1.28. The concept of shocked motion is presented more completely in Chapter 4, but as a summary: The potential present in spiral arms is observable as a negative shift in the observed velocity of arm-based emission or objects. The velocity-distance trace in Figure 1.28 shows the behaviour for a single line of sight, since this may vary with Galactic longitude. The shocked motion can cause, in some places, a triple valued function i.e. near-side arm, far-side arm and exterior-arm. In contrast to the inner-Galaxy - for a given line of sight, it is possible for the emission to reside at three distances, refer to Figure 1.28. For example; along a single line of sight, at a velocity of $\simeq$ -40km/s, the emission may lay at $\approx$1.9kpc, $\approx$2.2kpc or $\approx$4kpc - shown in Figure 1.28. Though the internal arm separations are not large, the difference between whether the emission is arm/shock based or exists beyond the spiral potential is a significant difference which can damage the validity of cloud catalogues' derived parameters. This is just assuming that there is a single spiral potential beyond the solar position, with the Perseus, Outer and newly identified outer Scutum-Centaurus arm (Dame & Thaddeus 2011), potentially, there exists three.

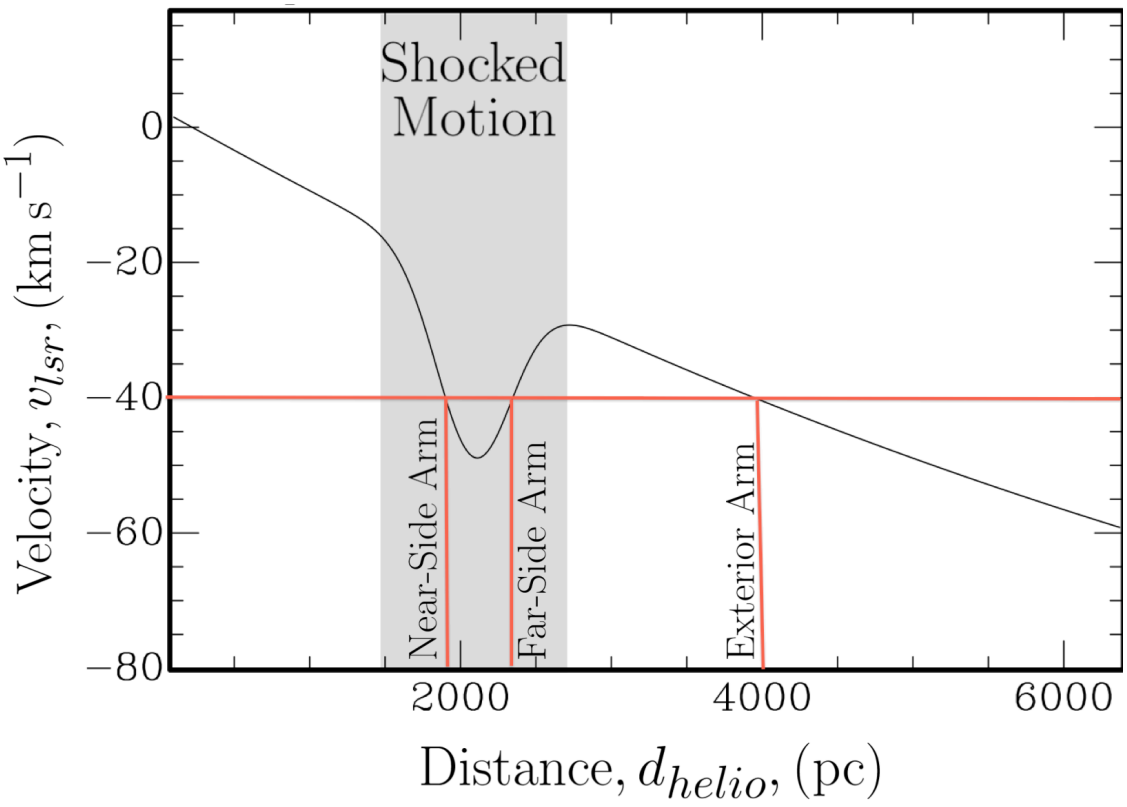

Figure 1.28: Outer-Galaxy distance ambiguity for velocity observations. x-axis shows the heliocentric distance (parsec) and the y-axis corresponds to the line-of-sight velocity (km s^{-1}) at that distance, the grayscale box shows the region of the shock potential associated with a single spiral feature (Perseus arm). The existence of the negative shift in the velocity of arm-based material causes a multi-valued mapping to the velocity-distance relation.

1.6 Preliminary Work - The Mass:Age Relation of ISM:YSC

There was a body of work completed prior to the work on Galactic structure and dynamics which lays the ground work for the research presented within this Thesis. Building on the work of Leisawitz, Bash, & Thaddeus (1989), I investigated the mass-to-age dissipation rate of molecular material surrounding young stellar clusters. As such, this work appears to be out of place amongst the work of modelling spiral structure but sets up the motivation nonetheless. When this work was conducted - included for completeness in Appendix C - it was found that several areas which left room for improvement:

- Non-kinematic distance measurements to the stellar clusters
- Age determinations of the stellar clusters
- Dynamical models of the Perseus spiral arm

Of the three possible improvements stated above, I decided that the improvement in the understanding of the dynamical structure of the Perseus arm was the area which would be easily

controllable - i.e. not reliant on the acquisition of new data and be attainable within the time available. It is with that, I introduce in the remainder of this thesis, a new model of the spatial and kinematic nature of Galactic spiral structure; The Shock-Motion-Model, which is presented herein.

1.7 Thesis Content & Overview

As is implied by its subtitle, it is the intent of this thesis to demonstrate the potential of the interstellar medium. This thesis endeavours to present how the ISM forms stars (i.e. what it can become) and also how the density and gravitational gradients manifest themselves in the observations and how best we can compensate for, or at least reduce, these effects. Having presented the history of and motivation behind the field leading to my work, this thesis is divided into five further chapters as follows;

- *Chapter 2* - Details the data and surveys which were used to complete the research detailed herein.
- *Chapter 3* - Introduces the concepts involved in the Shocked-Motion-Model of spiral structure, devised as part of this work. It consists of looking into how the non-circular and shocked motions can best be described and modelled to produce a spatial-velocity model which reflects current observations and also the streaming motions of gas as it enters spiral potentials.
- *Chapters 4* - Presents the benefits of reducing the biases in observational data and endeavours to produce an extragalactic style view of the Milky Way's spiral structure by using the model detailed in Chapter 3 and resampling the spectral velocities to create the spiral arm maps.
- *Chapters 5* - The models derived in Chapter 3 and maps created in Chapter 4 will be subjected to large scale dynamical and compositional analysis. These results are then compared to Galactic and extragalactic determinations of the dynamical an compositional structure of spiral class galaxies. The maps are subjected to a molecular cloud decomposition at 5 different linear resolutions (ΔL= 5, 10, 20 and 50 pc), with the derived catalogues' parameters and relations compared to Galactic and extragalactic cloud samples and their properties discussed.
- *Chapter 6* - Concludes and discusses the work and its findings with an overview of what has been completed, the implications for the results on a whole, possible areas of improvement and discussion of the possibility of further research in this area and where it would be best directed, both personally and in the wider Astronomical community.

CHAPTER 2

Source Data & Observations

"Errors using inadequate data are much less than those using no data at all."
Charles Babbage, 1791-1871

This Chapter introduces and discusses the various data, surveys and catalogues which have been used over the course of this research. Mainly I have used (sub-) mm and cm wave observations of CO and HI, respectively for the work into Galactic structure and cloud composition, whereas for the work into stellar clusters (Appendix C), online legacy catalogues were used and are discussed forthwith.

2.1 The Exeter-FCRAO of ^{12}CO and ^{13}CO Northern Galactic Plane Survey

The full Ex-FCRAO comprises of six individual survey regions (Table 2.1) mapping the **J**(1-0) transition of various isotopologues of CO. The coverage and statistics of which can be seen in Table 2.1. For a full and in-depth description of the survey and how to obtain the data release, I refer the interested reader to Brunt et al. (in prep). Here, however, is presented an abridged summary of the survey design, regions and content.

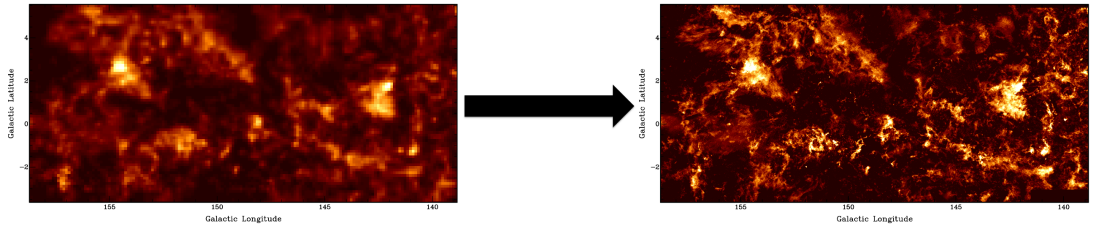

Figure 2.1: The panels above show the difference/improvement in resolution comparing the same region of sky in the Dame et al. (2001) (left) and Brunt et al. (in prep) (right)

Table 2.1: Survey coverage and content. [a]Brunt et al. (in prep); [b]Heyer (1996); [c]Jackson et al. (2006). A Figure showing the coverage of each of the surveys regions can be seen in Figure 2.2.

Galactic Survey Region	ℓ-range (deg.)	b-range (deg.)	Emission Line **J**(1-0)	Sampling (arcsec.)	Δv (kms^{-1})
Anti-centre[a] (ACS)	192.5→175.5	-3.5→+5.5	^{12}CO ^{13}CO	22.5	0.13
Extended-Outer[a] (EOGS)	175.5→141.0	-3.5→+5.5	^{12}CO ^{13}CO	22.5	0.13
Outer[b] (OGS)	141.5→102.5	-3.5→+5.4	^{12}CO	50.22	0.82
Cygnus[a]	102.5→65.0	-1.0→+1.5	^{12}CO ^{13}CO	22.5	0.13
Vulpecula[a]	65.0→55.7	-1.0→+1.0	^{12}CO ^{12}CO C^{18}O	22.5	0.13
Galactic Ring[c] (GRS)	56.0→18.0	-1.0→+1.0	^{13}CO	22.14	0.21

The observations for the Ex-FCRAO survey (Brunt et al. in prep) were conducted with the 13.7m FCRAO (Five College Radio Astronomy Observatory) over a period of 23 months between May 2004 and April 2006. The spectra were obtained using the SEQUOIA focal plane array scanning two main large-scale regions of the sky; one wide latitude band encompassing the **ACS, EOGS** & **OGS** regions and the other being confined to a lower Galactic latitude extend in the **Cygnus** and **Vulpecula** regions. These observations were combined with the BU-FCRAO GRS to create a complete CO map of the Galactic plane between $193^\circ < \ell < 18^\circ$allowing this new CO survey to offer a factor of ten improvement in resolution to previous works, for example that by Dame et al. (2001) (see Figure 2.1). The coverage of the surveys in Galactic coordinates - and also in Galactocentric coordinates - can be seen in Figure 2.2. The data, excluding the OGS, have an overall spectral velocity range of ~ 130 km s^{-1} with a spectral channel width of ~ 0.13 km s^{-1} at frequencies corresponding to the observed CO lines; the channel sampling was selected such that the spacing is 1.21 times the achieved velocity resolution. For maximum potential coverage, the surveys described have different central velocities with respect to the local standard of rest.

The data were subjected to calibration scans every ten minutes to determine the system temperatures, of which were typically in the range 200-600 K for ^{12}CO and 130-400 K for ^{13}CO & C^{18}O within the survey. The system temperatures were then transformed into T_A^* which is the effective temperature of the source about the atmosphere, this was completed using the chopper

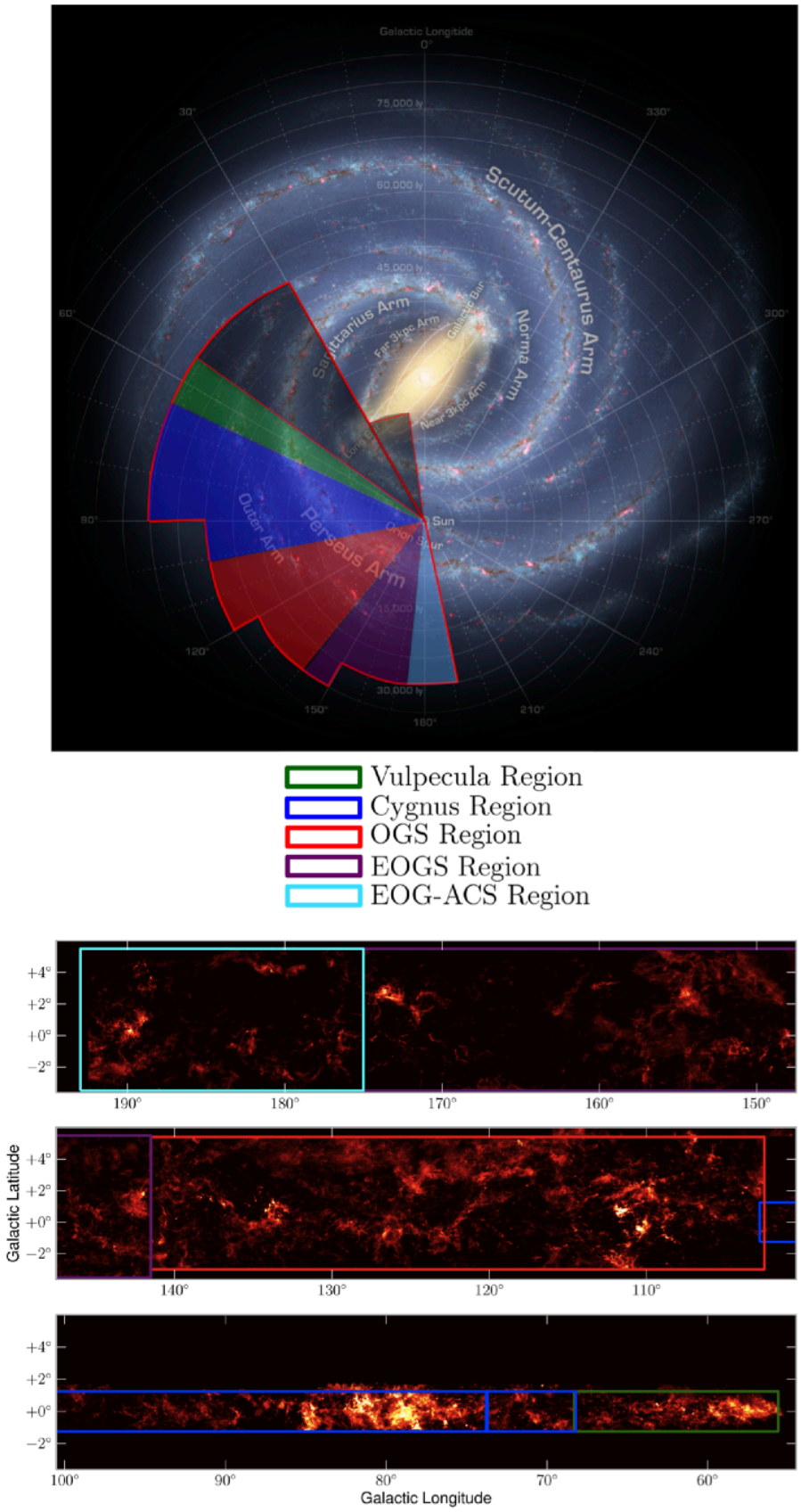

Figure 2.2: The Above Figure shows the surveys regions in the Ex-FCRAO CO survey described in Brunt et al. (in prep). The top panel is the *approximate* kinematic coverage of the survey regions overlaid on an image inspired by GLIMPSE observations (the greyed-scale shows the low longitude supplement of Dame et al. (2001)). The bottom panel shows an integrated map of $\int_{v_{min}}^{v_{max}} \mathrm{T}(l, b, v)\, dv$. The parameters for each of the regions defined above can be seen in Table 2.1.

wheel method which is outlined in the Kutner & Ulich (1981). The need for the corrections arise because - at the mm wavelengths - the Earth's atmosphere is translucent. In addition to this innate difficulty, the level of transparency of the atmosphere can vary greatly over relatively small periods of time with the moisture content of the atmosphere - resulting in a loss of achievable angular resolution.

The corrections are applied to the T_A^* data to convert to main-beam temperature (T_{mb}) which takes in to account the efficiencies. Using noise maps of $\sigma(T_A^*)$, the data were transformed into T_{mb} via a combination of the main-beam efficiency (η_{mb}) and the efficiency of forward scattering (η_{ffs}). This efficiency factor - for the ExFCRAO data - was calculated and provided by Brunt (priv. comm.) as $\eta_{eff}=\frac{1}{0.66}$.

2.2 The International Galactic Plane Survey (IGPS)

The *International Galactic Plane Survey* (hereafter IGPS[1]) is an effort to map the ISM, in the cm, mm and infra-red, across the whole sky. Though the IGPS includes the Heyer (1996) release of the OGS, only the cm-wave HI observations will be used from this complete catalogue in the form of the CGPS and VGPS, both of which are described subsequently.

The HI (21-cm) component of the Canadian Galactic Plane Survey (CGPS) began with a pilot study by Normandeau et al. (1997). The observations were conducted using the Dominion Radio Astrophysical Observatory (DRAO) in British Columbia, Canada. The DRAO is formed of a single dish (26 m) and multi dish array (Synthesis Telescope), for the 21-cm HI detections the DRAO-ST was used to obtain the spectral-line information. The current release of the the CGPS[2], Taylor et al. (2003), was used for this work. The data are a series of 5x5 degree mosaics covering a Galactic longitude range of $63^o < l < 184^o$ with a latitude range of $-3.5^o < b < 5.5^o$ across the whole longitude range, but with a latitude extension between $100^o < l < 116.5^o$ up to $-3.5^o < b < 17.5^o$. The spatial resolution of the data used is $\delta\theta_{lb} = 0.05^o$ and a spectral resolution of δv_{lsr}=1.56kms^{-1}.

The VLA Galactic Plane Survey (VGPS), Stil et al. (2006), provides bridging coverage between the northern and southern hemispheres through the longitude range of $18^o < l < 67^o$, it is within this region that the Galactic plane cuts through the celestial equator. The latitude coverage of the VGPS is not constant across the whole survey, there are three steps in latitude coverage; $|b| < 1.3^o$ for $18^o < l < 46^o$; $|b| < 1.9^o$ for $46^o < l < 59^o$; $|b| < 2.3^o$ for $59^o < l < 67^o$.

2.3 Supplemental Spectral Data Surveys

In addition to the Ex-FCRAO and IGPS data, for ^{12}CO and HI respectively, these surveys will be supplemented to extend the latitude and longitude coverage to as much of the Milky Way as possible, Figure 2.3 shows the coverage of the surveys in question. The ^{12}CO data will be supplemented by the ^{12}CO observations from 2011 update of the Dame et al. (2001)[3] survey

[1] http://www.ras.ucalgary.ca/IGPS/

[2] Data available for download from *http://cadcwww.dao.nrc.ca/cgps/*

[3] Data available for download from *http://www.cfa.harvard.edu/rtdc/CO/*

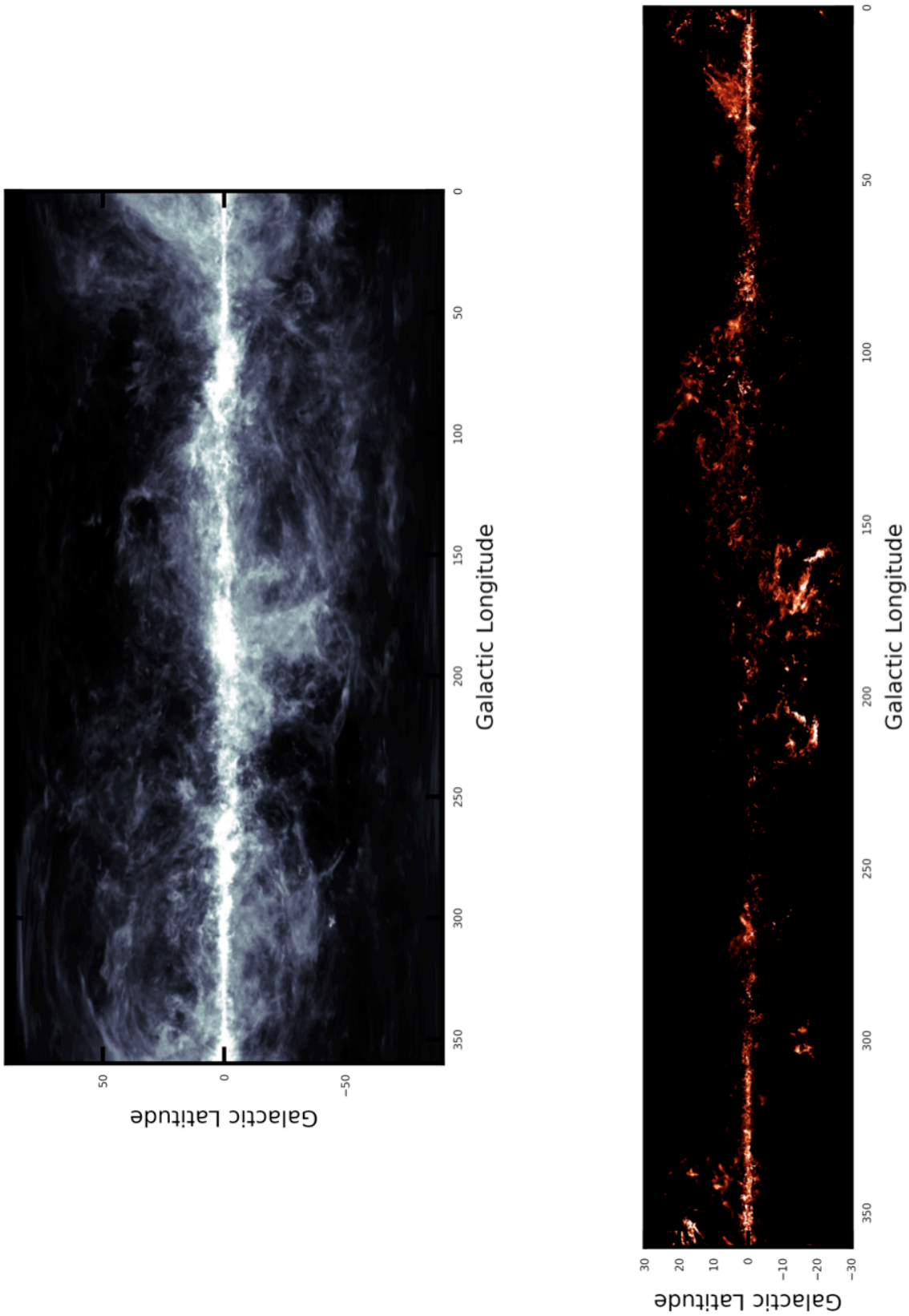

Figure 2.3: Top panel shows L.A.B. HI survey coverage (P. M. W. Kalberla et al. 2005). The bottom panel shows the Dame & Thaddeus (2011) ^{12}CO coverage across its range of Galactic longitude.

Table 2.2: Contributions to the complete CGPS Survey, for the purpose of this work only the 21-cm HI will be used (DRAO-ST). Adapted from English et al. (1998)

Frequency (Wavelength)	Telescope	Comments
151 MHz (190 cm)	**MRAO CLFST** The Mullard Radio Astronomical Observatory's Cambridge Low-Frequency Synthesis Telescope	- Continuum emission images. - **Ionised and relativistic plasmas**
232 and 327 MHz (130 and 92 cm)	**BAO** Beijing Astronomical Observatory	- Continuum emission images. - **Ionised and relativistic plasmas**
408 and 1420 MHz (74 and 21 cm)	**DRAO ST** Dominion Radio Astrophysical Observatory Synthesis Telescope **DRAO 26 m** dish for HI line data	- HI 21 cm line continuum at 1420 and 408 MHz with polarisation at 1420 MHz - **Neutral Hydrogen intensity** - **Ionised and relativistic plasmas** - **Magnetic field information**
115 GHz (2.6 mm)	**FCRAO** University of Massachusetts' Five Colleges Radio Astronomy Observatory	- Emission from CO J(1-0) - **Tracer of molecular Hydrogen**
3 and 5 THz (100 and 60 μm)	**IRAS** Infrared Astronomical Satellite	- **Radiative emission from dust**

which is a composite of 37 smaller ^{12}CO surveys. These data are lower resolution than the Ex-FCRAO, with the spatial resolution of the data is $\delta\theta_{lb} = 0.125^{o}$ where the spectral resolution of δv_{lsr}=1.3kms^{-1}. The 21-cm HI IGPS survey is supplemented by the Leiden-Argentine-Bonn (LAB) survey of Galactic HI[4], described in the work of P. M. W. Kalberla et al. (2005). As with the Dame et al. (2001) data the resolution is coarser than the IGPS, with the spatial resolution being $\delta\theta_{lb} = 0.5^{o}$ and a spectral resolution of δv_{LSR} =1.03kms^{-1}.

2.4 Stellar Cluster Samples & Catalogues

The first part of this work, described in Appendix C but summarised in Section 1.6, is to find the relationship between the mass of molecular material surrounding young stellar clusters and

[4]Data available for download from *http://cdsweb.u-strasbg.fr/cgi-bin/qcat?J/A+A/440/775*

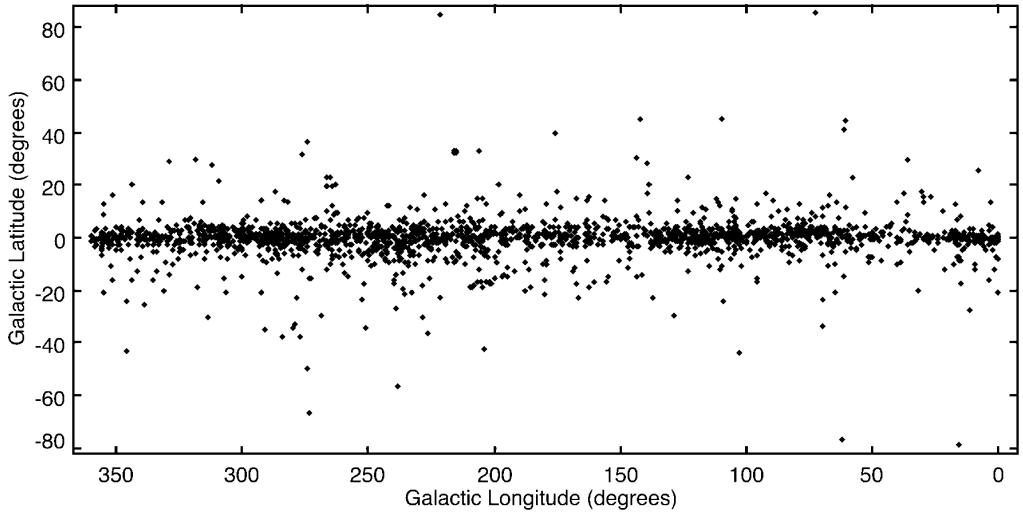

Figure 2.4: The Figure above shows the ℓ, b distribution of all 2095 clusters within the Dias et al. (2010) stellar cluster catalogue.

its dissipation time. Having already described the gaseous spectral data above, this section will describe the catalogues used for the stellar clusters.

2.4.1 The WEBDA Catalogue of Stellar Clusters

The WEBDA[5] online catalogue of Galactic stellar clusters and Magellanic clouds hosted by the Institute of Astronomy at the University of Vienna and is maintained by Ernst Paunzen and Christian Stütz. The goal of the catalogue is to collate all published data for stars in open stellar clusters, it was initially described in Mermilliod (1988) with a sample of 570 clusters, the database now stands a 100,000 stars in the New General Catalogue of Nebulae and Clusters of Stars (NGC & IC prefix, Dreyer (1888)) and also included some anonymously classified clusters. Stars within the catalogue have astrometric, photometric and spectroscopic properties and also has a cross-reference listing of all papers where each of the clusters are published, including *interesting* results.

Though it is a good resource from which we are able to obtain, with relative ease, the properties of the clusters; it is important to understand how the properties were measured. The main contributing problem for this work is how the distances for each cluster is determined, the distances are a mix of kinematically determined and spectroscopically measured distances. The problem is that a kinematically determined distance is dependant on the rotation curve/velocity field used in the work and as such is not an objective way to determine distances - as discussed in Chapter 1. The alternative way to measure a distance is to determine it spectroscopically via the fitting of isochrones to CMDs (Colour Magnitude Diagrams), shown in Appendix C.

[5]http://www.univie.ac.at/webda/

2.4.2 A Catalogue of Optically Visible Open Clusters, Dias et al. (2010)

For a complete catalogue description I refer the interested reader to Dias et al. (2002, 2007, 2010). The stock data included as the basis of the Dias catalogue are the available coordinates, age, size, distance and colours. The new objects, unique to the Dias catalogue, were cross-referenced with the SIMBAD[6] online repository to compile a complete bibliographic listing to obtain the kinematical data for each of the clusters (where available). At time of writing the full Dias catalogue includes virtually all presently known clusters (2095), shown in Figure 2.4.

Both the Dias and the WEDBA catalogue will be used and compared where possible. The cluster sample will be subjected to spatial and parametric cuts. The spatial restraints imposed were the extent of the Ex-FCRAO ^{12}CO survey, i.e. Galactic longitude range of $55.7^{o} < l < 192.5^{o}$ with a latitude range of $-3.5^{o} < b < 5.5^{o}$. The next constraint applied to the data sample is the velocity limits of the Ex-FCRAO surveys.

2.5 Summary

Here I have introduced the main surveys and catalogues of data which form the basis of the work presented within this thesis. How these data are treated and used specifically at each stage of the work is presented at the beginning of each Chapter. The spectral line data is used in both the preliminary work presented in Appendix C and also forms the basis for work on Galactic structure, whereas the stellar cluster data is solely for use in the work presented in Appendix C.

In addition to the general data-sets introduced here; for constraining the spatial structure of the spiral arms, there are additional samples of data used, such as maser sources, clusters etc. These were compiled from the literature and are presented in tabular form - when needed - in their appropriate Chapters. For completeness the compiled sample of arm tracers was based on the state of the literature as of December 2011.

[6] http://simbad.u-strasbg.fr/simbad/

CHAPTER 3

A New Model Of Galactic Spiral Structure: The Shocked Motion Model

"They didn't know it was impossible...
...So they did it anyway."
Mark Twain, 1835 - 1910

3.1 Introduction to Chapter

Any study of star formation, and the timescale over which it occurs, must include an understanding of molecular clouds and the ISM. It is accepted that molecular clouds are the sites of all known star formation, hence wherever one observes an area where young stars reside, it is assumed one will also find molecular material, Blitz & Williams (1999). Most star formation occurs in the spiral arms of S-class Galaxies, it is, therefore, valuable to have information as to the spatial and velocity locations of the spiral arms. Though the Milky way is known to possess spiral structure, the extent - regarding actual positions and number is still contested Reid et al. (2009). It is found that optical Spiral Arms are well traced by CO emission, in that the CO traces the molecular material which in turn traces the spiral arms. Unlike other tracers, such as HI, CO is clumpy and it is this level of sub-structure which allows one to use it to trace the molecular clouds and hence the spiral arms where they reside.

Galactic astronomers have both the advantage and the curse of being within the body they are trying to observe. It is an advantage in that we are relatively close to the objects we are trying to observe and hence we are able to attain a higher resolution than the currently possible for extra-Galactic observations. Though with the advent of the next generation of instruments - such as ALMA and the SKA (Obreschkow et al. 2009) - this will be much improved upon. Since the observer resides within the disc of the Milky Way, Galactic plane observations are attenuated by a significant volume of material and the methods by which the data are taken limit the knowledge of the Galaxy's structure (i.e. mm/cm wave spectral line surveys). In spectral line surveys such as the International Galactic Plane Survey (English et al. (1998)) the data are taken in terms of

position-velocity coordinates, therefore to transform the observed velocity into an actual linear distance from the observer one needs to convert the observed velocity to a *kinematic distance*. Since the kinematic distance is closely related to the chosen Galactic rotation curve, the distances obtained can vary. From a simple flat rotation curves where one assumes circular rotation and have constant orbital velocity across the whole Galactic disc, to more complicated rotation curves which can incorporate the presence of the spiral arms (Brand & Blitz 1993; Blitz & Williams 1999; Russeil et al. 2007; Reid et al. 2009). It is important at this juncture to emphasise that the kinematic distance is *not* an actual distance and as such can be wrong - since it is a distance determined from the object's velocity which itself is dependant on the chosen rotation curve - which can mislead the observer into misplacing key structural features in the Galaxy.

One also suffers from complications for material $\approx 0\,\mathrm{km\,s^{-1}}$, since it becomes confused with local emission. This velocity compression occurs in around the centre and anti-centre regions - again, leading to confusion in the observed velocities.

As was discussed in Chapter 1, Galactic astronomers are well aware of the near-far distance ambiguity inherent with inner-Galaxy observations, however there is also a similar situation in the outer Galaxy (Brunt et al. 2002). The shock present in spiral arms can cause, in some places, a triple valued function i.e. near- or far-side arm and exterior-arm, as can be seen in the schematic, Figure 1.28. Yielding similar complications as for the inner Galaxy; i.e. "how large is the cloud I'm observing?", since the size of the cloud, its volume and consequently its mass is uncertain. Due to the distance dependance on the mass , $\mathcal{M} \propto \frac{1}{\mathrm{d}^2}$, accurately determining the distance to the material is important when deriving a cloud's parameters.

Though the internal arm separations are not large, within the Milky way at least, the difference between whether the velocity corresponds to arm/shock based material or exists at a further distance beyond the spiral potential can cause inconsistencies when classifying emission in these regions. Of course, this is the case were a single spiral potential in the Outer Galaxy, but Galactic astronomers know of at least two further arms; Outer (Bok 1959) and the far-outer part of Scutum-Centaurus (Dame & Thaddeus 2011) beyond the Perseus arm. We are able to trace the spiral arms using parallax measured distances to known arm-based regions, so as to give anchor points for a spiral arm as it sweeps through the Galaxy. This work models the spiral features of the Milky Way as a logarithmic spiral extending around the Galactic centre, each with material within the arm subject to a shock of constant magnitude. The work presented here concentrates on the definition and description of the Perseus spiral arm model and aims to create a set of spatially convolved maps for a series of tracers in our Galaxy to create a data-set allowing an "*extra-galactic style view*" of our own Galaxy, the importance of which I will describe later.

We are able to observe possible spiral features in spectral line data when expressed in terms of longitude and velocity, see Figure 3.1. Spiral arms are where most of a galaxy's star formation occurs and a pre-requisite for star formation is the presence of a reservoir of molecular material from which the stars can form. By mass, the main constituent of molecular clouds is molecular Hydrogen, which not easily detected directly, therefore, I use a tracer molecule for the hydrogen - carbon monoxide (CO). CO - like HI - is a good tracer of optical spiral structure, but unlike HI , CO's clumpy nature gives a better indication of the spiral arm's sub-structure.

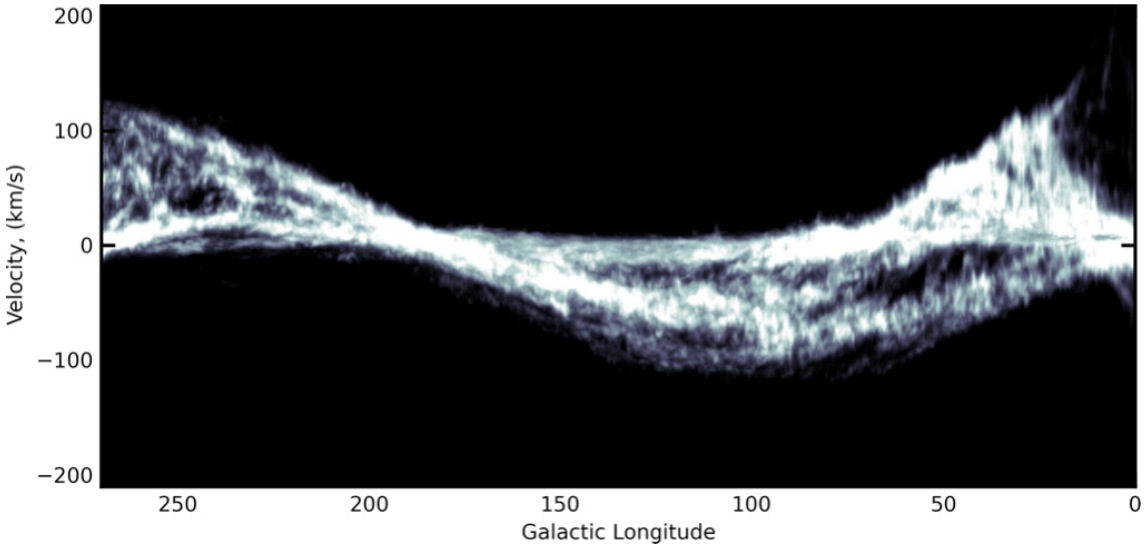

Figure 3.1: Longitude velocity map of HI , taken from LAB HI survey, with the HI integrated through the *b*-axis. The figure suggests the presence of kinematic spiral structure in the longitude-velocity plane in the form of the bands of emission at negative v_{LSR} at 150°< ℓ <25°.

3.1.1 The Perseus Arm

The Perseus arm is the closest large-scale structure in the observable Galaxy and extends from just beyond the anti-centre down to a longitude of $\approx 50^o$, the arm moves from the outer to the inner-galaxy around ≈ 65°, (Oort et al. 1958; Bok 1959; Verschuur 1973) and has been identified as a site of major Galactic star formation. The longitude-velocity structure of the Perseus arm is apparent in spectral line surveys (Figure 3.1), therefore any attempt to identify the potential of star formation in the form of observing the gas within the arm must include an understanding of the spiral arm dynamics. The work of Roberts (1972) were the first to attempt to describe the longitude-velocity structure of the outer Galaxy in the form of the Two Arm Spiral Shock model. The basis of the model is that material within an arm experiences a shock and is slowed with respect to Galactic rotation. The model involves the implementation of a two-arm spiral density wave within the Galaxy - it was then applied to the region where the Perseus arm was thought to reside. From modelling the gas as it passes through the arm, Roberts (1972) were able to derive pitch angles of $6^\circ < \phi_{pitch} < 15^\circ$ over a range of Galactocentric radii. This is not dissimilar to modern estimates of its trajectory ($10 < R < 13$ kpc), as we will soon see. Gas within the Perseus arm was found to be moving 6-10 km s^{-1} slower than the 'non-arm' gas - and were found to be consistent with contemporary observations. By identifying a longitude-velocity and longitude-distance relation for the Perseus arm, we are able to combine these and assign distances to kinematically determined arm emission. The Perseus emission maps are then convolved and smoothed to a common linear resolution across the arm to observe the relative differences in the sizes of the clouds and to have a map with fewer observational biases (i.e. varying linear size with angular position due to the arm's varying distance with ℓ).

3.1.2 The Outer Arm

The Outer spiral arm, prior the discovery of the far-outer Scutum-Centaurus arm (Dame & Thaddeus 2011), was once thought to be the outer-most spiral feature of the Milky Way and is the next observable large-scale structure beyond the Perseus arm. Figure 3.1 shows the arm Outer arm and can be seen, kinematically, as a shift to a more negative Galactic rotation speed - like Perseus, (Clemens 1985, Figure 3 therein). The arm has been traced in all four Galactic quadrants using various methods. Maser emission in the first (Hachisuka et al. 2009; Sanna et al. 2011) and second (Reid et al. 2009) quadrants; molecular and atomic gas (Dame, Hartmann, & Thaddeus 2001; Nakanishi & Sofue 2003; McClure-Griffiths, Dickey, Gaensler, Green, Haverkorn, & Strasser 2005), measurements of the *Blue Plume* components of open stellar clusters (Pandey et al. 2006) in the second and third quadrant; spectroscopic observations detections of early-type stars (Negueruela & Marco 2003, 2008) in the second and third, detections of HII regions in the first quadrant (Russeil et al. 2007). So there are a number of *known* Outer arm objects and tracers which can be used to more accurately determine the trajectory of this structure as it spans our Galaxy.

3.2 Source Data

The molecular data is the taken from Exeter-FCRAO (Five College Radio Astronomy Observatory) CO Northern Galactic Plane Survey. The composite survey data are made from the FCRAO Outer Galaxy Survey (OGS) the data were taken between May 1994 and September 1997, originally described in Heyer et al. (1998) and again in a reprocessed form in Brunt et al. (2002). There are three further regions of data taken; the Extended Outer Galaxy Survey and Extended Outer Galaxy Anti-Centre Survey are described in Brunt et al. (in prep). These ^{12}CO data are supplemented at higher latitudes by the Composite CfA CO Survey of Dame et al. (2001). I also use the high resolution HI components of the *International Galactic Plane Survey* (IGPS) described in English et al. (1998). As with the ^{12}CO , this Galactic plane HI is supplemented at higher latitudes by data taken from the Leiden/Argentine/ Bonn (LAB) Galactic HI survey described in P. M. W. Kalberla et al. (2005) - full data descriptions can be seen in Chapter 2.

3.3 Defining the model - The Perseus Spiral Arm

The aim here is to obtain a quantitative description of both the distance, d_{per}, and the mean LSR velocity of the Perseus Arm, v_{per}, as a function of Galactic longitude, ℓ. Together these will then allow a transformation of LSR velocity into distance at each line-of-sight for which the arm is observable. The function $d_{per}(\ell)$ is derived from a logarithmic spiral fit to Perseus Arm sources with accurately known distances. From a purely practical point of view, any quantitative representation of $v_{per}(\ell)$, such as a polynomial fit to sources in the Perseus Arm with known velocities, could be used. However, it is more informative to apply a simple model to the kinematic structure, so that a parameterised deviation from flat, circular rotation may be analysed and discussed. The spatial and kinematic structure of the Perseus Arm are discussed and analysed in turn below.

Table 3.1: Perseus Arm maser sources. The distance to S252 is taken from Reid et al. (2009), but the LSR velocity is taken from Shiozaki et al. (2011). R09 - Reid et al. (2009); O10 - Oh et al. (2010); N11 - Niinuma et al. (2011); S11 - Shiozaki et al. (2011)

Object	ℓ (degrees)	b (degrees)	v_{LSR} (km s^{-1})	Heliocentric Distance (kpc)	Ref.
AFGL 2789	94.6	–1.79	–44.0	3.07±0.30	O10
NGC 7538	111.54	0.78	–57.0	$2.65^{+0.23}_{-0.11}$	R09
IRAS 00420	122.02	–7.07	–44.0	$2.11^{+0.18}_{-0.08}$	R09
W3(OH)	133.95	1.06	–45.0	$1.95^{+0.08}_{-0.04}$	R09
IRAS 06061+2151	188.79	1.03	–1.6	$2.02^{+0.13}_{-0.12}$	N11
S252	188.95	0.89	(+11.0) **+3.0**	**2.10** (1.76±0.57)	R09/O10
G192.16–3.8	192.16	–3.89	5.7	1.52±0.08	S11

3.3.1 Modelling the Spatial Structure

To define the spatial structure of the Perseus Arm in the Galaxy, a sample of sources with reliably known distances determined from trigonometric parallaxes of methanol and water maser emission within high-mass star-forming regions (Reid et al. 2009; Oh et al. 2010; Shiozaki et al. 2011) was compiled. These distances are determined geometrically, so no assumptions about the properties (such as luminosity, metallicity and extinction) of the sources are made, thus reducing the associated uncertainty (Reid et al. 2009). Sources identified as Perseus Arm sources in these works are summarised in Table 3.1. I note that two discrepant distances and velocities for S252 are derived from methanol masers and water masers, suggesting that the maser distance method is not as reliable as usually claimed. In preference to the 1.76±0.57 kpc distance of Oh et al (2010), I have adopted the 2.10 kpc distance of Reid et al (2009) as it is more consistent with previous spectroscopic distances determined for this source and nearby sources in the Gem OB1 complex (see Carpenter et al 1994 for a compilation). However, the LSR velocity of +11 km s^{-1} reported for S252 by Reid et al (2009) lies outside the bulk of CO emission visible towards this source in the FCRAO CO data. For the kinematic analysis below, I have therefore adopted the Oh et al LSR velocity of +3 km s^{-1} which is more consistent with the CO observations. Following Reid et al. (2009), I also exclude NGC 281, which, although nominally a Perseus Arm source, resides within an expanding bubble (Sato et al. 2008) and as a result is not a good tracer of spiral structure since its parallax is offset from the rest of the sample.

We fitted the Perseus arm with a logarithmic spiral model:

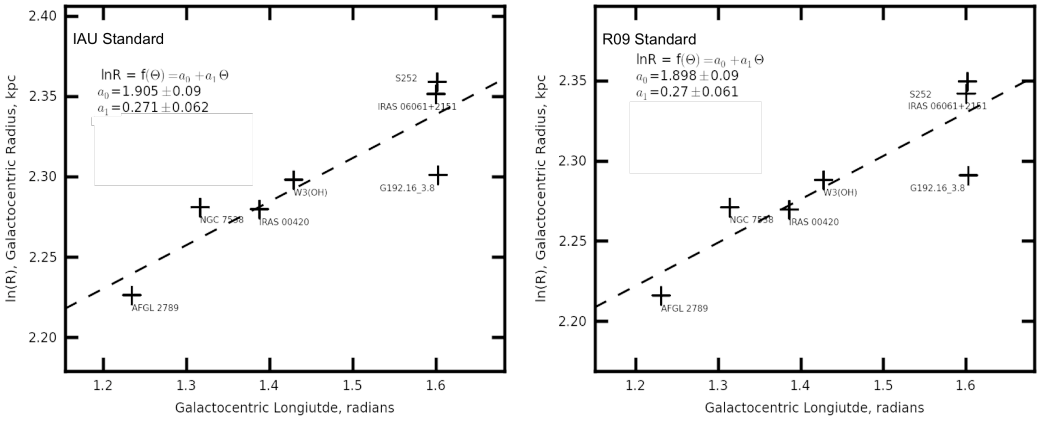

Figure 3.2: Logarithmic spiral fit (Equation 3.1) to tracers taken from Reid et al. (2009), Oh et al. (2010); Shiozaki et al. (2011), showing both the fit taking $R_0 = 8.4$ kpc [right] and also the fit obtained with IAU standard $R_0 = 8.5$ kpc [left].

$$\ln\left(\frac{R_{arm}(\theta)}{[kpc]}\right) = a_0 + a_1 \frac{\theta}{[radians]}, \tag{3.1}$$

where R_{arm} is the Galactocentric radius of the spiral arm, and the Galactocentric longitude, θ, has its origin along a line emerging from the Galactic Centre parallel to $\ell = 90°$, with θ increasing anticlockwise from this point. Galactocentric radii for the maser sources were computed from their distances and Galactic coordinates for two different geometries: using the IAU Standard distance to the Galactic Centre of $R_0 = 8.5$ kpc, and using the slightly smaller value $R_0 = 8.4$ kpc given in Reid et al (2009). One may then obtain an estimate of the pitch angle of the Perseus arm, ϕ_{pitch} via;

$$\phi_{pitch} = \arctan\left(\frac{d}{d\theta} ln(R_{arm}(\theta))\right) = \frac{\pi}{2} - \arctan\left(\frac{1}{a_1}\right) \equiv \arctan(a_1) \tag{3.2}$$

The best fitting lines to the maser sample are shown in Figure 3.2. The standard deviation of the sources' Galactocentric radii about the best-fitting arm-centre can be used as an estimate of the physical width of the Perseus arm. I found a standard deviation of 200 pc in Galactocentric radius, which implies a standard deviation of 190 pc along a direction perpendicular to the arm's length. Assuming a Gaussian form for the density of sources within the arm, this corresponds to a full width at half maximum width of ~450 pc, which is comparable to other measures the Perseus arm and of the widths of spiral arms in other galaxies, Foster & Routledge (2003); Egusa et al. (2010) respectively. The pitch angle of the arm is found to be $\phi_{\rm pitch} = 15.1 \pm 3.3°$which is consistent with other determinations of the pitch angle of Perseus (Vallée 2002; Reid et al. 2009).

The fitted form of $R_{per}(\theta)$ can be transformed, using simple trigonometry, into the distance to the Perseus Arm, d_{per}, as a function of Galactic longitude, ℓ. The dependence of R_{per} and d_{per} on ℓ for both choices of R_0 is shown in Figure 3.3. While, naturally, $R_{per}(\ell)$ is different for the different choices of R_0, the resulting $d_{per}(\ell)$ relations are negligibly different. According to the fits, the Perseus Arm has a closest-approach of 1.7 kpc at $\ell = 161.4°$ in the second quadrant, and

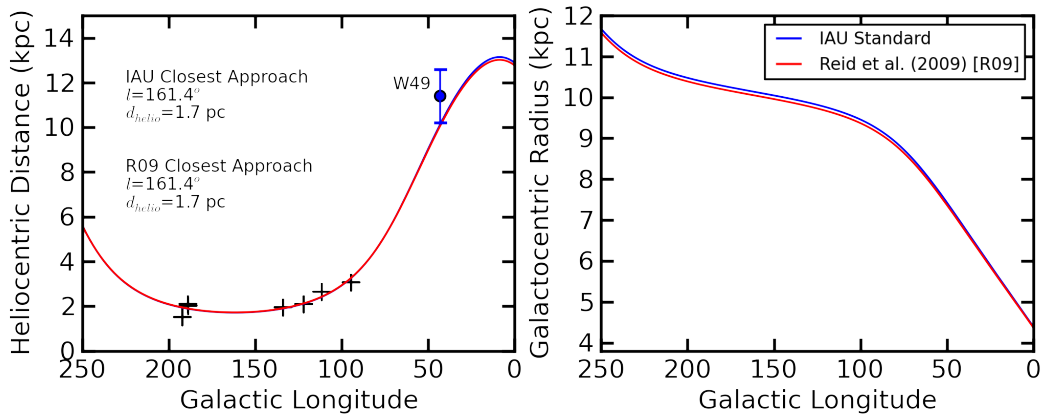

Figure 3.3: The Figure above shows the dependence of d_{per} [left] and R_{per} [right] on ℓ for both choices of R_0 over plotted with the Perseus arm Masers listed in Table 3.1. Note this model also predicts W49 as a Perseus arm object, parameters from Gwinn et al. (1992) (see text).

recedes from us from this point into the third quadrant (where it is poorly-defined observationally) and into the first quadrant where it has a distance of 9 kpc at $\ell \sim 50°$ (the point at which it transitions from negative to positive v_{LSR}). Also shown in Figure 3.3 is the longitude and distance of the maser source in the HII region W49 (Gwinn et al. 1992) which I subsequently identified as a Perseus Arm candidate source on the basis of its distance and LSR velocity (see Section 3.2.5 for further discussion).

3.3.2 Modelling the Kinematic Structure

Overview of ℓ-v_{LSR} Structure in the CO Maps

Figure 3.4 shows a peak temperature map of CO J=1–0 derived from the Composite CfA CO Survey (Dame et al. 2001), projected over the b-axis. This gives an overview of the kinematic structure of the molecular material in the Galaxy. Overplotted on this map are the ℓ–v_{LSR} maser positions from Table 3.1 which lie within a major band of CO emission traditionally identified as the (kinematic) Perseus Arm. Vallée (2008) compiled a list of works that make this identification, though Vallée (2008) criticised these works, claiming that this kinematic feature was inconsistent with a simple Perseus Arm model based on circular rotation. However, it has been known for about half a century that the Perseus Arm is placed kinematically at significantly more negative v_{LSR} than is predicted by circular rotation (Bok 1959; Janák & Mayer 1959), specifically the two-armed spiral shock model of Roberts (1972) probably being the most successful. A sophisticated analysis of the kinematic structure of HI based largely on the Roberts (1972) picture was carried out by Foster & MacWilliams (2006) with impressive results and I refer the interested reader to that reference for further analysis.

Other notable features in Figure 3.4 are worth briefly describing here. A band of emission at more negative v_{LSR} than the Perseus Arm, most obvious near $\ell = 70° - 80°$, $v_{LSR} \sim -70$ km s^{-1}, but extending weakly to more negative velocities at higher longitude (visible in this image up

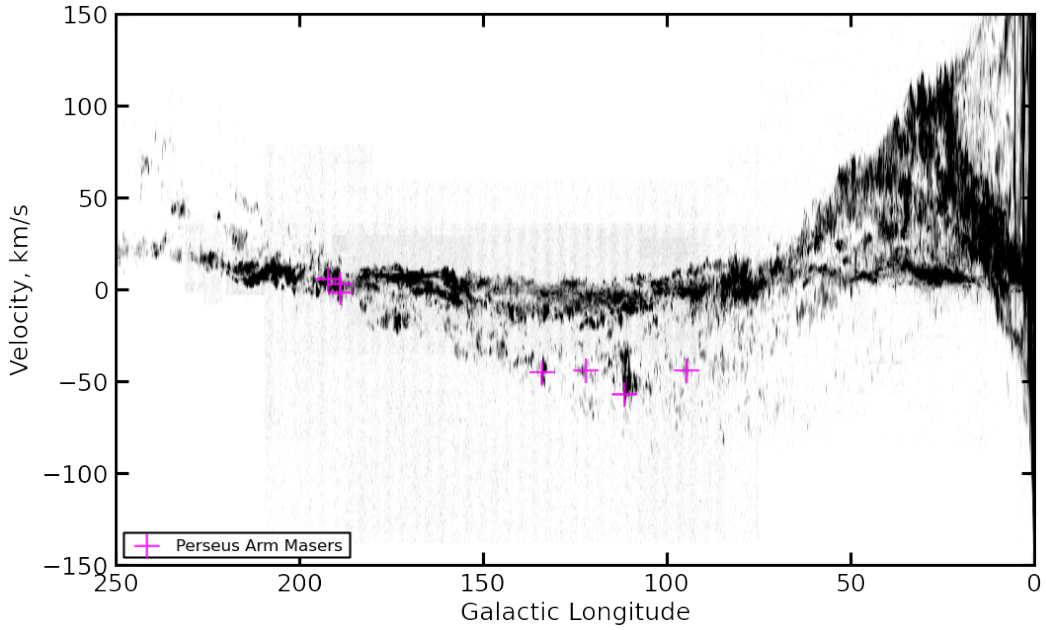

Figure 3.4: The Figure above shows the longitude-velocity structure ^{12}CO in the Dame et al. (2001) survey. The magenta crosses show the locations of the Perseus arm masers listed in Table 3.1.

to $\ell \sim 150°$), originates from the Outer Spiral Arm (Kimeswenger & Weinberger (1989) ; and described more fully in the following section. The Outer Arm is visible down to $\ell \sim 15°$ where it transits across the $v_{LSR} = 0$ km s^{-1} boundary. A small fraction of the CO emission at negative v_{LSR} below $\ell = 50°$ has been identified as originating from an extreme Outer Galaxy spiral arm at higher latitude than the Outer Arm (Dame & Thaddeus 2011).

Emission near $v_{LSR} = 0$ km s^{-1} originates primarily from "local" molecular material within ~ 1 kpc of the Sun, but also includes slightly more distant sources such as the intense emission from the Cygnus X region at $\ell \sim 80°$, located at a distance of ~ 1.7 kpc (Schneider et al. 2007). Below $\ell \sim 70°$, emission from the Inner Galaxy ($R < R_0$) is visible at positive v_{LSR}.

Both the local emission and the Outer Spiral Arm emission are clearly separated from the Perseus Arm by notable gaps in v_{LSR}, though these gaps naturally close near the anti-centre due to the lack of projection of circular Galactic rotation in this region. However, it is clear that the Perseus Arm remains at negative v_{LSR} (~ -5 to -10 km s^{-1}) even at $\ell = 180°$, emphasising the importance of non-circular rotation in its kinematics. The Perseus Arm can be traced as a coherent structure from the anti-centre region, through the entire second quadrant, and down to $\ell \sim 55°$ where it merges with local emission at $v_{LSR} = 0$ km s^{-1}. In the third quadrant, two bands of emission are evident (at least between $\ell \sim 200°$ and $\ell \sim 250°$) which I identify as the Perseus Arm and Outer Arm, again separated kinematically by the projection of Galactic rotation.

Lee J Summers

Image Copyrighted.
Original source image can be found:

Figure 3, Dobbs & Pringle (2010)

Third Party Copyright Marker

Figure 3.5: The Figure above, taken from Dobbs & Pringle (2010), shows the trajectories of particles as they flow through a fixed spiral potential (the grey regions). The trajectories may be interpreted as stream lines of material, with the points within the Figure representing the location of material as it flows through the potential at 2, 50 and 100 Myrs.

Definition of the Kinematic Model

Employing a simple kinematic model to objectively model the Perseus Arm's kinematic structure, the purpose of which is two fold: (1) to define an initial kinematic locus (in ℓ, v_{LSR}) around which a sample of CO-defined molecular clouds may be extracted from the spectral line data; (2) to investigate a possible physical explanation of the deviations from flat circular rotation known to exist in the Perseus Arm.

The kinematic model is inspired by numerical hydrodynamic simulations of spiral arms generated by stellar potential wells (Dobbs & Pringle 2010). Figure 3.5 is a reproduction of Figure 3 from Dobbs & Pringle (2010) showing the streamlines of gaseous material traversing a spiral potential. Material entering the arm in circular rotation is diverted to flow along the potential well, before emerging downstream on the far side of the arm, and resuming circular rotation.

Gaseous material confined in this way will define a gaseous spiral arm, as the material is held for some time (Dobbs & Pringle 2010, $\sim$ 50 Myr) in the potential well. Molecular material collected or formed in such a compressed region would presumably be destroyed by subsequent star formation occurring in the arm, or dissolve into the lower pressure environment some time after exiting the arm, depending on the disk's surface density (Dobbs et al. 2006).

Figure 3.6 shows the concept of this model in terms of the molecular material as it flows through Galaxy. The molecular material orbits the Galactic centre with circular rotation, at velocity v_{circ}, until it reaches the spiral arm. Once the molecular material encounters the spiral arm it is

subject to a shock as it encounters material already collected in the potential well, and begins to flow along the arm at velocity v_{arm} (Dobbs et al. 2006; Dobbs & Pringle 2010) . The arm bisects a line of constant radius at angle $\phi_{\rm pitch}$, the pitch angle of the arm. The angle, $\phi_{\rm shock}$, defines the angle at which the material traverses the arm. If $\phi_{\rm shock} = 0°$ then the material would not traverse the arm, but instead would travel down the arm ad infinitum. The deviation from $\phi_{\rm shock} = 0°$ allows the material to move across the arm, and finally to exit the arm and resume circular motion. I do not attempt to model any detailed flow structure within the arm itself. I assume that v_{circ}, $\phi_{\rm pitch}$(= 15.1° determined above), v_{arm} and $\phi_{\rm shock}$ are constant, with the latter two quantities to be fitted from the relevant data.
According to this model, material located in the Perseus Arm will be observed to have a line-of-sight (LSR) velocity, given by:

$$\mathrm{v_{per}} = \mathrm{v_{arm}}\sin(\epsilon) - \mathrm{v_{circ}}\sin(\ell), \tag{3.3}$$

where ϵ is the angle which projects the arm motion along the line-of-sight, and is given by:

$$\epsilon = \arcsin\left(\frac{\mathrm{R_0}}{\mathrm{R}}\sin(\ell)\right) - \Delta\phi_{\rm sp}, \tag{3.4}$$

where $\Delta\phi_{\rm sp}$ is the difference between the pitch angle, $\phi_{\rm pitch}$, and the shock angle, $\phi_{\rm shock}$:

$$\Delta\phi_{\rm sp} = \phi_{\rm pitch} - \phi_{\rm shock}. \tag{3.5}$$

Kinematic Model of the Perseus Arm - Fit to Maser Positions

By Equation 3.3 to the maser data in Table 3.1 via computing the residuals of the masers' v_{LSR} positions from model predictions based on their longitudes. Two choices for the Solar constants were investigated: the IAU Standard $R_0 = 8.5$ kpc, $v_0 = 220$ km s^{-1} (hereafter "IAU" definition), and the values $R_0 = 8.4$ kpc, $v_0 = 254$ km s^{-1} preferred by Reid et al (2009) from analysis of their maser sources (hereafter "R09" definition). For each choice of (R_0, v_0) I ran a grid of models over a range of $\Delta\phi_{\rm sp}$ and over a range of v_{shock} where:

$$v_{arm} = v_0 - v_{shock} \tag{3.6}$$

is the *scalar* difference between the circular velocity and the arm velocity, and v_{circ} = const. = v_0. To a first approximation, increasing the value of v_{shock} has the effect of amplifying the model's v_{LSR} curve, whereas changing the value of $\Delta\phi_{sp}$ moves the curve laterally in longitude; e.g. a non-zero $\Delta\phi_{sp}$ results in a non-zero v_{per} at the anti-centre.

There is very little practical difference between the best-fitting curves obtained from the different (R_0, v_0) choices over the range of longitudes where direct constraints from the maser sources were available ($94 < \ell < 192$), though of course these curves correspond to different fitted values of $\Delta\phi_{sp}$ and v_{shock}. Contour plots of the measured dispersions of the masers' observed v_{LSR} about each model are shown in Figure 3.7. The best-fitting models identified by these plots are $v_{shock} = 26.0$ km s^{-1}, $\Delta\phi_{sp} = 2.4°$ (IAU) and $v_{shock} = 20.0$ km s^{-1}, $\Delta\phi_{sp} = 2.0°$ (R09).

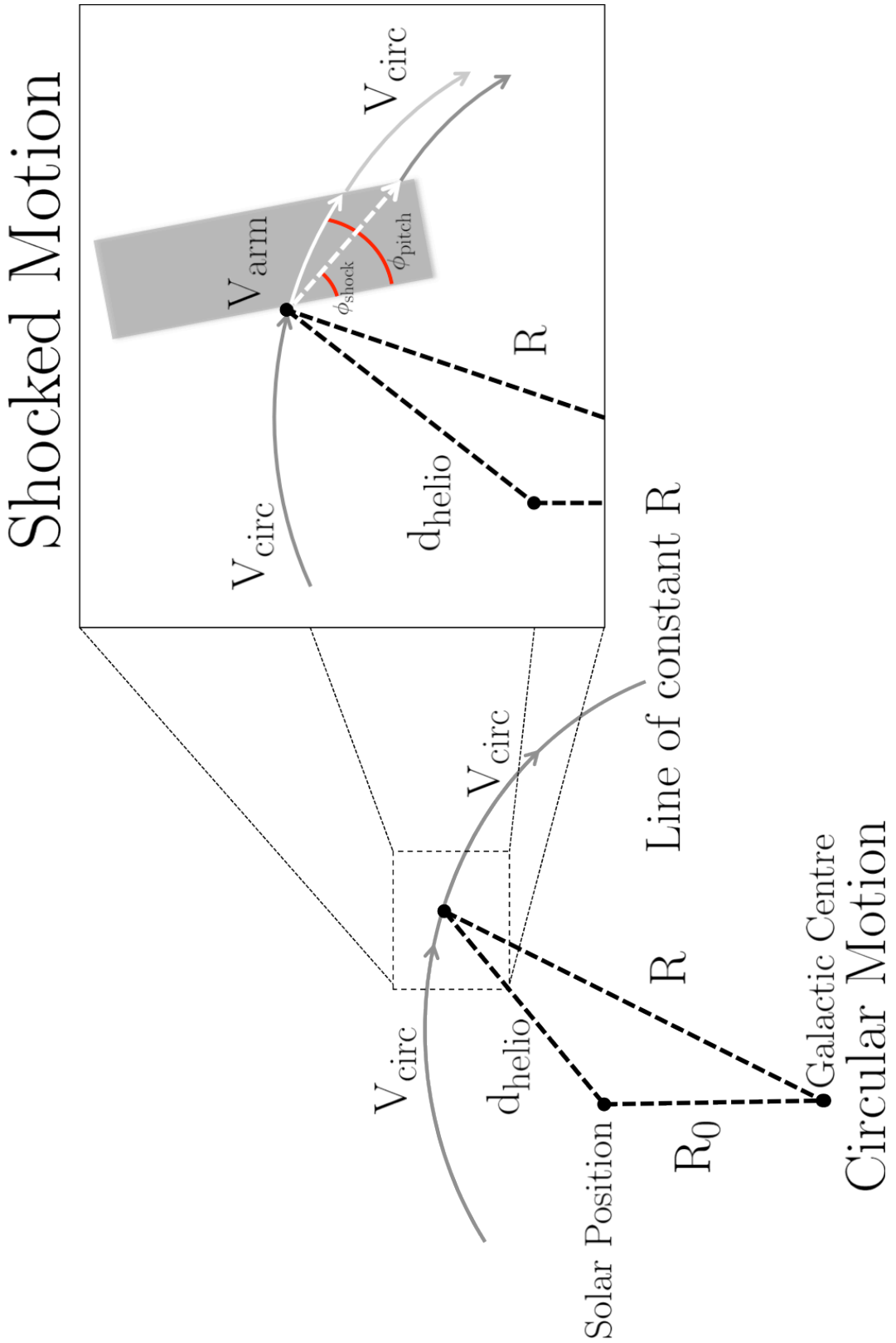

Figure 3.6: Shocked-Motion-Model concept, assuming a flat rotation curve taking into account the presence of the shock in the region of the spiral arm. The molecular material flows into the arm, where it is shocked at some angle, $\phi_{\rm shock}$. The cut-out panel shows the geometry of the model at the point of the observation. The grey lines show the circular motion component in the pre and post arm regions, the white curve shows the trajectory of material were it not subjected to the shock and the dashed white line shows the trajectory of the shocked material within the arm.

The Perseus Arm kinematic loci $v_{per}(\ell)$ defined by the best-fitting models are shown in Figure 3.4, along with the ℓ–v_{LSR} loci predicted by flat circular rotation (given $R_{per}(\ell)$ defined by the logarithmic spiral fits) for each (R_0, v_0) choice. The deviation of the fitted models from the flat circular rotation curve prediction is typically $\sim$ –20 km s^{-1} for $\ell \lesssim 150°$, but becomes progressively smaller in magnitude towards the anti-centre. The flat circular velocity predictions are poor representations of the kinematic Perseus Arm – instead they lie in an apparent inter-arm region. In our model, material immediately upstream of the spiral shock (still in $\sim$ circular rotation, and lying close to the Perseus Arm distance) would appear in this region of ℓ–v_{LSR} space.

In terms of the model, the small best-fit values of $\Delta\phi_{sp}$ indicate that the material entering the arm is not strongly diverted from circular motion, with the main effect being that the material is simply slowed down by the shock. To quantify this further, the deviations from flat circular rotation caused by the motion in the spiral arm can be expressed in terms of radial and azimuthal velocity components.

The *retrograde* azimuthal component is:

$$v_\theta = v_{arm}\cos(\Delta\phi_{sp}) - v_0, \tag{3.7}$$

and the *inward* radial component is:

$$v_R = v_{arm}\sin(\Delta\phi_{sp}), \tag{3.8}$$

both of which are constant deviations at all positions along the arm. In the R09 system, I find that $v_\theta = 20.1$ km s^{-1} and $v_R = 8.1$ km s^{-1}, while in the IAU system, I find $v_\theta = 26.2$ km s^{-1} and $v_R = 8.1$ km s^{-1}. In other words, the material in the arm appears to be rotating around the Galactic Centre slightly slower than predicted by the overall Galactic rotation curve, by $\sim$ 20–26 km s^{-1} depending on the choice of (R_0, v_0). The small inward radial component of $\sim$ 8 km s^{-1}, common to both the IAU and R09 systems, accounts for the non-zero (negative) v_{LSR} of the Perseus Arm at the anti-centre. (Clearly, no purely circular motion, regardless of whether the rotation curve is flat or not, can account for this kinematic feature - since sin(180°)=0.) For comparison, Reid et al (2009) found retrograde azimuthal and inward radial velocity residuals of maser velocities around a flat rotation curve (R09 definition) of 14.7 km s^{-1} and 2.3 km s^{-1} respectively. The maser sample contributing to this analysis extended over a larger region of the Galactic disk and was not restricted to the Perseus Arm, however. It is clear from the residual map inReid et al. (2009) – their Figure 5 – that the deviations from flat circular rotation appear to be somewhat greater for Perseus Arm sources than for the sample as a whole. Oh et al. (2010) found slightly larger values of the retrograde of the azimuthal and radial velocity residuals for their Perseus Arm sources. While these were referred to a different (R_0, v_0) system, the residuals were still in the same inward, retrograde sense. This suggests that it may be profitable to model deviations from circular rotation on an arm-by-arm basis, or possibly as a function of Galactocentric radius, as the Perseus Arm data cover only a restricted range of Galactocentric radius. A practical use of the velocity residuals, for distance estimation, will be discussed further in Section 4.3.4.

The fitted curves provide a good representation of the kinematic Perseus Arm over most of

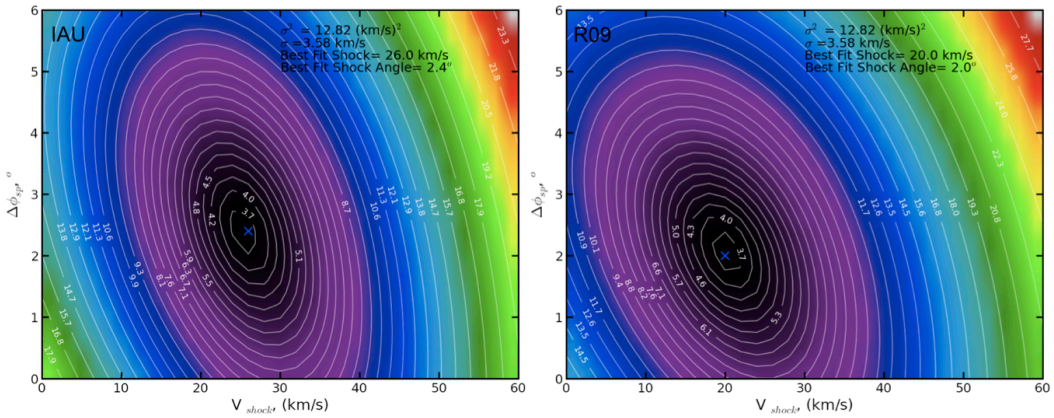

Figure 3.7: The Figure above shows the error ellipses to the least squares fit for the fits in Figure 3.11. The contours denote the σ thresholds.The velocity dispersion is consistent with the fit to the XZ velocity spectrum in Figure 4.25. The colour scale is proportional to the contour values.

the longitude range where Perseus is readily identified. Outside the range where direct constraints from maser data are available, the two fitted curves diverge from each other slightly (near $\ell = 60°$ and beyond the anti-centre). There is a standard deviation of ~ 3.6 km s^{-1} of the masers' observed v_{LSR} around the best-fitting curves in both cases, with no significant difference between the two fits. We will base the rest of the analysis on a single (R_0, v_0) definition – that of R09 – with the following motivations. Firstly, the practical differences between the IAU and R09 systems are small: the $d_{per}(\ell)$ relations (Figure 3.3) are practically indistinguishable, as are the $v_{per}(\ell)$ loci over most of the useable longitude range (Figure 3.4). Secondly, the R09 definition is consistent with the well-constrained angular velocity at the Solar position ($\Omega_0 = 30.3$ km s^{-1} kpc^{-1} – see Reid et al 2009). Finally, the R09-based fit is (qualitatively) more successful in representing the CO emission at lower longitudes (near $\ell = 60°$) where high-resolution data are available (though beyond the anti-centre, the IAU-based fit is arguably more successful).

Kinematic Model of the Perseus Arm - Refinement by ^{12}CO Centroids

Using the FCRAO data between $55 < \ell < 193$, I ran a cloud finding algorithm (Brunt et al. 2003) to extract discrete CO features from the $T(\ell, b, v_{LSR})$ emission structure. Closed emission contours are used to define clouds above a minimum temperature threshold of $T_{min} = 4$ K - for the initial polynomial fitting - and 2 K -for the shocked motion fitting - both in the T_A^* scale. The cloud minimum size was set to be $N_{min} = 10$ pixels are needed for a cloud detection. The cloud decomposition was carried out at 1 arc-minute angular resolution and 1 km s^{-1} spectroscopic resolution.

Polynomial Fitting ℓ–v_{LSR} Structure

The first iteration of the kinematic fit was to use a polynomial fit to the ^{12}CO data that the initial fit identified as 'Perseus arm based emission'. This would then be used to map the ℓ-v_{LSR} of the Perseus arm in the ^{12}CO (Summers 2010). The initial thoughts for using the a polynomial for

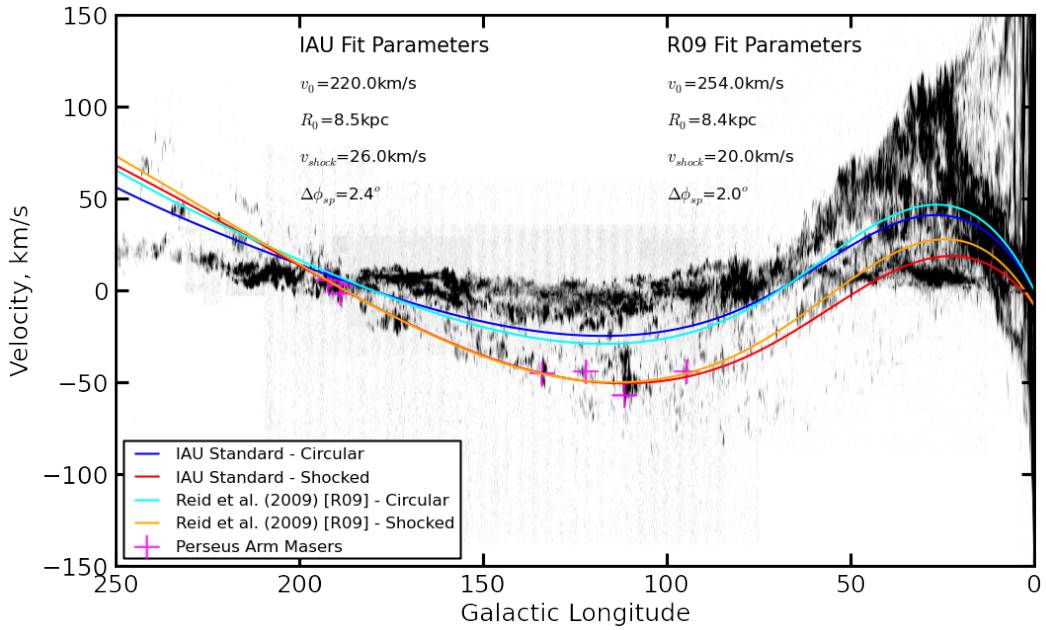

Figure 3.8: The Figure above shows the kinematic models for the IAU and R09 standards for models fit tot the tracers in Table 3.1. The models plot are those assuming circular motion and also those assuming shocked-motion.

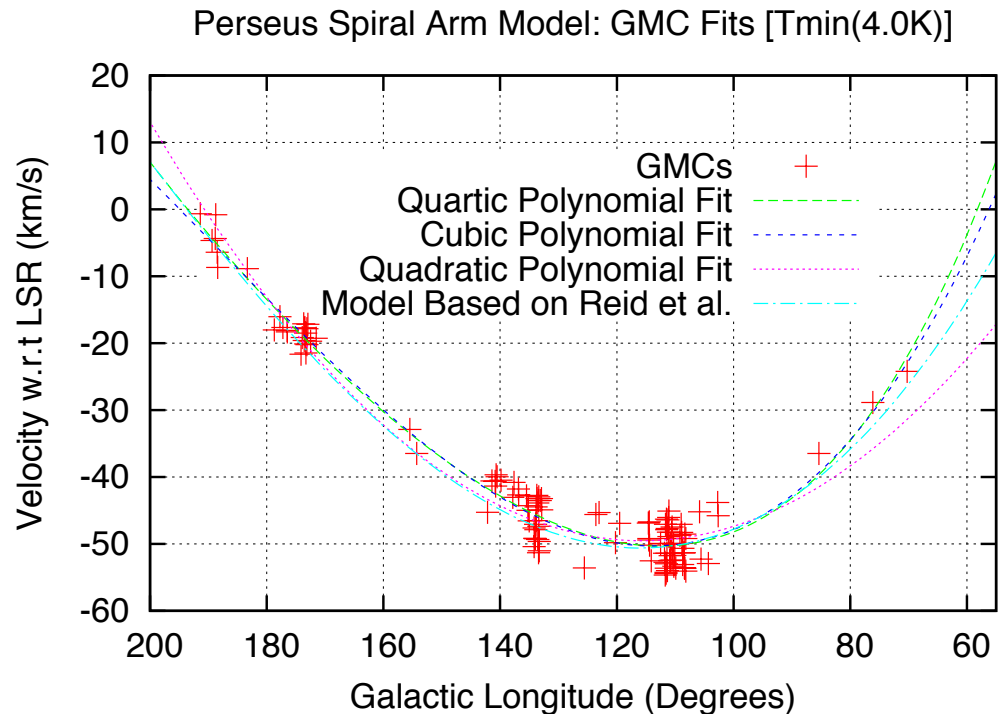

Figure 3.9: Perseus Spiral Arm kinematical model determination using polynomial fit to the ^{12}CO centroids from the ExFCRAO - see the main text for a full description.

Table 3.2: Perseus and Outer spiral arm polynomial coefficients

Longitude Term (°)	Perseus Arm Velocity Centre Coefficient	Outer Arm Velocity Centre Coefficient
l^0	160.37	-2.48
l^1	-4.11	-1.23
l^2	$2.24\text{x}10^{-2}$	$-7.43\text{x}10^{-3}$
l^3	$-9.85\text{x}10^{-6}$	$1.47\text{x}10^{-4}$
l^4	$-8.90\text{x}10^{-8}$	$-3.76\text{x}10^{-7}$

extracting the data was that it would be faster to implement an modify compared to the alternative of the time which was to recalculate the velocity at each point depending on it's effective $\ell - R$ position. The second benefit of having a polynomial expression for the $\ell - v_{LSR}$ is that, though the initial ^{12}CO fitting locus is defined by the spatial fitting to the arm, the actual $\ell - v_{LSR}$ sub-structure of the arm is independently defined. Figure 3.9 shows the positions of the ^{12}CO centroids and also the models fit to them, the data were fit of the form;

$$v_{arm} = \sum_{0}^{n} a_i.\ell^i \tag{3.9}$$

Having overplot the polynomials on the continuous ^{12}CO data, it was decided that the quartic polynomial provided the best fit to the data available at the time - see Figure 3.10. In Figure 3.10 I have included both polynomial fit to the Perseus and Outer spiral arms , since the Outer arm was also subject to this form of analysis. As can be seen in Figure 3.9 but more so in Figure 3.10, the polynomial fits to the data - especially with Perseus - at low ℓ is not a good fit to the data. For completeness, the polynomial coefficients are shown in Table 3.2. With the development of a parallel fitting program I was able to use the Shocked motion treatment for fitting to the maser emission on the ^{12}CO data, meaning that the kinematic fit is drastically improved. It would also be beneficial at this juncture to bring attention to the number of maser points used to fit the distance structure of the Perseus and Outer arms. At the time when the polynomial treatment was implemented, the number of arm tracer points were fewer than the final samples presented in Tables 3.1 and 3.3 for Perseus and Outer respectively. The polynomial description was adequate for the level of constraint which was available at the time. However, with a better constrained spatial relation, the need for a more accurately descriptive kinematic model became apparent.

Shocked Motion Fitting $\ell - v_{LSR}$ Structure

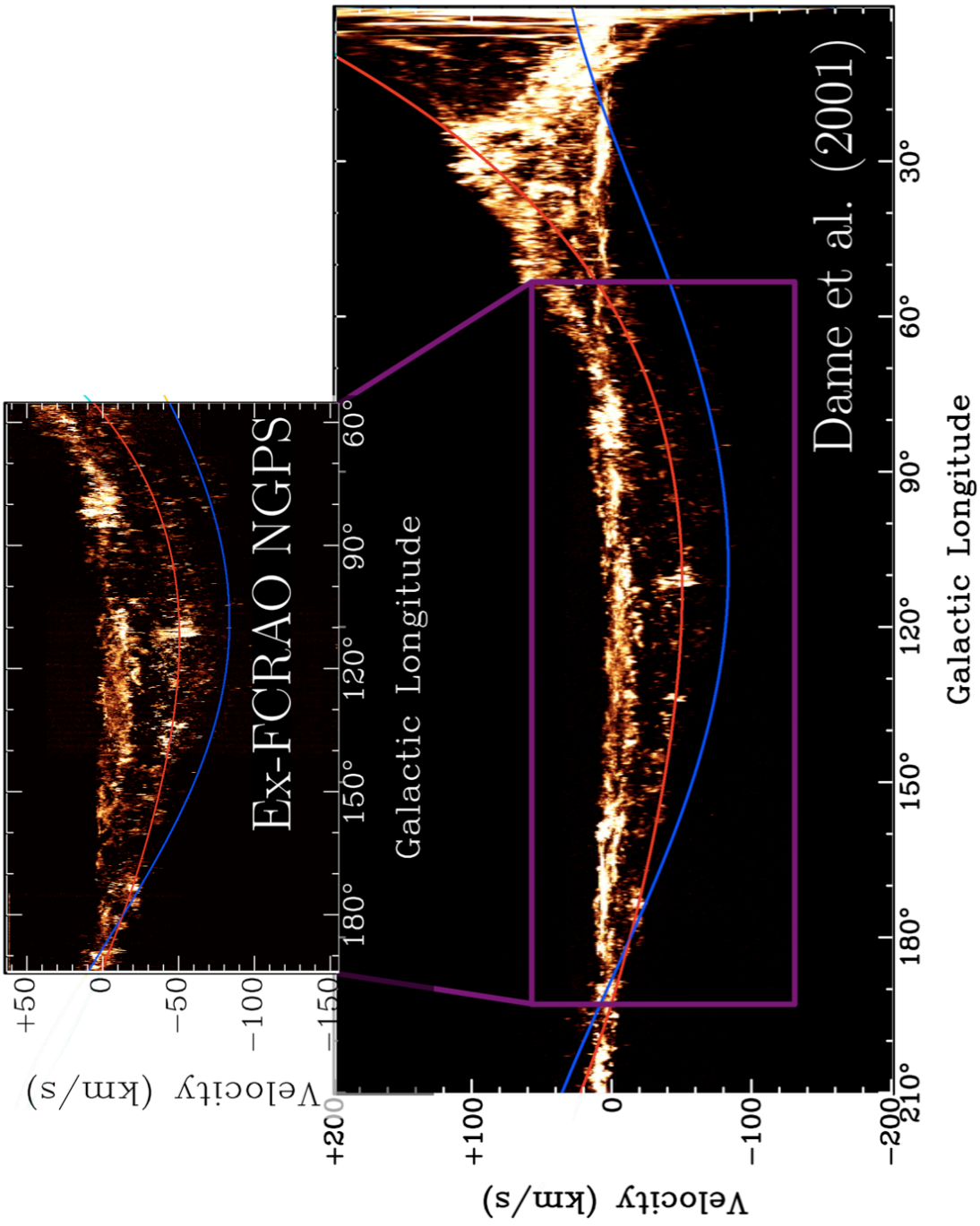

Figure 3.10: Perseus [Red] and Outer [Blue] Spiral Arm best fit polynomials over plot on ^{12}CO data taken from the CfA composite survey and the ExFCRAO ^{12}CO survey. As discussed in the text, the polynomial functions do not adequately describe the arm features at low Galactic longitude.

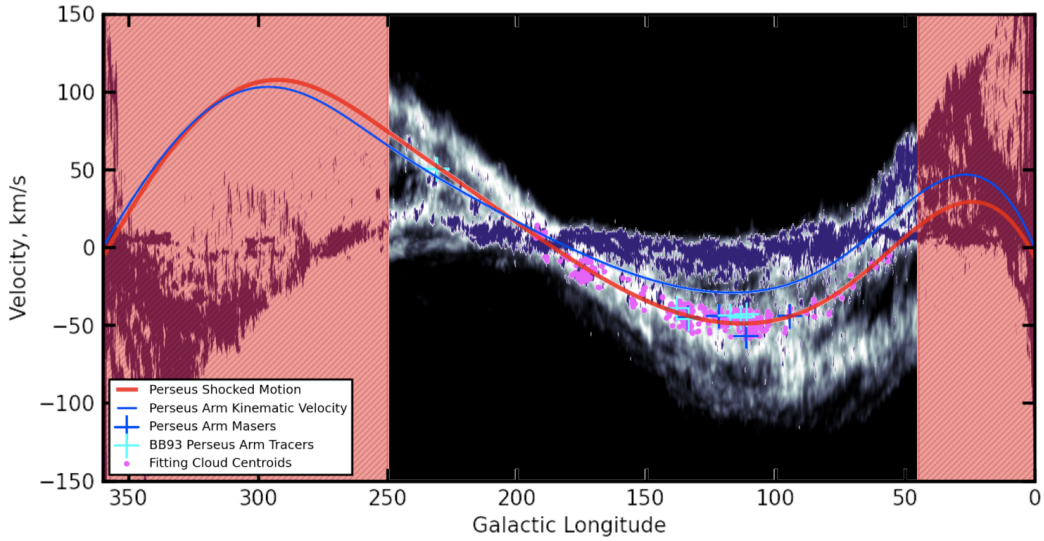

Figure 3.11: The above Figure shows the longitude-velocity structure of material at the distance of the Perseus arm under circular motion (blue line); the longitude-velocity relation of material at the distance of the Perseus arm under shocked motion (red line); the shocked motion fit to the clouds in the Ex-FCRAO survey with a T_{min}= 5.0K (magenta points). The red hatched area shows where the model is unconstrained. The purple emission is ^{12}CO from the Ex-FCRAO overlaid on HI from from the LAB-HI survey.

The motivation for this additional stage of refinement was twofold: firstly to provide a consistency check between the locus defined by the masers with what constitutes the molecular Perseus arm (as shown in the band of emission in Figure 3.4) and secondly to provide an additional constraint of the kinematic locus at lower ℓ. I do not model any intra-arm structure nor kinematics. Instead, I view these deviations as random motions and turbulent velocity dispersion within the arm.

For analysis, I selected all clouds within ± 10 km s^{-1} of the $v_{per}(\ell)$ best-fit to the maser data (R09 definition), excluding the region within ± 5 km s^{-1} of v_{LSR} = 0 km s^{-1} in order to filter out local emission contaminating the sample, whilst keeping a velocity window of uniform width when approaching these regions (i.e. the window was tapered to ensure that the $v_{per}(\ell)$ line remained centred in the window). I found that clouds within the data sample which have a peak brightness temperature greater than 5 K (T_A^* scale) provide good discrimination of the Perseus Arm, while retaining a useful number of clouds for analysis. The $T_{peak} > 5$ K sample was used to constrain a least squares fit to refine the v_{shock} and $\Delta\phi_{sp}$ parameters derived from the masers. I found that the best fit to these clouds are v_{shock} = 20.0 km s^{-1}, $\Delta\phi_{sp}$ = 1.6°, which can be seen in Figure 3.11, showing that the fit to the masers was a good first approximation to the kinematic locus of the arm - the goodness of fit ellipse is shown in Figure 3.12.

One consideration, which must be acknowledged, is the degeneracy of Perseus arm shocked velocities with un-shocked velocities. This effect can be seen in Figure 3.13, where I have represented the projection of Galactic rotation, including the deviation from flat circular rotation in the Perseus Arm, as a colour map. It's clear that the velocity of Perseus Arm material can also

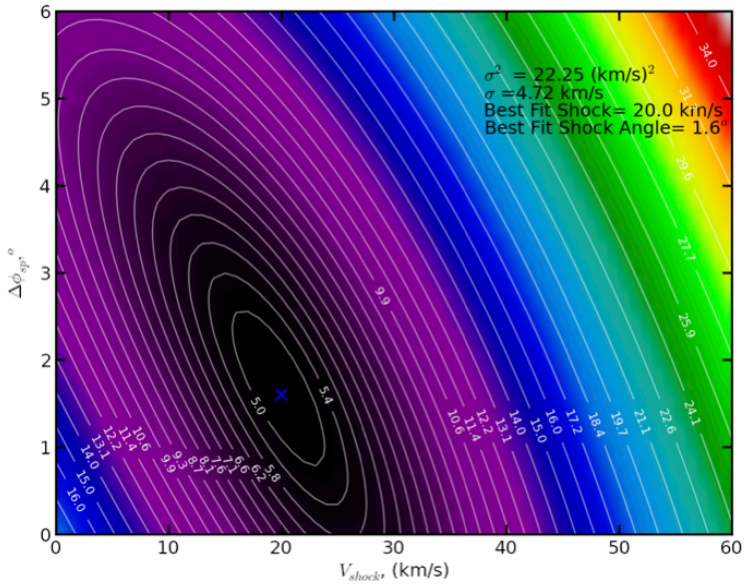

Figure 3.12: Goodness of fit ellipse to the Shocked Motion Fit to the Perseus arm ^{12}CO centroids in Figure 3.11. The contours show the σ values for the fitting routine, the colour scale is proportional to the values of the contours.

correspond to an un-shocked motion at (e.g.) typically twice the Perseus Arm distance in the Second Quadrant. Therefore, when I select the Perseus arm material kinematically, it is possible that in the window which defines the Perseus arm selection, material could - in principle - include more distant material in ~ circular rotation. However, the presence of distinct gaps in the ℓ–v_{LSR} diagram argues against a significant widely-distributed population of inter-arm molecular clouds, and their contribution to the nominal Perseus Arm emission is likely to be small, especially given the fact of their greater distance and typically smaller size and mass (Stark & Lee 2006).

3.3.3 Predicting the Perseus Arm Trajectory in the inner-Galaxy

By using the coupled spatial and kinematic fits to the Perseus arm it is possible to see how well the models predict spatial and kinematic regions outside our initial constraints. Extending the model outside the constrained region allows it to predict the trajectory of the Perseus arm as it enters the inner Galaxy. In Figure 3.3 it is shown how the distance to W49 is consistent with our prediction for the Perseus Arm distance at its observed longitude. Figure 3.14 shows the ℓ–v_{LSR} map for the ^{13}CO J=1–0 Galactic Ring Survey (Jackson et al. 2006), produced by projecting the peak temperature of emission over the b direction. Plotted on this map is the velocity of W49 (12.1 km s^{-1}) determined by identifying the peak in a summed ^{13}CO emission spectrum, 0.1-deg^2 about the (ℓ, b) position of the maser source. This shows that both the distance and velocity of W49 are consistent with our model, and suggests that W49 is a distant Perseus Arm source. Note that since W49 is near the Solar Circle, the assumed rotation curve is still a good approximation here.

Overplotted on Figure 3.14 are also ℓ–v_{LSR} loci for the Sagittarius and Scutum/Centaurus

Spiral Arms. These are preliminary fits to these spiral arms obtained with the same assumptions as underlie our Perseus Arm model. As these structures traverse somewhat smaller Galactocentric radii, we used the Clemens (1985) rotation curve scaled to the R09 definition (although there are no notable deviations from the flat rotation curve predictions for positions near $R \approx R_0$). The far-distance points of each curve become unreliable near the Galactic Ring at $\ell \sim 20°$–$30°$, but are otherwise good representations of the near-distance and far-distance points above $\ell \sim 30°$. For now, these loci are simply placed on the ℓ–v_{LSR} map to guide the eye towards significant Inner Galaxy structures that interfere with the identification of the Perseus Arm. At the higher longitude end, the main interfering source is the near-distance Sagittarius Arm, as this is an order of magnitude closer than the Perseus Arm, it does not present much difficulty. Clouds in the Sagittarius Arm are of large angular extent, with narrow line widths, compared to expected Perseus Arm clouds with smaller angular sizes and broader line-widths (of which W49 is an example). Identification of the Perseus Arm becomes significantly more difficult below $\ell \sim 30°$ where it starts to blend with the near-distance Scutum/Centaurus Arm. On the basis of visual inspection, there is a plausible population of small, broad lined clouds that follow the Perseus ℓ–v_{LSR} locus, very obvious at the higher longitude end near $\ell = 50°$, but further analysis of this is beyond the scope of this thesis. The difficulties in detecting the Perseus Arm in the first quadrant in ^{13}CO have been also described by Roman-Duval et al. (2010).

3.3.4 Distance Estimation using the Shocked Motion Model

Using the difference between the circular and shocked motion longitude-velocity fits, I am able to attempt to correct the well-known over-estimation of kinematically determined distances for Perseus Arm sources. The definition being that sources lying within the kinematic window defined by our shocked ℓ–v_{LSR} locus are candidate Perseus Arm sources. A simple procedure to correct the kinematic distance of such sources is as follows:

1. Identify candidate arm source;
2. At the source's observed longitude, calculate the LSR velocity difference between shocked and circular rotation models;
3. Subtract the difference from the source's observed v_{LSR};
4. Calculate a new kinematic distance based on the *corrected* velocity.

I have collected a sample of star formation regions defined in Brand & Blitz (1993), BB93; HII regions and SNRs taken from Foster & MacWilliams (2006), FM06; the maser emission associated with high mass star forming regions from Reid et al. (2009), R09; water masers associated with the Perseus arm from Oh et al. (2010), O10, and Shiozaki et al. (2011), S11. For the objects in the S11, O10 and R09 samples the analysis conducted here is a self-consistency test, in effect.

Having defined the objects within the sample as either "arm" or "non-arm", an arm object has a velocity of ± 10 km s^{-1} of the modelled arm centre. In addition to the kinematically defined non-arm objects, I also remove objects within $\pm 10°$ of the centre and anti-centre. This is to remove

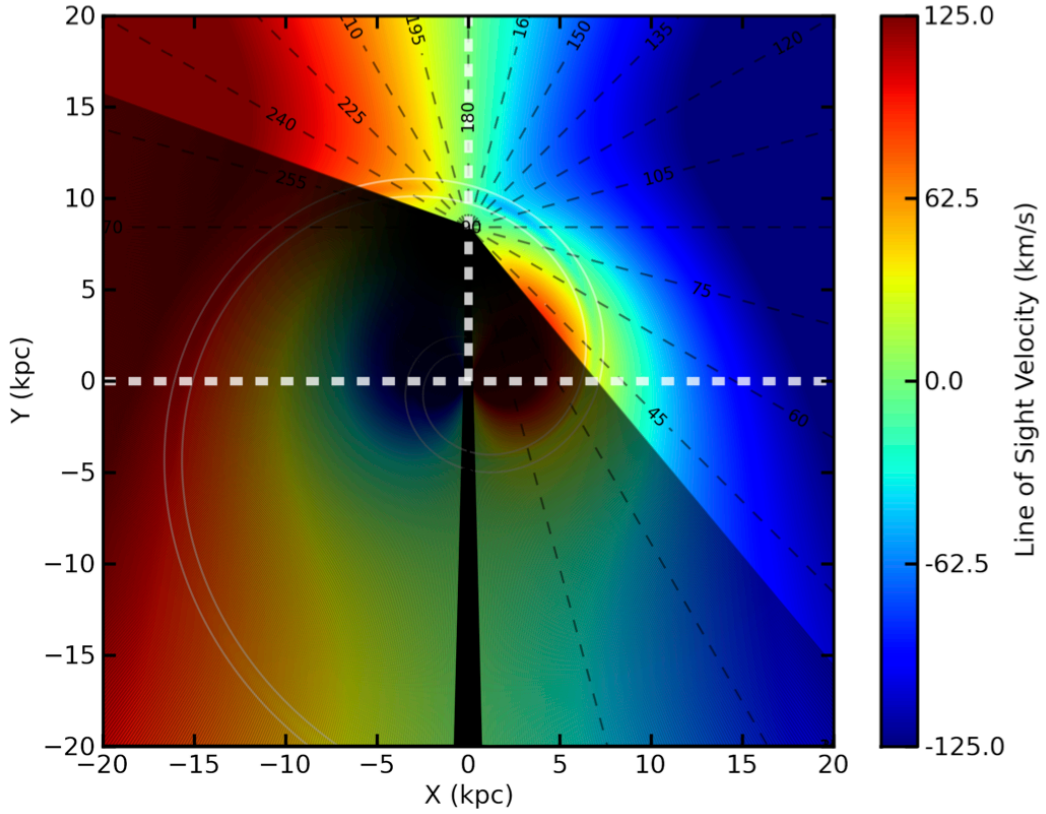

Figure 3.13: Perseus Spiral Arm Model Velocity Structure, assuming a flat rotation curve taking into account the presence of the shock in the region of the spiral arms. The x-y projection is with respect to the Galactic Centre. The black dashed contours show the Galactic Longitude over a single line of sight, the white dashed lines show the divisions of the Galactic quadrants and the grey spiral contours show the extent of the Spiral arm locations within the model. The shaded region shows where the model is unconstrained and its prediction not trusted.

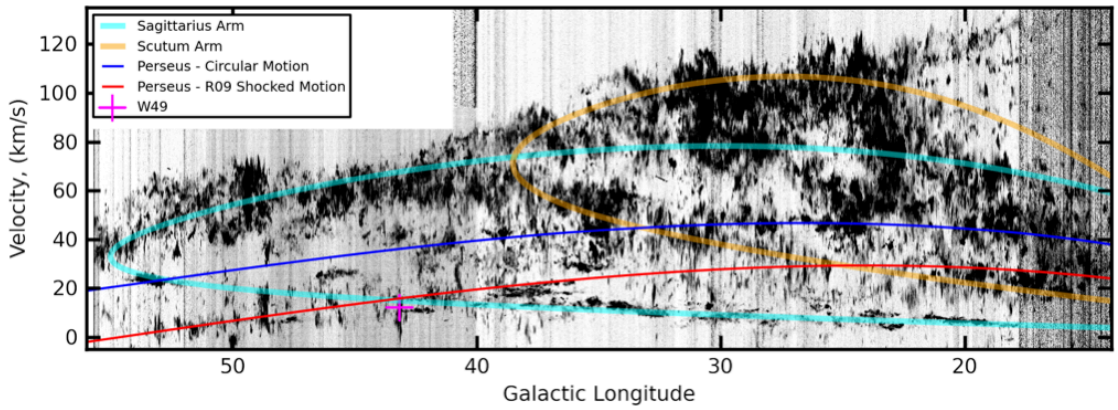

Figure 3.14: The Figure shows a longitude-velocity map, integrated between $|b|$ <0.75° (corresponding to approximately one calculated scale height for Perseus at that distance) for the Galactic Ring Survey ^{13}CO data (Jackson et al. 2006). The traces show the circular and shocked motion fits in blue and red respectively. The star forming region W49 is placed as the magenta cross.

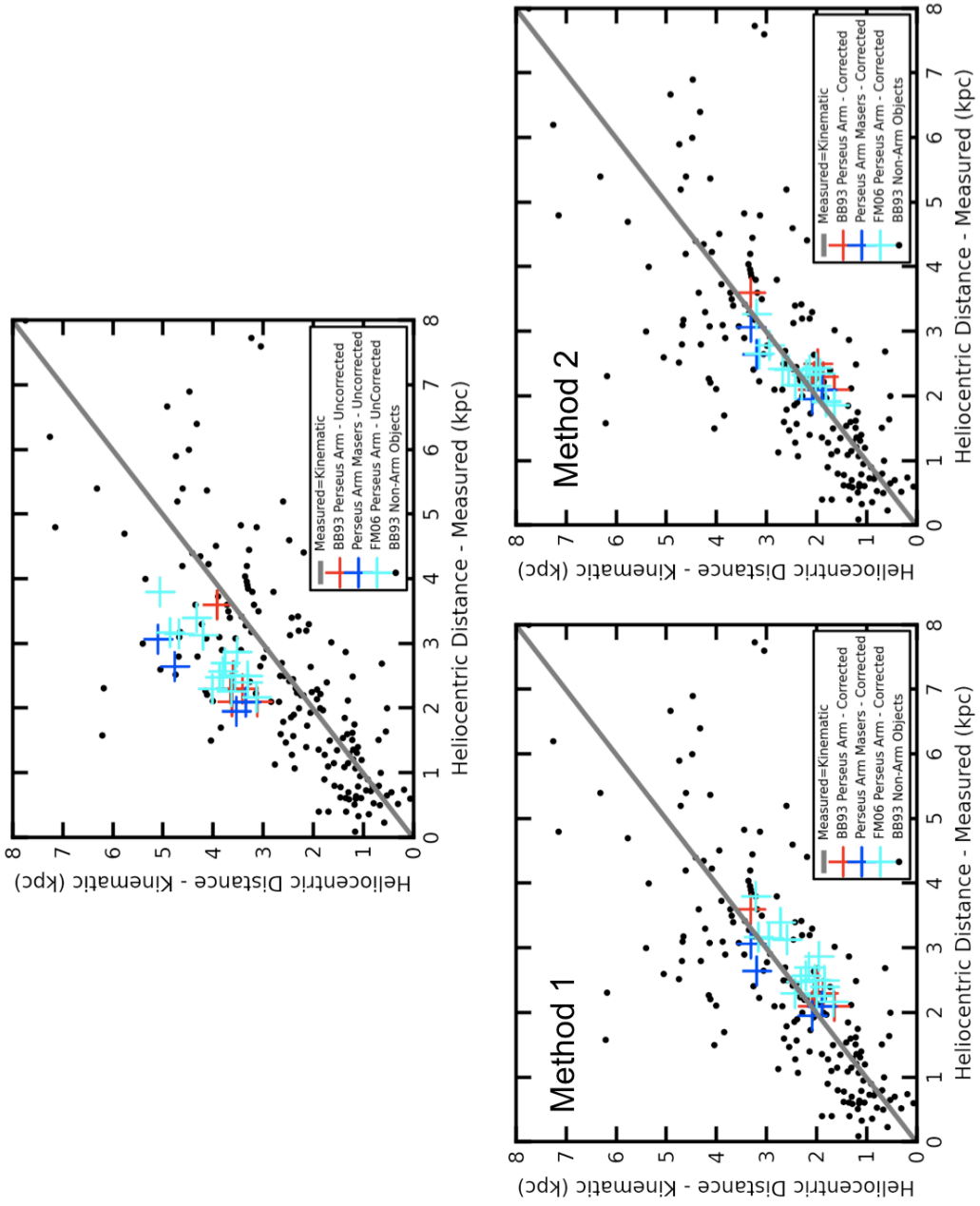

Figure 3.15: The above Figure shows the correction effect for kinematically determined distances. The top panel shows the uncorrected distances. The left panel shows objects where the observed velocities were modified via the Δv_{kin} function prior to the kinematic distance being determined. The bottom right panel shows the same data, but where objects defined as Perseus arm kinematically are assigned a distance of d_{per} for that line of sight.

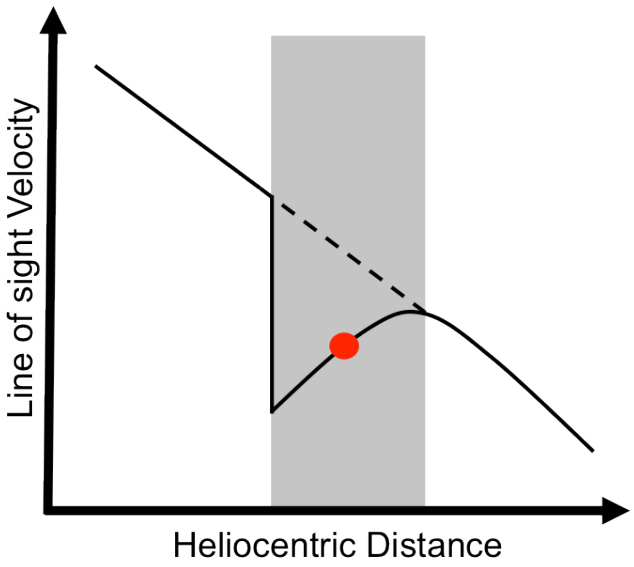

Figure 3.16: The above Figure shows a schematic shock in terms of velocity and distance. The greyed area shows the region defined kinematically as arm-based, the red point show the kinematic arm centre.

objects whose observations suffer from the velocity compression in these regions and as such, when the correction is applied causes the corrected velocity to be erroneous. As can be seen in Figure 3.15, the FM06 sources - when using this method - are corrected too much and lie beneath the one:one relation. This can be explained by considering the projected velocity gradient across the Perseus arm kinematic window. The procedure detailed above (here after method 1) assumes that as one crosses the kinematic window defining the Perseus arm, the velocities become more negative with increasing distance - as with the usual case for circular rotation. However, this is not necessarily true. A more careful consideration of the flow of material through a spiral shock reveals that a velocity reversal must exist across the arm (Roberts 1972; Foster & MacWilliams 2006) and therefore material on the near-side of the arm-centre will have more negative a velocity than material at the far side. Hence assigning kinematic distances to intra-arm material has the effect of underestimating the distance to the far side material and overestimating the distance of near-side material. Whether or not this mean flow structure is directly observable with current data is an open question since it must be seen against the presence of velocity dispersion due to turbulence in the arm. Figure 3.15, the method-1 correction implies that the FM06 sample of Perseus arm objects contain a number of SNRs and optically visible HII regions which are relatively evolved objects and are preferentially down-stream on the far-side of the arm-centre. In their more involved modelling, FM06 were able to reconcile their determined distances with their model distances by accounting for the intra-arm flow.

To investigate this further, I define a second method for assigning a distance to kinematically determined arm-based material.

The procedure, hereafter method-2, is similar to that of method-1;

1. Identify candidate arm source;

2. At the source's observed longitude assign the Perseus arm distance, $d_{per}(\ell)$ to the source.

Method-2 is also superior to method-1 in that it is not limited to only being able to assign distances outside the centre and anti-centre regions since there is no dependance on $\sin(\ell)$. Looking at the FM06 corrected method-2 points in Figure 3.15, it can be seen that they no longer are off-set from the direct mapping trend line. It can be argued that assigning to distances kinematically to sub-arm precision is unwise, as can be seen in the difference between the scatter in the method-1 correction and the correlation in the method-2 correction. Taking this to mean that there is a velocity reversal of the flow pattern across the Perseus arm, it is recommend that candidates interior to the kinematic window of Perseus be assigned the Perseus arm distance for that line of sight. The simpler model (method-2) offers a straightforward practical solution that achieves comparable accuracy to FM06.

3.4 Defining the Model - The Outer Spiral Arm

Having defined the Perseus arm in terms of its kinematic and spatial structure, I move on to describing the next apparent spiral feature in the Milky Way - the Outer spiral arm.

As was discussed earlier, the rotation curve of the Milky Way is uncertain. Since, especially in the outer Galaxy, its spatial structure has been widely determined using kinematically determined distances - the uncertainty in an accurately descriptive rotation curve can lead to the over- or under-estimation of distances when observing in these regions. In conjunction with the differences in one's chosen rotation curve, there is also differences in one's chosen set of solar constants. I found that the Reid et al. (2009) (R09) solar constants of R_0=8.4 kpc and v_0=254.0 km s^{-1} provided a better fit our data than the IAU standard R_0=8.5 kpc and v_0=220.0 km s^{-1} , so it is the R09 convention I adopt. The chosen rotation curve, for exterior arm rotation, will be a flat rotation curve assuming circular motion as for Perseus.

Here I extend the Shocked-Motion-motion to the Outer arm and investigate whether the increase range of R associated with the Outer arm over the same span of ℓ as for Perseus, allows any conclusions to whether the strength of v_{shock} varies with R.

3.4.1 Modelling the Spatial Structure

To fit the spatial structure of the Outer arm, a list of known Outer arm objects is compiled - see Table 3.3. It is to be noted that not all the tracers have both v_{LSR} and d_{helio}, so not all tracers are used in both the spatial and kinematic fits. There are three different methods for determining the distances to the tracers in the sample I obtained. The first is via measurement of trigonometric parallaxes to maser emission from high mass star forming regions (Hachisuka et al. 2009; Reid et al. 2009; Sanna et al. 2011). The second method is via spectroscopically and photometrically determined distances from young open clusters (Moffat & Vogt 1973; Negueruela & Marco 2003, 2008). The final method of measuring the distance to the tracers in the sample measurement of the distance to background *Blue Plume* (BP) stellar populations in the fitting to colour-magnitude-diagram (CMD) of open clusters (Pandey et al. 2006). It is noteworthy to mention that Sh2-217 and

Table 3.3: Outer Arm tracers used for the spatial and kinematic fits to the arm. The *Type* codes are; HII - HII region; Ph/Sp - Photometric or Spectroscopically determined distance; MASER - Trigonometric parallax to Water or Methanol maser; BP - *Blue Plume* CMD fitting. M73 - Moffat et al. (1973); F84 - Fitch & Blitz (1984); D03 - Deharveng et al. (2003); N03 - Negueruelaet al. (2003); K05 - Kharchenko et al. (2005); P06 - Pandey et al. (2006); R07 - Russeil et al. (2007); H09 - Hachisuka et al. (2009); B11 - Brand et al. (2011); R09 - Reid et al. (2009); S11 - Sanna et al. (2011).
Note: The clusters associated with the Blue Plume arm candidates are foreground clusters and not the actual tracer. Also the R07 H II regions have no errors quoted in their source data-table.

Associated Tracer	ℓ (*degrees*)	b (*degrees*)	v_{LSR} (km s^{-1})	$v_{LSR\ error}$ (km s^{-1})	d_{helio} (kpc)	Tracer Type	Ref (d_{helio}/ v_{LSR})
HII Region	12.4	0.0	-18.0	-	-	HII	- / R07
HII Region	25.4	0.0	-10.0	-	-	HII	- / R07
HII Region	66.0	1.4	-66.0	-	-	HII	- / R07
HII Region	68.3	1.2	-63.0	-	-	HII	- / R07
HII Region	69.9	1.5	-63.0	-	-	HII	- / R07
G75.30+1.32	75.3	1.32	-56.8	-	9.25	MASER	S11 / S11
HII Region	96.3	2.6	-95.0	-	-	HII	R07 / R07
NGC 7235	102.7	0.78	-	-	5.75	Ph/Sp	N03 / -
NGC 7380	107.1	-0.88	-	-	5.25	Ph/Sp	N03 / K05
Cep OB5	108.4	-2.75	-	-	6.31	Ph/Sp	N03 / -
Cep OB5	108.5	-2.75	-	-	7.24	Ph/Sp	N03 / -
NGC 7654	112.82	0.43	-	-	6.40	BP	P06 / -
NGC 129	120.27	-2.54	-	-	4.80	BP	P06 / -
Be 7	130.14	0.38	-	-	5.20	BP	P06 / -
IC 1805	134.6	0.92	-	-	4.37	Ph/Sp	N03 / -
IC 1805	134.8	0.92	-	-	4.79	Ph/Sp	N03 / K05
WB89-437	135.28	2.8	-72.0	3.0	5.98	MASER	H09 / H09
Waterloo 1	151.287	1.97	-	-	4.37	Ph/Sp	M73 / -
NGC 1624	155.36	2.61	-	-	6.03	Ph/Sp	D03 / -
Sh 2-217	159.16	3.06	-	-	4.17	Ph/Sp	D03 / BB11
Sh 2-219	159.36	2.57	-	-	5.25	Ph/Sp	D03 F84
NGC 1912	172.25	0.7	-	-	4.30	BP	P06 / -
NGC 1907	172.62	0.31	-	-	4.60	BP	P06 / -
NGC 1960	174.53	1.07	-	-	4.20	BP	P06 / -
Be 17	175.65	-3.65	-	-	4.60	BP	P06 / -
NGC 2099	177.64	3.09	-	-	6.20	BP	P06 / -
NGC 2168	186.59	2.22	-	-	4.90	BP	P06 / -
S269	196.45	-1.68	20	3.0	5.29	MASER	R09 / R09
NGC 2244	206.4	-2.08	36.6	5.5	7.59	Ph/Sp	N03 / K05
NGC 2244	206.4	-2.08	-	-	5.25	Ph/Sp	N03 / -
Dolidze 25	211.94	-1.27	-	-	5.80	BP	P06 / -
Be 33	225.42	-4.62	-	-	7.70	BP	P06 / -
Tombaugh 1	232.3	-6.31	-	-	7.70	BP	P06 / -
NGC 2383	235.27	-2.46	-	-	8.80	BP	P06 / -
NGC 2384	235.39	-2.39	-	-	8.80	BP	P06 / -
NGC 2367	235.64	-3.85	-	-	8.50	BP	P06 / -

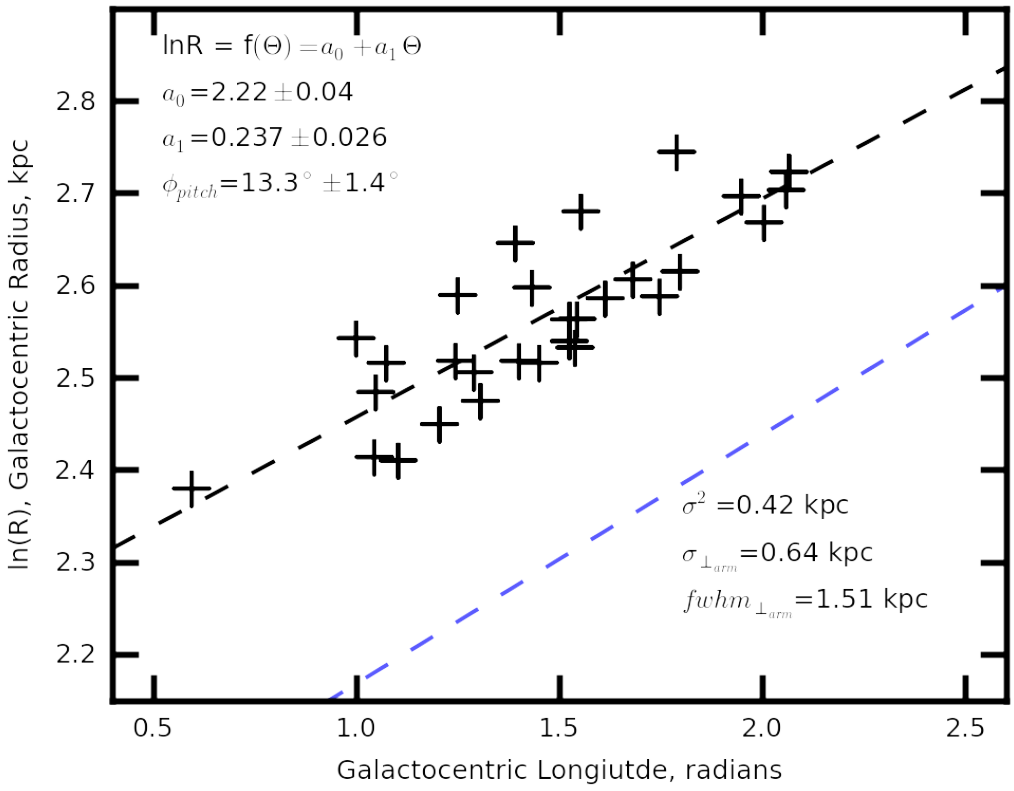

Figure 3.17: The Figure above shows the logarithmic spiral fit to the spatial tracers listed in Table 3.3 The black dashed line shows the fit and the dashed blue line shows the relative position of the Perseus arm fit from earlier.

Sh2-219 have velocities within their host paper, when plot on the ℓ-v_{LSR} diagram their assigned velocity places them within the Perseus arm window. These objects reside with ≈20°of the anti-centre and as such are subject to the velocity compression which was described earlier. Therefore, though their distances - which are consistent with an Outer arm occupancy - the velocities are disregarded for the purpose of this analysis. I fit the Outer arm using a linear logarithmic spiral form from Equation 3.1 whose pitch angle, ϕ_{pitch} is described by Equation 3.2 - Figure 3.17 shows the spatial fit to the Outer spiral arm.

Where R_{outer} is the Galactocentric radius of the Outer arm at the point of Galactocentric longitude, θ. The spatial fit was obtained to the tracers with measured distances from Table 3.3, regardless of whether they had associated v_{LSR} values. The fit to the data, including the relative position of the Perseus arm fit from earlier, can be seen in Figure 3.17. I find that the pitch-angle, ϕ_{pitch}=13.3±1.4°to be consistent with other determinations of the pitch-angles of Galactic arms (Vallée 2002, Table 1) also the Outer arm has a shallower pitch angle than that of Perseus which reflects the findings of Reid et al. (2009) - but not its value, possibly due to the small number of Outer arm tracers used to calculate the pitch angle in their sample. I calculated the dispersion of the tracers about the best-fitting arm centre, I found the standard deviation perpendicular to the arm to be ≈ 0.64 kpc which corresponds to a full width at half maximum (defined to be a measure

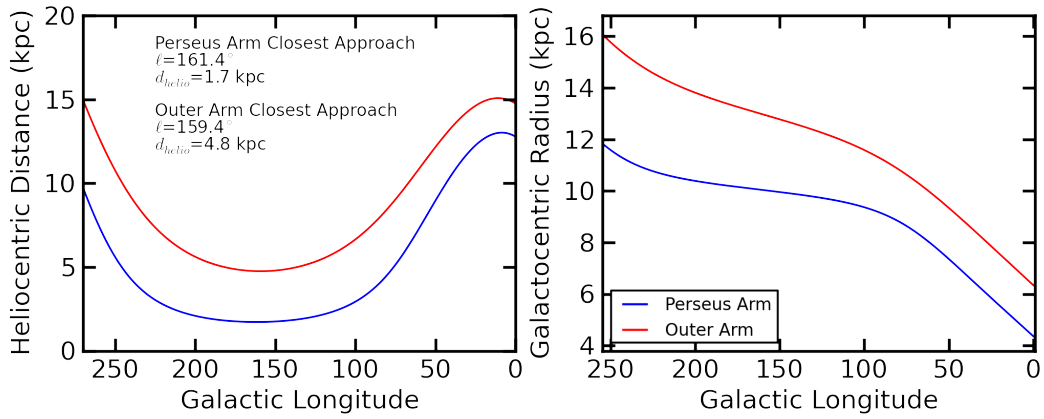

Figure 3.18: The Figure above shows the relation between the Outer and Perseus spiral arms, in terms of the variation of d_{helio} [left] and R_{gal} [right] with Galactic longitude, ℓ.

of the arm's width) of ≈1.51 kpc . Though an arm-width of 1.5 kpc appears to be very large when compared the Perseus arm width - as a fraction of the Outer arm's total length, its width is not significant. This suggests that the spiral arms in the outer regions of the Milky Way are less well defined - as is seen in other galaxies (Helfer et al. 2003).

Considering the spread of tracers in the logarithmic fit in Figure 3.17 there appears to be a two bands of tracers with the fit residing between them. It should be said that when looking where each of the tracers reside in the plot, there is no dependence on the distance measurement method used. Figure 3.18 show the variation of the spatial parameters, d_{outer} and R_{outer} as a function of ℓ and how this compares to the Perseus arm model. The logarithmic fit to the Outer arm gives the closest approach to be in the second Galactic quadrant at ≈4.8 kpc at ℓ=159.4°. It is in this region where the Outer and Perseus arms are not that observationally distinct from one another, but, it is to be noted that the offset in the ℓ values for closest approach is equal to the difference in the pitch angles of the Perseus and Outer arms which is consistent with the geometry of the system.

3.4.2 Modelling the Kinematic Structure

A number of the interesting features in the data are dependant on the relative locations of Perseus and outer arms, therefore I shall describe the kinematical modelling before moving on to describing noteworthy points within the data itself.

As with Perseus, beginning by obtaining an initial fit to the Outer arm to obtain an ℓ–v_{LSR} locus which corresponds to the kinematically defined Outer arm. I achieve this by, initially fitting the ℓ–v_{LSR} structure of the arm to the tracers used in defining its distance fit. Though in this case, they are supplemented by other tracers (not used in the spatial fit) thought to be based in the Outer arm which do not have associated distances - or whose distances were determined kinematically. The following expression defines the Outer arm's line-of-sight velocity, w.r.t local-standard-of-rest (LSR).

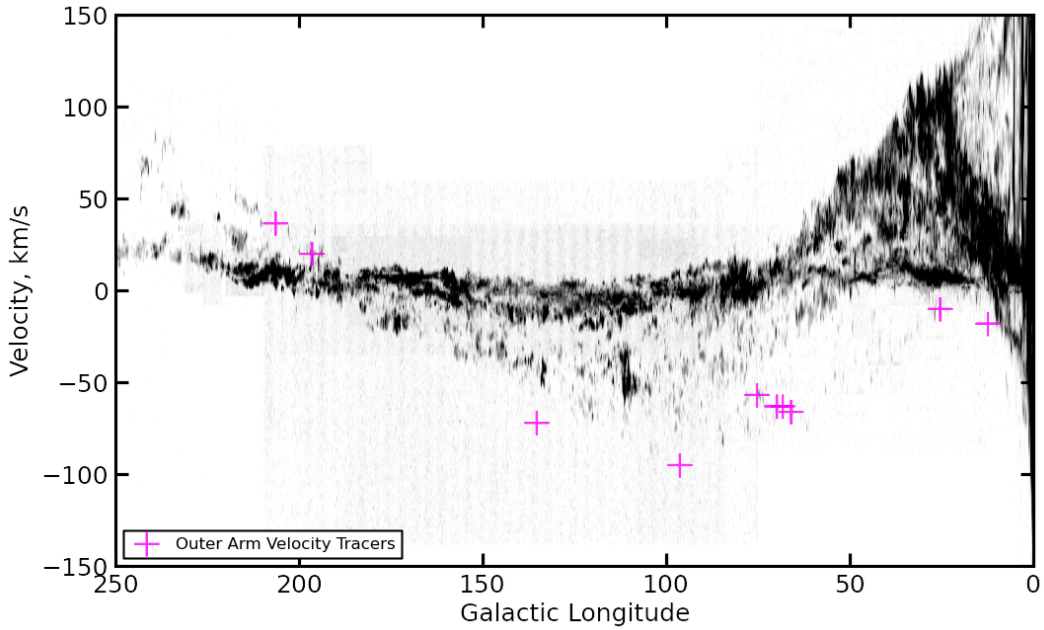

Figure 3.19: ℓ-v_{LSR} map of taken from the CfA composite ^{12}CO , Dame et al. (2001), over-plot with the kinematic tracers (magenta).

$$\mathrm{v_{outer}} = \mathrm{v_{arm}}.\sin(\epsilon) - \mathrm{v_0}.\sin(\ell) \tag{3.10}$$

Where v_0 is the Galactic rotation and v_{arm} is the scalar difference between the Galactic and arm-based rotation about the Galactic centre.

$$\mathrm{v_{arm}} = \mathrm{v_0} - \mathrm{v_{shock}} \tag{3.11}$$

The quantity ϵ corresponds to the angle which projects the shocked-motion along the observer's line-of-sight as defined in Equation 3.4.

Kinematic Model of the Outer Arm - Fit to Tracer Locations

As explained in section 3.3, I adopt the R09 solar constants of v_0 = 254 km s^{-1} and R_0 =8.4 kpc for this work. The kinematic tracer locations in the parameter space can be seen in Figure 3.19, using these locations I run a series of models varying the shock parameters; v_{shock} and $\Delta\phi_{\mathrm{sp}}$ to provide the best least-squares fit to the tracers defined above. The minimised model can be seen over-plot on the ^{12}CO and tracers in Figure 3.20. The minimisation routine found the best fit parameters to be v_{shock} = 13.0 km s^{-1} and $\Delta\phi_{\mathrm{sp}}$ = 3.3 °. The goodness of fit ellipse for the minimising routine can be seen in Figure 3.21.

There is a degree of coincidence with the circular motion fit to the Outer arm matching with the inter-arm emission in between Perseus and the Outer arms. As with the Perseus arm, the least-squares fit to the data provides a fit to the tracers, but it doesn't track the ^{12}CO at lower longitudes and is consistently too positive in v_{LSR} . At higher longitudes, the fit does appear to track the ^{12}CO

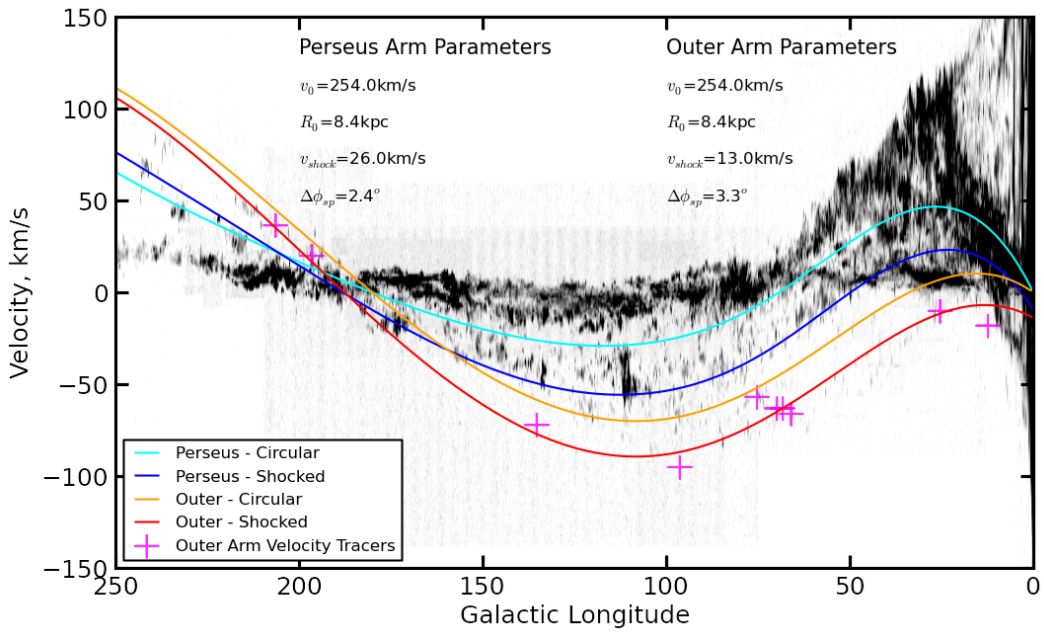

Figure 3.20: ℓ-v_{LSR} map of taken from the CfA composite ^{12}CO , Dame et al. (2001). Over-plot with the kinematic tracers (magenta) and the Perseus and Outer arm best least-squares fit to the Masers and the spatial tracers in Table 3.3 respectively.

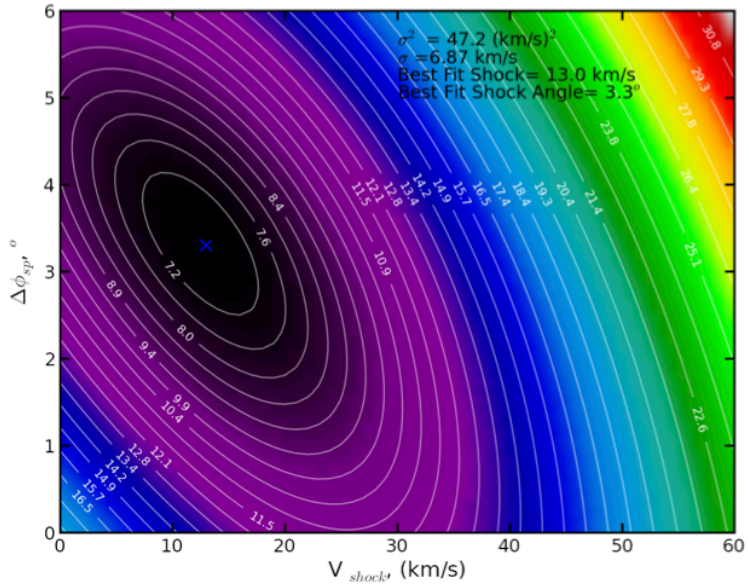

Figure 3.21: Goodness of fit ellipse for the least-squares minimisation to the kinematic tracers listed in Table 3.3. The minimised parameters for the best fit were found to be v_{shock} =13 km s^{-1} with $\Delta\phi_{sp}$=3.3°.

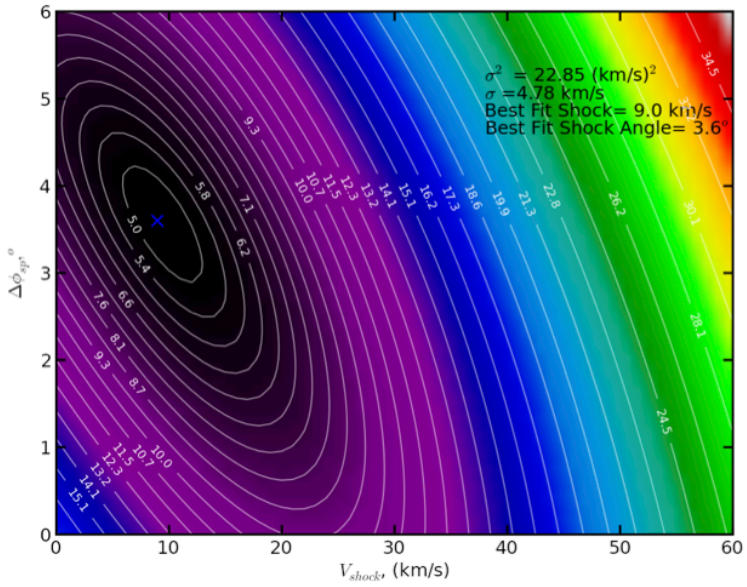

Figure 3.22: Goodness of fit ellipse for the least-squares minimisation to the ^{12}CO centroids for the Outer arm. Contours show the σ boundaries with the colour scale being proportional to those values.

, but it is in the anti-centre where the Outer arm becomes kinematically indistinguishable from the Perseus arm. However, beyond the anti-centre as the arm moves into the third quadrant the fit once again tracks the more positive Outer emission associated with the Outer arm. To improve the fit at lower longitudes, I then refined the model by fitting the ℓ–v_{LSR} structure to ^{12}CO centroids.

Kinematic Model of the Outer Arm - Refinement to ^{12}CO Centroids

Using both the CfA composite and ExFCRAO ^{12}CO surveys, I compiled a clump catalogue of the Outer arm region using the clump finding algorithm described in Brunt et al. (2003). Using the parameters of T_{min} = 1.0 K (T_{A^*}) and N_{min}=10 pixels for cloud detection. By fitting to the ^{12}CO centroids I will be able to better define the fit at longitudes where there are a lack of confining points, this will provide a better fit to the gaseous distribution of the Outer arm. As with the least-squares fit to the tracers, I conducted a minimisation routine on the cloud positions defined to be within ±10 km s^{-1} of the tracers' least-squares fit. In addition to this constraint I excluded all cloud within ±5.0 km s^{-1} of v_{LSR} =0 km s^{-1} and also varied the window depth in this region to maintain a constant velocity width per line of sight for the cloud fitting. The degeneracy between arm-based shocked and post-arm un-shocked material is discussed in section 3.6.

Figure 3.22 shows the goodness of fit ellipse for the minimisation routine whilst Figure 3.23 shows the best least-squares fit to the ^{12}CO centroids. The minimised shock parameters were found to be v_{shock} = 9.0 km s^{-1} and $\Delta\phi_{\rm sp}$ = 3.6 °. With the exception of the fit to the atomic component - which is discussed in section 3.4.3 - with respect to the ^{12}CO the fit still appears to be too positive at ℓ <100° but is still a good representation of the ^{12}CO continuous data at higher longitudes. This could imply the presence of a shock which is not constant across the arm's length.

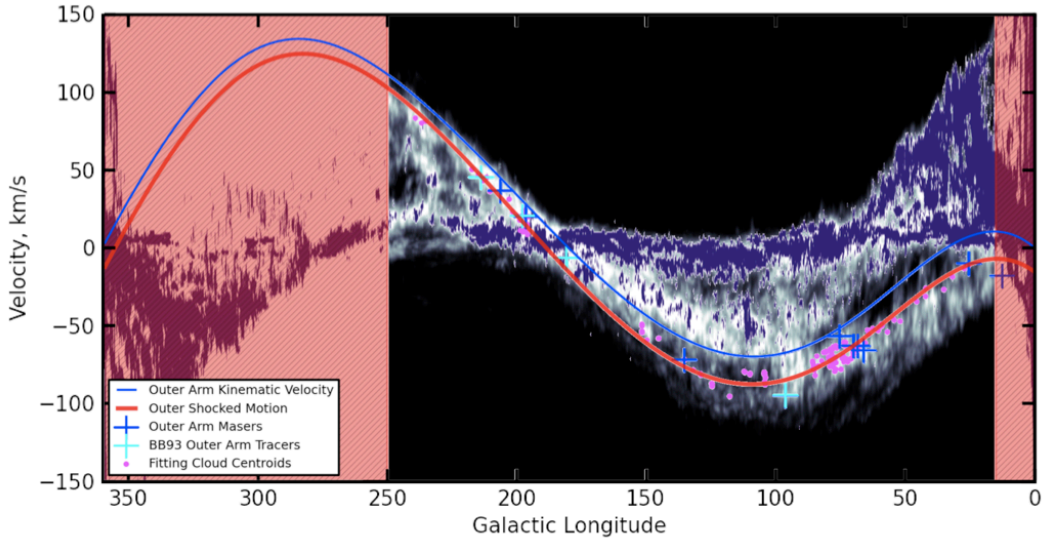

Figure 3.23: Longitude-velocity diagram showing the Outer arm shocked motion best least squares fit to the ^{12}CO centroids. Overplot with the kinematic tracers from Table 3.3 and objects fulfilling the arm selection criteria from Brand & Blitz (1993).

Kinematic Model of the Outer Arm - Assuming a variable v_{shock}

The initial assumption used in definition the first iteration of the kinematic model was that the spiral arms are subject to a constant v_{shock} across its length. Where this appears to have been a good first-order approximation for the relatively small span of Galactocentric radii corresponding to the Perseus arm ($R \approx 4$ kpc $\rightarrow$12 kpc), for the Outer arm it spans a much larger range of radii, see Figure 3.18, almost 10 kpc in span over the same range of longitude.

Since the least-squares fit,at lower longitude was too positive - this corresponds to smaller Galactic radii (Figure 3.18) - therefore, I require a stronger shock at smaller R. I achieve this by modifying equation 3.11 to incorporate a non-constant shock, which I parameterise via:

$$\mathrm{v_{shock}} = \mathrm{v_a} - \mathrm{v_b}.\left(\frac{\mathrm{R}}{\mathrm{R_0}} - 1\right) \tag{3.12}$$

This means that at smaller Galactocentric radii, the value of v_{shock} is larger - the assumption for a constant value of $\Delta\phi_{\mathrm{sp}}$ still remains at this juncture. Using this new parameterisation for v_{outer} , I proceeded with the same method as for the constant shock assumption: firstly minimising to the tracers in Table 3.3, then by refining this fit with ^{12}CO centroids. I found that the best least-squares fit variable shock parameters to be; $v_a = 16.0$ km s^{-1} , $v_b = 9.8$ km s^{-1} and $\Delta\phi_{\mathrm{sp}} = 3.1$ °. This means that for larger values of R, the magnitude of v_{shock} decreases - in difference with the constant-shock model where the magnitude of v_{shock} was invariant with R. The assumption for a constant $\Delta\phi_{\mathrm{sp}}$ appears to still be accurate since the minimised $\Delta\phi_{\mathrm{sp}}$ is of the approximate order of the $\Delta\phi_{\mathrm{sp}}$ derived from the constant shock motion fit to the tracers.

To refine the variable-shocked-motion model I then used the tracer fit to define a window through the CO data from which I would extract the ^{12}CO centroids - as I did with the constant-

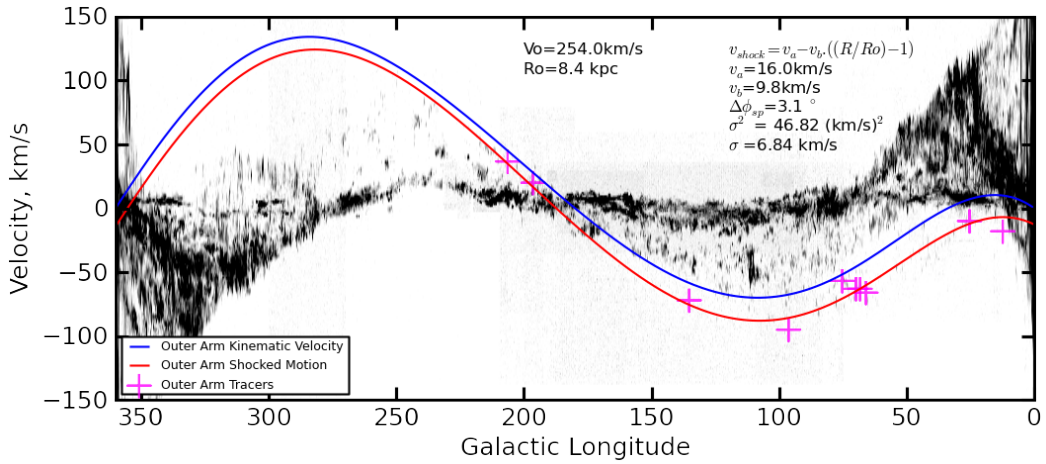

Figure 3.24: Longitude-velocity diagram showing the Outer arm variable-shocked-motion best least squares fit to the kinematic tracers in Table 3.3 assuming a variable shock potential.

shock model. The best least squares fit - and the positions of the fitting centroids - can be seen in Figure 3.25. The best fit shock parameters were found via the same minimisation routine; v_a = 22.5 km s^{-1} , v_b = 37.0 km s^{-1} and $\Delta\phi_{\rm sp}$ = 2.8 °. Consideration of the individual error ellipsoid is not possible, but slices through the minima of each axis is shown in Figure 3.26. The fit using the variable-shocked-motion model appears to track the continuous emission more tightly than the constant-shock-model. Therefore, for the remainder of this work, I will adopt the variable-shock-motion model. Later, in Chapter 5, I will investigate to see if the variable shocked motion model is has the effect on the expected velocity similar to that of a rising rotating curve.

Perseus Arm Retrospective - A variable v_{shock}

For completeness I performed the variable shock analysis on the Perseus arm data to see if the Perseus arm fit is improved with the incorporation of a variable shock. So I ran the routine again firstly on the maser emission, Figure 3.27, then defined the window about the kinematic fit to the masers and refined the model fit to these centroids, Figure 3.28. With the exception of a small change in best-fit value for $\Delta\phi_{sp}$, the contribution by the variation parameter, v_b, is 0 km s^{-1} in both cases - when fit to the masers and also the ^{12}CO centroids. The implication being that the shock is variable with a larger span of R - and by extension X - as can be seen when modelling the Outer spiral arm which spans a larger fraction of the Galaxy (in R). Whereas in the Perseus arm has a span of R which is sufficiently low that the constant shock approximation is valid.

One may argue that the addition of a variable v_{shock} is comparable to including a non-flat rotation curve. The possibility of this and also the effect of modelling a constant-v_{shock} with a non-flat rotation curve is presented in Chapter 5.

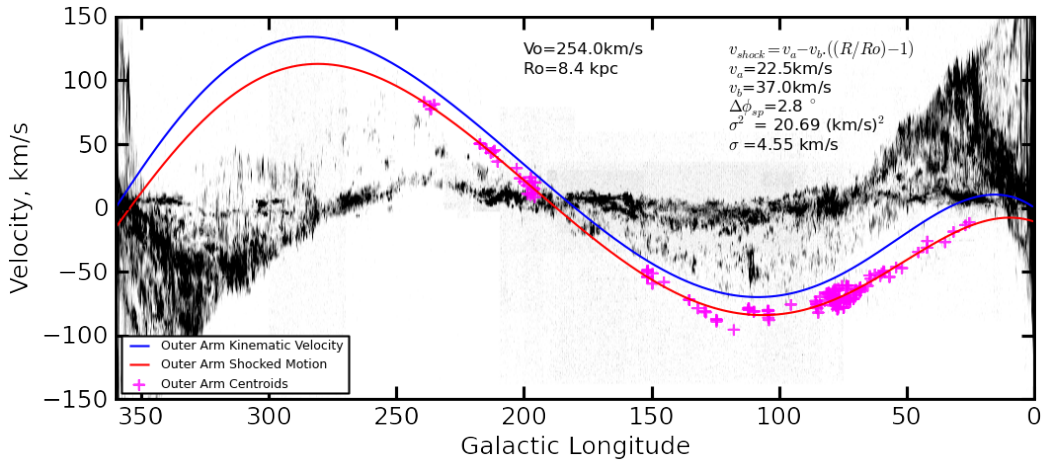

Figure 3.25: Longitude-velocity diagram showing the Outer arm variable-shocked-motion best least squares fit to ^{12}CO centroids in the CfA composite and Ex-FCRAO surveys, assuming a variable shock potential. The goodness of fit ellipses can be seen in Figure 3.26.

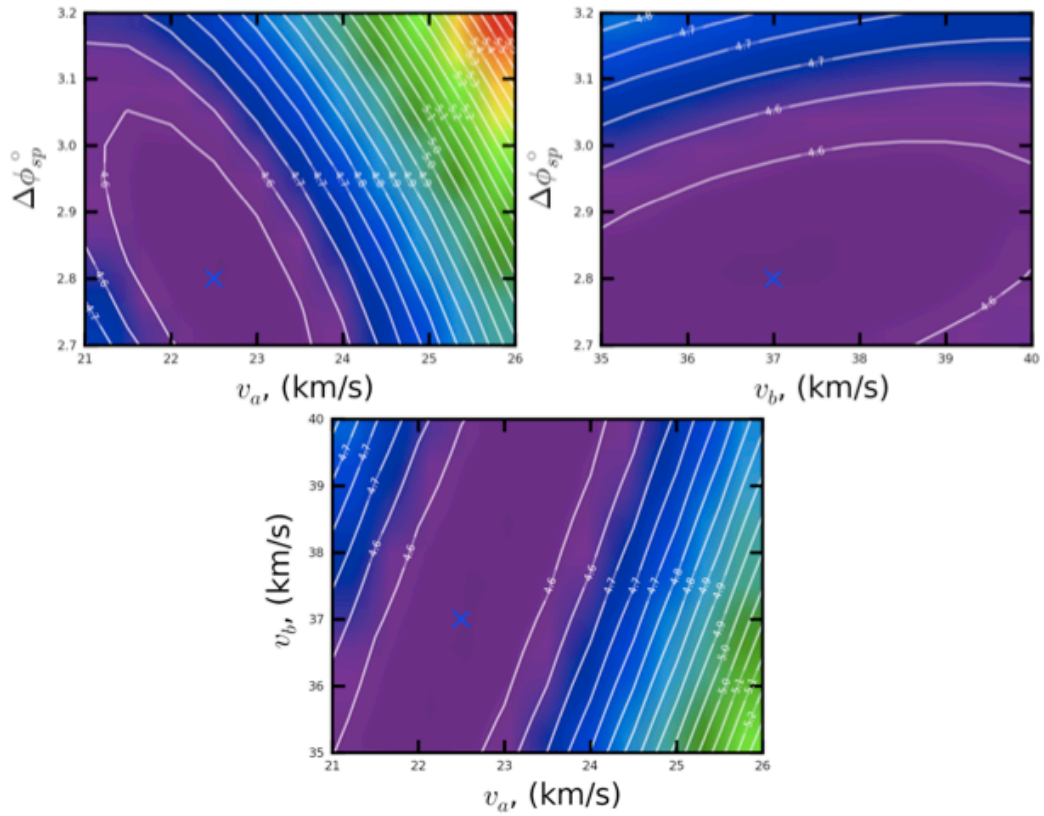

Figure 3.26: Error ellipses taken from the goodness of fit ellipsoid produced from the least-squares fitting to the ^{12}CO centroids for the variable-shock-motion model. The relationship between each of the three parameters are shown here, each 2D plot shows the relationship between the two displayed parameters at the minimum of the third. The blue cross shows the location of minimum.

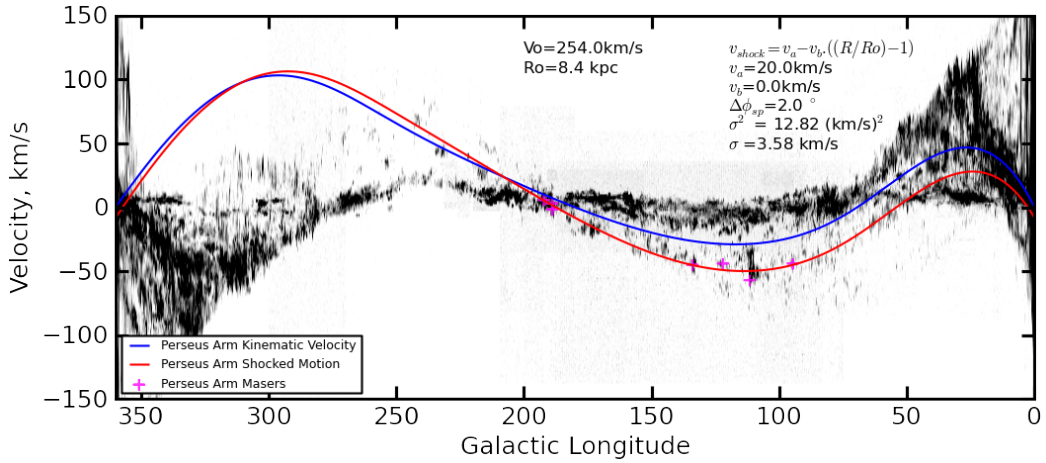

Figure 3.27: Longitude-velocity diagram showing the Perseus arm variable-shocked-motion best least squares fit to the masers in Table 3.1.

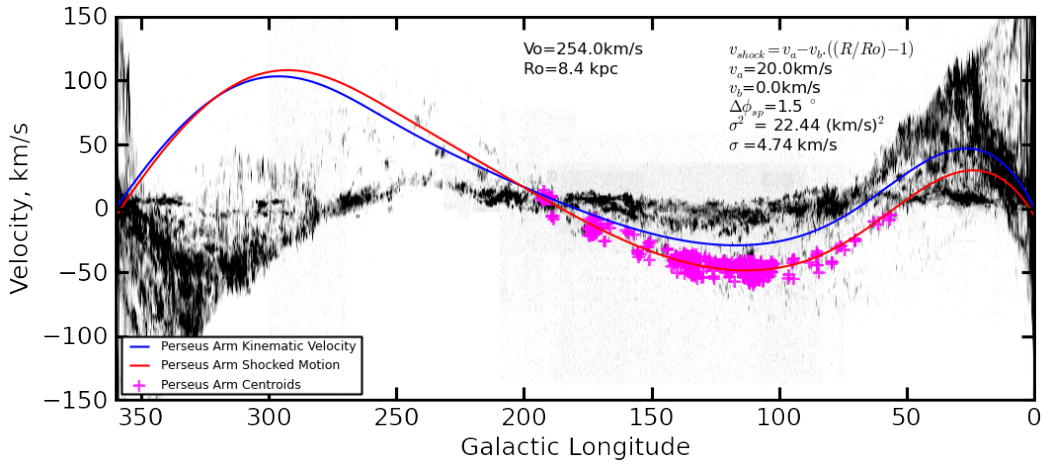

Figure 3.28: Longitude-velocity diagram showing the Perseus arm variable-shocked-motion best least squares fit to ^{12}CO from the Ex-FCRAO survey. Each magenta cross corresponds to a ^{12}CO centroid used to fit the model.

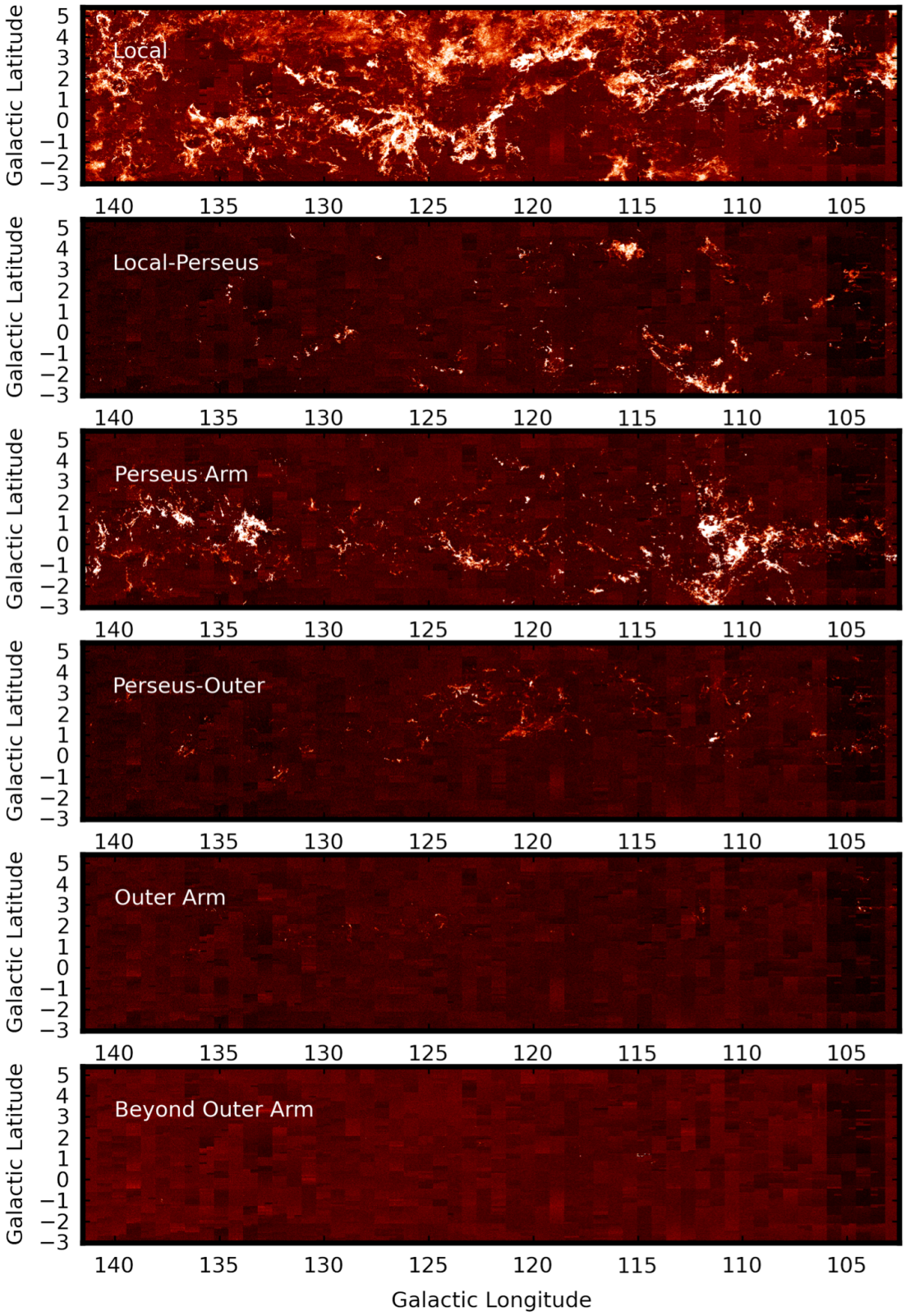

Figure 3.29: The Figure above shows peak temperature maps of the various kinematically defined regions within the *ogs* region of the Ex-FCRAO ^{12}CO survey (Brunt et al. in prep). v_{LSR} tracks from more positive to more negative from top to bottom.

3.4.3 Musings on the ℓ-v_{LSR} Structure of the Outer Arm

The plot in Figure 3.19 shows an $\ell - v_{LSR}$ map for the CfA composite ^{12}CO data over-ploted with the tracers from Table 3.3 which have a measured velocity. The band of emission identifying the location of the Outer arm is found at more negative v_{LSR} than that of Perseus. The arm is not as pronounced in ^{12}CO emission as Perseus, possibly even implying a wispy (not quite flocculent) structure - at least in terms of the molecular component - at the distance of the Outer arm.

Shifting our attention from the molecular to the atomic component of the Milky Way at this juncture and to Figure 3.34. In the ℓ-v_{LSR} map of HI in Figure 3.1 shows a *knot* of material at bound by 90°< ℓ <100°spanning between the kinematic structure associated with Perseus and the Outer arms. This feature could be showing the location, in ℓ–v_{LSR} , of the co-rotation radius of the Milky Way - the point where the spiral density wave changes from being a leading to a trailing front (Lin et al. 1969). This means that at the point of co-rotation, the rotational velocity of material equals the pattern speed of the spiral potentials. However, it is not known whether the pattern speed for a set of potentials is indeed constant across the whole Galactic disc (Foster & Cooper 2010). The spatial location of the co-rotation radius has been investigated by other works using statistical analyses, (Mishurov & Zenina 1999). Mishurov & Zenina (1999) find that the ΔR displacement, ΔR=(R_0 - R_c) where R_c is the co-rotation radius, from the Solar position is ΔR ≈0.1 kpc . This was improved upon later by Dias & Lépine (2005), who found the ratio $\frac{R_c}{R_0}$=1.06±0.08, again placing the corotation point near the solar position. The more recent work by Acharova et al. (2011) found this resonance to occur in the region R_c ≈7.0-7.6 kpc (associated error being 0.4-0.6 kpc), they use the solar constant of R_0=9.3 kpc , so the values of R_c found are consistent with the definition of the displacement from R_0 from Mishurov & Zenina (1999); Dias & Lépine (2005) . What these studies show is that the point where $\Omega_p = \Omega$, the pattern speed rotation equalling to the local Galactic rotation speed occurs in the approximate solar neighbourhood, $R \approx R_0$, (Mishurov & Zenina 1999; Fernández et al. 2001; Dias & Lépine 2005; Acharova et al. 2011).

However, what I observe in Figure 3.1 is a local *bottleneck* of atomic material bound by 90°< ℓ <100°extending, kinematically, from just negative-wards of the local emission, through Perseus to the Outer arm. This does not correspond to a region which is kinematically in the solar neighbourhood. The works of Popova & Loktin (2005); Popova (2006), using kinematical measurements of OB stars and open stellar clusters, suggest that R_c exists between 8.9 kpc < R <10.9 kpc , placing its probable location beyond the Perseus arm at R_c=10.5 kpc and also goes on the imply that R_c is unlikely to be found in the vicinity of the solar circle. In supplement to the Popova & Loktin (2005) findings - Russeil et al. (2007) identified the co-rotation radius to be between the Perseus and Outer (Cygnus) arms at R ≈12.7 kpc , (IAU standard solar constants), thus placing R_c mid-way between the Perseus and Outer arms in spatial coordinates. What is observed in Figure 3.1 is an excess of HI emission in the region kinematically between the Perseus and Outer spiral arms as defined by the model presented. Assuming a mapping between the observed arm velocities to their actual distances, where emission which is kinematically midway between the arms would also be spatially mid-way between them, this places the emission at R ≈10.3 kpc at ℓ =95°. If this emission does indeed correspond to the co-rotation point within the observations, then this work also places the R_c position beyond the Perseus arm.

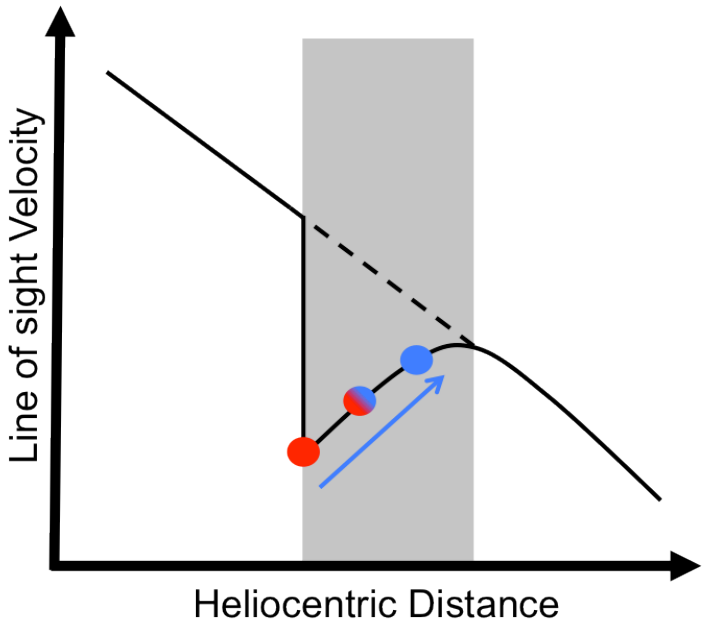

Figure 3.30: Schematic d_{helio}–v_{LSR} diagram representing the velocity reversal in Spiral potentials. The grey bound shows the spiral arm extent, the red point shows the point where the material is mainly atomic, the blue - molecular. The arrow points the direction of evolution from the atomic to molecular gaseous state.

In the ℓ–v_{LSR} diagram of ^{12}CO in Figure 3.19, there is a band of emission between the Perseus and Outer arms. In terms of its (ℓ, b) distribution, which can be seen in Figure 3.29 it tracks a latitude coverage comparable to the - relatively - high latitude Outer arm. One may see in the Figure that the molecular content of the Galaxy decreases to larger R - corresponding to a more negative v_{LSR} . Considering the ℓ–v_{LSR} structure associated of these regions, one may observe that this material in the inter-arm (Perseus-Outer) region can be described, in ℓ–v_{LSR} , as material at the distance of the Outer arm under circular - and not shocked - motion (Figure 3.20). Whether this represents a bifurcation of material implying a flocculent arm structure at this distance, or whether it is a structure in its own right is not certain. This apparent structure is also visible in the HI over this kinematic range, so it would seem to imply the former.

3.4.4 Velocity Gradient Reversal Within Spiral Arms

When investigating the Perseus arm, I alluded to a potential velocity gradient reversal in the region of the Perseus arm. It was concluded that since it was difficult to assign accurate distances to material on the intra-arm scale that this implied that there was not a monotonic mapping of velocity-to-distance within an arm.

When fitting the Shocked-Motion model to the Outer arm based material I found that the Outer arm as kinematically defined by the ^{12}CO was not coincident with the HI. Figure 3.23 shows the ^{12}CO fitting centroids over-plot on the HI, it can be seen that a majority of the bright ^{12}CO

clumps exist on the positive velocity edge of the HI arm. Though, in retrospect this was also present - to a lesser extent - in the Perseus arm, the greater distance of the Outer arm makes this effect more easily observed. Taking the representation in Figure 3.30 as a basis for this explanation: Assuming that material evolves within the arm as star formation occurs, the atomic material enters the arm and is shocked at a *near* distance (w.r.t the arm width) - referred to as point A. Therefore the atomic material experiences a maximum shock for that line-of-sight and as such has the most negative observed velocity. As the atomic material traverses the arm and condenses to become molecular gas, its velocity - w.r.t point A - becomes more positive. This means that on the intra-arm scale, material with a more positive velocity w.r.t. the arm-centre exists at a further distance the reverse of what one would usually expect exterior to the arm. Thus, molecular material needing a finite time for form from the shocked material, exists at a slightly further intra-arm distance *and* at a more positive velocity - hence explaining the more positive velocities of the molecular tracing ^{12}CO in the ℓ-v_{LSR} maps. This is also found in the literature in extra-galactic systems where the HI is offset from the stars in the spiral arms, Roberts (1967). Though there are those whom believe that the atomic hydrogen we observe is a product of star formation and not the precursor to it, Allen (2001), however the evidence of gradient reversal would appear to imply that the spiral arm based HI is a precursor to the star formation process.

In addition to the velocity gradient reversal, the observed velocity has a double valued mapping to distance. With the ubiquity of HI throughout the Galaxy, when compared to the molecular gas which resides mainly within spiral arms, the velocity window may be contaminated by far-distance atomic material which would artificially broaden the arm emission in ℓ-v_{LSR} – see Figure 3.34.

3.5 Beyond the Outer Arm : Scutum-Centaurus

As was mentioned earlier in this Chapter - the Outer arm, in spite of its name, is not the outer most structure in the Galaxy. Dame & Thaddeus (2011) discovered a probably molecular arm beyond the Outer arm which is thought to be the outer galaxy part of the Scutum-Centaurus (Sct-Cen) arm as it passes behind the Galactic centre and re-emerges on the Solar side of the Galactic centre, it is tracked to $\ell \approx 50°$. With the current model and understanding I am unable to map the whole arm from inner- to outer-Galaxy, but I attempt to map the outer segment of arm discovered in Dame & Thaddeus (2011). As a test for the variable-shocked-motion model, I used the positions of ^{12}CO centroids defined to be within it from Dame & Thaddeus (2011). Because of the low longitude of these points, I were able to use the Reid et al. (2009) method for correcting a kinematically determined distance to more accurately represent these centroids' true distance. It is important to realise that the arm is not well constrained in this regions, but as a first approximation to the general location of the arm it is suitable.

3.5.1 Compensating for the Kinematic distance estimates

The method for correcting the distance estimate is outlined in full in Reid et al. (2009), but in the absence of any other constraint the method detailed below is adopted to correct for the kinemati-

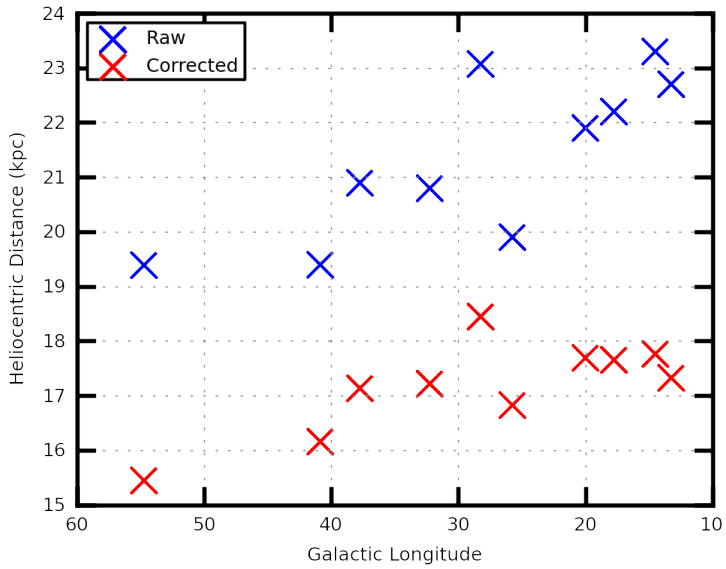

Figure 3.31: The kinematic distances for the Dame & Thaddeus (2011) tracers (Blue) corrected via the Reid et al. (2009) method (Red).

cally determined distances of the ^{12}CO centroids;

1. Identify candidate arm source;
2. Subtract -15 km s^{-1} from the source's observed v_{LSR};
3. Calculate a new kinematic distance based on the *corrected* velocity.

Correcting the distances in this manner compensates for the over-estimation of the distance, the effect of which can be seen in Figure 3.31. This is not a robust treatment to give an accurate representation of the emissions' actual distance, but it does provide a starting-point from which I are able to estimate the distance structure of the arm.

3.5.2 Spatial fit to the Sct-Cen molecular emission

By fiting a logarithmic spiral to the kinematically corrected data (Figure 3.32) and derived the spatial parameters, I found that the fit gave the pitch angle of the fitted Sct-Cen arm to be ϕ_{pitch}=13.2±2.3°- comparable to that of the Outer arm. I found the arm width for Sct-Cen to be ≈1.06 kpc , which is of the same order as the Outer arm but still significantly larger than that of Perseus. However, as with the Outer arm, the width compared to the length of the arm is relatively small since Dame & Thaddeus (2011) suggest the arm could span over 60 kpc of the Galaxy.

Finally, I fit the ℓ-v_{LSR} structure of the Sct-Cen segment using the variable-shocked-motion model to perform a least-squares minimisation to the ^{12}CO centroids from Dame & Thaddeus (2011), resulting in a set of best-fit parameters calculated to be; $v_a = 20.0$ km s^{-1} , $v_b = 22.0$ km s^{-1} and $\Delta\phi_{\rm sp} = 2.7$ °. The number of ^{12}CO centroids in this region made refining this initial fit to the

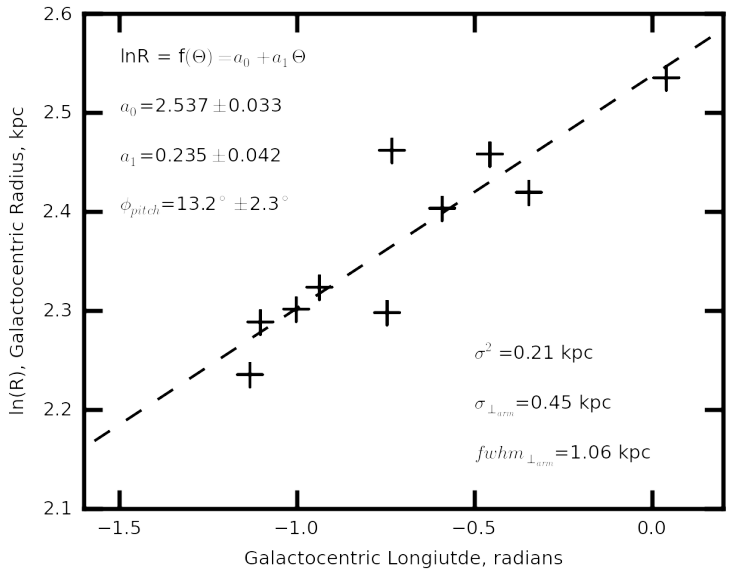

Figure 3.32: The logarithmic spiral fit to the outer part of the Scutum-Centaurus arm to kinematically corrected ^{12}CO centroids presented in Dame & Thaddeus (2011).

tracers redundant. Whether this is an accurate representation of this section of structure is unknown at this time and will require further constraint - however, the longitude-velocity map in Figure 3.33 appears to suggest that the ℓ-v_{LSR} locus exists below the modelled Outer arm. In Chapter 4 I present the possible ℓ, b structure of the Sct-Cen arm.

3.5.3 Modelling the kinematic structure of Sct-Cen

Unlike the Perseus and Outer spiral arms, the number of ^{12}CO centroids in this region made refining this initial fit to the tracers redundant. Figure 4.7 shows the emission associated with the Sct-Cen arm model using the Arm Centric Mapping process (described in section 4.2), the Sct-Cen arm can be seen to track the Galactic warp with a rising and falling b distribution, with emission within the arm confined to a common latitude spread - so is unlikely to be contaminated with near-far ambiguities. Also, with the exception of 90°< ℓ <120°- the outer Sct-Cen arm appears a contiguous structure, so, using the prediction of the arm trajectory from low longitude, it may be possible to identify possible molecular emission associated with this spiral feature at higher longitude - see section 4.2.4.

3.6 Coupling of the Spatial & Velocity Models

3.6.1 Milky Way Velocity Field

Using the spatial fits and the shocked-motion velocity models it is possible to use them in conjunction to create an XY projection of the Milky Way velocity field as defined by the models thus far. The arms included are the Perseus, Outer and outer-Sct-Cen arms - The Perseus kinematic struc-

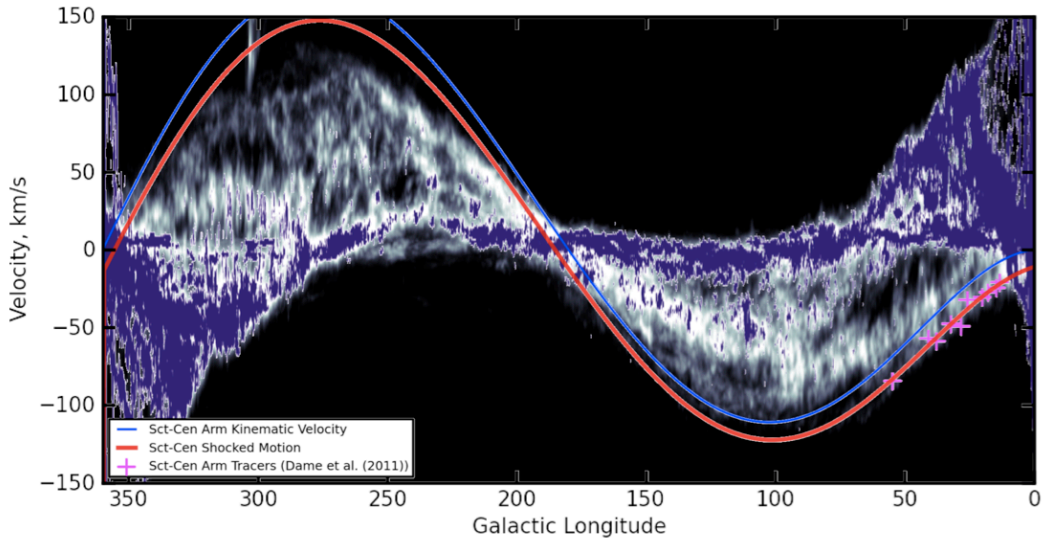

Figure 3.33: The ℓ–v_{LSR} fit to the Scutum-Centaurus arm. The blue line shows the ℓ–v_{LSR} for material at the distance of Sct-Cen, but under circular motion. The red line shows the best least-squares fit to the ^{12}CO centroids (magenta crosses). The models are unconstrained above ℓ=70°- though in the subsequent Chapter I identify possible molecular cloud candidates beyond this limit.

ture is modelled by the constant-shocked-motion model and the Outer and Sct-Cen kinematics are modelled by the variable-shocked-motion-model. The spatial fit to each arm is the logarithmic spiral form defined from the tracers which track the arms. It has been mentioned how the kinematic selection of material can cause the velocity window to be contaminated by material at a further distance and this can be seen clearly in Figure 3.34. Figure 3.34 shows the velocity field for the Milky Way, as defined by the model and assumptions presented her..As can be seen in Figure 3.34, for a given line of sight, material at two separate distances can share a common measured velocity - which can cause kinematically selected data to be contaminated by material at the further distance. Outside the centre and anti-centre regions, the contamination is generally due to inter-arm emission at a further distance being confused with shocked arm-based material.

3.7 Summary

Presented in this chapter is an interpretation of how the non-circular component of velocity behaves in the regions of the Galaxy which are subject to a spiral potential. There are three aspects to the model which must be considered;

- Spatial fit to the arm using a logarithmic spiral
- Kinematic fit to the arm incorporating a constant shock
- Kinematic fit to the arm incorporating a variable shock

It was found that the Perseus, Outer and outer Scutum-Centaurus arms were well fit, spatially, by logarithmic spirals and the distance structure was constrained using known arm tracers.

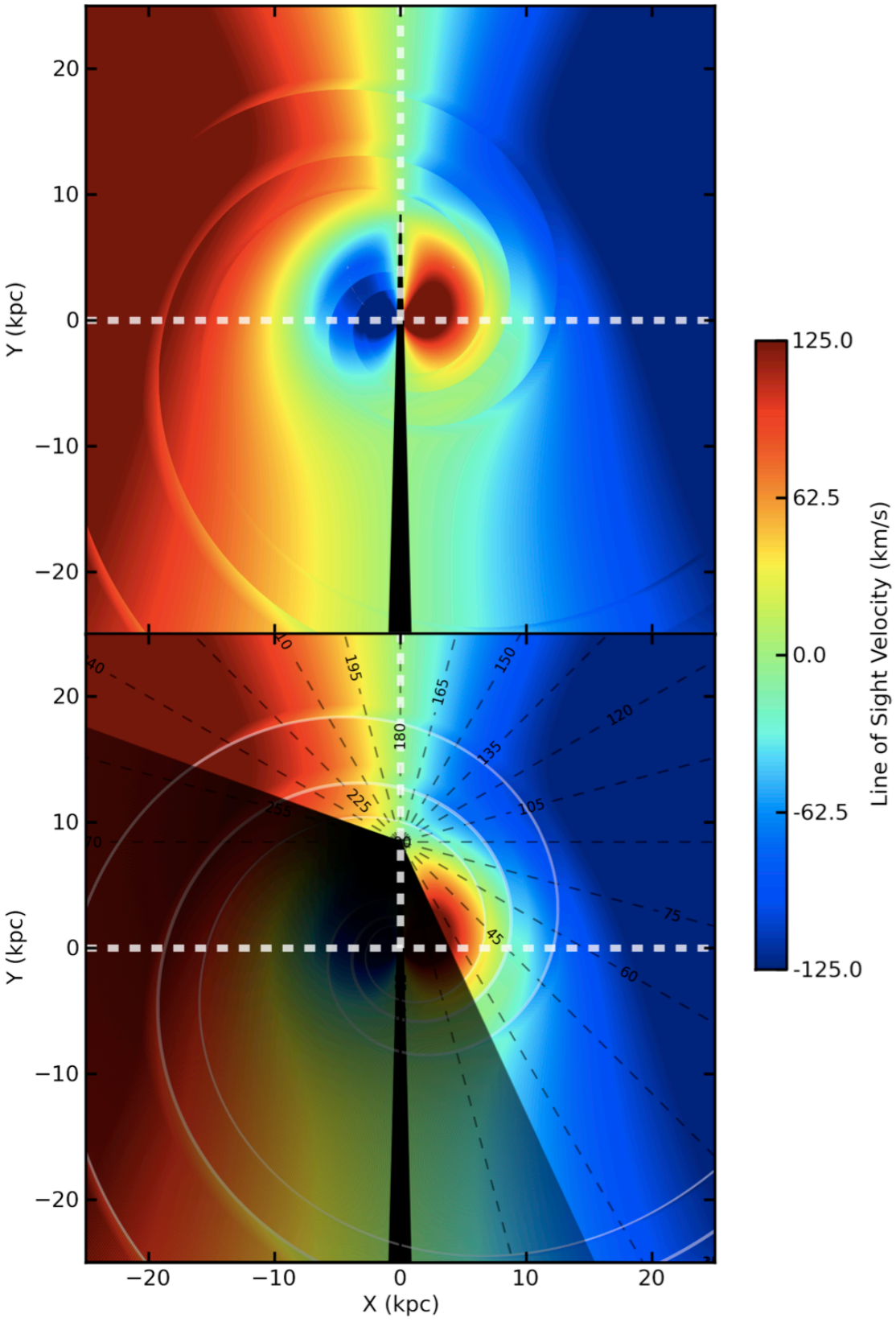

Figure 3.34: The Figure above shows an XY projection of the modelled velocity field. Exterior to the arms, I assume circular motion, within the Perseus arm I assume a constant shock parameters For the Outer and Sct-Cen arms assuming a constant shock angle but incorporating the variable shock potential from Equation 3.12. The top panel shows the field. The bottom panel is overplot with lines-of-sight at constant ℓ, the shaded regions show where the arms are constrained and the white contours show the position of the arm shock fronts.

The kinematic structure, however, is more complicated. The Perseus arm longitude-velocity structure was described well by the model when constant shock parameters were used. The Outer and Sct-Cen arms were best described by a constant shock angle, but a variable shock velocity. This implied that the magnitude of the shock is variable with Galactic radius which is why its effect is more obvious in the outer arms, since they traverse a significant fraction of R. Encouragingly, it was found that the model predicts the arms' trajectories fairly accurately outside the regions of initial constraint .

3.7.1 The Perseus Arm

I have presented a new model of spatial and kinematic structure of the Perseus spiral arm using the solar constants derived in Reid et al. (2009) (R09) of R_0=8.4kpc and Θ_o=254km/s. I conducted spatial and kinematic fits using both the R09 and IAU standards, but found that the data were better fit by the R09 constants - in agreement with Hou et al. (2009). The spatial fit - using R09 - was determined via a logarithmic fit to maser emission from high mass star forming regions, with $\ln\left(\frac{R_{per}(\theta)}{[kpc]}\right) = a_0 + a_1 \frac{\theta}{[radians]}$, where a_0=1.898±0.09 and a_1=0.270±0.061 with a pitch angle of ϕ_{pitch}=15.1±3.3°. To model the kinematic structure of the arm, It was found that material within the Perseus arm can be described by a constant shock across the whole length of the arm at a non-zero angle. After refining the model and fit, I found the best fit parameters for the kinematic structure of the Perseus arm is v_{shock}=20.0km/s at an angle, ϕ_{sp}= 1.6°. Using these coupled models I was able to extract Perseus arm material kinematically and assign it a distance based on the model. I found that the presence of a velocity stream reversal within the kinematic window made assigning kinematic distances to intra-arm precision did not accurately predict a candidate's distance. Instead, I suggest assigning objects residing within the arm kinematic window a distance of $d_{per}(\ell)$. I was able to provide a correction for the kinematic determination of distance, to more accurately reflect an object/emission's heliocentric distance more accurately. I also found that the model predicts, within error, the trajectory of the Perseus arm - outside the original constrained range - slightly into the third Galactic quadrant and also as it sweeps into the inner-Galaxy recognisable in the ^{13}CO emission in this region from the GRS. The shocked-motion model predicts the location of W49 in the inner Galaxy, both kinematically and spatially - and also tracks the continuous ^{12}CO emission to approximately ℓ=250°.

3.7.2 The Outer Arm

Using an improvement to the shocked-motion-model to incorporate a variable v_{shock} , it was found that the Outer arm is well fit by a logarithmic spiral, which I constrain using measured distances to known Outer arm objects. Using the spatial fits I were able to determine the outer arm has a pitch angle, ϕ_{pitch}=13.3±1.4°, a width of 1.51 kpc - with its closest approach is at ℓ=159.4°at a distance of d_{outer} =4.8 kpc . From the spatial fit I was able to define a kinematic model which is initially fit to the measured v_{LSR} of known Outer arm objects - which is then refined using ^{12}CO centroids. I found that the variable-shocked-motion model provided a better fit to the emission canonically identified to be the Outer arm in ^{12}CO , with the variable shocked motion model of the form

detailed in Equation 3.12, I find the shock parameters to be; v_a = 22.5 km s^{-1} , v_b = 37.0 km s^{-1} and $\Delta\phi_{\rm sp}$ = 2.8 °- the implication of which is that the magnitude of the effective v_{shock} decreases with R. Whilst investigating the longitude-velocity structure of the Outer arm region in ^{12}CO and HI, I evidence of a velocity gradient reversal within the Outer arm. Meaning, on the intra-arm scale, the material with a more positive velocity is actually at a further distance.

3.7.3 The Outer Scutum-Centaurus Arm

Using the variable shocked motion model, it was possible to isolate material which is probably associated with the outer Galaxy segment of the Sct-Cen arm. By modifying the kinematically corrected distance estimates for the arm-based regions a fit to a logarithmic spiral was obtained to provide a spatial fit to this segment of spiral arm. Using its spatial fit, the outer Sct-Cen arm was found to have ϕ_{pitch}=13.2±2.3°, a width of 1.06 kpc . I then modelled the kinematic structure of outer Sct-Cen arm and found that it too was well described by the variable-shock-motion - implying that the shock potential varies with large changes in Galactic radius, which is why Perseus was well fit by a constant shock. The variable-shocked-motion model parameters of v_a = 20.0 km s^{-1} , v_b = 22.0 km s^{-1} and $\Delta\phi_{\rm sp}$ = 2.7 °- the implication being the same as for the Outer arm, the magnitude of the effective v_{shock} decreases with R.

The next step is to implement these models to isolate and extract the spiral arms from the data as single structures for analysis. This is presented in the subsequent Chapter.

CHAPTER 4

Galactic Spiral Arm Cartography

"A good map tells you everything, except how to re-fold it."
Anonymous

4.1 Introduction to Chapter

Having introduced, defined and modelled the spatial and kinematic structures of the spiral arms in the previous Chapter - it is now possible to use them. In this Chapter I discuss the three forms of mapping I will use to present and be the basis of the analyses for the data. There are three mapping regimes described here.

- Spiral Arm Centric Velocity Mapping (**ACM**)
- Common Resolution Spiral Arm Centric Velocity Mapping (**CRM**)
- Common Resolution Spiral Arm Mid-plane Function Mapping (**AMF**)

There are three different co-ordinate systems used in the three different mapping methods. The ACM data are expressed in regular galactic co-ordinates, ℓ, b but with the velocity axis resampled relative to the kinematic arm centre, i.e. Δv_{arm} =0 km s^{-1} is coincident to the kinematic centre of the modelled arm. The ACM data are then transformed into a linear co-ordinates for expression and analysis in the CRM and AMF forms. These co-ordinate systems are explained and defined in further detail in the following sections. The rescaling of the velocity axis to be arm-centric, allows one to extract each spiral arm within each of the surveys using a constant $\pm\Delta v_{arm}$ which also reduces the cartesian velocity gradient. This velocity gradient is not that of the velocity gradient reversal described in the previous Chapter, but instead the velocity gradient in terms of differing value of v_{arm} (ℓ, b) as a spiral feature traverses the galaxy. Having extracted the arm, in terms of its $\ell, b, \Delta v_{arm}$, it will be possible to perform a convolution on the ℓ, b data to smooth the angular

data to maps of the arms at a common linear resolution - thus minimising the biases inherent in angular observations.

The arm velocity centering allows easy definition of the kinematic arm centre, meaning that the relative kinematic position of the arm is constant over a run of ℓ. It is possible to assume that the kinematic centre is coincident with the spatial arm centre therefore I have a mapping from kinematic position to distance. The angular, ℓ, b, maps suffer that for a single angular size, material at an arm's closest approach is significantly closer - hence smaller linear size - to the observer than when compared to regions where the arms are recessing from the observer - a larger linear size. Mentioned in previous chapters, this causes difficulties when deriving cloud properties since there is a $\frac{1}{d^2}$ relation to mass, so the relative sizes and gaseous content of clouds has conversion factors which are *also* dependent on ℓ. By convolving the maps to a common linear resolution, this distance dependence is eliminated and all the clouds across the map are at a constant linear size. Meaning that the relative sizes of clouds and emission in the data are directly comparable to one another and the distance variation is no longer a factor.

In this Chapter I describe the mapping methods used to extract and present the Perseus, Outer and Scutum-Centaurus arms in terms of their ($\ell, b, \Delta v_{arm}$), ($X, Z, \Delta v_{arm}$) and ($X, Z_{arm}, \Delta v_{arm}$) in preparation for their analysis in the subsequent chapter.

4.2 Spiral Arm Velocity Centric Mapping (ACM)

4.2.1 The ACM Process

The straight-forward process referred to as the Arm Centric Mapping (ACM) process involves the resampling of the spectral velocity axis so that a 0 km s^{-1} velocity corresponds to the kinematic arm centre; This means the velocity presented ($\Delta\ v_{arm}\ (\ell)$) is the deviation of gas from what is considered to be the arm centre. The spectra are then re-sampled to redefine the velocity axis with respect to the spiral arm centre. This is completed by just not resampling the velocity axis per-se, I redefine the the zero velocity as the centre fit.

$$\Delta v_{arm}(\ell) = v_{lsr}(\ell, b) - v_{arm}(\ell) \tag{4.1}$$

The effect the ACM process has on the ℓ, v of the data, for the Perseus arm, can be seen in top panel of Figure 4.1. With the data arm centred, one may extract each of the arms over a single $\Delta v_{arm}(\ell)$=±10 km s^{-1} window for analysis. It is these maps which are presented in the subsequent subsections.

4.2.2 Perseus Spiral Arm

Here I consider the ℓ, b Perseus ACM for the ^{12}CO and HI ACMs in Figures 4.2 and 4.3 respectively. Returning briefly to the top panel in Figure 4.1 - there is an evident band of emission around the 0 km s^{-1} velocity in the CO distribution, this is the Perseus arm. The curved feature present at comparatively high positive velocity is local emission and is not part of the Perseus arm.

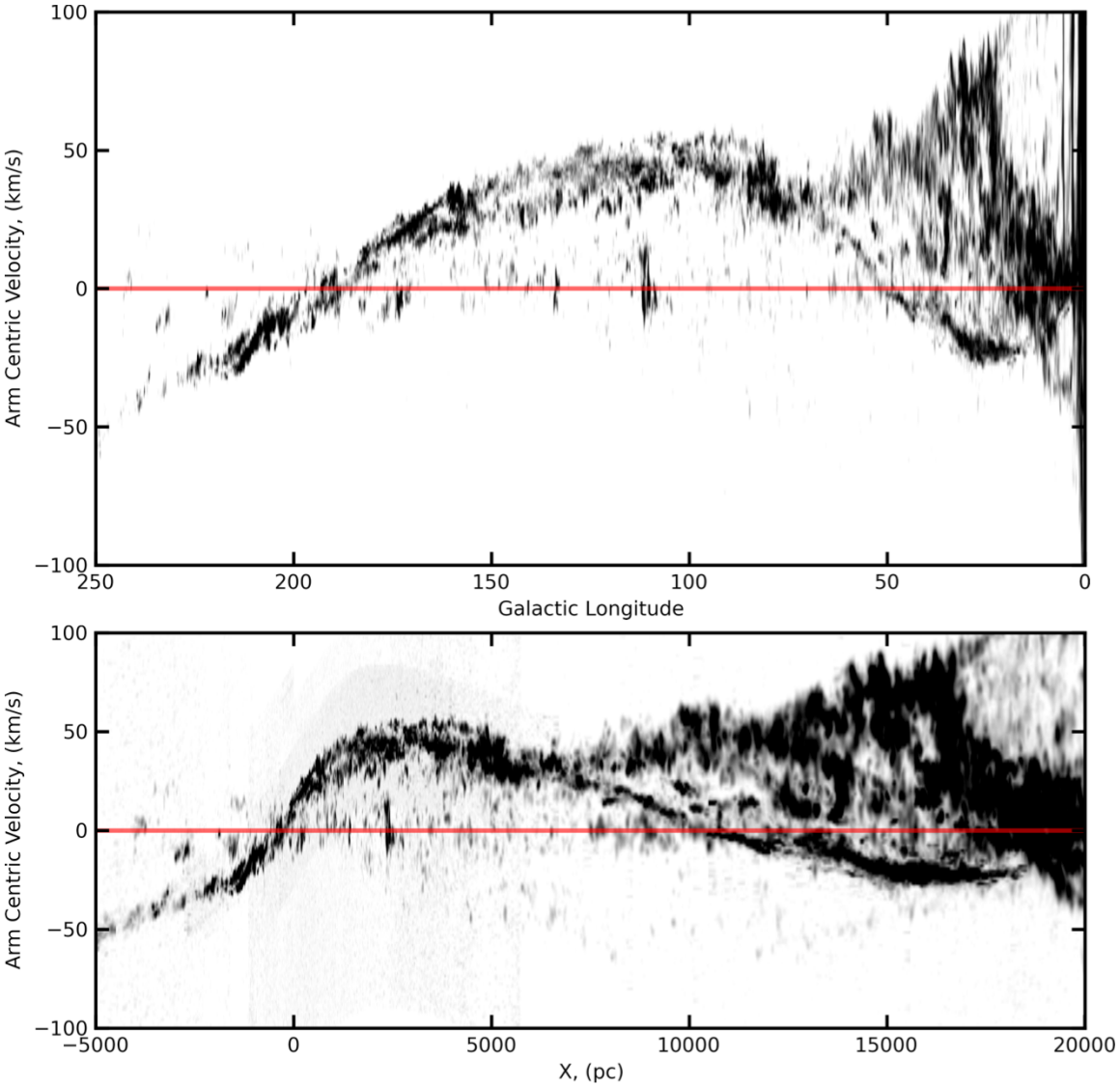

Figure 4.1: Perseus arm centric velocity plot of, Top panel: ^{12}CO in *lbv*. Bottom Panel: ^{12}CO in XZv (co-ordinates defined in main text), taken from Dame et al. (2001). Both plots are grey-scale peak temperature maps through the effective Galactic height axis (b for the angular coordinates and Z for the CRM data). The red line shows the 0 km s^{-1} velocity centre of the Perseus arm the unshaded region in the longitude-velocity plot shows the range which corresponds to the displayed arc-length range, they are not linearly related.

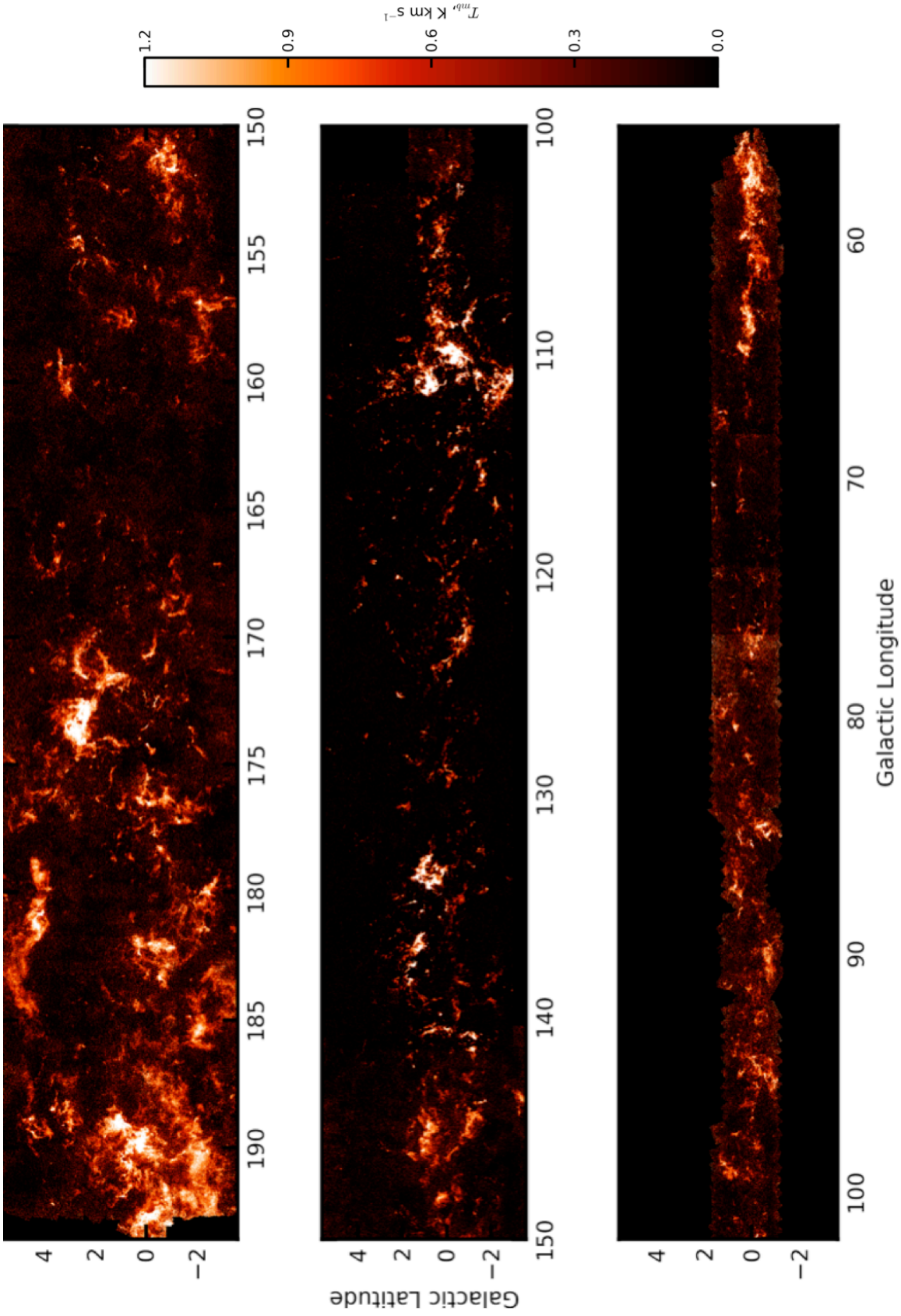

Figure 4.2: Integrated summed temperature map of the ACM ^{12}CO data, taken from the ExFCRAO CO NGPS. This is a log-summed ($10^0 \rightarrow 10^{1.2}$K km s^{-1}) T_{MB} through ± 10 km s^{-1} of the Perseus arm centre. The black spaces at $|b|$ >2°in the bottom panel reflect the small latitude coverage in the Vulpecula and Cygnus regions (see Chapter 2)

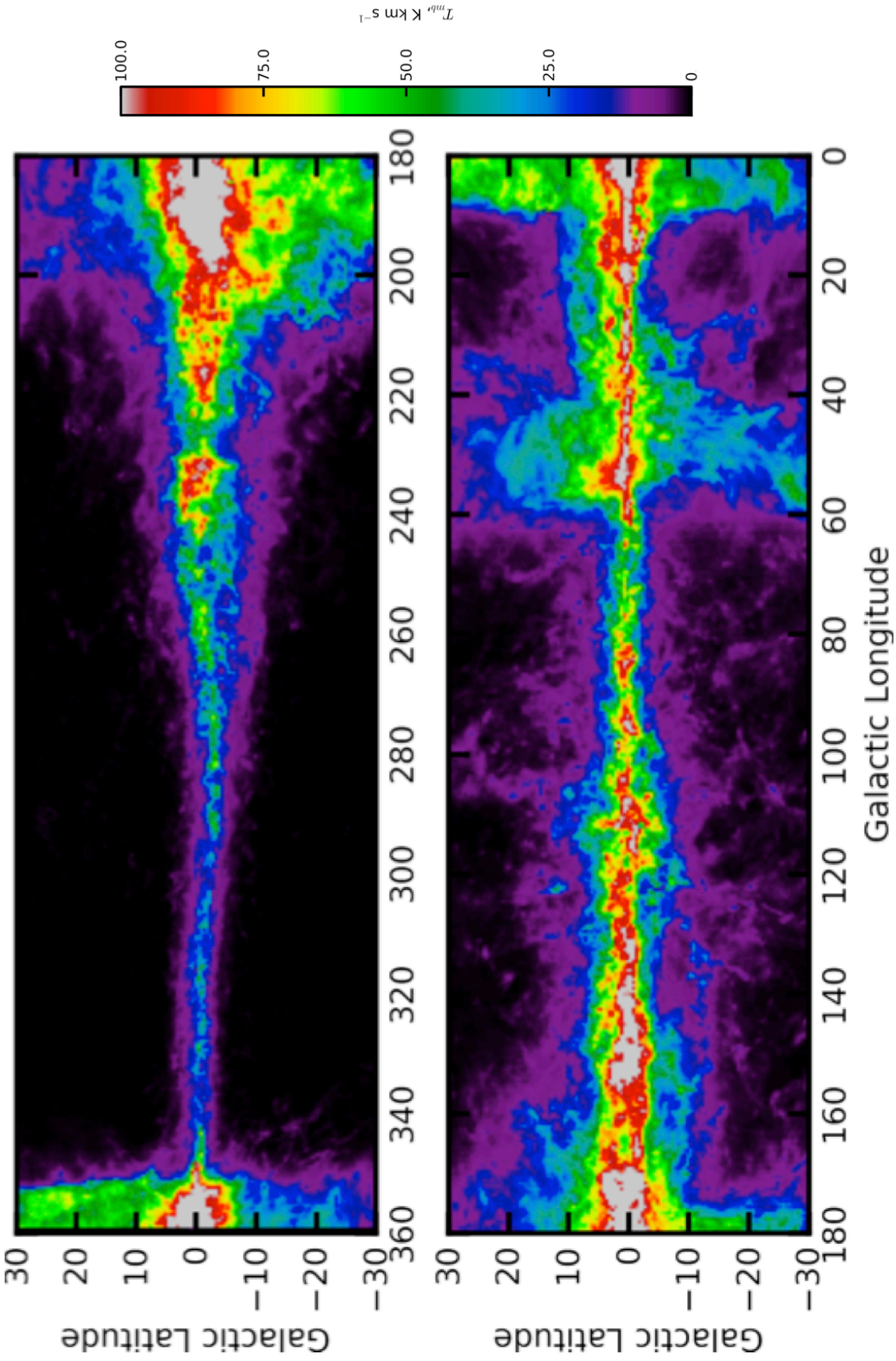

Figure 4.3: A peak temperature Perseus ACM HI data, taken from the LAB HI. This is a peak temperature, T_{MB} (0→100 K km s^{-1}) through ± 10 km s^{-1} of the Perseus arm centre. the regions ℓ >250°and ℓ <60°are unreliable but are included for completeness.

The formation of these ACM maps allow the Perseus arm to be extracted as a single coherent structure through the data, by selecting it using a constant velocity window, thus reducing the velocity gradient across any clouds within the spectral data which is caused by the heliocentric projection of Galactic rotation. The effect of arm-centring on the ℓ–v structure of the data can be seen in the top panel of Figure 4.1, which shows the emission being centred on the model's arm-centre. The (ℓ, b) ACM ^{12}CO map for the ExFCRAO data can be seen in Figure 4.2, with the HI presented in Figure 4.3. Both Figures show that the Perseus arm emission resides mainly within the plane of the Galaxy. Comparing Figures 4.1 and 4.2, the effect of the velocity compression around the anti-centre can be seen in a confusion in emission of the the 170°< ℓ <193°range. Where there is an excess of emission which is spread over a much larger range of b, implying that he emission is from a range of distances and but still existing within the velocity window. In the HI, the region ℓ <60°there is the wider latitude coverage synonymous with kinematic window contamination from non-arm distances, with planar compact arm-like emission can be seen though the middle of this material.

4.2.3 Outer Spiral Arm

The Outer arm exists at more negative v_{LSR} than Perseus, therefore the low longitude segment of the Outer arm remains unconfused with local emission to lower longitudes. Figure 4.4 shows the Outer ACM for ^{12}CO taken from the Ex-FCRAO survey, the Outer arm contains less emission than Perseus and tracks a much higher latitude. Unfortunately, due to the non-uniform latitude coverage of the Ex-FCRAO we 'lose' the Outer arm around ℓ =103°until we pick it back up again around ℓ=85°. Using the full ℓ, b coverage available from the LAB HI survey, I am able to extrapolate out model to the unconstrained regions above ℓ=250°.

The Outer arm in HI (Figure 4.5) follows a similar tight latitude distribution across its length appearing to track the warp beginning at ℓ ≈100°, which corresponds to R ≈12 kpc . Foster & Cooper (2010) suggest that R_{warp}, the Galactic radius where the warp beings to occur is given by $R_{warp} \approx \frac{3}{2}R_0$. For the R09 set of parameters, R_{warp} ≈12.6 kpc which, allowing for the error on our fit to the arm tracers, appears to be consistent with the observation within the ACM HI map.

In both HI and ^{12}CO maps, the velocity compression and confusion - with local emission and with the Perseus arm - at the anti-centre can be seen by the excess of emission in these regions. The extension of the HI to the centre means that at extreme low longitude, the kinematic window incorporates some local emission (the wide latitude spread diffuse emission), but the Outer arm is still visible as the concentrated (in latitude) bright emission at b=0°. Equally it could be argued that we are able to track , what appears to be an arm-like feature, beyond the initial constraints of ℓ=250°into the third and fourth quadrants. But the degree to which this material is actually the Outer arm is unknown.

4.2.4 Outer Scutum-Centaurus Spiral Arm

Figures 4.6 and 4.7 show the atomic and molecular Sct-Cen arm respectively. They show the emission associated within ±10 km s^{-1} of Sct-Cen arm model using the Arm Centric Mapping

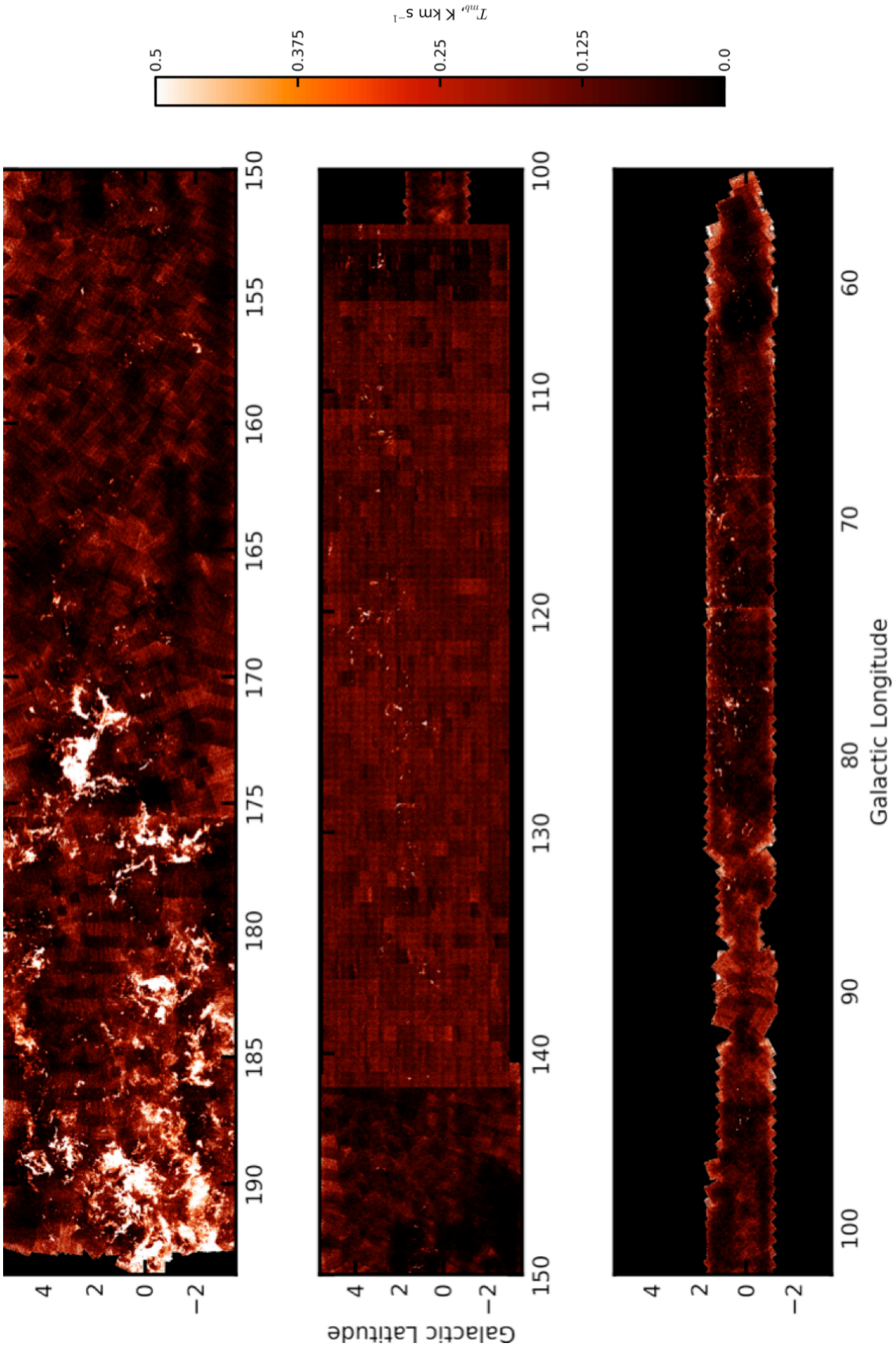

Figure 4.4: Integrated peak temperature (0< T_{peak} <0.5 K km s^{-1}) ^{12}CO Arm Centric Map - the peak temperature is needed to make the Outer arm emission more distinct from the background. The Outer arm can be seen tracking through high latitude in the central panel.

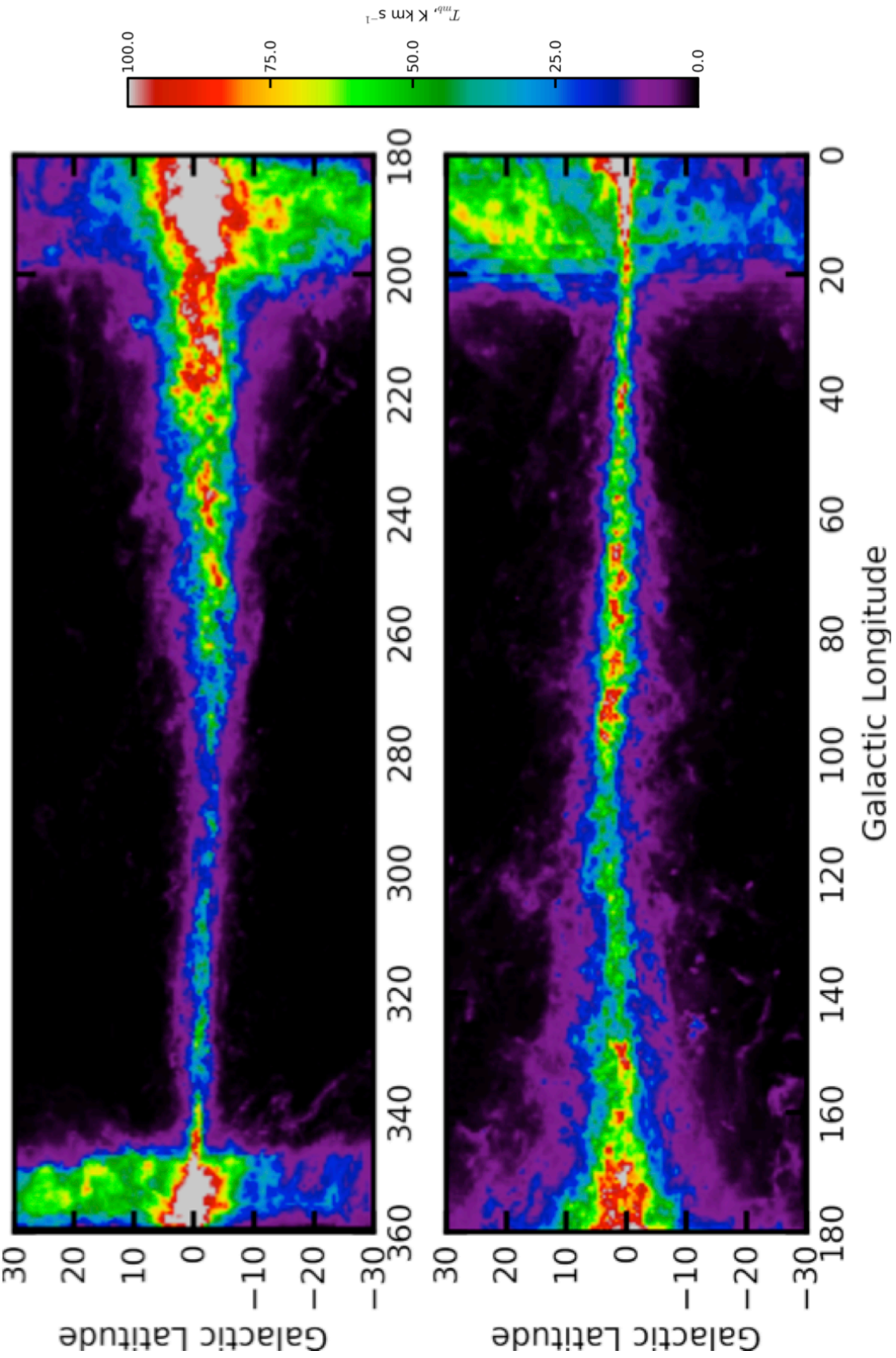

Figure 4.5: A peak temperature Outer ACM HI data, taken from the LAB HI. This is a peak temperature, T_{MB} (0→100 K km s^{-1}) through ± 10 km s^{-1} of the Outer arm centre. the regions ℓ >250°and ℓ <60°are unreliable but are included for completeness.

Table 4.1: Outer Scutum-Centaurus arm molecular cloud candidates. The velocity and distance information is of the Sct-Cen arm at the candidates' ℓ.

ℓ ($degrees$)	b ($degrees$)	$v_{sct-cen}(\ell)$ (km s^{-1})	$\frac{d_{sct-cen}(\ell)}{cos(b)}$ (kpc)	$\frac{R_{sct-cen}(\ell)}{cos(b)}$ kpc)
122.325	1.729	-113.28	9.28	16.07
122.727	2.534	-112.93	9.92	16.08
123.381	1.600	-112.35	9.87	16.11
137.750	–1.0125	-95.62	9.47	16.67
166.794	–3.244	-42.24	9.48	17.77
168.444	–1.050	-38.63	9.52	17.83
169.044	–1.706	-37.30	9.53	17.85

process (described above). The Sct-Cen arm appears to track the Galactic warp with a rising and falling b distribution, the emission appears to track a common latitude so is unlikely to be contaminated with near-far ambiguities and - with the exception of 90°< ℓ <120°- is a contiguous structure. In addition to the gaseous content structure of the Sct-Cen I have also identified possible molecular cloud candidates at values of ℓ beyond the sample originally identified in Dame & Thaddeus (2011). The higher longitude molecular emission candidates can be seen in Figure 4.6 and they are listed in Table 4.1 - it is important to remember that these are are well beyond the original indications of Dame & Thaddeus (2011), but exist at a v_{LSR} sufficiently different from the Outer arm that in this model they can be described as independent features.

4.3 Common Resolution Mapping (CRM)

4.3.1 The CRM Process

Having resampled the original data velocity axis so that the velocities are centred on the chosen spiral feature, the data were projected from the original angular observations and re-gridded on to a map of constant linear scale. The degree to which convolution smoothes the data is dependant on the arm location's distance from the observer. So, for example, material at an arm's closest approach will be smoothed to a lesser extent than the material at further distances. Expressing the maps in terms of a uniform linear measurement forms a pseudo extra-Galactic view of the arm's structure. This process also changes the co-ordinate system, as touched on in the previous section but is defined below, to be in terms of the arm itself i.e. length along the arm (X) and also height out of the Galactic plane (Z). These linear maps will make the relative sizes of clouds across

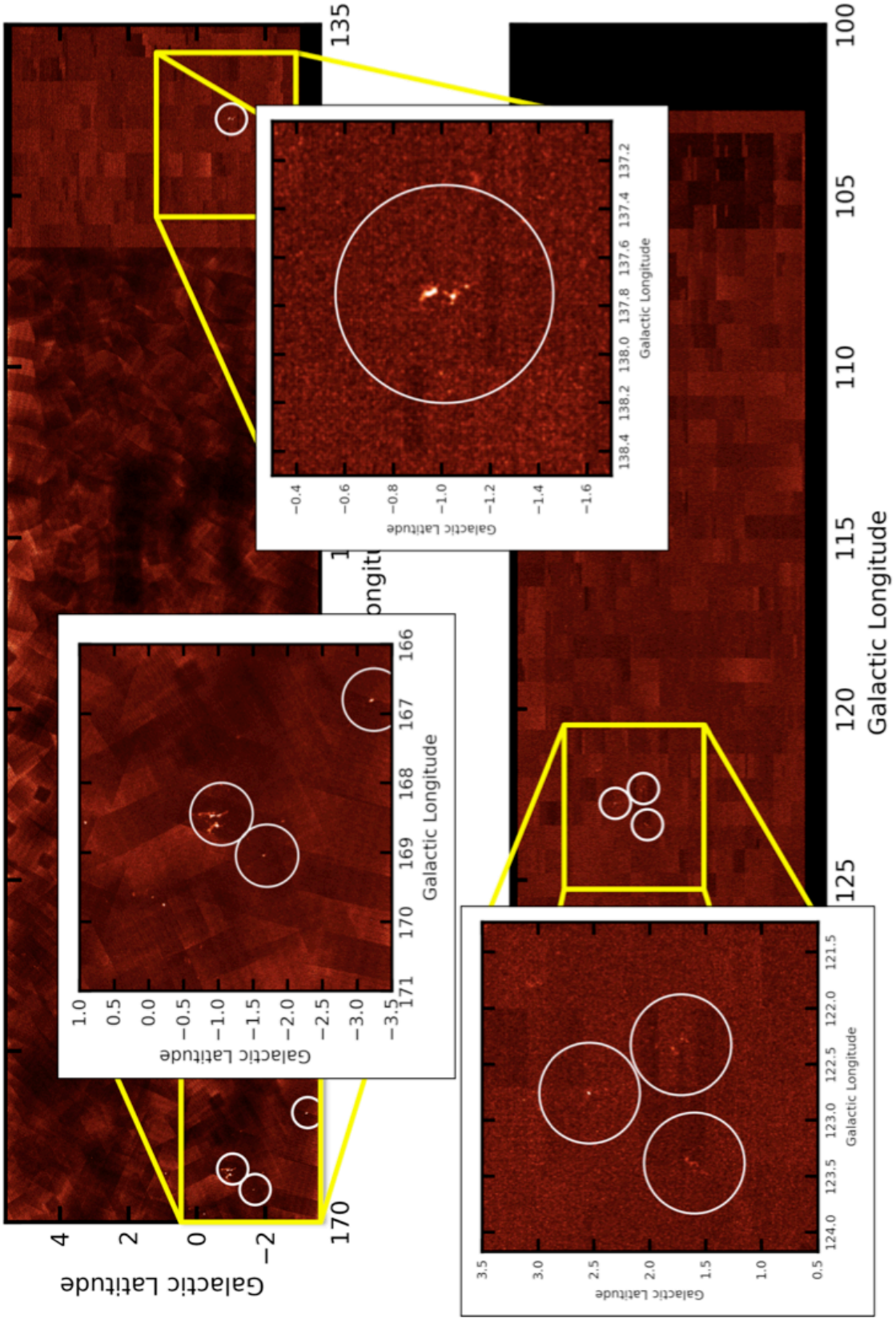

Figure 4.6: The Figure above shows a peak temperature map of the (ℓ, b) distribution of ^{12}CO within ± 10 km s^{-1} of kinematically modelled Scutum-Centaurus arm. The data are taken from the EX-FCRAO survey with the associated emission included in the cut-outs.

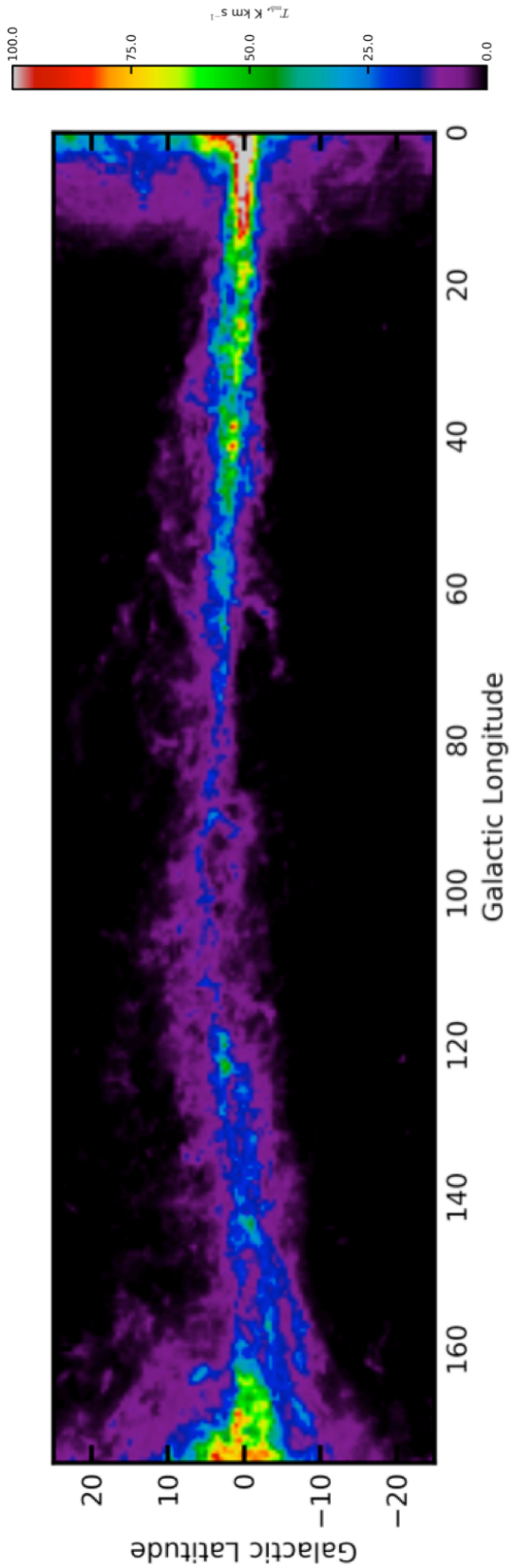

Figure 4.7: A peak temperature outer Sct-Cen ACM HI data, taken from the LAB HI. This is a peak temperature, T_{MB} (0→100 K km s^{-1}) through ± 10 km s^{-1} of the kinematically modelled Sct-Cen arm centre.

the whole arm be comparable in linear size with no angular observational biases. The maximum achievable linear resolution for each of the surveys, based on their angular resolution is shown in Figure 4.8.

The convolution is performed by applying a Gaussian smoothing kernel to the data, over a grid of varying angular size with arm distance - smoothing more distant objects out whilst not smoothing the closer material as much. The conversion of longitude and latitude to the new absolute system of X and Z - which are length along the arm, with 0pc co-incident with the anti-centre, varying inversely with ℓ - and height out of the plane of the Galaxy respectively. the change in X, dX, is obtained via calculating the differential of the arc-length for the logarithmic spiral spatial fit;

$$dX^2 = \left(r^2 + \left(\frac{dr}{d\theta}\right)^2\right).d\theta^2 \;\equiv\; (r^2 + (a_1 r)^2).\, d\theta^2 \tag{4.2}$$

From the relation between a_1 and ϕ_{pitch} from Equation 3.2;

$$dX^2 = (r^2.(1 + \tan(\phi_{pitch})^2)).\, d\theta^2 \;\equiv\; r^2.\left(1 + \frac{\sin^2(\phi_{pitch})}{\cos^2(\phi_{pitch})}\right).\, d\theta^2 \tag{4.3}$$

Via trigonometric identities;

$$dX = \frac{r.d\theta}{cos(\phi_{pitch})} \tag{4.4}$$

Since I have a functional form for the logarithmic spiral, I can explicitly find the values of arm azimuth, X;

$$X = \int_{\theta_1}^{\theta_2} \frac{r.d\theta}{\cos(\phi_{pitch})} \tag{4.5}$$

We define X =0 kpc to be coincident with ℓ =180°($\theta = \frac{\pi}{2}$) and varies inversely with ℓ. Therefore for a given value of theta, the arc-length, X, is obtained via;

$$X = \left[\frac{exp(a_0 + a_1.\theta')}{a_1.\cos(\phi_{pitch})}\right]_{\theta}^{\frac{\pi}{2}} \tag{4.6}$$

The displacement out of the Galactic plane, Z, is obtained via ;

$$Z = d_{arm}(\ell).\tan(b) \tag{4.7}$$

The routine which is used to smooth, convolve and convert the $\ell, b, \Delta v_{arm}$ data to the $X, Z, \Delta v_{arm}$ co-ordinate system, defined above, needs certain input parameters passed to it before the convolution can be completed. The main input quantities to be indicated before starting the convolution are; ΔL which is the desired target linear resolution to smooth the data to, θ_{res} is the angular resolution of the survey data input and θ_{eff} is the effective angular resolution at a distance d_{arm} of the linear resolution ΔL along a given line of sight.

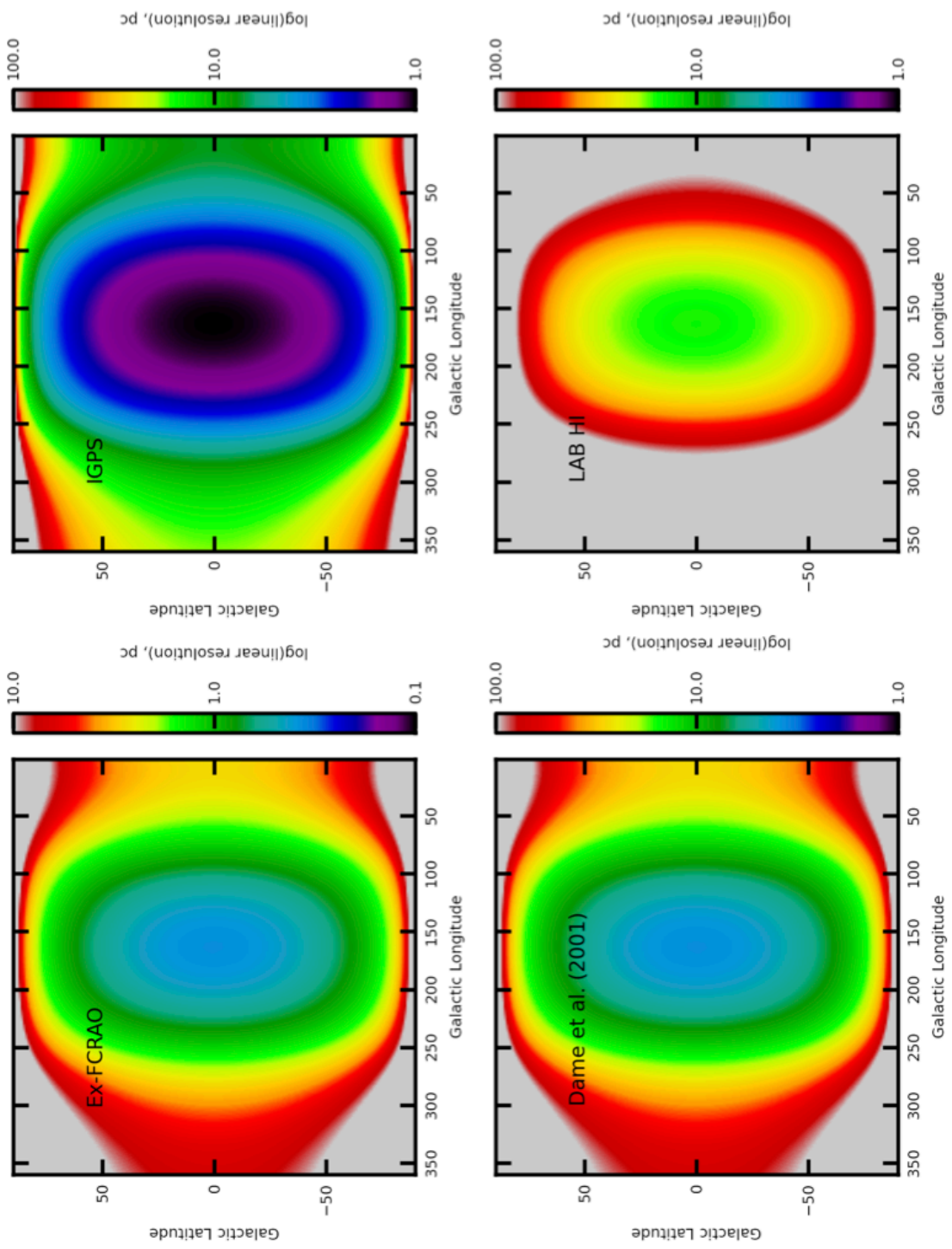

Figure 4.8: Colour maps showing the maximum achievable linear resolution for each of the surveys based on their angular resolution and the logarithmic fit to the Perseus arm. It should be noted that the logarithmic colour scale for the Ex-FCRAO is scaled differently than the other surveys, to reflect its higher angular resolution.

$$\theta_{fwhm} = \sqrt{\left(\frac{\Delta L}{d_{arm}(\ell)}\right)^2 - (\theta^2_{res})} = \sqrt{(\theta^2_{eff}) - (\theta^2_{res})} \tag{4.8}$$

$$\sigma = \frac{\theta_{fwhm}}{2\sqrt{2\ln(2)}} \tag{4.9}$$

The θ_{fwhm} in angular units is then converted to pixels by dividing by the bin-width of the input data-cube. This is used to form a grid centred on the (ℓ_0, b_0) and twice the θ_{fwhm} to give $\theta_{fwhm_{pix}}$. These parameters are then used to smooth out the input data to the linear resolution defined above, centred on the (ℓ_0, b_0) within the convolution grid corresponding to each (X, Z) point in the output . The convolution routine uses a 2D gaussian function to smooth over N x θ_{fwhm}, I take N=2 and enforcing a minimum source convolution grid of 13×13 pixels.

Due to the resampling of the velocity axis, each of the lines of sight may not contain a complete spectra or may even be blank entirely. To stop incomplete spectra or null values having an influence on the smoothing and causing erroneous contributions to the weight, before the input data are submitted to the routine each of the spectra are checked to make sure that each line of sight is non-zero for at least 90 percent of the spectral line of sight.

4.3.2 Perseus Spiral Arm

The CRM maps for Perseus above 10kpc are to be viewed with caution since the Perseus arm definition in these region is confused with emission from the more nearby Sgt and Sct-Cen arms.

These new data are are not subject to the distance biases mentioned earlier, i.e. the mass-per-pixel complications which arise to using angular spectral data, in that the cloud/clump sizes are now all in a scheme where their relative sizes are directly comparable to one another. The common resolution maps smoothed to a constant linear resolution of 10 pc are shown as X, Z projection in Figure 4.9 and 4.10. The $X, \Delta v_{arm}$ projection of the CRM data is shown as the bottom panel in Figure 4.1. It shows that in the outer Galaxy a large spread in ℓ does not correspond to an equally large spread in X, almost 100° of ℓ is contained within a couple of kpc, this can be more quantifiably seen in Figure 4.11.

4.3.3 Outer Spiral Arm

Having extracted the Outer arm as a single structure from the data I can perform the common resolution mapping routine, I convert the ℓ, b input data into CRMs. As with Perseus I use the same modified 2D gaussian function to smooth over two FWHM (θ_{fwhm}) and forcing the convolution grid to be a minimum of 13×13 pixels. How each of the parameters; ℓ, X and R_{out} vary with one another is shown in Figure 4.12 and the maximum achievable linear resolution for each of the surveys are shown in Figure 4.19.

The CRM data which are presented here are the half-beam (nyquist) sampled ΔL=20pc maps over a - maximum - range; -15 kpc $< X <$30 kpc , $|Z| <$5 kpc . The source data used here is the angular higher resolution Ex-FCRAO ^{12}CO data (supplemented by the CfA composite at wider latitudes and extended longitudes) and IGPS HI (supplemented at wider latitudes and

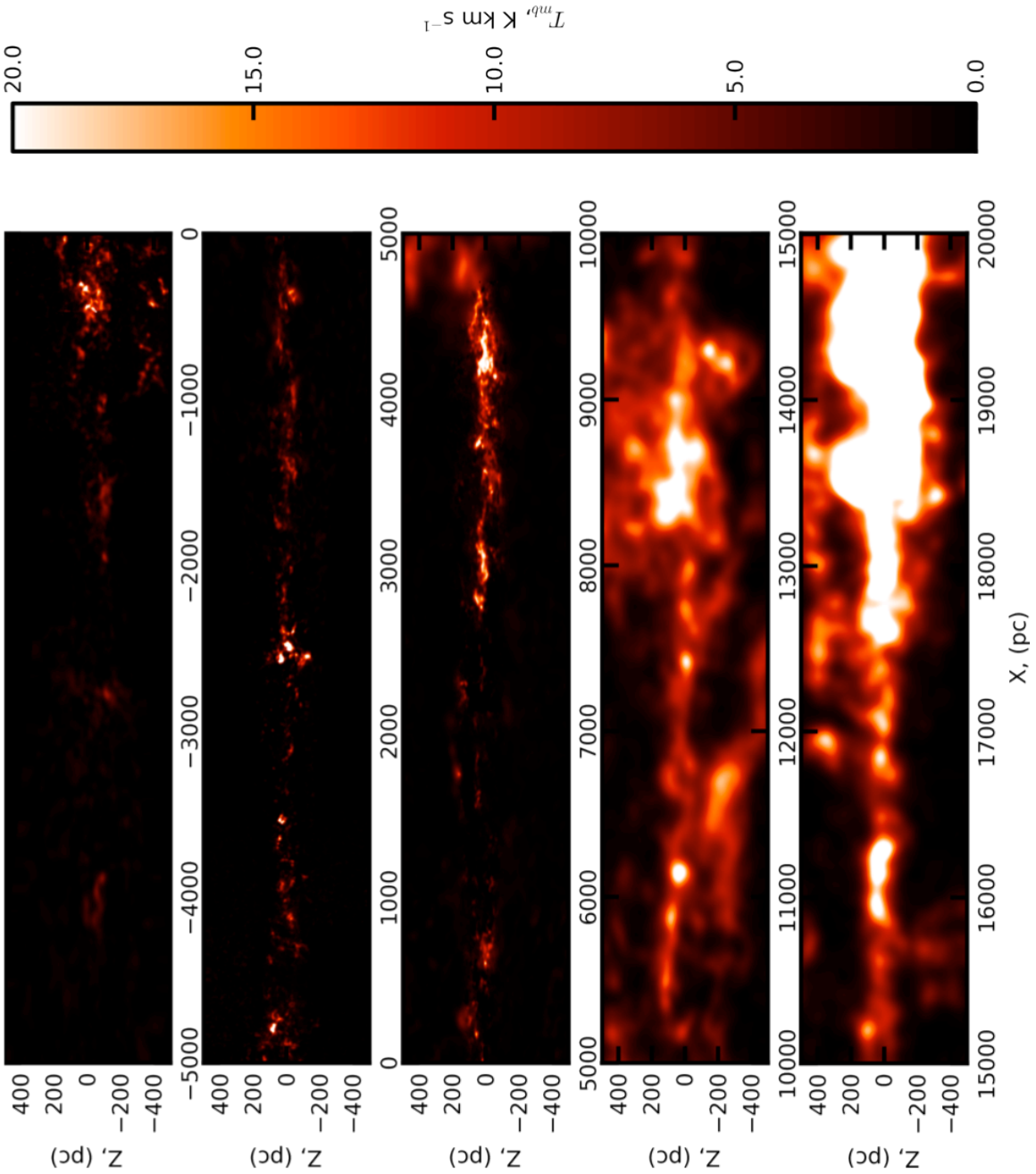

Figure 4.9: An integrated temperature map of the Perseus arm CRM data, smoothed to a common linear resolution of 10.0pc, for the Ex-FCRAO ^{12}CO data integrated through ± 10 km s^{-1}, supplemented at higher latitudes by ^{12}CO from the Dame et al. (2001) survey. At X >18 kpc the map becomes saturated due to *local* emission contaminating the kinematic window.

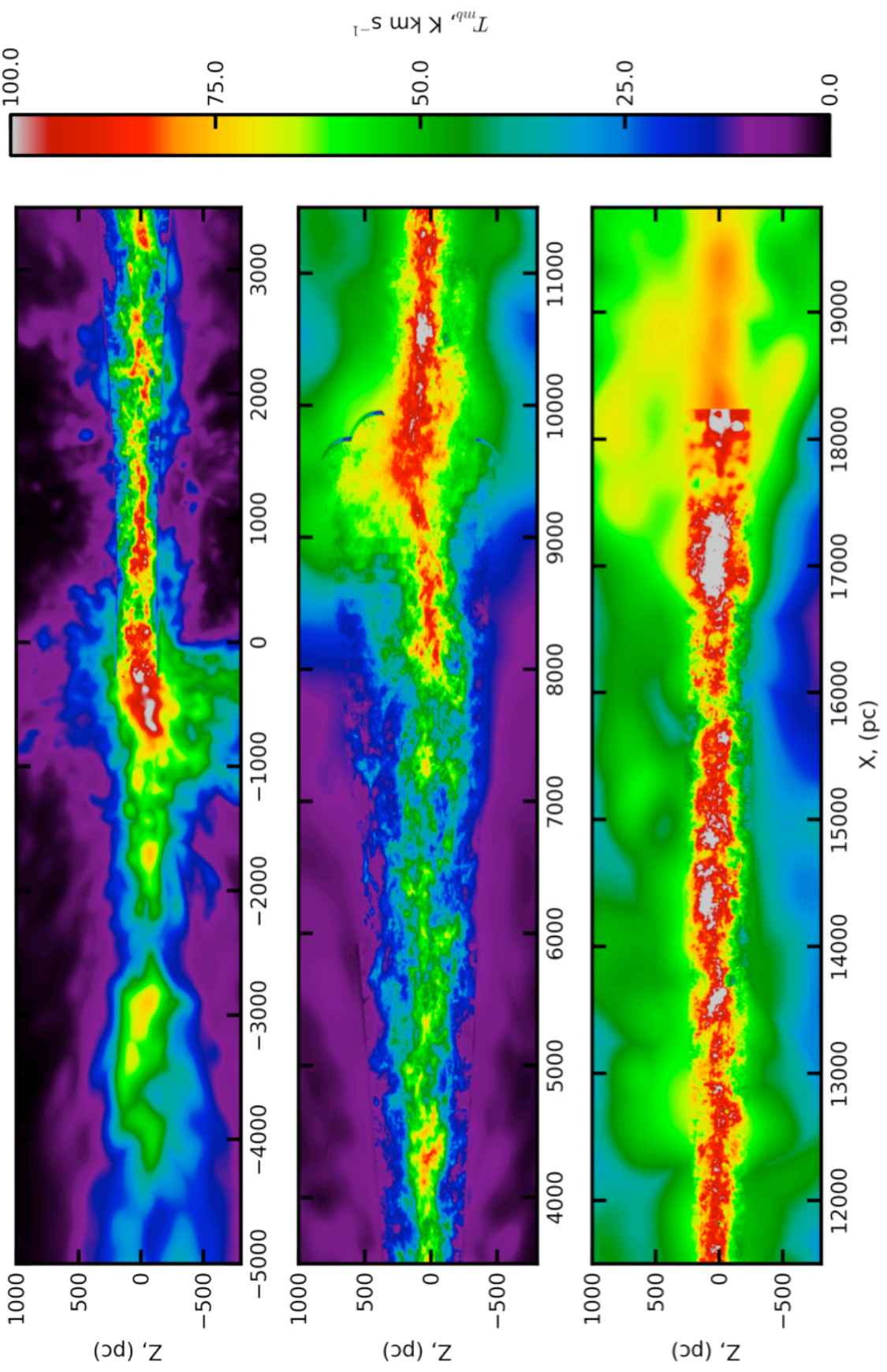

Figure 4.10: A peak temperature map of the Perseus arm CRM data, smoothed to a common linear resolution of 10 pc, for a sample of the LAB HI data inset with the IGPS.

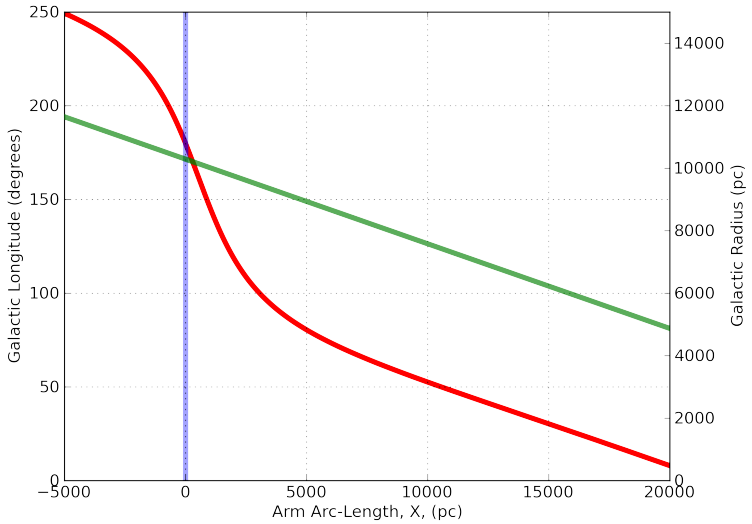

Figure 4.11: The red line shows how the value of X varies with Galactic Longitude, the blue vertical line shows the position of the $[X = 0 \text{ pc} : \ell = 180°]$ crossover and the green line shows how Galactic Radius varies with X.

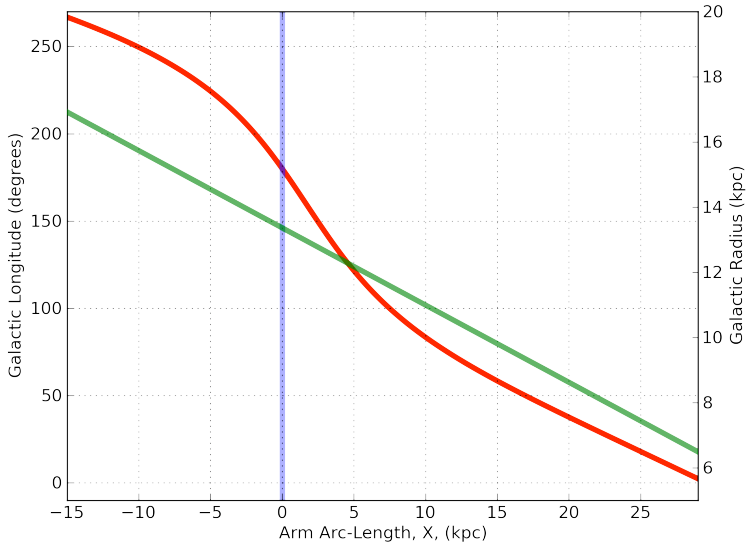

Figure 4.12: The Figure above shows the relation between arc-length, X, and longitude, ℓ, (in red). Also between arc-length, X, and Galactocentric Radius, R, (in green).

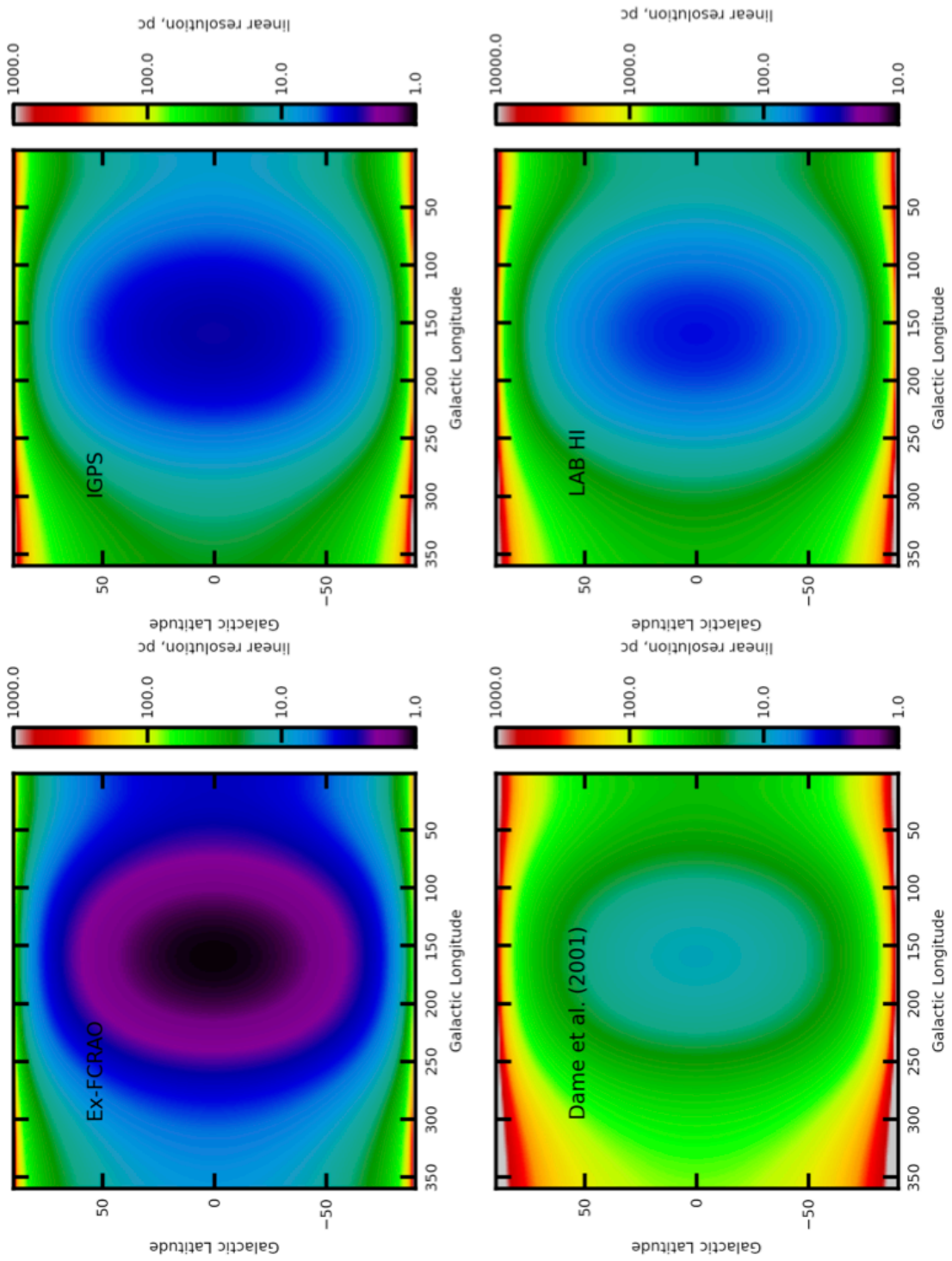

Figure 4.13: Maximum achievable linear resolution at the distance of the Outer arm depending on the angular resolution of the survey.

extended longitudes by the LAB HI survey). Occasionally the LAB HI is shown on its own to more easily show contiguous features, like, for example - Figure 4.5. From the CRM maps of ^{12}CO (Figure 4.14) and HI (Figure 4.15) I define the Outer arm to be unambiguous between 1 kpc $< X <$25 kpc .

4.3.4 Outer Scutum-Centaurus Spiral Arm

The CRM for the outer Sct-Cen arm is shown in Figure 4.20 over the I, II and the start of the III Galactic quadrants. The model predicts that the outer Sct-Cen arm has a span in X of 40 kpc in QI and QII, which is twice that of the Perseus arm due to its much further distance. The Z distribution is similar to that of the Outer arm - i.e. tracking the warp - with a contiguous structure across its length. The only deviation from this continuous band of emission is in the region of X =10 kpc where the arm appears to become more filamentary in nature, after which, it then returns to being a continuous band of emission in the region of the anti-centre (ℓ=180°; X =0 kpc) - probably due to the outer Sct-Cen and Outer arms becoming blended in velocity as they traverse this region. It is unlikely that the outer Sct-Cen exists much beyond the anti-centre if it is indeed an extension of the inner Scutum arm. Skipping ahead to the plane-centric-maps - Figure 4.23 - beyond the anti-centre the emission of the Sct-Cen drops dramatically, though one may say that this is only because the model does not describe its structure correctly. However, looking at the ℓ-v_{LSR} diagram of the Galaxy and its kinematic model it is more likely that either; the Sct-Cen arms remain blended in v_{LSR} *or* the Sct-Cen dissipates in this region since even at ℓ=190°, the outer Sct-Cen is at almost R = 19 kpc .

4.4 Spiral Arm Mid-plane Function Mapping (AMF)

The low resolution maps are shown here as a proof of concept, the full analysis of these AMF data can be seen in Chapter 5.

4.4.1 The AMF Process

The AMF is similar to the ACM process, but in addition to making the data arm-centric in velocity, the data are centred on the mid-plane of the arm. Thus making these maps completely arm-centric in all dimensions. Therefore, as with the velocity, a position of the arm mid-plane is used as the reference point with the X, Z being transformed into X, Z_{arm}. The Z_{arm} transform is calculated via;

$$Z_{arm} = Z - Z_{midplane}(X) \tag{4.10}$$

Where $Z_{midplane}(X)$ is the position of the arm's mid-plane as function of length along the arm, X. $Z_{midplane}(X)$ is calculated over $\pm$ 2 $\times$ σ_Z (HI).

The effect of remapping of the maps to be completely arm-centric - i.e. in both velocity and displacement from the spatial arm-centre - will be greater on the outer most arms, since the Perseus arm resides mainly in the plain so the re-centring will have little effect. It will also allow for easier identification of arm-structure in the X–v_{LSR} plane since the arm emission will be compressed in

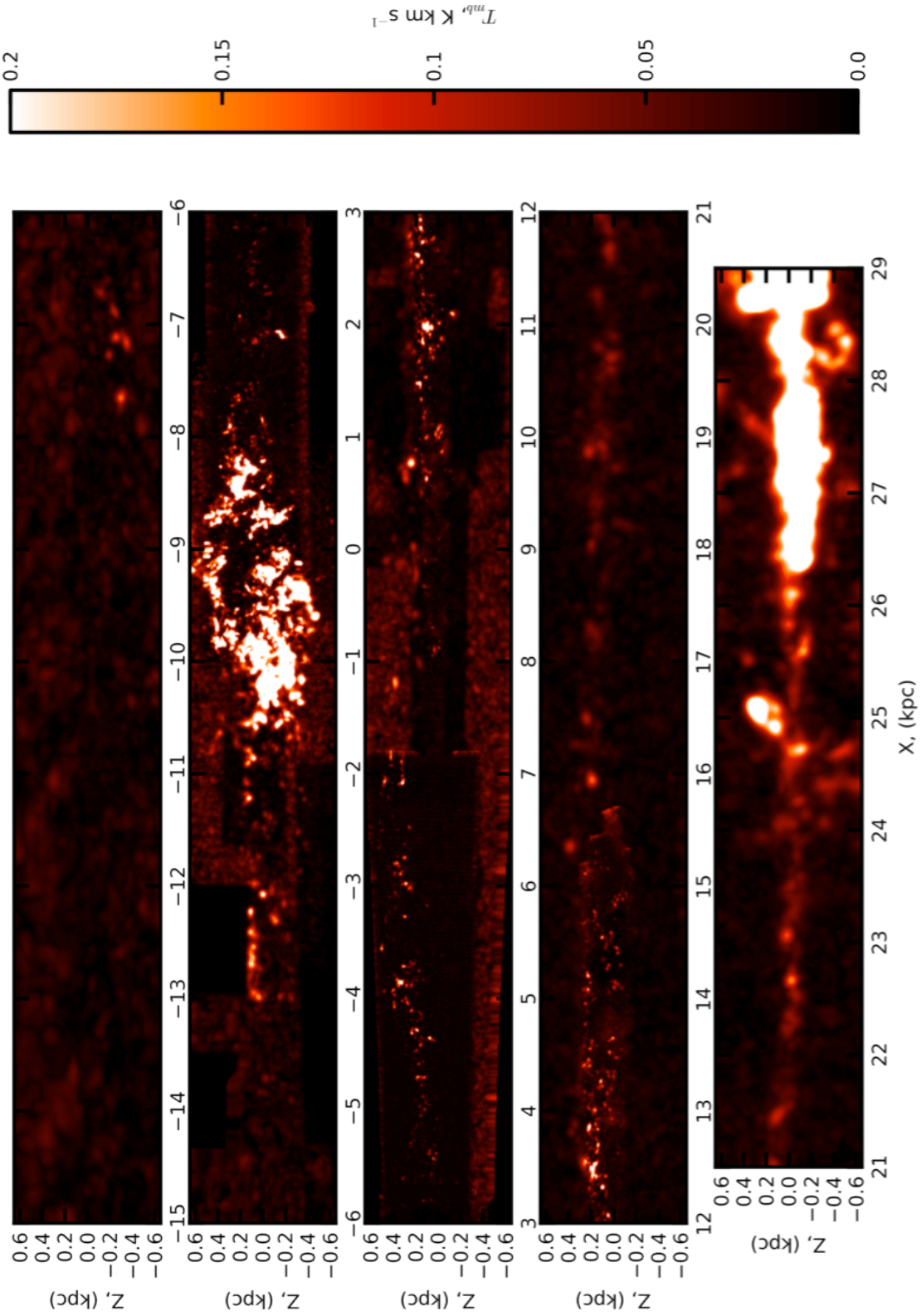

Figure 4.14: Peak temperature, 0.0 km s^{-1} →0.2K km s^{-1} , CRM map of the ^{12}CO defined to be within the Outer spiral arm. ΔL=20pc, data taken from ExFCRAO and CfA composite ^{12}CO surveys. At X >26 kpc the map becomes saturated due to *local* emission contaminating the kinematic window

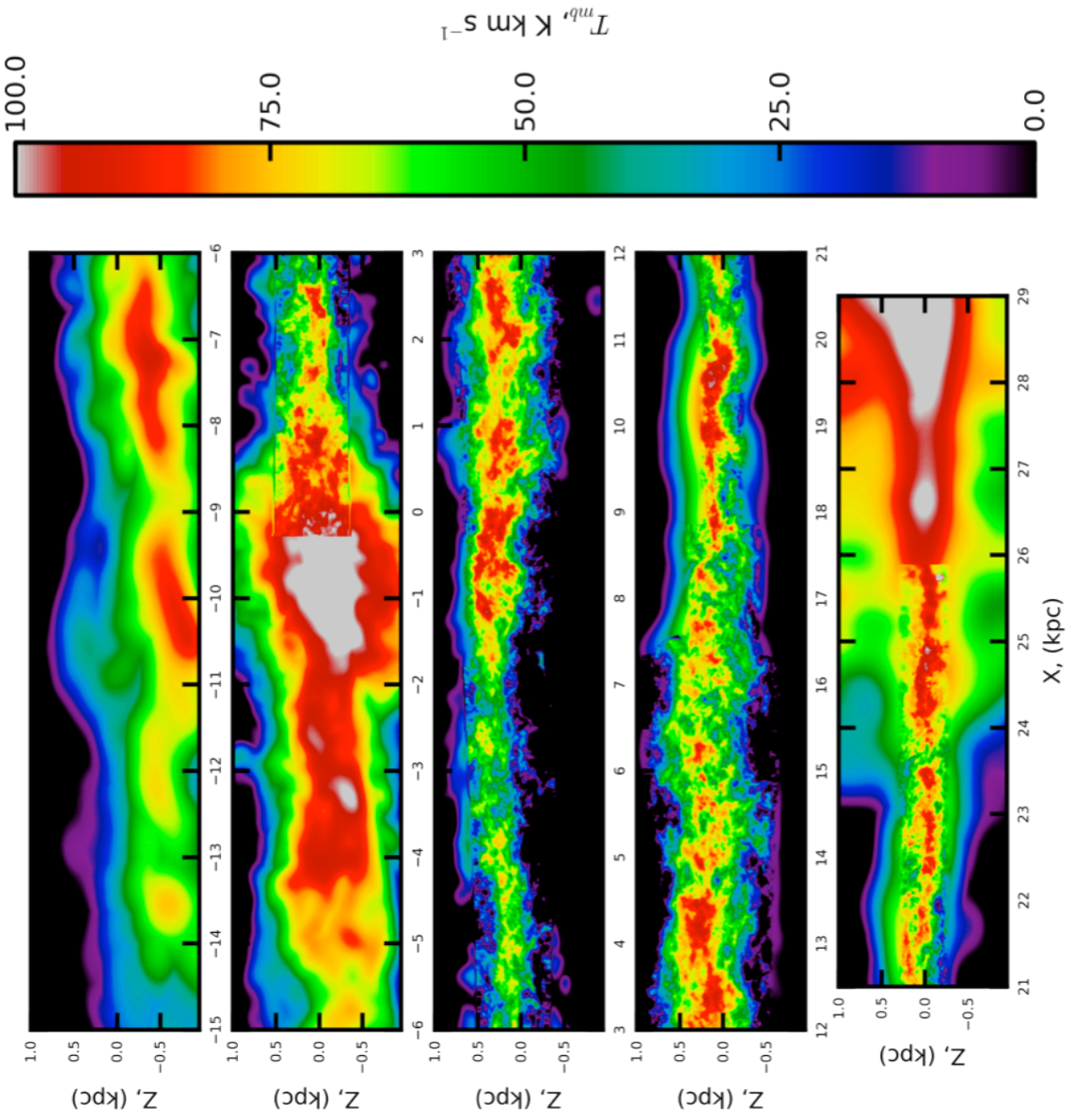

Figure 4.15: Integrated summed temperature CRM map of the HI defined to be within the Outer spiral arm. ΔL=20pc, data taken from IGPS (inlaid) and LAB HI surveys.

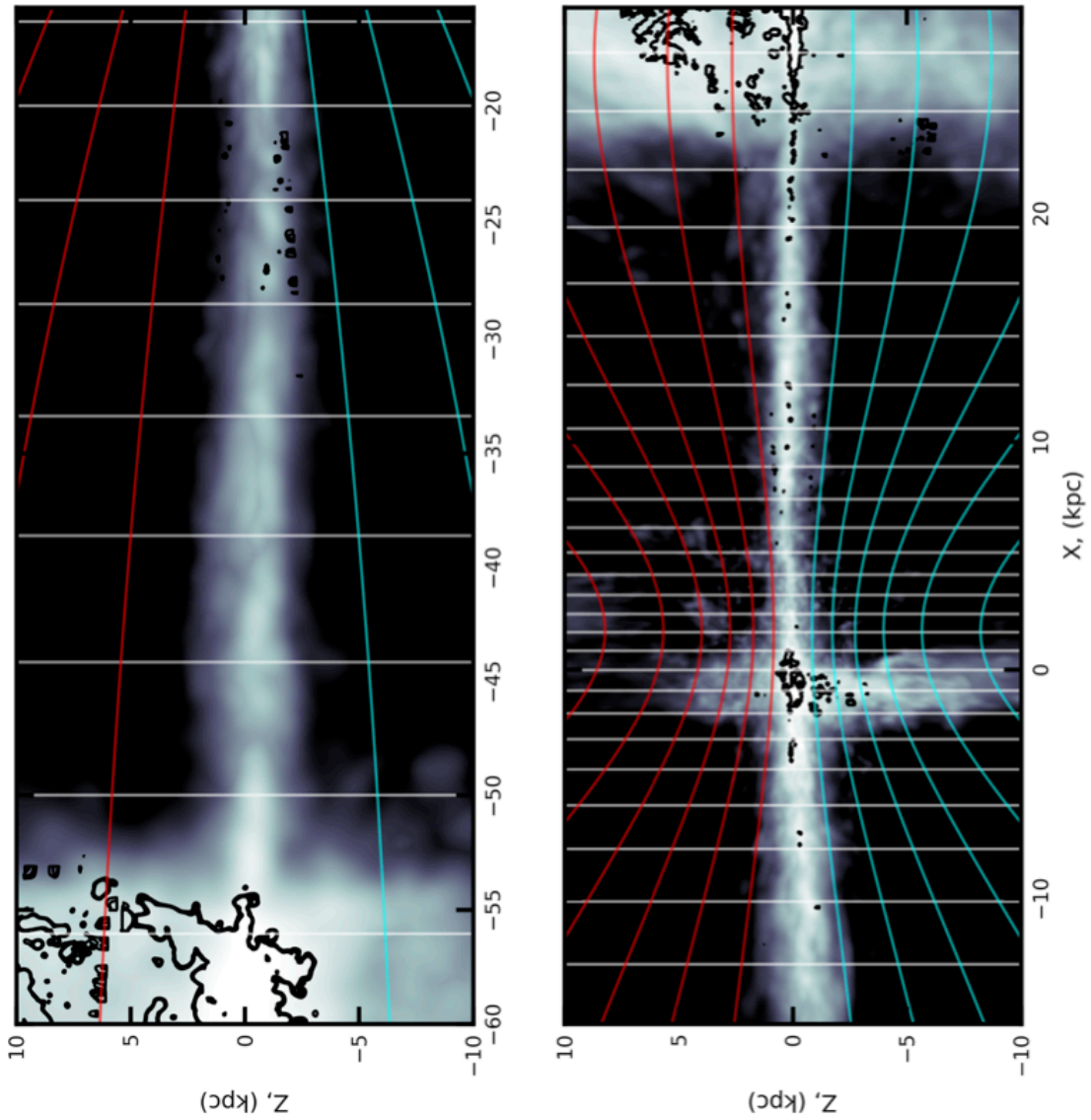

Figure 4.16: A grey-scale logarithmic peak temperature, 10^{-2}K km s^{-1} $\rightarrow 10^{2}$K km s^{-1} , CRM map of the HI defined to be within the Outer spiral arm over all four Galactic quadrants. The CRM resolution is ΔL=500pc with data taken from the LAB HI surveys. The white - vertical - contours show lines of constant ℓ, spaced at 10°intervals. The red and cyan contours show lines of constant positive- and negative- b respectively, spaced at 10°intervals from $|b|$ <60°. The black contours show the ^{12}CO emission from the CfA composite survey over this range.

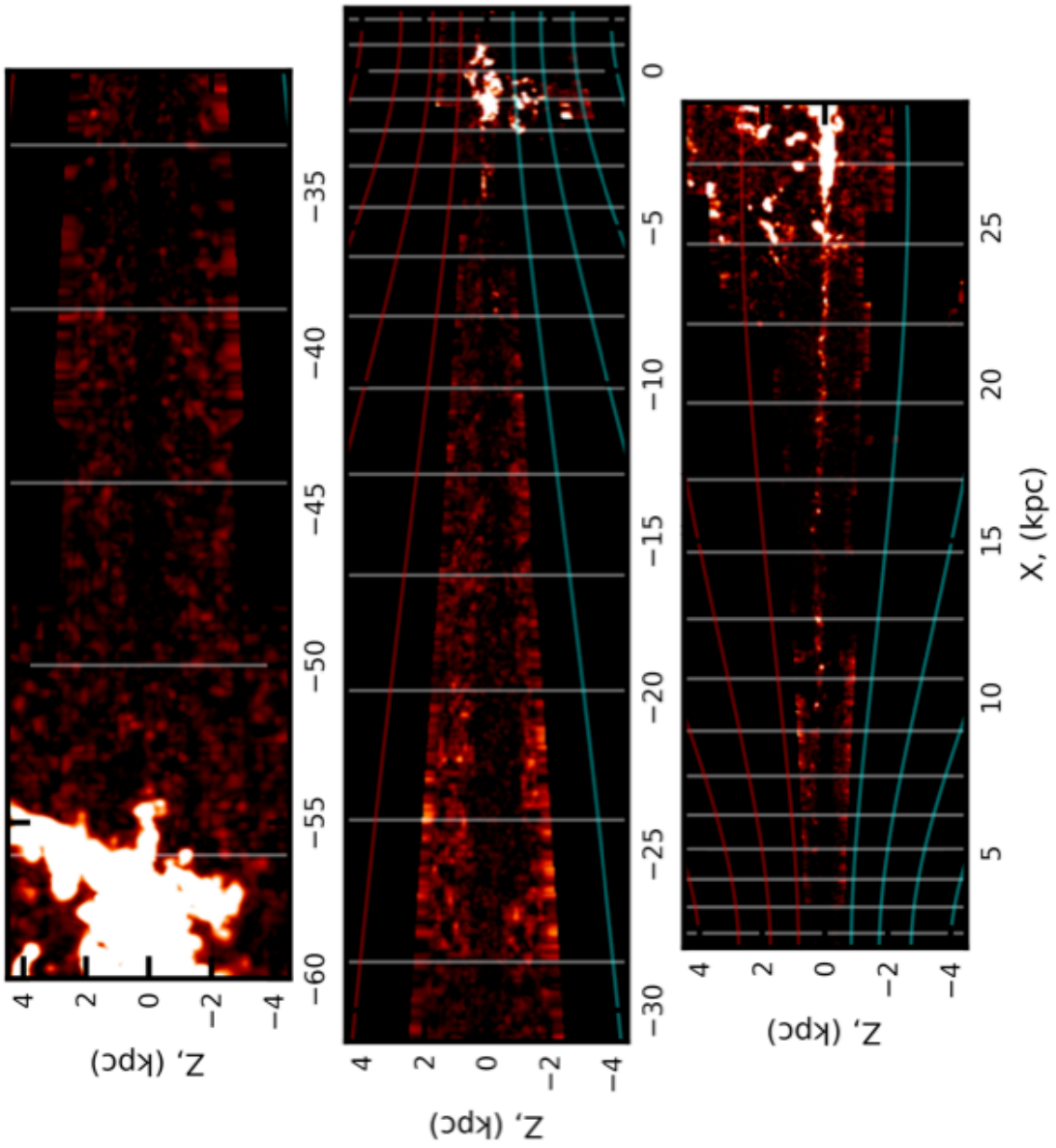

Figure 4.17: Figure above shows a logarithmic peak temperature, 10^{-2}K km s^{-1} $\rightarrow 10^{2}$K km s^{-1} , CRM map of the ^{12}CO defined to be within the Outer spiral arm over all four Galactic quadrants. The CRM resolution is ΔL=500pc with data taken from the CfA Composite ^{12}CO survey. The white - vertical - contours show lines of constant ℓ space 10°< ℓ <350°spaced at 10°intervals. The red and cyan contours show lines of constant positive- and negative- b respectively, spaced at 10°intervals from $|b|$ <60°.

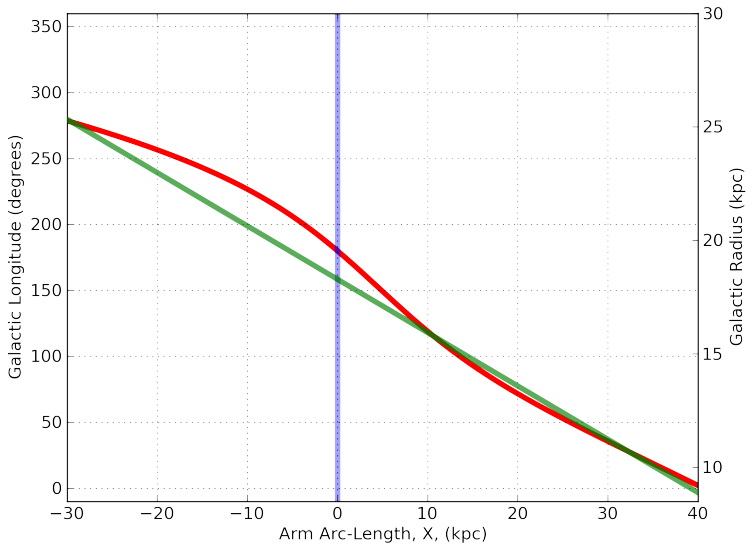

Figure 4.18: The Figure above shows the relation - for the outer Sct-Cen arm - between arc-length, X, and longitude, ℓ, (in red). Also between arc-length, X, and Galactocentric Radius, R, (in green).

dZ. All the maps presented here are expressed over the same temperature range and in the *spectral* colour scheme so that one map compare the relative amounts of emission within each arm. The subsequent sub-sections provide a brief overview of the the map pertaining to each spiral arm. The analyses of these maps, unlike the ACM and CRM data are presented in Chapter 5.

4.4.2 Summary of Spiral Arm AMF Data

The Perseus arm - Figure 4.21 - as was suggested in the opening paragraph of this section, has not significantly modified the AMF data emission. The Perseus arm's CRM showed that the emission is approximately coincident with the Galactic mid-plane and this is reflected in the AMF map with the deviation of the emission about the arm's mid-plane being fairly unmodified when compared to its variation about the Galactic mid-plane. Observationally, the emission of the Perseus arm appears to be confined to ±1kpc of the arm mid-plane (full analysis later) which is the most compact of the three arms presented here.

The Outer arm - Figure 4.22 - is modified more that the Perseus arm was with respect to its displacement from the Galactic mid-plane. Comparing the Outer arm AMF to its CRM (Figure 4.15 and 4.17), the overall structure of the arm now is significantly more planar than in its Galactic plane-centric representation. The effect of the Outer arm beginning to track the warp at certain regions of X caused the arm to track at higher latitude, which in-turn implies higher Z. With the exception of the centre and anti-centre regions, the ΔZ_{arm} appears to be well confined to the Z_{arm}=0 kpc plane with the material out of the plane being due to kinematic contamination of distance ambiguous emission at further distances.

Finally considering the out Sct-Cen arm - Figure 4.23 - is the most affected by the AMF routine since it is at a much further distance (Figure 4.12). As with the Outer arm, the majority of

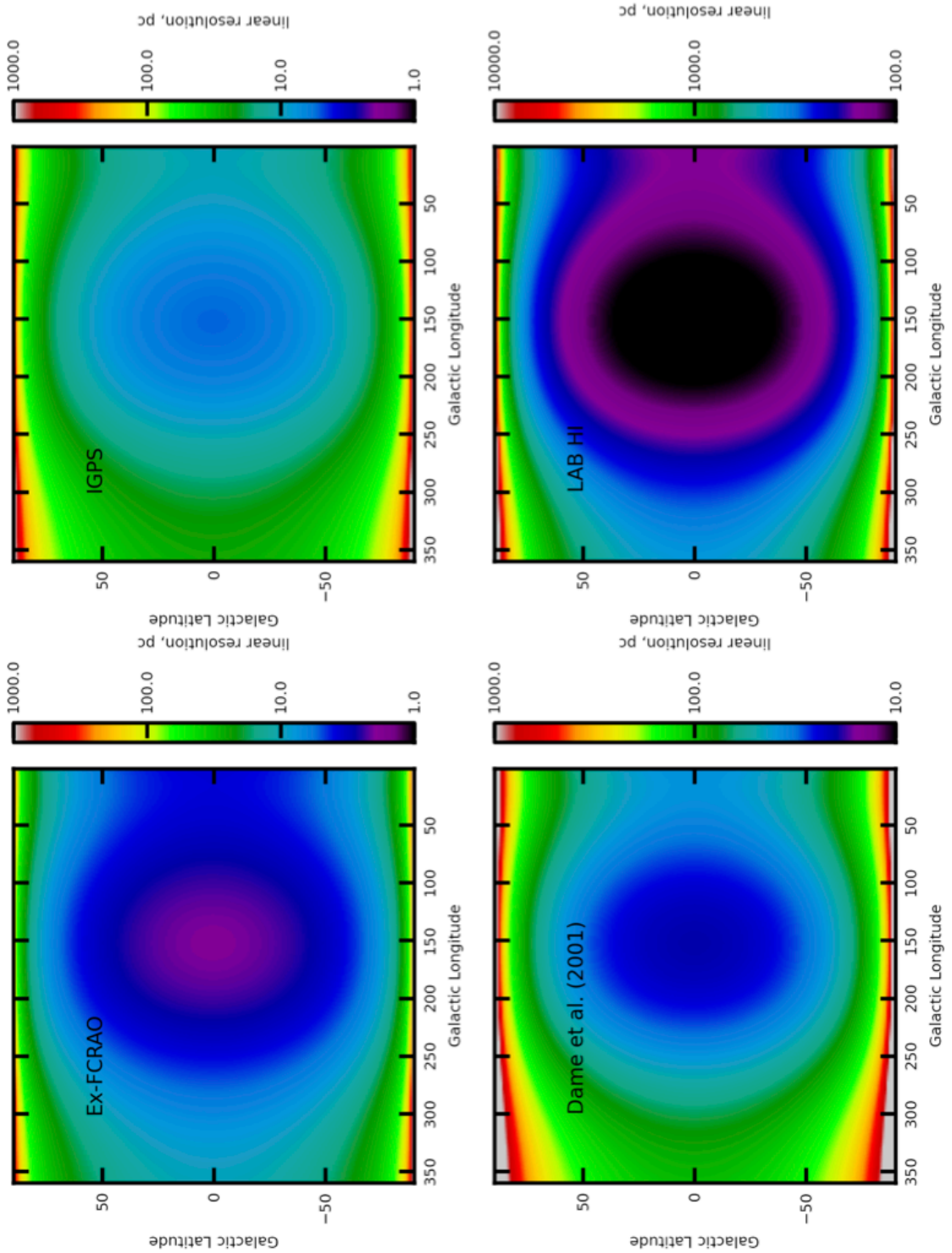

Figure 4.19: Maximum achievable linear resolution at the distance of the outer Sct-Cen arm depending on the angular resolution of the survey.

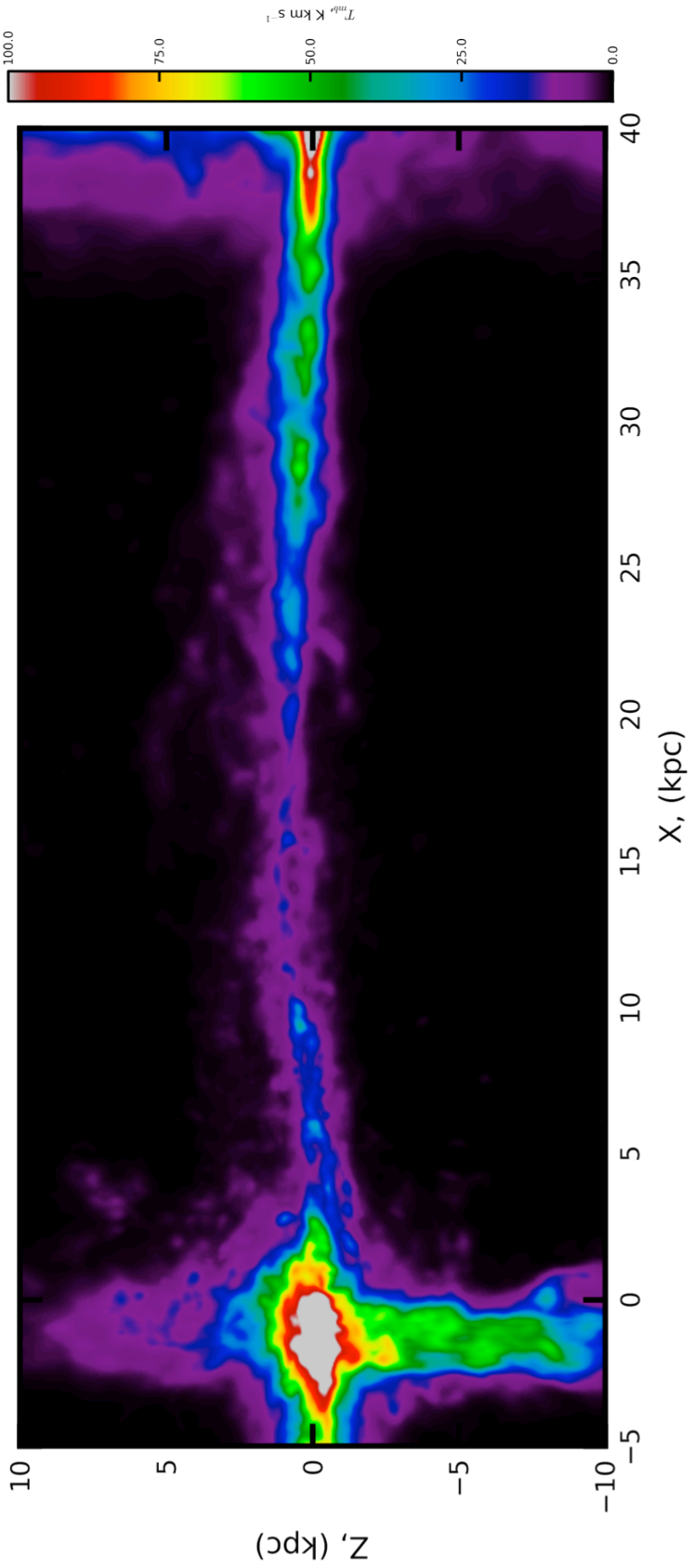

Figure 4.20: Figure above shows a peak temperature, 0K km s^{-1} →100K km s^{-1} , CRM map of the HI defined to be within the Outer Sct-Cen spiral arm over Q I, II & III Galactic quadrants. The best CRM resolution achieved is ΔL=100pc with data taken from the LAB HIsurvey.

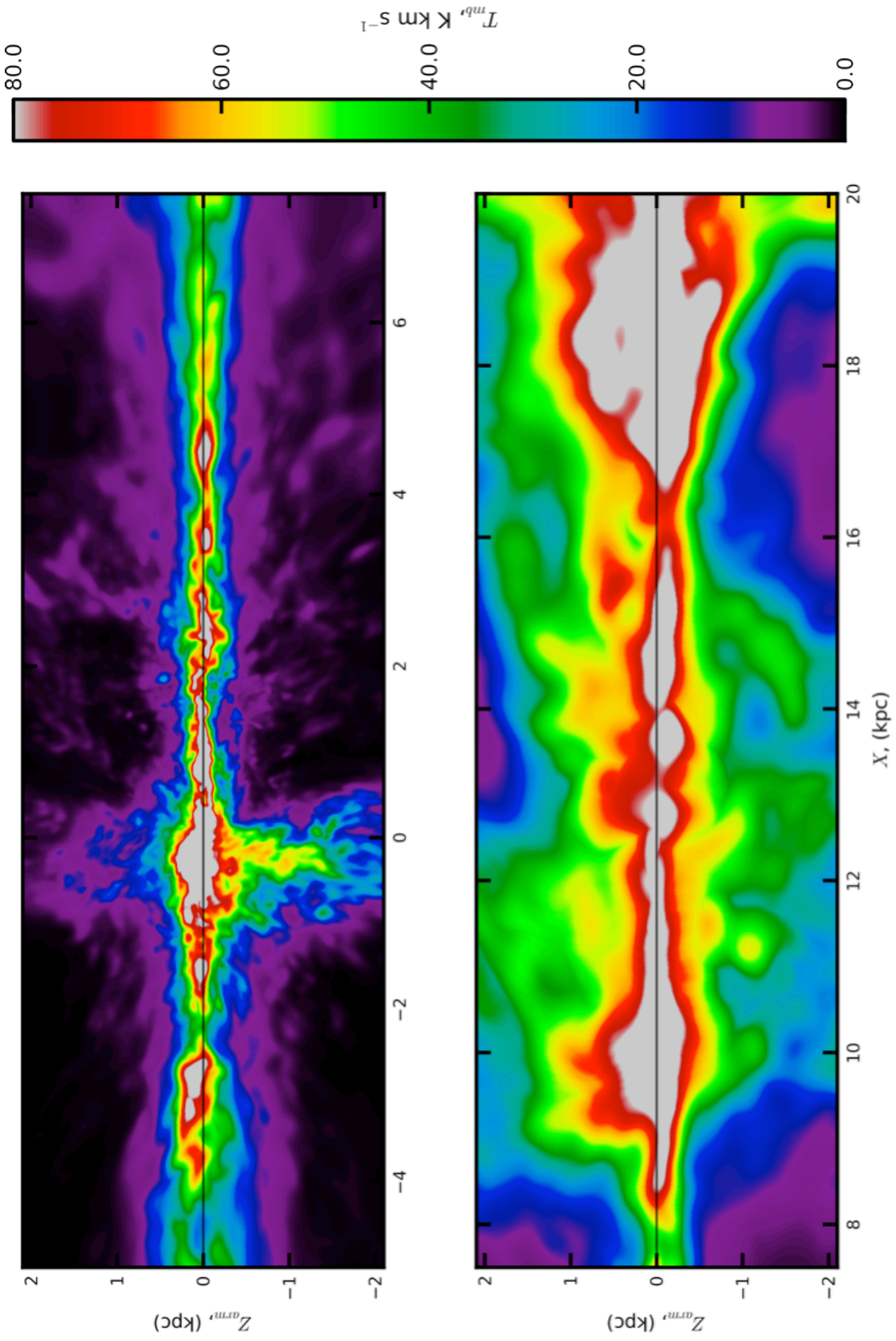

Figure 4.21: Figure above shows a peak temperature, 0K km s^{-1} →80K km s^{-1} , AMF map of the HI defined to be within the Perseus spiral arm over Q I, II & III Galactic quadrants. The centre of the arm is shown as the black horizontal line.

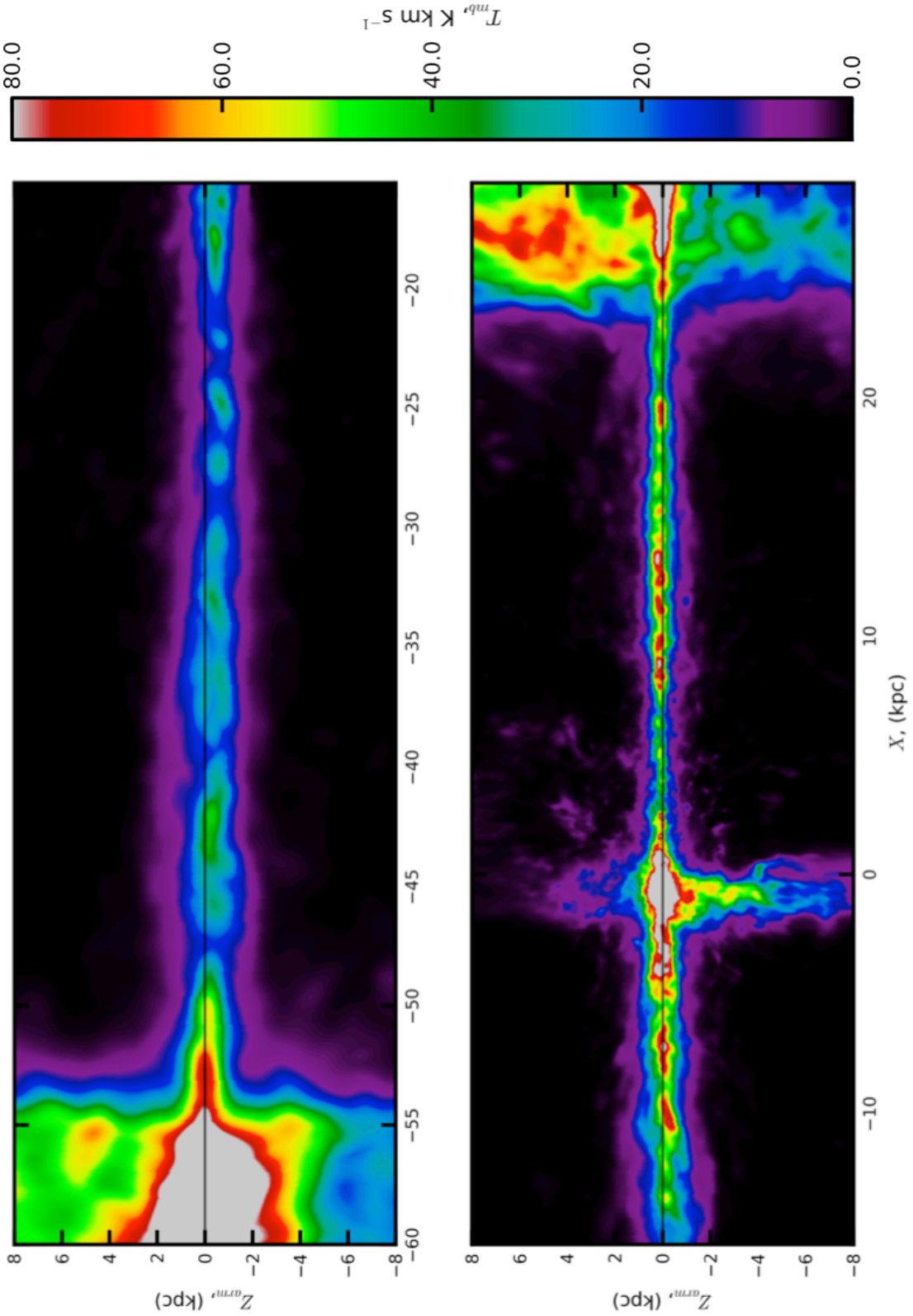

Figure 4.22: Figure above shows a peak temperature, 0K km s^{-1} →80K km s^{-1} , AMF map of the HI defined to be within the Outer spiral arm over Q I, II, III & IV Galactic quadrants. The centre of the arm is shown as the black horizontal line.

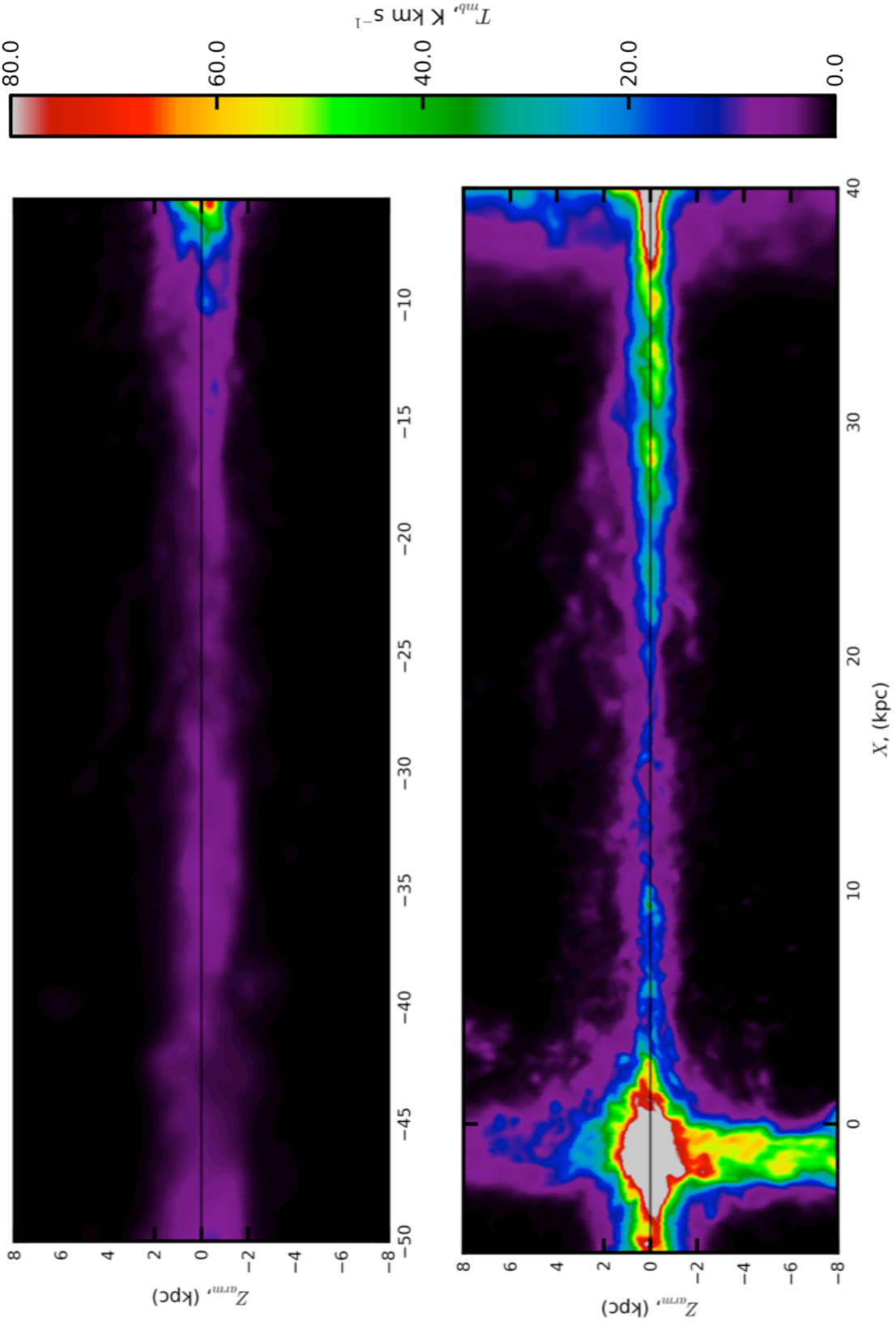

Figure 4.23: Figure above shows a peak temperature, 0K km s^{-1} →80K km s^{-1} , AMF map of the HI defined to be within the Outer Sct-Cen spiral arm over Q I, II, II & IV Galactic quadrants. The centre of the arm is shown as the black horizontal line.

the emission exists within the plane of the arm with little ΔZ_{arm} displacement about its centre.The break in emission at around X=20 kpc seems to suggest that this is where the Sct-Cen arm begins to diffuse and ceases to be a coherent structure and that the emission at more negative X at this point is more like to the linked to the Outer arm rather than the Sct-Cen. Since, within this region the outer arms begin to be kinematically blended and as such they are not well defined (see Figures 3.33 and 3.34).

4.5 Properties of the Spiral Arm Regions

4.5.1 The Perseus Arm

The Nature of the Perseus Arm

The ^{12}CO (Figure 4.9) and HI (Figure 4.10) CRM maps show that the Perseus arm emission is contained mainly within the plane of the Galaxy with fairly uniform latitude coverage over most of the arm. This implies that the material I have identified as Perseus arm is not contaminated with material from other distances - at different latitudes. In both HI and ^{12}CO maps, the velocity compression in the centre and anti centre regions is evident at $X\pm1$ kpc and though the local emission at X >10 kpc artificially increases the Z coverage of the Perseus arm, and excess of emission in the Galactic plane is still observable - though the degree to which this emission is related to Perseus is difficult to quantify.

As can be seen in the CRM Figures (4.9 & 4.10), the height of the Perseus arm remains relatively confined to the plane at approximately ± 150 pc around the perceived Galactic plane. For this work, the *full-width-half-maximum* (FWHM) of a Gaussian fit to the vertical distribution of emission for an arm map is taken as a measure of the scale-height of a spiral arm. For the data as a whole, it is possible to see the scale height increase as one enters the the inner Galaxy since the local emission tends to dominate the observer's line of sight. From the CRM data, the Perseus arm material tends to reside mainly within the plane of the Galactic disc and doesn't appear to be affected by the Galactic warp. Looking at the scale height for the arm as a whole, the HI appears to peak at higher Z than the ^{12}CO and also has a more expansive scale height distribution. This perhaps reflects is large scale nature over the clumpy nature of CO in the observational context. But this is obvious even in the normal CRM maps without the the dispersion calculations, the maps of ^{12}CO reflect the emission being fairly concentrated about it's mean, Z_o.

To compare the HI and CO emission in the 10pc maps, I produced surface-density plots for the complete CRM maps from -5kpc→20kpc in X for both the molecular and atomic components of the arm, the traces can be seen in Figure 4.29. The arm moves to the inner Galaxy, the $\frac{Atomic}{Molecular}$ surface-density ratio decreases, due to HI being more widely distributed in the outer Galaxy and the molecular content of the outer Galaxy being lower than the inner. I am able to over-plot the CO on the HI data to observe the correlation between the atomic and molecular components of the ISM. Previous works looking into the molecular-atomic gas relation in the Large Magellenic Cloud (Fukui et al. 2009) found that the velocity-integrated emission of CO and HI tended to track one another; i.e. the CO emission tended to be located towards the peaks in the HI component.

Our maps reflect these findings, with the ^{12}CO emission being located within HI maxima in the outer galaxy, and becoming more evenly distributed at larger values of X (lower ℓ).

Perseus Arm Velocity Dispersion - σ_{vel}

I calculated the σ_{vel}, about the kinematic arm centre of the molecular component of the Perseus arm about its centre. $\sigma_{vel}^{molec.}(X_{1.0}^{8.0}$ kpc)=8.37±0.01 km s^{-1} . I also calculated the velocity dispersion for the HI to be; $\sigma_{vel}^{atomic.}$(X$_{1.5}^{8.0}$ kpc) = 18.84±0.02 km s^{-1} . The molecular component is comparable with the inter-cloud dispersions on both Galactic (Stark & Brand 1989, 7.8±0.6 km s^{-1}) and extra-galactic (Walsh et al. 2002, 8.9±2.2 km s^{-1}) scales - it is also supported by Milky Way-like model (Tasker & Tan 2009, ≈10.0 km s^{-1}) observations. However, it is important to mention that the Walsh et al. (2002) study did not take into account the contributions of the internal cloud dispersions when calculating this value (Wilson et al. 2011).

Perseus Arm Scale Height & Mass

To obtain a more quantitative fit to the arm's scale height, I fit a single Gaussian to the data over 1-8kpc of X (excluding the confused regions) to ^{12}CO (Ex-FCRAO) and a combination of two one-dimensional gaussians to HI (LAB) mapping the thin and thick components of the gas, see Figure 4.26 and 4.28 respectively. The values for the Gaussian fits to the data can be seen in Figures. The scale heights and peaks of emission, implies that the majority of the Perseus arm material does stay in the plane of the Galaxy in both HI and ^{12}CO . Using the Gaussian fits I calculated the scale height and the mass of material for the atomic and molecular components across the 1-8 kpc range. I calculate the mass of the arm by converting the peak T_{mb} - in K km s^{-1} - within a Z_{FWHM} (i.e. a scale height) of the mean position of the arm in Z, to a mass expressed in M$_\odot$. I found the molecular component has $Z_{FWHM}^{molec.}$ =121.85±1.22 pc and has an arm mass of $M_{arm}^{molec.}(X_{1.0}^{8.0}$ kpc) = 5.68x10^{6}M$_\odot$ whereas the two-component atomic medium - fit well by two one-dimensional Gaussians - had Z_{FWHM}^{thin}(HI) = 213.07±0.71 pc, Z_{FWHM}^{thick}(HI) = 530.85±2.67pc and has a mass of $M_{arm}^{atomic.}(X_{1.0}^{8.0}$ kpc) 3.86x10^{7}M$_\odot$. If one were to look at the scale height profile in Figure 4.26 more closely; one may argue whether a two-component 1-D Gaussian fit to the ^{12}CO would be a more appropriate given the behaviour of the data, therefore, fitting two one-dimensional Gaussians to the ExFCRAO ^{12}CO , supplemented at higher Z by the CfA composite gives the scale height parameters to be; Z_{FWHM}^{thick}(H$_2$) =223.92±3.54pc, Z_{FWHM}^{thin}(H$_2$)=69.02±0.79pc, see Figure 4.27.

Perseus Arm Transverse Velocity Dispersion - σ_{vel_z}

The dispersion in velocity is not solely limited to the spectral velocity axis, there is also a component of the dispersion in the Z direction. The main assumption is that, for an arm to be supported to a scale height, Z_{FWHM}, through the internal pressure of its own internal turbulent motions - it would require a transverse dispersion of σ_{vel_z}. Using the method detailed in Lockman & Gehman (1991), of which the Z_{FWHM} calculated here is comparable to their determinations of individual component HI scale heights, one is able to equate the spectral and transverse dispersions in velocity, hence obtaining a value for σ_{vel_z};

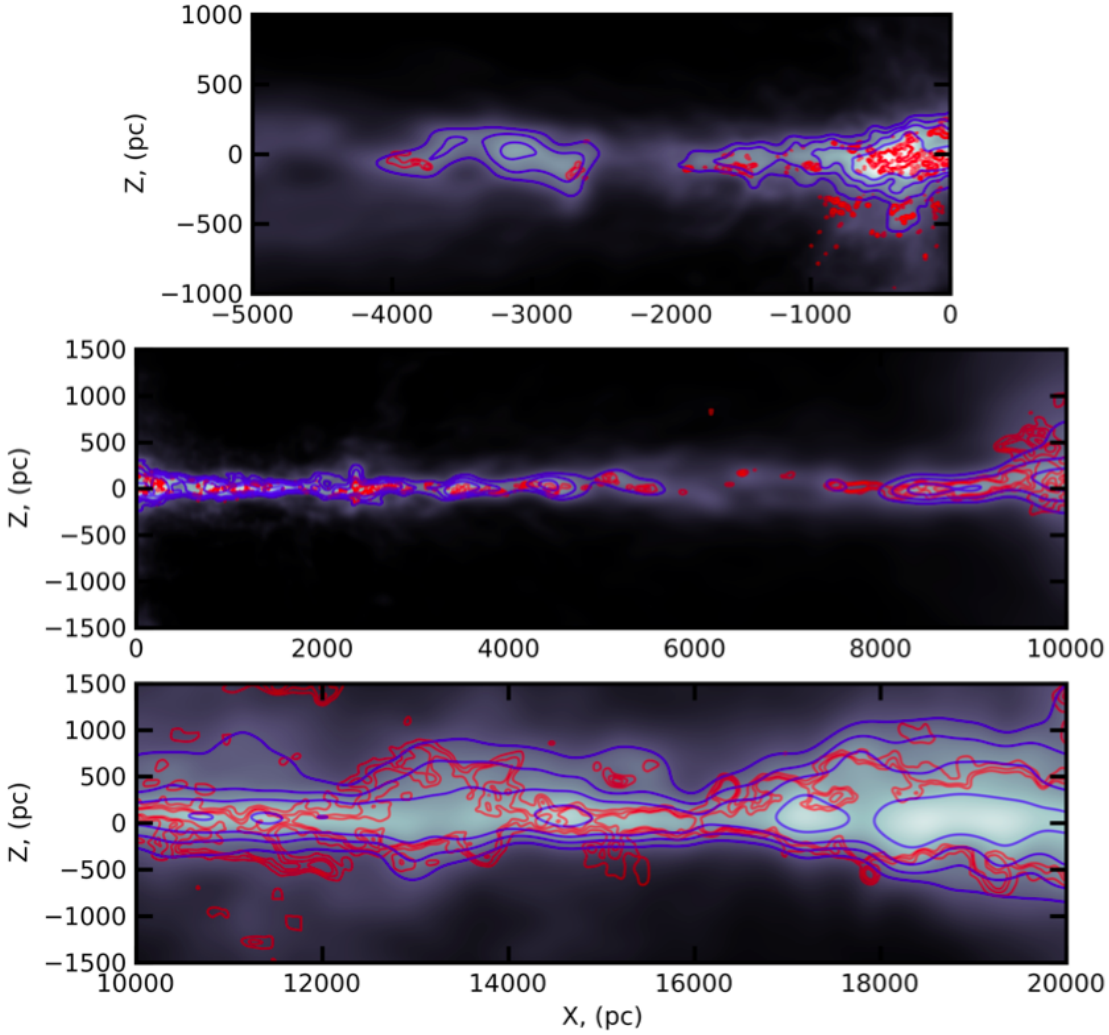

Figure 4.24: Sections of the 10pc HI CRM -in grey scale - with a HI and CO contour overlay. CO Contours (Red) begin at 2.4 K km s^{-1} and are spaced at 2.4 K km s^{-1} to 7.6 K km s^{-1}. HI Contours (Blue) begin at 1000.0 K.km/s and are spaced at 1200 K km s^{-1} to 1500 K km s^{-1}. The HI data - and its contours - are taken from the LAB survey and the CO contours are taken from a combined version of the ExFCRAO survey.

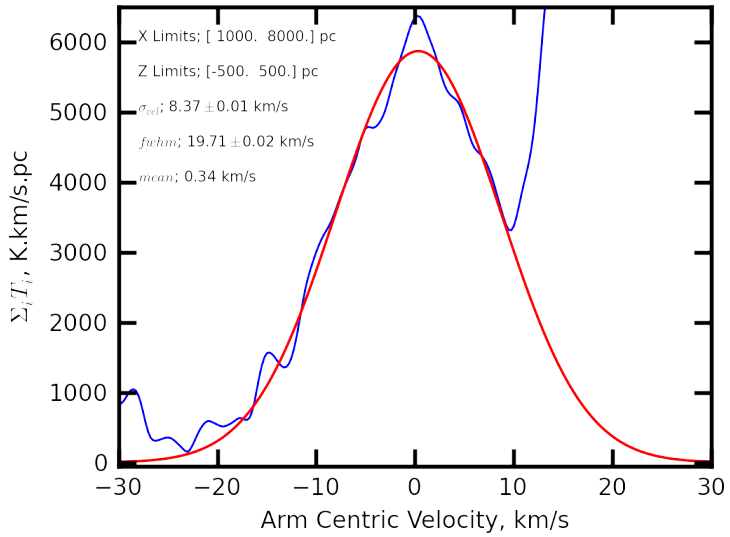

Figure 4.25: The above plot shows a Gaussian fit to the summed velocity spectrum of the 10pc ExFCRAO CRM map over the X, Z limits listed in the Figure. The main peak of emission at Δv_{per} = 0km/s is the Perseus arm, with the Outer Arm becoming visible at Δv_{per} = −30km/s. The spike in emission at Δv_{per}=+15 km s^{-1} corresponds to the velocity where the arm becomes confused with *local* emission.

$$\sigma_{vel_z} = \sqrt{\frac{3.24 \times 10^{-3}}{4ln(2)}}.Z_{FWHM} \tag{4.11}$$

I find the thick and thin atomic components to have $\sigma_{v_z}^{thick}$(HI) =18.05 km s^{-1} and $\sigma_{v_z}^{thin}$(HI) =7.24 km s^{-1} - both of which are consistent with the Lockman & Gehman (1991) models of a multi-component HI distribution. Whereas the molecular component of the arm has a vertical velocity dispersion of $\sigma_{v_z}(molec.)$ =4.14 km s^{-1} . For the two component fit to the molecular component I obtained; $\sigma_{v_z}^{thick}(H_2)$ = 7.61 km s^{-1} and $\sigma_{v_z}^{thin}(H_2)$ =2.35 km s^{-1} . The thick component of the atomic and molecular gas have a σ_{vel_z} comparable to their kinematic σ_{vel}. In both the atomic and the molecular case, the $\sigma_{vel}^{thin} < \sigma_{vel}^{thick}$ holds true for each two-component fit. Finally it is noteworthy to mention that the thin component of the atomic gas has a $\sigma_{vel_z}^{thin}$ comparable to $\sigma_{vel}^{molec.}$.

4.5.2 The Outer Arm

The Nature of the Outer Arm

I begin with a description of the XZ structure of the arm in the CRM data maps. Using the variable-shocked-motion model, I was able to extract 45 kpc of the Outer spiral arm in the first, second and third Galactic quadrants. Both ^{12}CO CRM (Figure 4.14) and HI (Figure 4.15) show the same trend in XZ which was observed in ℓ, b. The Outer arm tends to be limited to a relatively narrow band of emission at higher latitudes and due to its distance, this tracks the warp. This is apparent in the ^{12}CO CRM where I start to confidently detect the Outer arm at X=27 kpc it then begins to climb in Z to a height of 0.6 kpc out of the plane - it does so over 20 kpc of its length - in the second

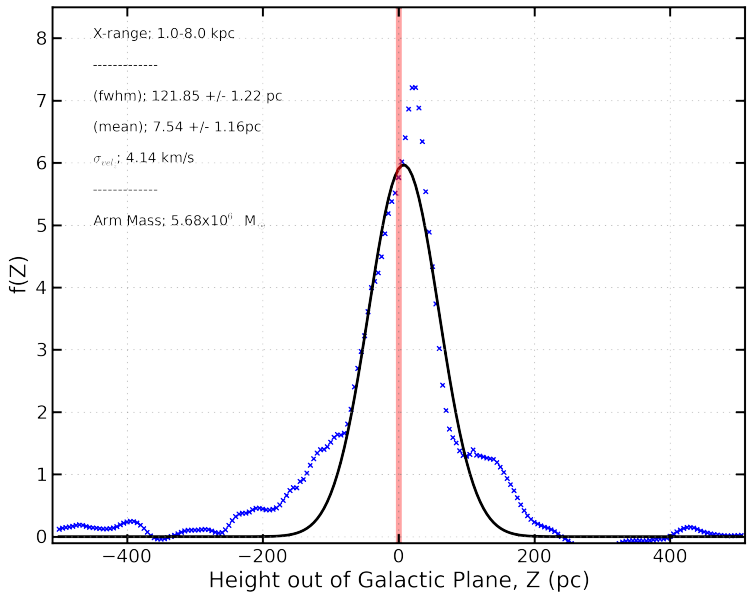

Figure 4.26: The Gaussian fit to the scale height of the ^{12}CO CRM data over the X range 1kpc-8kpc. The position of the Galactic plane is shown by the vertical red line. f(Z) is a measure of the relative intensity of the emission- its actual value is unimportant.

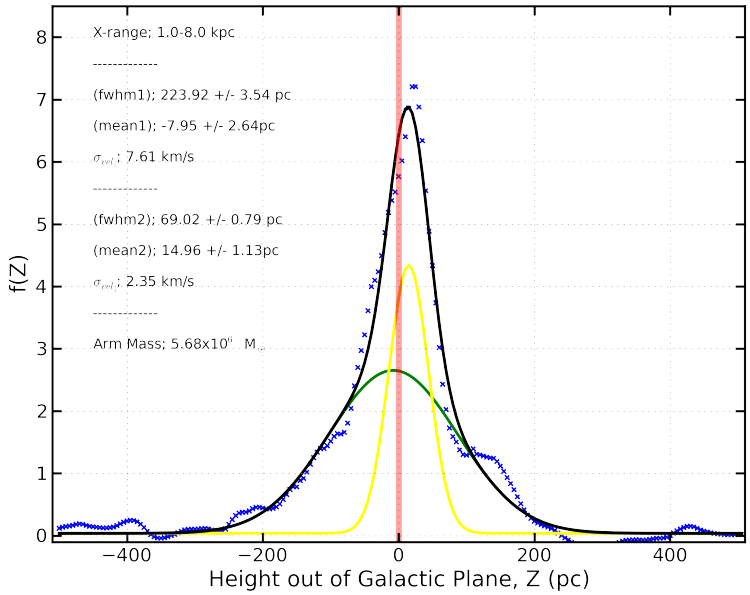

Figure 4.27: The two one-dimensional Gaussian fit to the scale height of the ^{12}CO CRM data over the X range 1kpc-8kpc. The position of the Galactic plane is shown by the vertical red line. For a full description, see the main text.

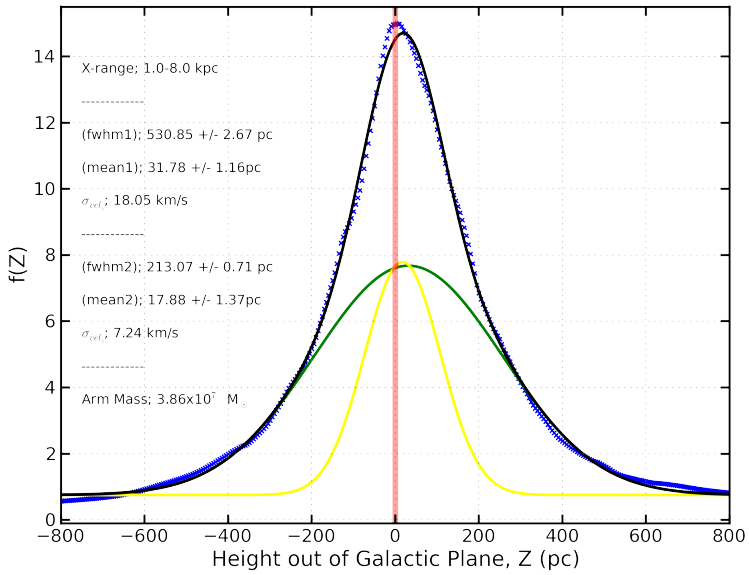

Figure 4.28: The two one-dimensional Gaussian fits to the scale height of the HI CRM data over the X range 1kpc-8kpc. The position of the Galactic plane is shown by the vertical red line.

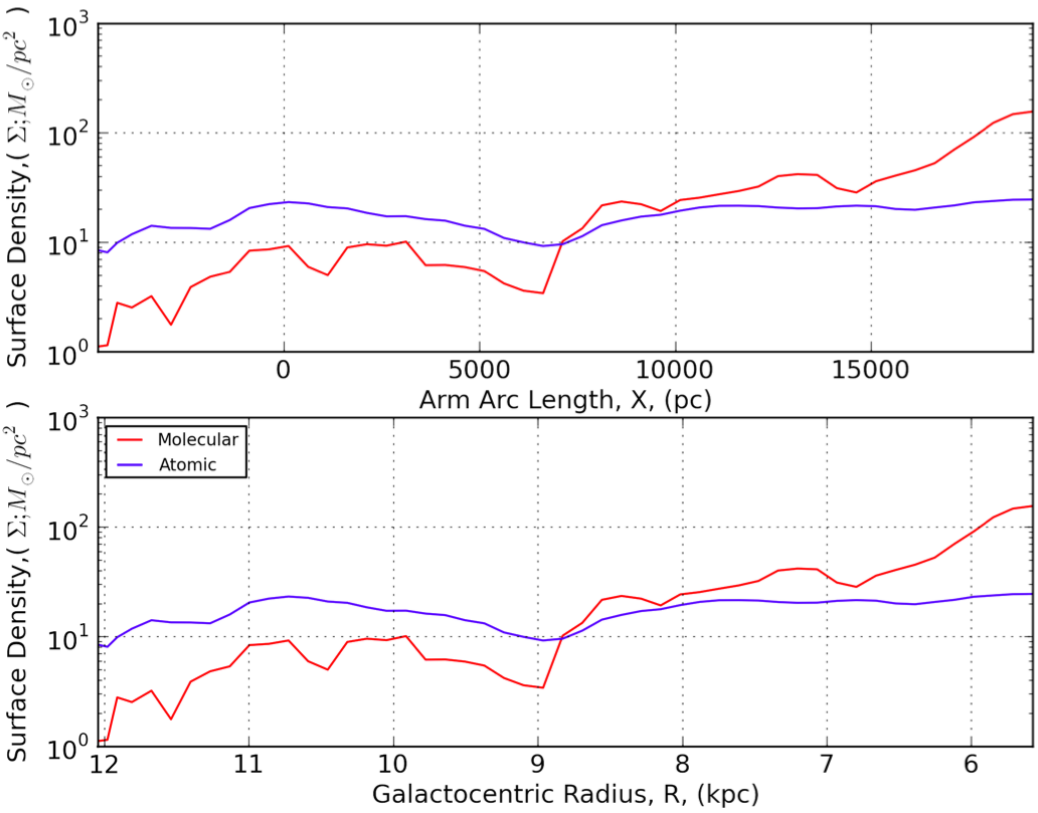

Figure 4.29: The plot above shows the variation of the surface density of material within the Perseus arm as a function of X [top panel] and in Galactocentric radius [bottom panel] . The data were binned in X at 500pc and used the 10 pc CRM data. In the region $R < R_0$ - and its associate X - the Perseus arm is not as well defined nor isolated.

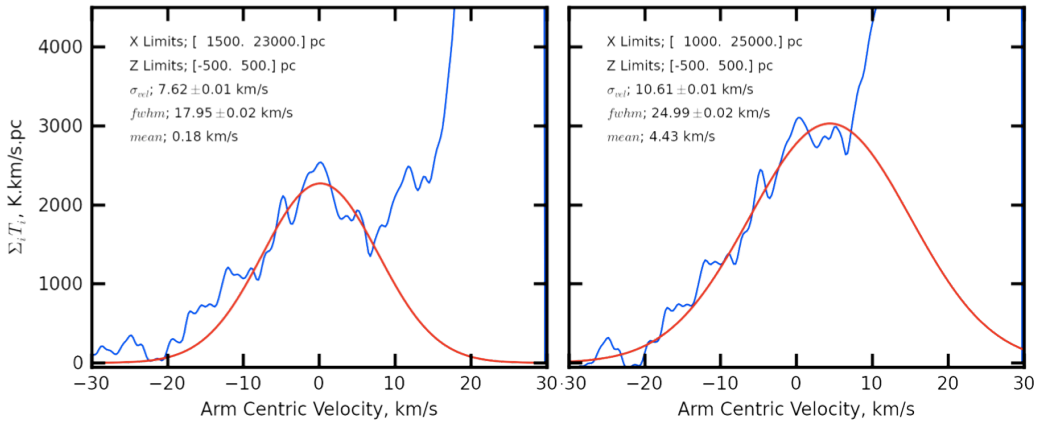

Figure 4.30: The Figure above shows the calculated velocity dispersion about v_{outer} =0 km s^{-1} for the ΔL=20pc ^{12}CO CRM map across two different X ranges. The left panel shows $X_{1.5}^{23.0}$(kpc) dispersion and the right panel shows the $X_{1.0}^{25.0}$(kpc) dispersive fit. The latter corresponds to the σ_{vel} of material used in the scale height and surface density calculations.

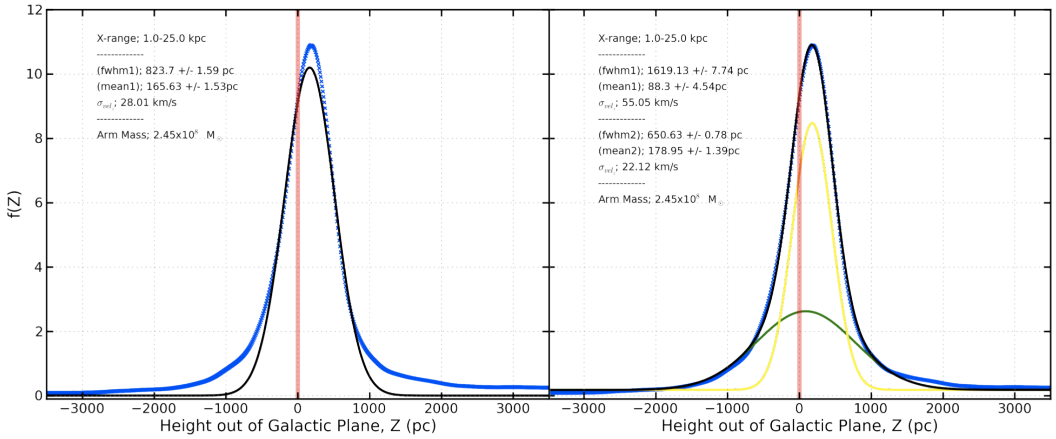

Figure 4.31: Gaussian fits to the scale height of the atomic component (HI) of the Outer arm. The left panel shows a single one-dimensional Gaussian fit and the right panel shows a two-component one-dimensional Gaussian fit.

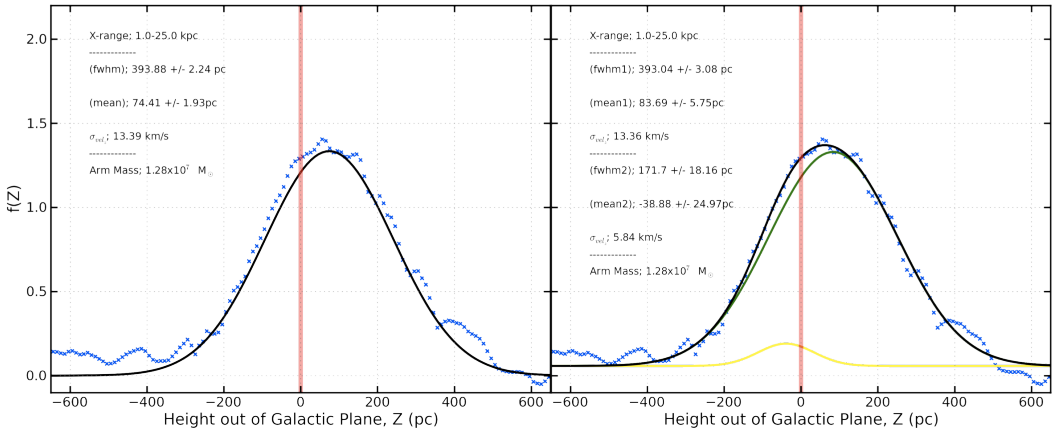

Figure 4.32: Gaussian fits to the scale height of the molecular component (^{12}CO) of the Outer arm. The left panel shows a single one-dimensional Gaussian fit and the right panel shows a two-component one-dimensional Gaussian fit. The two-component fit can be seen to not be a good fit, with no obvious second component (right panel).

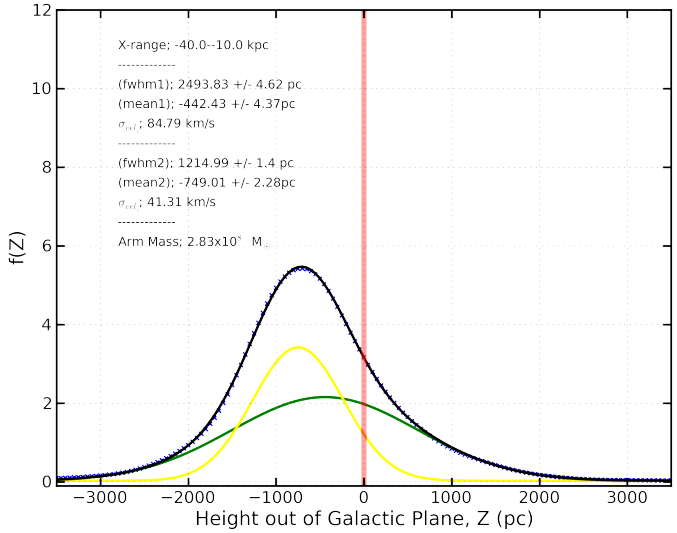

Figure 4.33: The Figure above shows the two-component Gaussian fit to the scale height of the atomic component (HI) of the third and fourth quadrant Outer arm over the range -40 kpc $< X <$-10 kpc . Though this region is unconstrained, it is included for completeness.

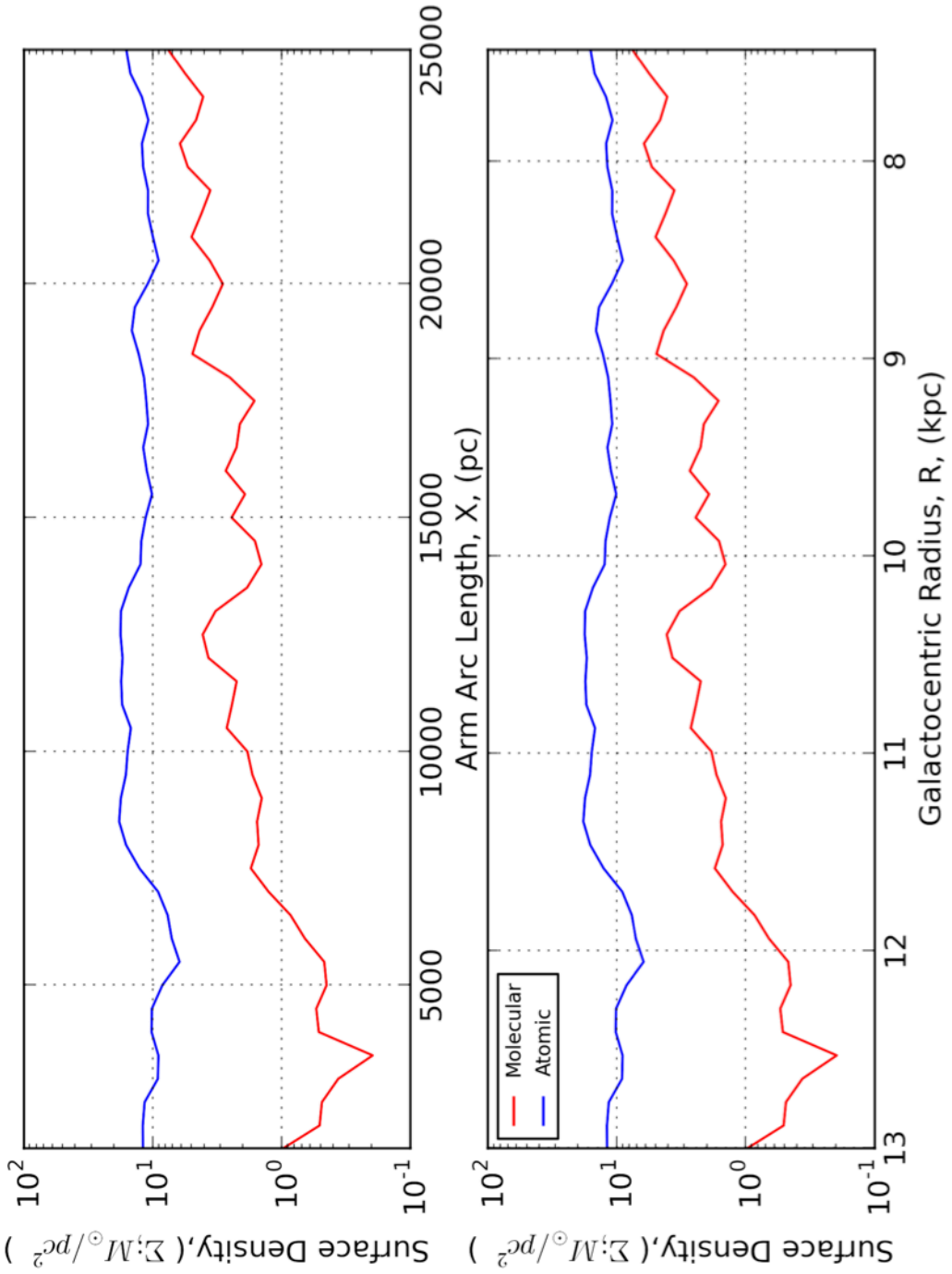

Figure 4.34: Gaussian fits to the scale height of the atomic component (HI) of the Outer arm. The left panel shows a single one-dimensional Gaussian fit and the right panel shows a two-component one-dimensional Gaussian fit.

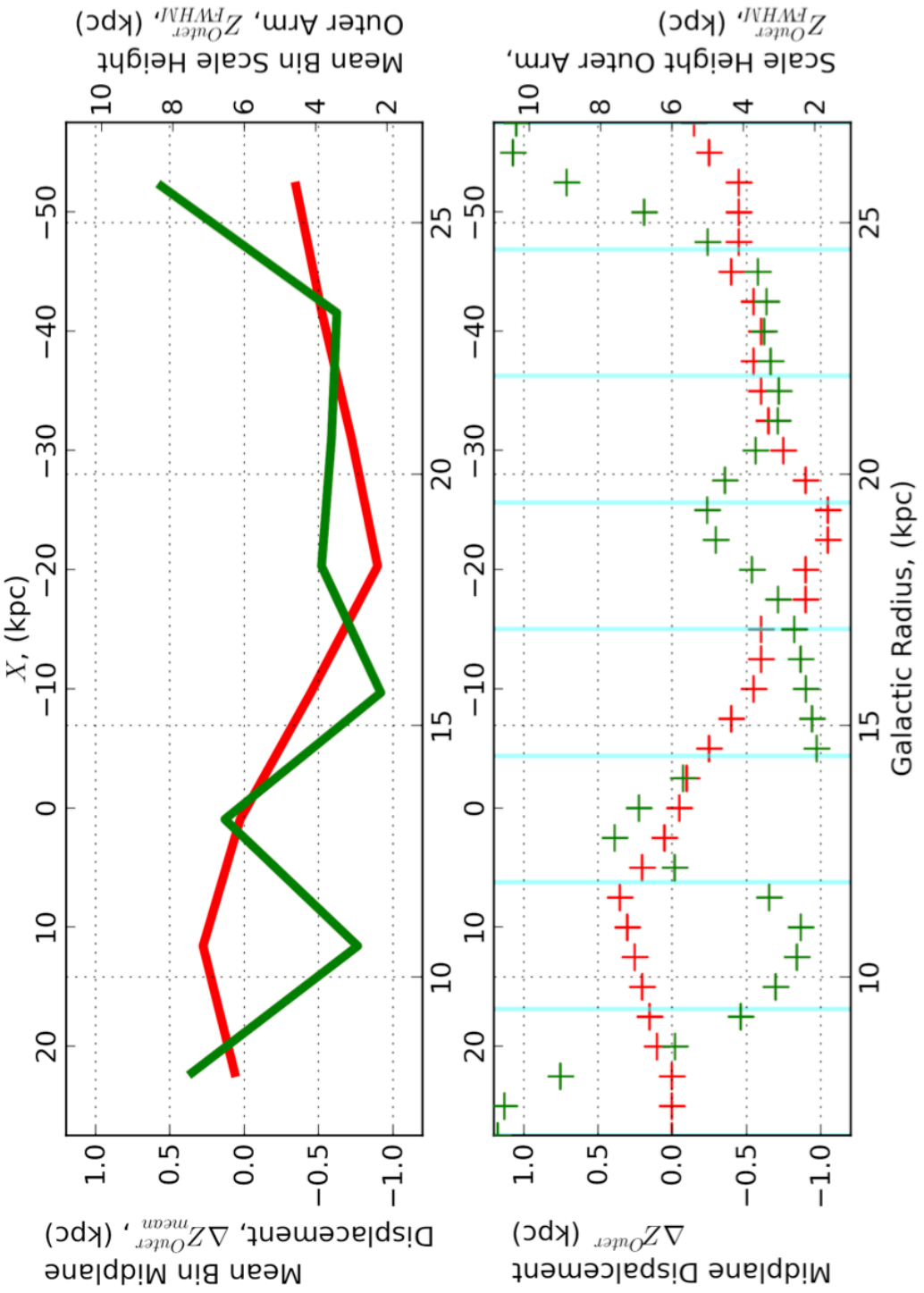

Figure 4.35: The variation of Outer arm displacement from the mid-plane with Galactic Radius, R, and X (red) and also the variation of the scale height of the atomic Outer arm with R and X (green). The top panel shows the plotted mean for each parameter per bin, the bin widths are shown by the vertical cyan lines in the bottom panel. The crosses in the bottom panel indicates a ΔX=0.25 kpc from the initial binning calculation from the raw data.

Galactic quadrant. As the arm continues through the second quadrant, it continues to follow the warp over the subsequent 5 kpc and descends in Z back into the plane. The Outer arm becomes confused with Perseus at $X = \pm 1$ kpc before I am able to isolate it once more at X=-1.5 kpc . The third quadrant the warping of the Galaxy's mid-plane causes the material to drop below the Z=b=0 plane, in this region we begin to lose the ^{12}CO . Shifting our attention to the HI for the remainder of the arm, it can be seen that the Outer arm continues to drop further below the plane over the next 10 kpc . It appears, looking at Figure 4.5, that we may be able to track the Outer arm into the fourth quadrant, however, it is important to bear in mind that the arm model is unconstrained at that point meaning the results obtained are unlikely to be representative of the truth. However, I include the full 360°plot of the Outer arm - using the LAB HI survey data at ΔL=500pc - for completeness. The data are well constrained between 1 kpc < X <23 kpc - at high positive X, the data can be confused with Perseus and local emission, at $X\pm1$ kpc the Outer arm is subject to the velocity compression discussed earlier and as such is confused once more. For X more negative that X =-1.5 kpc , the data are not well constrained - though there are tracers to X=-5 kpc - and should be treated as a predicted trajectory based on the model presented. The CRM data map presented spans -60 kpc < X <30 kpc and $|Z|$ <10 kpc can be seen in Figure 4.17. The Figure also includes an over-plot grid which shows lines of constant (ℓ, b) and how they relate to the XZ coordinate system. Though mentioned previously, the grid in Figure 4.17 assists in showing how large spans in Galactic longitude do not necessarily correspond to a large span in X - specifically in the region of the second quadrant (90°< ℓ <180°) where almost the entire quadrant is contained within a few kpc of arm.

Outer Arm Velocity Dispersion - σ_{vel}

The first analysis to be perform on the CRM data was to calculate the velocity dispersion, σ_{vel}, about the kinematic arm centre. I calculated the velocity dispersion of the molecular component of the Outer arm about its centre over two different ranges X-ranges. $\sigma_{vel}^{molec.}(X_{1.5}^{23.0})$=7.93±0.01 km s^{-1} and $\sigma_{vel}^{molec.}(X_{1.0}^{25.0})$=10.61±0.01 km s^{-1} , see left and right panels in Figure 4.30 respectively. The Outer arm is better discriminated using the $X_{1.5}^{23.0}$ cut, and as such this should be treated as "the Outer arm", though it is noteworthy to draw attention to the larger velocity dispersion calculated but the inclusion of the additional 2 kpc or arm - and the effect of the local emission has. As was calculated for the Perseus arm, the dispersions are comparable with the inter-cloud dispersions on both Galactic (Stark & Brand 1989, 7.8±0.6 km s^{-1}) and extra-galactic (Walsh et al. 2002, 8.9±2.2 km s^{-1}) scales - it is also supported by Milky Way-like model (Tasker & Tan 2009, ≈10.0 km s^{-1}) observations. I also calculated the velocity dispersion for the HI to be; $\sigma_{vel}^{atomic.}$(X$_{1.5}^{23.0}$ kpc) = 22.62±0.02 km s^{-1} and $\sigma_{vel}^{atomic.}$(X$_{1.0}^{25.0}$ kpc) = 29.53±0.03 km s^{-1} .

The predicted fourth quadrant segment of the Outer arm, in HI, has a significantly higher velocity dispersion, $\sigma_{vel}(X_{-40}^{-10}$ kpc) = 95.26±0.1 km s^{-1} , than the first and second quadrant part of the arm. Though obvious from the unconstrained nature of this region, it is further evidence that what has been isolated in the fourth quadrant is not the the Outer arm as such will not be included in further analysis.

Outer Arm Scale Height & Mass

Fitting to the vertical, Z, axis to find the scale height of the Outer arm will be able to calculate the mass of material contained within it. Earlier it was found that the HI scale height distribution was well fit by a two-component-one-dimensional Gaussian function (2C1D) - for the Outer arm I fit both a one-component-one-dimensional (1C1D) and a 2C1D Gaussian functions to the data. Figure 4.31 shows the 1C1D and 2C1D fits to the vertical distribution of material. The left panel of Figure 4.31 shows the 1C1D fit to the HI which does not appear to fit the data well. The fit gives a Z_{FWHM}(HI)=823.7±1.59pc, which I take as a measure of the scale height of the Outer arm. I can, however, improve the fit to the data by assuming using the 2C1D fit to fit the two separate - thick and thin - components of the atomic medium. the 2C1D fit to the data gives Z^{thick}_{FWHM}(HI)=1619.13±7.74pc and Z^{thin}_{FWHM}(HI)=650.63±0.78pc. Using the 2C1D fit, obtain a mass of the atomic component of the Outer arm to be; M^{atomic}_{Outer}=2.46x10^{8}M$_\odot$.

For Perseus, evidence was found of a two component molecular gas phase, so for the Outer arm I also fit 1C1D and 2C1D Gaussians to the molecular gas. The 1C1D fit to the ^{12}CO - seen in Figure 4.32 - shows it is fairly well fit by 1C1D function, giving a scale height of; Z_{FWHM}(H$_2$)=393.88±2.24pc peaking at Z_{mean}(H$_2$)=74.41±1.93pc above the plane as one would expect. The 2C1D fits to the ^{12}CO find Z^{thick}_{FWHM}(H$_2$)=393.04±3.08pc and Z^{thin}_{FWHM}(H$_2$)=171.70±18.16pc with a molecular arm mass of $M^{molec.}_{Outer}$=1.28x10^{7}M$_\odot$. As with Perseus I find the mass of the atomic component of the arm to be an order of magnitude higher than that of the molecular. The relative surface densities as a function of Galactocentric radius, R, and of arc-length, X, can be seen in Figure 4.34. Though, unlike Perseus, the surface density of the molecular component never exceeds that of the atomic over the range of the Outer arm - there is a definite trend of the molecular material increasing in abundance as R decreases. Which is consistent with the view that a majority of the molecular material within the Galaxy concentrated around the centre, whereas the atomic gas is spread throughout the disc. One may also observe this in the raw CRM data in Figures 4.14, 4.15 and 4.17 - the atomic arm is well populated with gas along all its length.

Instead of using the 2C1D fits to the HI data I measured the dispersion of the real data - rather than the fit - from which I obtained a measure of the scale height, Z^{real}_{FWHM}, variation with Galactic radius and X. I am able to track the warp of the disc in the HI, as mentioned earlier, but I present this in Figure 4.35. Figure 4.35 contains two panels: the bottom panel shows the variation of the displacement of the Arm centre from the mid-plane, which can be taken as a measure of the warp and also in the bottom panel is a measure of the scale height of the Outer arm. Both these data were calculated on the data presented in Figure 4.17, which were initially binned in steps of 1 kpc and are presented in the bottom segment of this Figure. I then divided the arm into 8 further bins (shown as the cyan blocks in the bottom Figure). The mean value in each bin is then plotted at the bin midpoint, which can be seen in the top panel of Figure 4.35. I do see the effect of the warping midplane in the tracking of the arm-centre with X and R (in red), with it rising towards the middle of the second quadrant before moving to more negative Z through the anti-centre into the third quadrant, before starting to rise again in the middle of the third quadrant. I do not see an linearly increase scale height with R in the outer arm. Excluding the anti-centre bin (X=0kpc), the scale height of the arm decreases through the first and second quadrants to a minimum as the arm

moves into the third quadrant. Once the arm reaches the third quadrant, the Z_{FWHM} does increase - not monotonically - with R to a maximum as it returns to the first quadrant. One interesting feature of the variation of scale height is that there is a local maximum at X=25 kpc , this corresponds to an region containing ^{12}CO emission which can be seen in Figure 4.17.

Transverse Velocity Dispersion - σ_{vel_z}

Estimating the vertical velocity dispersion in terms of the spatial FWHM, using the conversion given previously (Summers & Brunt submitted, Equation 10). Considering, first, the 1C1D fits to the gas' Z_{FWHM} gives the $\sigma^{atomic}_{vel_z}$=28.01 km s^{-1} and $\sigma^{molec.}_{vel_z}$=13.39 km s^{-1} . The molecular component's $\sigma^{molec.}_{vel_z}$ is of the same order of magnitude, but slightly larger than its σ_{vel}=10.61 km s^{-1} calculated from the dispersion about the arm's centre. The comparison of the atomic component's value with its σ_{vel} = 29.53±0.03 km s^{-1} shows that the velocity dispersion in the velocity plane is comparable to its velocity dispersion through the Z axis.

For 2C1D fits, the molecular gas the *thin* $\sigma^{molec.}_{vel_z}$[thin]=13.36 km s^{-1} , is almost identical to the 1C1D fit described above - with the *thick* $\sigma^{molec.}_{vel_z}$[thick]=5.84 km s^{-1} being significantly smaller. The implication of this is that at the distance of the Outer arm the molecular gas is dominated by its *thick* component, with the *thin* component giving a negligible contribution to the overall distribution of gas at this R due to the generally lower levels of molecular material in this region of the Galaxy (see Figures 4.5 and 4.17). I find, for the first and second quadrant atomic material - the $\sigma^{atomic.}_{vel_z}$[thin] = 22.12 km s^{-1} and the *thick* $\sigma^{atomic.}_{vel_z}$[thick] = 55.05 km s^{-1} implying that the *thin* component dominates the atomic phase velocity dispersion.

4.5.3 Postulating the Sct-Cen Arm Structure

Though the modelling, mapping and analysis of the full Sct-Cen arm is to be the subject of a current JCMT proposal and a future paper, I was able to present a preliminary set of data using the fit described in section 3.5. The Sct-Cen ACM data in are presented in Figures 4.7 and 4.6, though the degree to which this emission is unambiguous from the Outer is unknown. The molecular component of the Sct-Cen arm (if indeed the candidates identified in Figure 4.6 and Table 4.1 are within the arm) is not as continuous as the Perseus and Outer spiral arms, especially in the region where the emission breaks (90°< ℓ <120°), with the Outer arm atomic gas being continuous through its ℓ, b trajectory. Whereas the Sct-Cen emission appears to be be almost clumpy or filamentary - this is likely due to the HI not being as compact nor abundant in this region.

The CRM - Figure 4.20 - and the AMF - Figure 4.23 - show the linear (rather than angular, ℓ, b) structure of the outer Sct-Cen. The model predicts that the outer Sct-Cen arm has a span in X of 40 kpc in QI and QII, which is twice that of the Perseus arm due to its much further distance. The Z distribution is similar to that of the Outer arm - i.e. tracking the warp - with a contiguous structure across its length. The only deviation from this continuous band of emission is in the region of X =10 kpc where the arm appears to become more filamentary in nature, after which, it then returns to being a continuous band of emission in the region of the anti-centre - probably due to the outer Sct-Cen and Outer arms becoming blended in velocity as they traverse

this region. It is unlikely that the outer Sct-Cen exists much beyond the anti-centre if it is indeed an extension of the inner Scutum arm. Considering the AMF plane-centric-maps - Figure 4.23 - beyond the anti-centre the emission of the Sct-Cen drops dramatically, though one may say that this is only because the model does not describe its structure correctly. However, looking at the ℓ-v_{LSR} diagram of the Galaxy - and its kinematic model - it is more likely that either; the Sct-Cen arm remain blended in v_{LSR} *or* the Sct-Cen dissipates in this region since, even at ℓ=190°, the outer Sct-Cen is at almost $R = 19$ kpc .

4.6 Summary

4.6.1 The Perseus Arm

Using the kinematic model (defined earlier), the velocity axis of the spectral line data was re-centred to be relative to the kinematic arm centre to form a series of Arm-Velocity Centred Maps (ACM). Using these maps I could kinematically identify Perseus material within a single velocity window. The spatial fit, in conjunction with the kinematic model, were used to produce a series of maps a common linear resolution (CRM). Using the the extracted ACM map in conjunction with the distance fit from the maser emission I am able to, by applying a gaussian smoothing kernel, smooth the Perseus arm material to a common linear resolution across its full extent which has the effect of producing an essentially extra-Galactic view of Galactic material.

The scale height of the Perseus arm was calculated for both ^{12}CO and HI by fitting a gaussian profiles to the emission. It was found that a one-dimensional gaussian fit to the material provided a good fit to the ^{12}CO , but a poor fit to the HI. It was deduced that the two-component medium of the atomic component required separate fitting, so I fit two one-dimensional Gaussians; one for the thick and one for the thin component. I found that; the scale height - defined to be the *FWHM* of the Gaussian fit - of the Perseus arm remained fairly constant over most to the Perseus arm. The derived fit parameters for the arm were found to be $Z^{molec.}_{FWHM}$ =121.85±1.22 pc and has an arm mass of $M^{molec.}_{arm}(X^{8.0}_{1.0}$ kpc) = 5.68x10^{6}M$_\odot$. I used two one-dimensional gaussians to fit the scale height to the atomic gas - Z^{thin}_{FWHM}(HI) = 213.07±0.71 pc, Z^{thick}_{FWHM}(HI) = 530.85±2.67 pc and has a mass of $M^{atomic.}_{arm}(X^{8.0}_{1.0}$ kpc)=3.86x10^{7}M$_\odot$.After having considered the one-component Gaussian fit to the molecular component I considered fitting a two-component gaussian to improve the fit. I found that ^{12}CO have Z^{thick}_{FWHM}(H$_2$) =223.92±3.54 pc, Z^{thin}_{FWHM}(H$_2$)=69.02±0.79 pc, see Figure 4.27.

The dispersion of arm material's velocity in the spectral and Z axes was also obtained. The $\sigma^{molec.}_{vel}$ for the molecular component was found, within error, to be consistent with the findings of Galactic, extra-galactic and simulated data - with the σ^{atomic}_{vel} being approximately twice that of the molecular component. Then, using the Z_{FWHM} for each of the scale height fits, I was able to estimate the transverse velocity dispersion, σ_{vel_z}. I found, in each case, the thick component of each gas had a σ_{vel_z} comparable to its kinematic σ_{vel} with $\sigma^{thin}_{vel} < \sigma^{thick}_{vel}$ also being true for each two-component fit. It is noteworthy to mention, however, that the thin component of the atomic gas has a $\sigma^{thin}_{vel_z}$ comparable to $\sigma^{molec.}_{vel}$.

4.6.2 The Outer Arm

Having obtained the spatial and kinematic fit to the Outer arm, I applied the ACM and CRM routines to the data and extracted the Outer arm from the source data and expressed them as ACM and CRM data. I found that the the model predicts the Outer arm's trajectory into the third and fourth quadrants and that in this region the arm is mainly atomic in composition. The full $0°< \ell <360°$- assuming that the material isolated *is* Outer arm material - spans almost 90 kpc of arm. I find the velocity dispersion for the Outer arm to be $\sigma_{vel}^{atomic.}$ ($X_{1.5}^{23.0}$ kpc) = 22.62±0.02 km s^{-1} , $\sigma_{vel}^{atomic.}$($X_{1.0}^{25.0}$ kpc) = 29.53±0.03 km s^{-1} , σ_{vel}(X_{-40}^{-10} kpc) = 95.26±0.1 km s^{-1} , $\sigma_{vel}^{molec.}$ ($X_{1.5}^{23.0}$) = 7.93± 0.01 km s^{-1} and $\sigma_{vel}^{molec.}$($X_{1.0}^{25.0}$)=10.61±0.01 km s^{-1} - over the X ranges stated. The velocity dispersion of the atomic component of the Outer arm in the third and fourth quadrants was found to be larger than that of the first and second.

As with Perseus, the molecular and atomic gas scale heights of the Outer arm were best fit by a two-component-one-dimensional Gaussian function - fitting the thick and thin components of the gas - with the FWHM being used as a measure of the scale height in Z. The molecular gas was found to have a Z_{FWHM}^{thick}(H_2)=393.04±3.08pc and Z_{FWHM}^{thin}(H_2)=171.70±18.16pc with a molecular arm mass of $M_{Outer}^{molec.}$=1.28x10^{7}M$_\odot$ over the range 1 kpc < X <25 kpc . The atomic gas was found to have Z_{FWHM}^{thick}(HI)=1619.13±7.74pc and Z_{FWHM}^{thin}(HI)=650.63±0.78pc with a mass to be; M_{Outer}^{atomic}=2.46x10^{8}M$_\odot$ over the range 1 kpc < X <25 kpc . I also fit the scale height to the third and fourth quadrant section of the Outer arm (-40 kpc < X <-10 kpc .) - the low level of molecular emission made it difficult to fit to ^{12}CO so I only fit to the atomic gas - Z_{FWHM}^{thick}(HI)=2493.83±4.62pc and Z_{FWHM}^{thin}(HI)=1214.99±4.37pc - obtaining a mass of the atomic component of the third and fourth quadrant Outer arm of M_{Outer}^{atomic}=2.83x10^{8}M$_\odot$ being comparable to the mass of the outer arm in the first and second quadrants.

The final quantitative analysis performed was the calculation of the transverse velocity dispersion, σ_{vel_z}, for the Outer arm. I use the 2C1D fits to the vertical scale height to calculate σ_{vel_z} for molecular and atomic gas in the first and second quadrants and atomic gas in the third and fourth. I find that the molecular gas has $\sigma_{vel_z}^{molec.}$[thin]=13.36 km s^{-1} and *thick* $\sigma_{vel_z}^{molec.}$[thick]=5.84 km s^{-1} , the thin and thick components being larger and smaller - respectively - than the $\sigma_{vel}^{molec.}$ presented above. I found that the first and second quadrant atomic material has $\sigma_{vel_z}^{atomic.}$[thin] = 22.12 km s^{-1} and the *thick* $\sigma_{vel_z}^{atomic.}$[thick] = 55.05 km s^{-1} implying that the *thin* component dominates the atomic phase velocity dispersion. Extending the atomic analysis to the third and fourth quadrants I found that $\sigma_{vel_z}^{atomic.}$[thin] = 41.31 km s^{-1} and the *thick* $\sigma_{vel_z}^{atomic.}$[thick] = 84.79 km s^{-1} .

Lastly, for the Outer arm, I investigated how the scale height of atomic varied over the span of X and R the Outer arm covers. I found that he mean arm-centre displacement from the mid-plane appears to trace the Galactic warp through all four quadrants, I do not find that the scale height, Z_{FWHM}, linearly increasing with R. Instead it appears to decrease towards the anti-centre and increase in the third and fourth quadrants - I do find, however, that the $\frac{molec.}{atomic}$ ratio increases towards smaller Galactic radii. There is also evidence that in regions of relatively high molecular concentration, the scale height of the atomic gas experiences a local maximum.

4.6.3 The outer Scutum-Centaurus Arm

The outer Sct-Cen arm is not well constrained here, in that constraining points of the arm all below ℓ =58° - though there are higher ℓ molecular cloud candidates identified - the arm is not adequately described beyond this limit for any meaningful analysis to be worthwhile at this juncture. Further constraint of the spatial location of the arm would be beneficial - see Chapter 7 - and allow for the arm to be traced to a higher longitude.

However, the existance of the possible molecular cloud candidates - at higher ℓ - in Figure 4.7 may indicate that the arm extends to this region. Though with the initial constraining analysis from Dame & Thaddeus (2011) only identifying the arm to ℓ=58°, it would bring the validity of these additional molecular cloud candidates into question without bridging emission to match them to the originally identified arm.

CHAPTER 5

Galactic Dynamics & The Molecular Content Of The Outer Milky Way

"Don't try to solve my problem using hollow religion or false optimism. It won't work."
Adrian Plass, 2011

5.1 Introduction to Chapter

In this chapter I present a dynamical analysis of the three spiral arms mapped in the previous chapters as well as a cloud decomposition and analysis of the Perseus CRM data at a series of resolutions (5 pc,10 pc, 20 pc and 50 pc). I then compare the CRM cloud properties to the cloud properties of other Galactic (Solomon et al. 1987; Heyer et al. 2008) and extra-galactic cloud samples (Bolatto et al. 2008). The cloud decomposition is performed using the enhanced `CLUMPFIND` algorithm described in Brunt et al. (2003).

I also present a tertiary analysis of the data in terms of post-processing - in terms of the dynamical parameters which are able to be derived from the models presented and the large-scale structure of each arm. I investigate the effect of using a non-flat rotation curve (in terms of its kinematical structure with R) on the constant-shocked-motion-model and finally an analysis of the AMF data created in the previous chapter.

As mentioned previously, CO's clumpy nature allowed me to map out the spiral arms' substructure. Some of the ^{12}CO observations from the BIMA SONG catalogue of galaxies (Helfer et al. 2003) show that even with an extra-galactic point of view the discrete locations of the spiral arms are not always immediately evident (see Figure 5.1). Some of the galaxies included in the BIMA SONG catalogue infer that the absence of observation of structure does not always allow one to infer the absence of its presence. The work by Combes (1991) attempted to recover the grand design spiral structure of M51 assuming one was observer within it. It was shown that an observer within M51 using observational techniques similar to the techniques used for our own Galactic based observations to recover the distance structure of the galaxy, the spiral structure of M51 was not recovered. The synthetically observed cloud locations within M51 do not present the

Lee J Summers

Figure 5.1: Optical spiral arms are traced by ^{12}CO . The panels above show the data taken from the BIMA SONG catalogue of Galaxies. The degree to which spiral structure is traced by ^{12}CO is variable, in that the top panel shows NGC 628 which has apparent optical spiral structure in the top left panel, but it is not reflected as well in the ^{12}CO distribution (top right panel). In contrast to NGC 628, NGC 5194 presents grand design spiral structure in both the optical bands (bottom left panel) which is reflected in the ^{12}CO distribution (bottom right).

observer with discernible any spiral structure. The plots produced within the paper showed that the spatial density of the clouds appeared to correlate with the observer's line of sight, which is what is observed with data in the Milky Way if one does not account for the distance ambiguities in the inner and outer Galaxy. This has interesting implications for the Milky Way, in that the recovery of spiral structure in M51 suffered from similar observational biases as we observe within our Galactic observations. Therefore, the 'Fingers of God' effect which we can observe in the Milky Way - in terms that observations appear to be solar-centric (Hou et al. 2009) - and the ambiguity of the *observed* spiral features - is not necessarily indicative that the spiral arms of the Milky Way are not well defined, but it is a symptom of our observational methods - see example in Figure 5.1.

The properties of clumpy molecular material, be it within spiral arms or not, have been well studied over the decades but there is still debate over the basic properties and how it behaves. In the work of Larson (1981), there is set out a series of relations, known as *Larson's Laws* which describe the general properties of molecular clouds. The Larson (1981) study takes star-forming clouds (such as Orion and Ophiuchus) in approximate virial equilibrium; the internal velocity dispersion of the studied clouds were found to be correlated with the measured size of the respective clouds. Meaning that within the larger clouds there are relatively small areas of over-density (i.e. clumpiness) and also that the clouds studied were found to be transient in nature with a lifetime of around 10^7yrs. There is still ongoing discussion as to whether molecular clouds

are quiescent; Stahler & Palla (2004) suggest that clouds can comprise of both atomic and molecular Hydrogen with the clouds forming slowly through gravitational condensation and can exist for prolonged lengths of time through an equipartition of pressures - as described in Chapter 1. However other works post-Larson (1981) such as; Elmegreen (1990a,b); Ballesteros-Paredes et al. (1999); Klessen et al. (2004); Ballesteros-Paredes (2006) proposed that molecular cloud formation is due to random collisions, gravitational instabilities and turbulent motions due to more turbulent initial conditions (Glover & Mac Low 2007). A relatively recent study of molecular clouds by Solomon et al. (1987) who analysed 273 molecular clouds in the Galactic plane betweens longitudes of 8°and 90°, generally found that the clouds identified were in, or at least near to, virial equilibrium. The the size velocity line-width relation was found to be a 0.5 power-law characterised by a constant mean surface density of $170 M_{\odot}$ pc^{-2}. A power-law dependance of mass with CO luminosity, M α $L_{CO}^{0.81}$.

5.2 Galactic Rotation

5.2.1 Non-Flat Rotation Curves

In Chapter 3, I began with discussing the shock-motion-model assuming a flat rotation curve and constant deviation from that curve. For completeness, it would be interesting to see what would happen to the best fit constant-shocks if a non-flat rotation curve was used - one which incorporates a rise or fall beyond R_0 . When the constant shock was fitted to the Perseus and Outer arms, it was found that $v_{shock}^{Perseus}$=20.0 km s^{-1} and v_{shock}^{Outer}=9.0 km s^{-1} - could the weaker shock fit to the Outer arm be symptomatic of a non-flat rotation curve allowing a weaker shock and that the variable shocked motion model is effectively the arm being modelled with a rising (or falling) rotation curve? This is what is investigated here.

For a reference curve, I use the Brand & Blitz (1993) (hence forth referred to as BB93) rotation curve which was described and presented in Appendix C.4. The interpretation used for this rotation curve was that the modification of the arm velocity, v_{arm} incorporates a $\Theta(R)$ variance;

$$v_{arm} = \Theta(R) - v_{shock} \equiv \left(\Theta_0 + v_{prime}\left(\frac{R}{R_0} - 1\right)\right) - v_{shock} \tag{5.1}$$

Where the free fitting parameters are; v_{shock}- the constant shock - and v_{prime} - the coefficient for the linearly varying contribution to the rotation velocity. When fit, if v_{prime} >0 then the rotation curve rises with R, whereas if v_{prime} <0 then the rotation curve drops off with R. The ^{12}CO centroids which were used and defined for the best fit constant shocks were used to refine the model for Perseus, Outer and outer Sct-Cen - the results of which are shown in Figure 5.2. All three arms which were fitted, yielded positive values of v_{prime} implying the rotation curve rises with R - which is consistent with other works (Blitz 1979; Brand & Blitz 1993; Binney & Dehnen 1997). Figure 5.2 shows the best fits to the parameters. Notice that with addition of the linearly varying rotation curve, the values of v_{shock} for the Perseus and Outer arms has converged to ≈20 km s^{-1} with the gradient of the rotation, $\frac{d\Theta}{dR}$ being 2.32 km s^{-1} kpc $^{-1}$ and 3.63 km s^{-1} kpc $^{-1}$ for

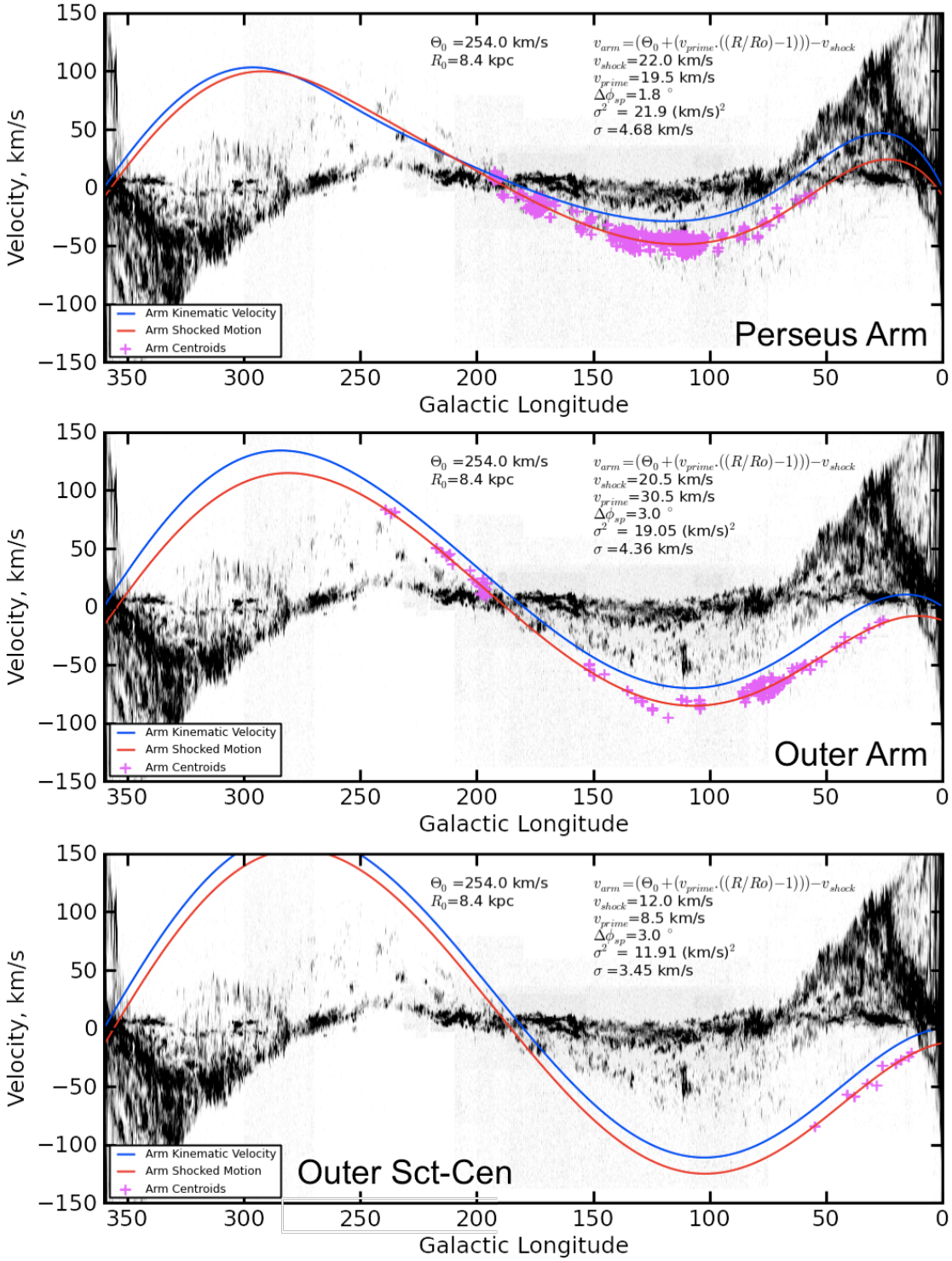

Figure 5.2: The Perseus [top], Outer [middle] and outer Sct-Cen [bottom] arm ℓ,v_{LSR} fits via the constant-shock-motion-model assuming a non-flat rotation curve. The magenta crosses show the locations of ^{12}CO centroids used to refine the fit (after fitting to the tracers), in the case for the Perseus and outer spiral arms, but for the complete fit to the Sct-Cen arm.

the models fit to the Perseus and Outer arms respectively - for a spatial model which assumes a constant pitch angle. The outer Sct-Cen arm does not follow the trend with v_{shock}, being almost half that of the other two arms with v_{shock}=12.5 km s^{-1} and $\frac{d\Theta}{dR}$ being 1.01 km s^{-1} kpc $^{-1}$. This could be due to the poor fit, or the fact that the arm is not fully modelled so therefore we do not have the complete picture. Similarly it could be because of the large range of R which the outer Sct-Cen, perhaps v_{shock}=const. is not a suitable approximation - and as such is not modelled correctly.

5.2.2 Estimation of Oort's Constants

Since we now have an estimate of the velocity gradient, $\frac{\mathrm{d}\theta}{\mathrm{dR}}$, I am able to provide an estimate for Oort's constants as defined by the model. Oort's constants provide an overall picture of the differential rotation of the Galaxy kinematics in a position independent manner - since from the combination of these constants one may obtain the radial and tangential components of velocity and also estimating the proper motions. From the models in section 5.2.1, an estimate of the values of Oort's constants (Oort 1927, 1928) can be made via;

$$A = \frac{1}{2}\left(\frac{\Theta_0}{R_0} - \frac{d\Theta}{dR}\right) \tag{5.2}$$

$$B = -\frac{1}{2}\left(\frac{\Theta_0}{R_0} + \frac{d\Theta}{dR}\right) \tag{5.3}$$

For the fits to the linearly rising rotation cure, I find the values of Oort's constants (Equations 5.2 and 5.3) for the Perseus and Outer arms to be; $A_{Perseus}$ = 14.0 km s^{-1} kpc^{-1}; A_{Outer} = 13.3 km s^{-1} kpc^{-1}; $B_{Perseus}$ = –16.3 km s^{-1} kpc^{-1}; B_{Outer} = -16.9 km s^{-1} kpc^{-1}, the uncertainty on the Perseus arm determination was found to be, $\sigma_{Perseus}$=2.8 km s^{-1} and for the Outer arm to be, σ_{Outer}=2.6 km s^{-1} . Though these differ from the IAU standard values of A_{IAU} = 14.4±1.2 km s^{-1} kpc^{-1}; B_{IAU} = -12.0±2.8 km s^{-1} kpc^{-1} they are consistent with the findings of Elias et al. (2006) (E06) who derived the values of Oort's constants from the proper motions of O and B stars in the HIPPARCOS catalogue. E06 found the values of Oort's constants to be; A_{E06} = 14.0±1.0 km s^{-1} kpc^{-1} and B_{E06} = -18.0±1.0 km s^{-1} kpc^{-1}. However, both the results presented here and the findings of listed in Dehnen & Binney (1998), the values of the A constant are comparable - within error - to the IAU standard *and* to other determinations of Oort's constant A detailed in Dehnen & Binney (1998). The value for B, however, predicts a too negative a value which is discrepant with other determinations of this value - see Table 5.1.

However, more recent simulations by Minchev & Quillen (2007) suggest that the presence of spiral perturbation to an otherwise axisymmetric disc affects the calculated values of A and B of the order ±5 km s^{-1} kpc $^{-1}$, in addition to this the A constant can be affected by disc with a high velocity dispersion, ≈ ±2 km s^{-1} kpc $^{-1}$. This effect could go some way to explaining the discrepancy between the values calculated within this work and the values in literature. Since here I have estimated the constants based on spiral arm based calculations.

Table 5.1: Determinations of Oort's Constants A and B from literature

Reference	A (km s^{-1} kpc^{-1})	B (km s^{-1} kpc^{-1})
Summers 2012 (Perseus)	14.0±2.8	-16.3±2.8
Summers 2012 (Outer)	13.3±2.6	-16.9±2.6
IAU Standard (Kerr & Lynden-Bell 1986)	14.4±1.2	-12.0±2.8
Hanson (1987)	11.3±1.1	-13.9±0.9
Feast & Whitelock (1997)	14.8±0.8	-12.4±0.9
Gould & Ramirez (1998)	14.5±1.5	-12.5±2.0
Elias et al. (2006)	14.0±1.0	-18.0±1.0
Elias et al. (2006) (Gould Belt)	11.0±2.0	-20.0±1.0
Elias et al. (2006) (Local Galactic Disk)	16.0±2.0	-16.0±1.0
Bobylev & Bajkova (2010) (Galactic Masers)	17.8±0.8	-13.2±1.5
Shen & Zhang (2010) (Galactic Cepheids)	17.42±1.17	-10.85±6.83
Branham (2011) (G giants)	14.05±3.28	-9.30±2.87

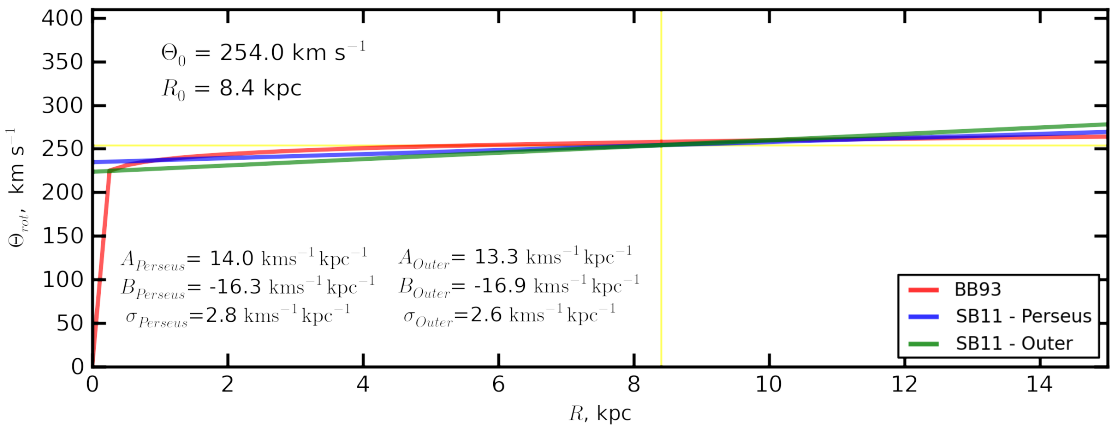

Figure 5.3: Brand & Blitz (1993) rotation curve (in red) plotted with the best fit linear-rising rotation curves. The the *blue* and *green* lines show the predicted rotation curve rise modelled on the Perseus and Outer arms respectively. The *yellow* lines show the solar constants chosen for the fit.

5.2.3 Comparisons with other determinations of Galactic Rotation

Having calculated a gradient parameter from the determinations above, I then overplot the modelled rotation curves for the Perseus and Outer arms in terms of $\Theta(R)$ - see Figure 5.3 - to compare them to the BB93 rotation curve. Both SB11 rotation curves have a steeper gradient than the BB93 curve for $R > R_0$. Considering the SB11 curves in terms of previous findings - the work of Blitz (1979) found that found that around $R \rightarrow 16$ kpc the rotation curve rises by approximately 30 km s^{-1} , which is comparable with the Outer arm SB11 curve. However the work of Pont et al. (1997) - who found that the rotation curve between $R_0 < R < 2R_0$ was flat *but* at about 30 km s^{-1} *less* than the Θ_0 used - this is consistent to what is presented within this thesis. The measurements were confirmed using two conventions for the Solar constants; the IAU standard and $\Theta_0 = 200$ km s^{-1} and $R_0 = 8$ kpc . Though it could be noted that Honma & Sofue (1997) state that the shape of the outer Galaxy rotation curve is sensitive to the adopted values of constants - which can give a negative gradient if one is to use $\Theta_0 \leq 200$ km s^{-1} . I would argue, however, that this is not the source of the discrepancy here. Let us consider the objects which were used to constrain these measurements - classical Cepheids. These are generally younger objects and would be concentrated within spiral arms (Efremov 2011) - over the $R \rightarrow 2R_0$ range both Perseus and Outer arms exist within this bound of R. It is possible that what was observed, as suggested in the paper, are objects residing within spiral arms and as such their velocity is shifted negatively - as per the Shocked-Motion-Model - though the it is interesting that even taking into account the errors on the measurements the negative shift is still larger than what is expected for v_{shock}.

5.3 Analysis of the AMF Data Maps

Before beginning an analysis on the cloud hierarchy and content and how this varies with the linear resolution to which the material is smoothed - I begin with an analysis of the distribution of material within the arm with respect to the arm's centre. In Chapter 4, I presented scale height and mean Z positions for the arms based in the Galactic reference frame, whereas here I present the analysis in terms of a fully arm-centric reference frame - both kinematically and spatially referenced. I use the same X-limits as for the CRM analyses for the Perseus and Outer arms however, the Sct-Cen arm will not be analysed here since the arm is not well constrained outside the second Galactic quadrant, as has already been discussed.

A similar analysis as for the CRM data will be performed here in terms of the scale-heights and relative Z_0^{arm} values for the Perseus and Outer arms. Since previously I fit the scale-height distributions to the arm relative to the Galactic plane, here, I will find these values relative the nominal arm-centre, Z_0^{arm}. Figures 5.4 and 5.5 show the comparison between the CRM and AMF data for the Perseus and Outer arms respectively. As was mentioned in Chapter 4, the correction to the Perseus arm is of a smaller magnitude than the Outer arm, since the Outer arm resides at a much further Galactic radius - it is subject to the warping effects of the Galactic mid-plane. As a result of this, the Outer arm - in the Galactic reference frame - resides at higher b, and hence higher Z, than Perseus.

As was completed for the CRM analysis, I fit the AMF map data using two one-dimensional

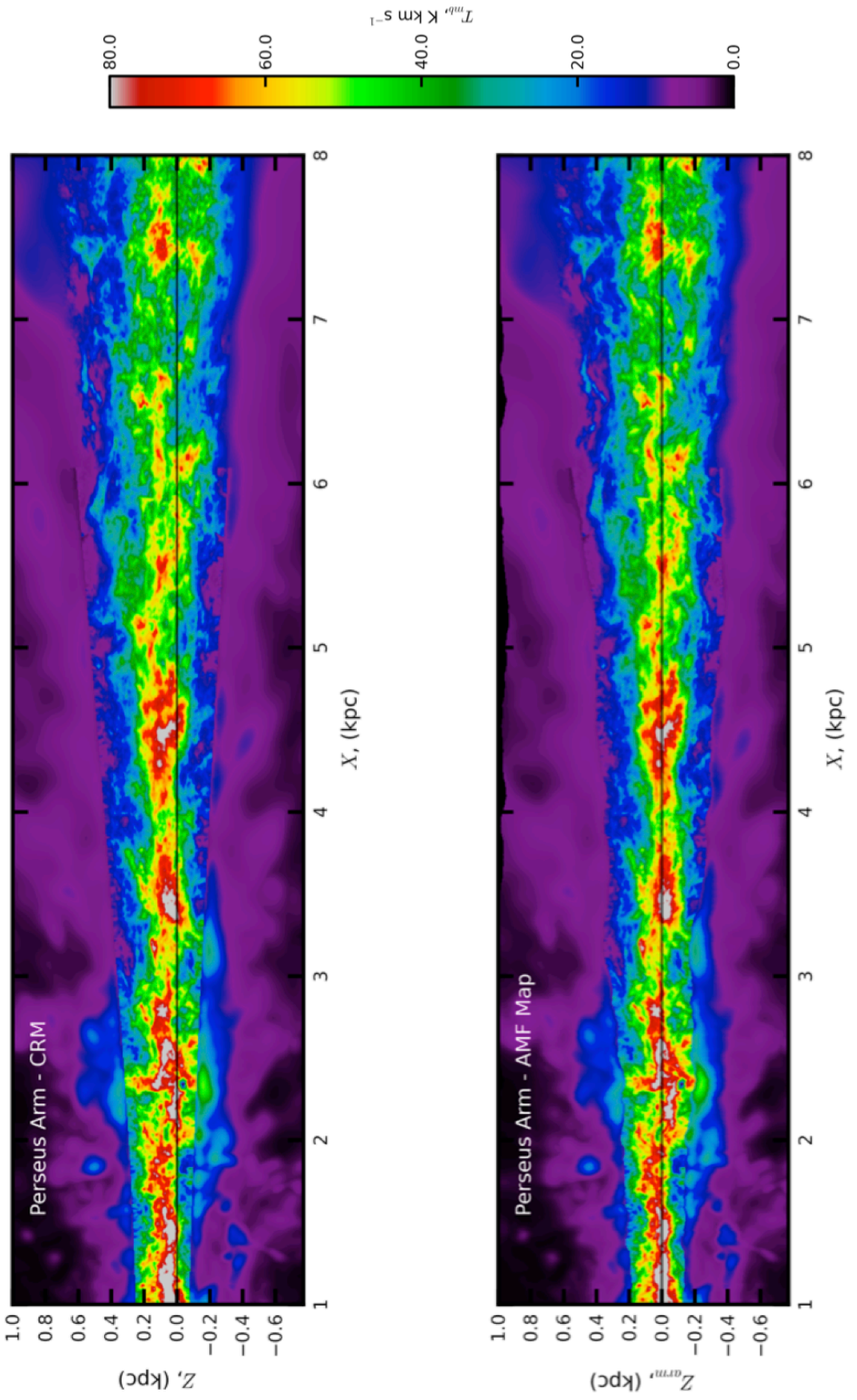

Figure 5.4: The CRM and AMF HI maps for the Perseus spiral arm - 1 kpc $< X <$ 8 kpc . The black horizontal line in the CRM shows the location of the Galactic plane - in the AMF the location of the Perseus arm mid-plane.

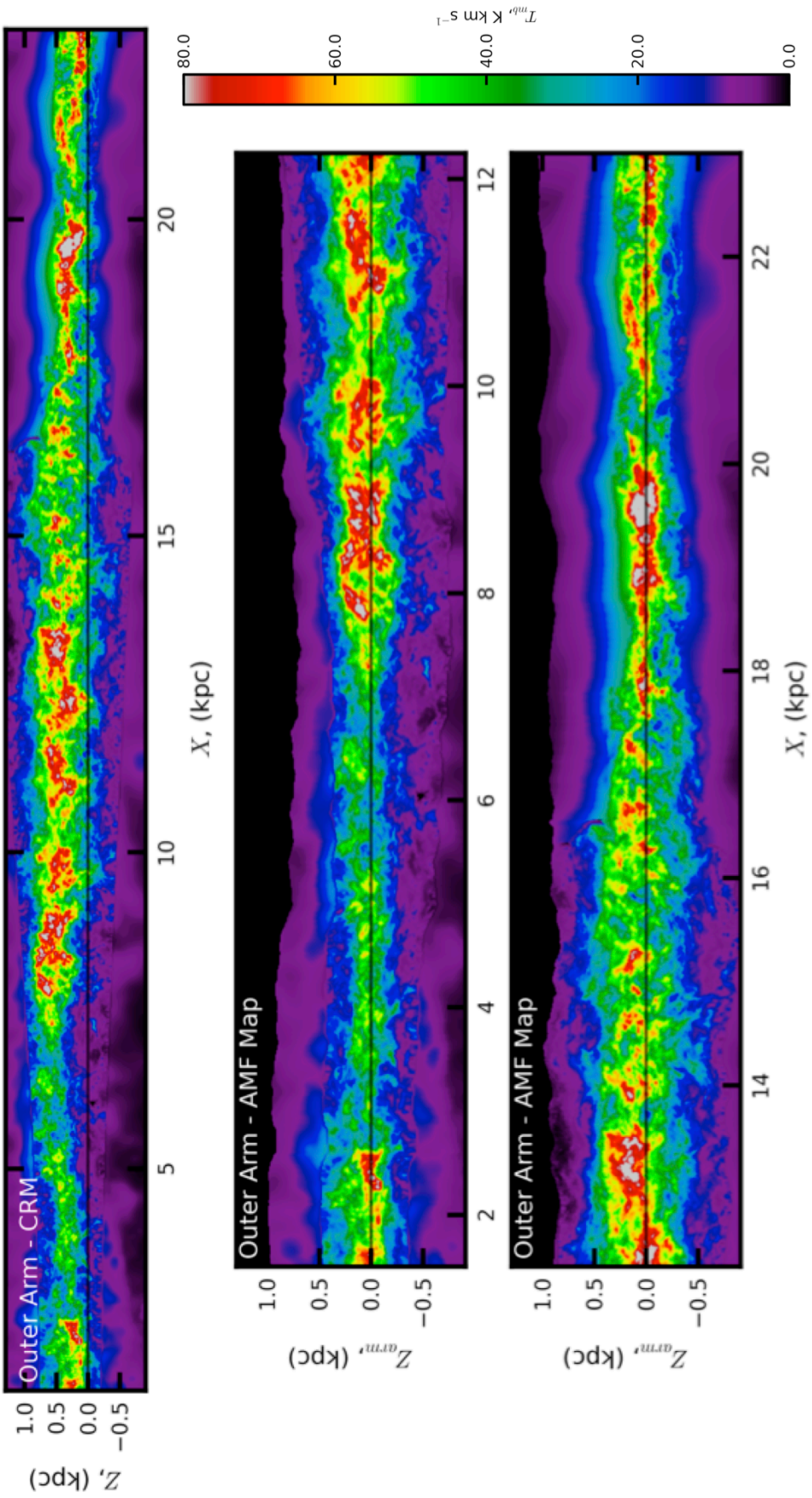

Figure 5.5: The CRM and AMF HI maps for the Outer spiral arm- 1.5 kpc $< X <$ 23 kpc . The black horizontal line in the CRM shows the location of the Galactic plane - in the AMF maps the location of the Outer arm mid-plane.

Gaussian functions, I adopt the same nomenclature and investigate the large-scale structure of the Perseus and Outer spiral arms. The Outer arm has a Z_{FWHM} of approximately twice that of the Perseus arm.

5.3.1 The Perseus Arm AMF

As with the regular CRM data maps I fit a single- and two- component Gaussian function to the distribution to the emission in Z_{arm}. The arm is unconfused with local or kinematically compressed emission over the range $1.0 < X(\text{ kpc }) < 8.0$, it is this range which over which I fit the functions in the previous Chapter and as such is repeated here. Figure 5.6 shows the one component Gaussian is not a good fit the emission well whereas the two component fit describes the emission better. The thick and thin component of the atomic emission is found as Z^{thick}_{FWHM}(HI) = 530.85±2.67 pc and Z^{thin}_{FWMH}(HI) = 213.07±0.71 pc which is larger, in both cases, than when compared to the CRM Z_{FWHM}. Trivially, the mean position of the emission in Z_{arm} is closer to the arm-centre which is as to be expected since the emission has been centred on the nominal arm-centre. The resultant gaussian fit, taking into account both the thin and thick components of the atomic medium, is $Z^{Per.}_{FWHM}$(HI) = 359.85±1.29 pc giving an arm height which is consistent with literature measurements of the Perseus arm's height, 0.2 kpc from Foster & Routledge (2003). The FWHM is a suitable analogue for the arm's scale height since I fit a Gaussian function to the arm emission, hence the FWHM is the full Z extent of the arm - effectively twice the $HWHM$ making it comparable, both qualitatively and quantitatively, to the Foster & Routledge (2003) value.

I also obtain an estimate to the transverse velocity dispersion - the internal velocity dispersion needed to support an arm to $Z^{Per.}_{FWHM}$ if supported only by internal turbulence - to both thick and thin components; $\sigma^{thick}_{v_z}$(HI) =20.57 km s^{-1} and $\sigma^{thin}_{v_z}$(HI) =8.17 km s^{-1} . The larger σ_{v_z} for both individual components are reflective of the larger value for the scale height since they are linearly related to one another (see Chapter 4). Again, as with the CRM data, the thin component of the atomic emission is more comparable to the spectral velocity dispersion - the more compact atomic emission tends to be reflective of the molecular emission being embedded within the thin, compact, atomic component. The resultant Gaussian fit to Perseus has a calculated transverse velocity dispersion of $\sigma^{Per.}_{v_z}$(HI) =12.23 km s^{-1} .

5.3.2 The Outer Arm AMF

Figure 5.7 shows the CRM and AMF fits to the distribution of emission in Z, from Figure 5.5. Here I use the $1.5 < X(\text{ kpc }) < 23.0$ arm selection where the outer arm is unconfused with near/far emission. Like the Perseus arm emission, the Outer arm atomic medium is well fit by a two component gaussian fit in both the CRM and AMF mapping methods. Qualitatively assessing the distributions first, the AMF fits (bottom panels Figure 5.7) make the dual component nature of the atomic gas more noticeable since one may observe a sharper peak of emission in the region of the arm-plane surrounded by more diffuse wider spread emission. The measured scale height to the Outer arm is found to be approximately twice that of Perseus with, Z^{Outer}_{FWHM}(HI) = 601.26±3.22 pc.

The larger scale height of the Outer arm could be indicative of the flaring of the HI disk in

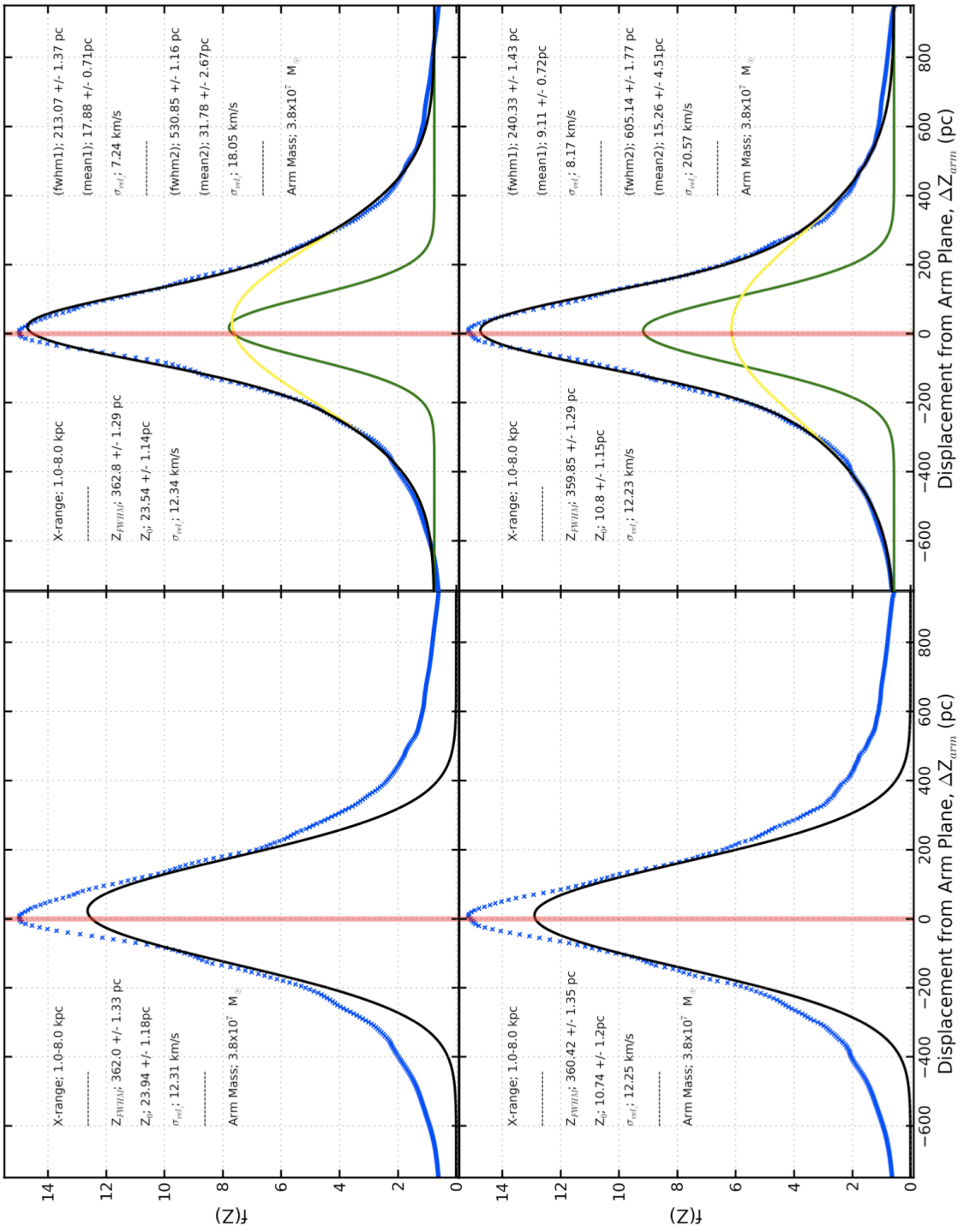

Figure 5.6: The CRM [top] and AMF [bottom] scale height fit relative to the Galactic and Perseus arm centre. HI one Gaussian fit [left] two component Gaussian fit [right] to the Perseus arm. In both cases, the two-component fit to the HI emission provides a better fit to the vertical distribution.

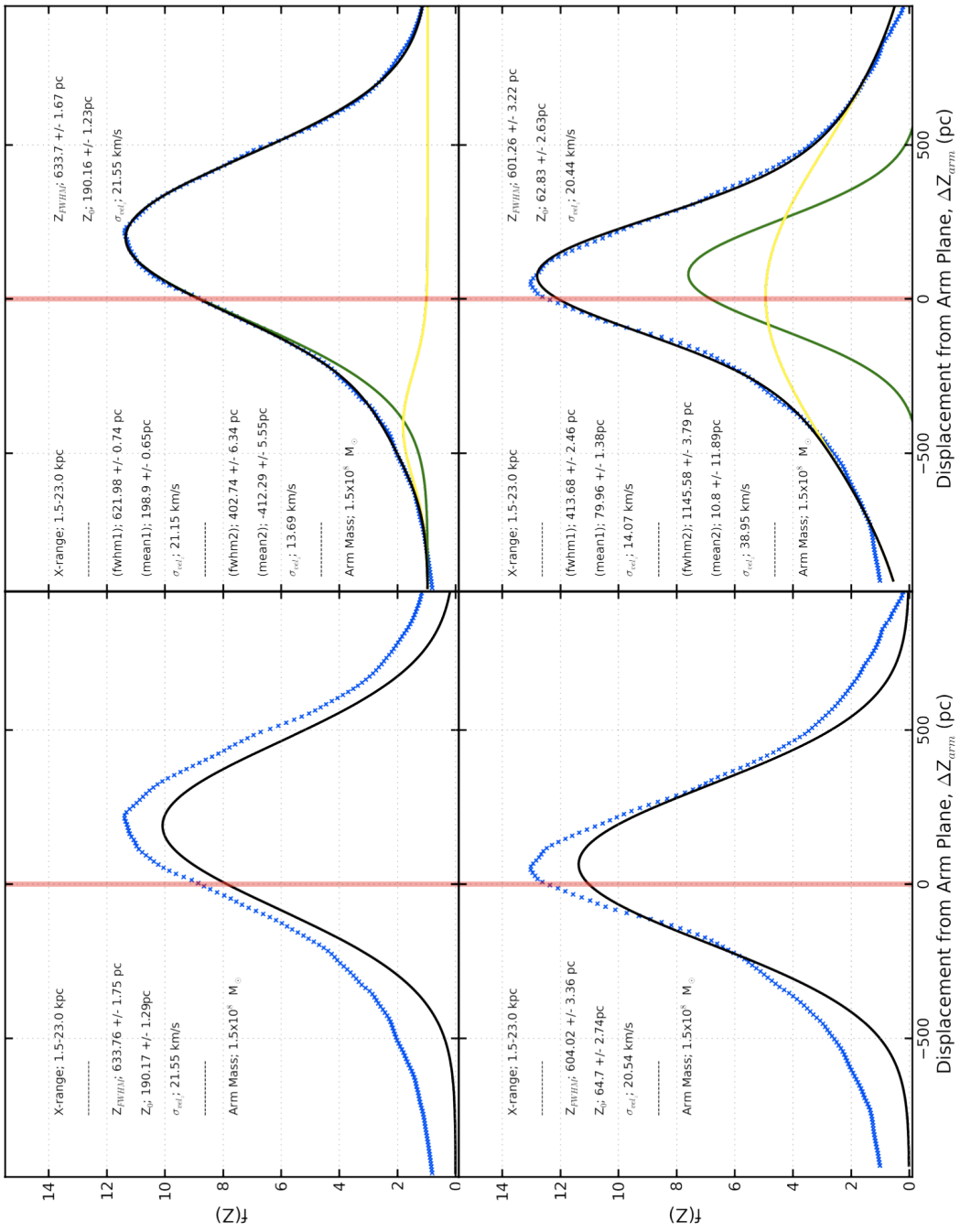

Figure 5.7: The CRM [top] and AMF [bottom] scale height fit relative to the Galactic and Outer arm centre. HI one Gaussian fit [left] two component Gaussian fit [right] to the Outer arm. Unlike the Perseus arm, the two-component fit is not a good match to the vertical emission in the CRM data (top right). However, the AMF data are better fit by a two-component Gaussian (bottom right) to its vertical distribution of emission.

Lee J Summers

Image Copyrighted.
Original source image can be found:

Figure 7, Kalberla & Dedes (2008)

Third Party Copyright Marker

Figure 5.8: HI disc flare using the models derived in Kalberla et al. (2007); adapted from Kalberla & Dedes (2008), Figure 7. The red line shows the mean flaring of the HI gas. The blue line shows the Northern HI and the green line the Southern HI within the Milky Way. The black dashed line shows an exponential fit to the HI.

the region of the Outer arm. Figure 5.8 shows how the HWHM of the HI disc varies with Galactic radius. Over the nominal range of $20^\circ < \ell < 250^\circ$, the range of Galactic radius covered by the Outer arm is 7.5 kpc $< R_{Outer} <$ 15.8 kpc . One may argue that the larger Z_{FWHM}^{Outer} for the Outer arm could be due to the natural flaring of the HI disc over this range.

As with Perseus, it is possible to recover the transverse velocity dispersion from the height of the arm; $\sigma_{v_z}^{thin}$(HI) =14.07 km s^{-1} and $\sigma_{v_z}^{thick}$(HI) =38.95 km s^{-1} for the thin and thick components individually and for the arm as a whole construct - $\sigma_{v_z}^{Outer}$(HI) =20.44 km s^{-1} . On the whole the larger transverse dispersion reflects the flaring of the disc (Kalberla et al. 2007; Kalberla & Dedes 2008). It is noteworthy to question the source of the dual component HI medium - could it be the atomic arm is described by the thin component and the flaring of the disc described by the thick component with the overall distribution of gas being a super-position of the two? Or could it be that the two components describe two different potential or thermal regimes? Though both hypotheses are essentially valid, the former has evidence suggesting it to be true. The thin component of the atomic emission tends to be more comparable to the molecular component of each of the arms - which suggests that the thin atomic component tracks the molecular gas more so. Studies such as Braun & Walterbos (1992); Strasser & Taylor (2004); McClure-Griffiths et al. (2005); Strasser et al. (2007); Kalberla & Kerp (2009) suggest the two-component HI is sources by two thermal phases of the ISM, the cold and warm neutral components thereof (see Chapter 1) - with each being described by the thin and thick component respectively.

5.4 Cloud Decomposition & Analysis

The CRM data maps were subjected to the cloud finding algorithm described in Brunt et al. (2003), then compare the findings to Galactic (Solomon et al. 1987; Heyer et al. 2008) and extra-galactic (Bolatto et al. 2008) cloud samples and analyses. The benefit of the CRM analysis will be that the clouds within the map will have comparable sizes since they can all be assumed to be at a common distance, since in the previous Galactic work of Solomon et al. (1987) compared clouds which existed at a range of distances and as such was comparing the smaller local objects with the large clouds which are at a much further distance.

The Perseus arm decomposition is performed on each of the resolutions mentioned in section 5.1. Before beginning the analysis of the *clouds* it is important to consider, as I alluded to in Chapter 1, just what does constitute a cloud? It is vital that we remember that the ISM is a continuum of density and what we observe as relative maxima and minima are exactly that; relative densities. In this analysis I will not be making the division, between clouds; clumps and cores - since I do not believe that this distinction is needed. I am more interested in the large-scale structure of the spiral arms and as such will present a single decomposition and where I refer to *clouds* as isolated emission of density enhancements in an otherwise continuous medium. I begin by describing the cloud catalogue for the Perseus arm and how they are defined in terms of the parameters input to the cloud-finding routine.

5.4.1 The Cloud Sample & Parameters

The cloud sample is defined per resolution cube, there are four clouding variable inputs;

- $\mathbf{T}_{min}$, minimum temperature, in T_A, threshold cut.
- $\mathbf{N}_{min}$, minimum number of pixels before the program constitutes a clump as coherent structure.
- σ, the standard deviation of the noise for the CRM cube.
- **dT**, temperature step per threshold.

For this analysis $T_{min} = dT = 5\sigma$ for all Perseus Ex-FCRAO CRM cubes. Firstly, I will look at the effect of *clumping* or *splitting* on the overall numbers of clouds within each resolution cube, this was achieved by changing the pixel minimum, N_{min}, which has four values for each resolution, N_{min}=10, 15, 20, 25 and 30 pixels. It is important to note that this is not a selection by linear size, just a raw number of pixels. So therefore the actual linear size corresponding to each pixel selection is effectively a minimum area. The parameter "ΔL" is the same as when the CRM maps were presented in the previous Chapter, i.e. ΔL is the target resolution for each CRM data map. The four choices of ΔL used are; 5 pc, 10 pc, 20 pc and 50 pc. These were selected such that the finest resolution, ΔL=5 pc, is the resolution attainable over the full extent of the Perseus Ex-FCRAO CRM cube. The coarsest resolution, ΔL=50 pc, was selected because the supplementary CO survey - the CfA composite Dame et al. (2001) - is a factor of 10 in resolution worse that the Ex-FCRAO survey and is reflected in the choices, and spread, of ΔL.

When looking at the level of sub-clumping (i.e. the choices of N_{min}), using the ΔL=5pc with N_{pix} <30 was too noisy and did not yield meaningful cloud hierarchy, so the only the N_{pix}=30 is presented for further analysis. Obviously, as one would expect, the number of clouds decomposed in each resolution is N_{pix} dependent and with the resolution and pixel cuts allow the probing to smaller cloud scales. The purpose of these analyses is to present an overview of the properties of the molecular content of the Perseus arm - and not a full decomposition - therefore only the *Parent* cloud definitions will be used, with a Parent cloud being defined as those at the top level of the hierarchy. The N_{min}=30 selection appears to be most representative of the selection of clouds. The smaller selections of N_{min} breaks up the clouds too much and splits objects into smaller sub-clumps which should, in fact, be a single coherent structure.

5.4.2 Mass Spectrum

The first analysis performed on the data is the plotting of a mass spectrum for Perseus arm clouds. I compare the results for each resolution to the Galactic sample of Solomon et al. (1987); Heyer et al. (2008). The mass of each cloud was calculated by multiplying the ^{12}CO by the X-factor which gives a number which can then be converted into the a representation of the cloud's mass - see Chapter 1. A mass spectrum may then be plotted, the clouds' masses are binned with above the lower detection limit. The mass spectrum for all four resolutions is presented in Figure 5.9, with the best fit parameters for the mass-functions being summarised in Table 5.2.

Table 5.2: Perseus arm mass spectrum best fit parameters.

ΔL	Coefficient	Exponent, m
5 pc	$10^{3.13\pm0.03}$	-1.60 ± 0.03
10 pc	$10^{2.77\pm0.25}$	-1.72 ± 0.10
20 pc	$10^{1.77\pm0.19}$	-1.52 ± 0.08
50 pc	$10^{0.41\pm0.36}$	-1.11 ± 0.13

All the resolutions presented of the parent cloud sample in Figure 5.9 fit a power law of slope which is slightly flatter - see Table 5.2 - than the Salpeter mass function (Salpeter 1955) exponent of m_{S55}=-2.35±0.2, angular observations based on the *ogs* region in Heyer et al. (2001) found the slope of m_{H01}=-1.80±0.03, but the slope obtained here is more comparable to the Blitz (1993) (B93) value of m_{B93}=-1.6±0.2 (sourced from Pineda et al. (2009)).

More recent works, fitting to ^{13}CO emission within molecular cloud regions to deepen the completeness limit, Pineda et al. (2009) (P09) find a slope of m_{P09}=-2.4. The P09 work investigated the effects of varying the parameters of the input to `CLUMPFIND` had on the output parameters derived. They concluded that the parameters derived - specifically the mass spectrum,

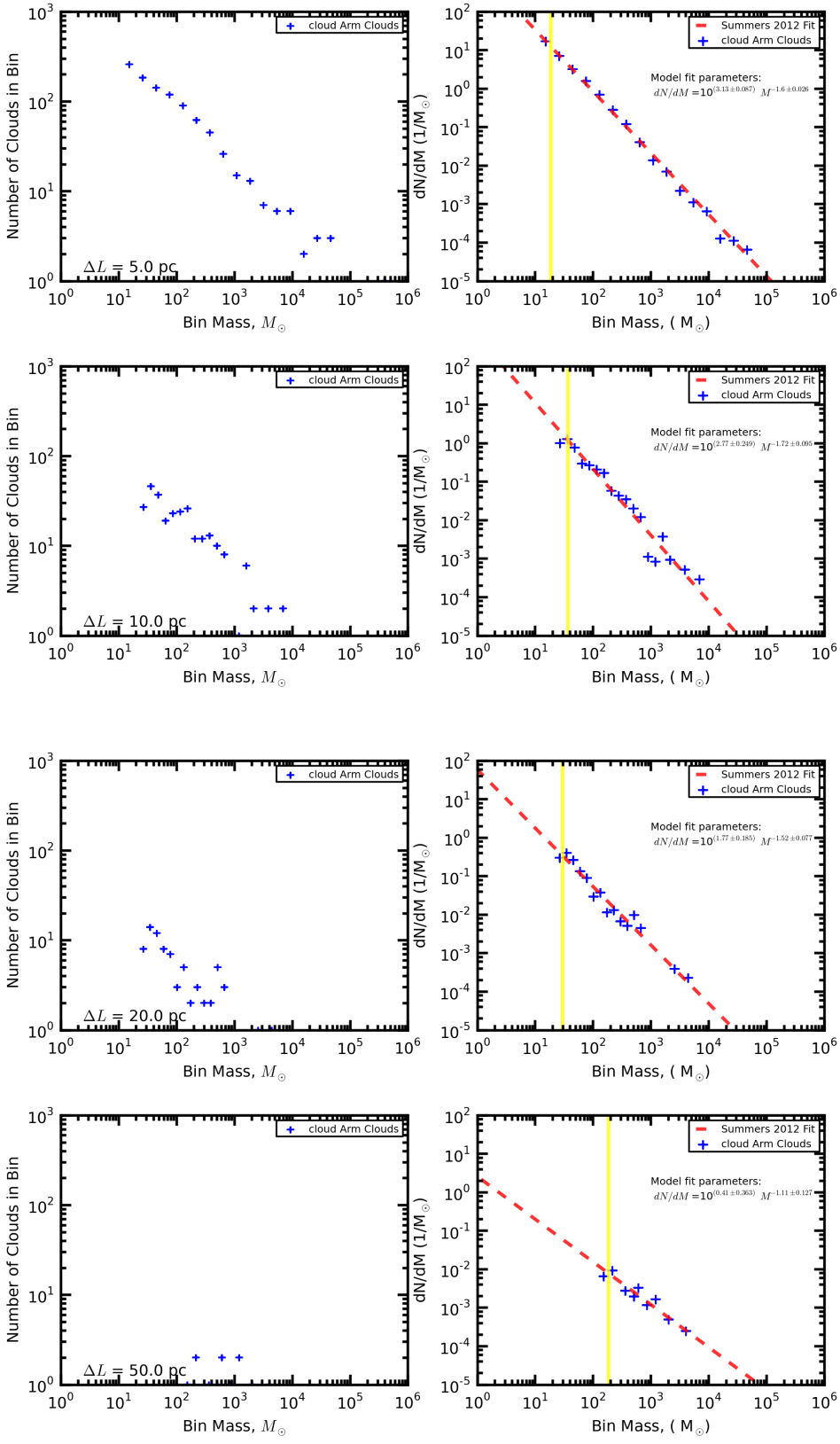

Figure 5.9: The Parent cloud mass spectrum for the Ex-FCRAO data. The blue points show the clouds whose geometric centroid exists within Δv_{arm}=±10 km s^{-1} of the kinematic arm centre. The target ΔL increases from top to bottom with the yellow vertical line showing the minimum detectable mass for each resolution.

but also by inference other parameters may be affected - are dependant on the resolution of the input observational data. The reason for this being due to the hierarchical structure of, not only the general ISM but also on, that of the the individual *clouds* - i.e. a resolution effect, see Section 5.4.5. This could go come way to explaining the the flatter slopes presented here and as the resolution decreases, so to does the steepness of the slope. This could be due to the emission in the CRM data being more spread out and the smaller, lower mass, clouds being omitted from the sample and only the larger mass clouds being resolvable, the findings of Keto et al. (2005), who studied the molecular content of M82, gives credence to this explanation since they present a mass function of slope m_{K05}=-1.5±0.1 which is shallower than the the slope found in the Galactic samples. The slope of the function may also be partially indicative of the relative age of the environment, with studies of younger massive clusters finding slopes of m_{H12}=-1.3±0.1 for Trumpler 14 and 16 (Hur et al. 2012) - both clusters having comparable distances to the Perseus arm d_{helio}=2.9±0.3 kpc (Hur et al. 2012). The slope is shallower still for NGC 3603, which is thought to reside in the Sagittarius-Carina spiral arm, with m_{S04}=-0.9±0.1 (Sung & Bessell 2004) - again possibly relating to the age of the region whether the sample is extracted, i.e. being a Spiral arm.

5.4.3 Size - Line Width Relation

There are two forms of 'size' measurement used here - the first is an effective radius, R_{eff}, based on the 2-dimensional projection of the cloud's area;

$$R_{eff} = \left(\frac{\mathcal{A}_{cloud}}{\pi}\right)^{\frac{1}{2}} \tag{5.4}$$

Where; $\mathcal{A}_{cloud}$ is the cloud's 2-dimensional projection of its area. The second size definition is based on the size parameter presented in Solomon et al. (1987) (hereon S87). The S87 size, S_{87}, is calculated via;

$$S_{87} = d_{helio} \tan(\sqrt{\sigma_\ell . \sigma_b}) \simeq \sqrt{\sigma_X . \sigma_Z} \tag{5.5}$$

Where the σ_ℓ and σ_b is the dispersion in ℓ and b directions of a decomposed cloud and d_{helio} the heliocentric distance to the cloud - this gives a size in linear units. Preliminary analysis found that if I merely translated the dispersions in ℓ, b to be in terms of X, Z - whilst omitting the distance dependance since all the clouds are a common linear scale - the scatter of the size parameter was greater than would be expected when compared to the R_{eff} size definition. As a result, the fitting to the relation was consistently too steep - see Figure 5.11. Also the S_{87} sizes are significantly smaller than those calculated via the R_{eff} - see Figure 5.10.

The additional scatter is introduced because originally, S87 were converting from an angular size to a linear and since the CRM data are a constant linear scale, the assumptions from S87 do not hold true when the data are expressed linearly. At a constant linear, the S_{87} size is effectively the same as the R_{eff} parameter with a factor of $\pi^{-\frac{1}{2}}$ difference, since the $\sigma_X \sigma_Z$ is dimensionally and area. Therefore, I modify the size-parameter's definition assuming the CRM data are at a constant linear scale - which they are. S_{solo}, is defined to be the length of the line bisecting the

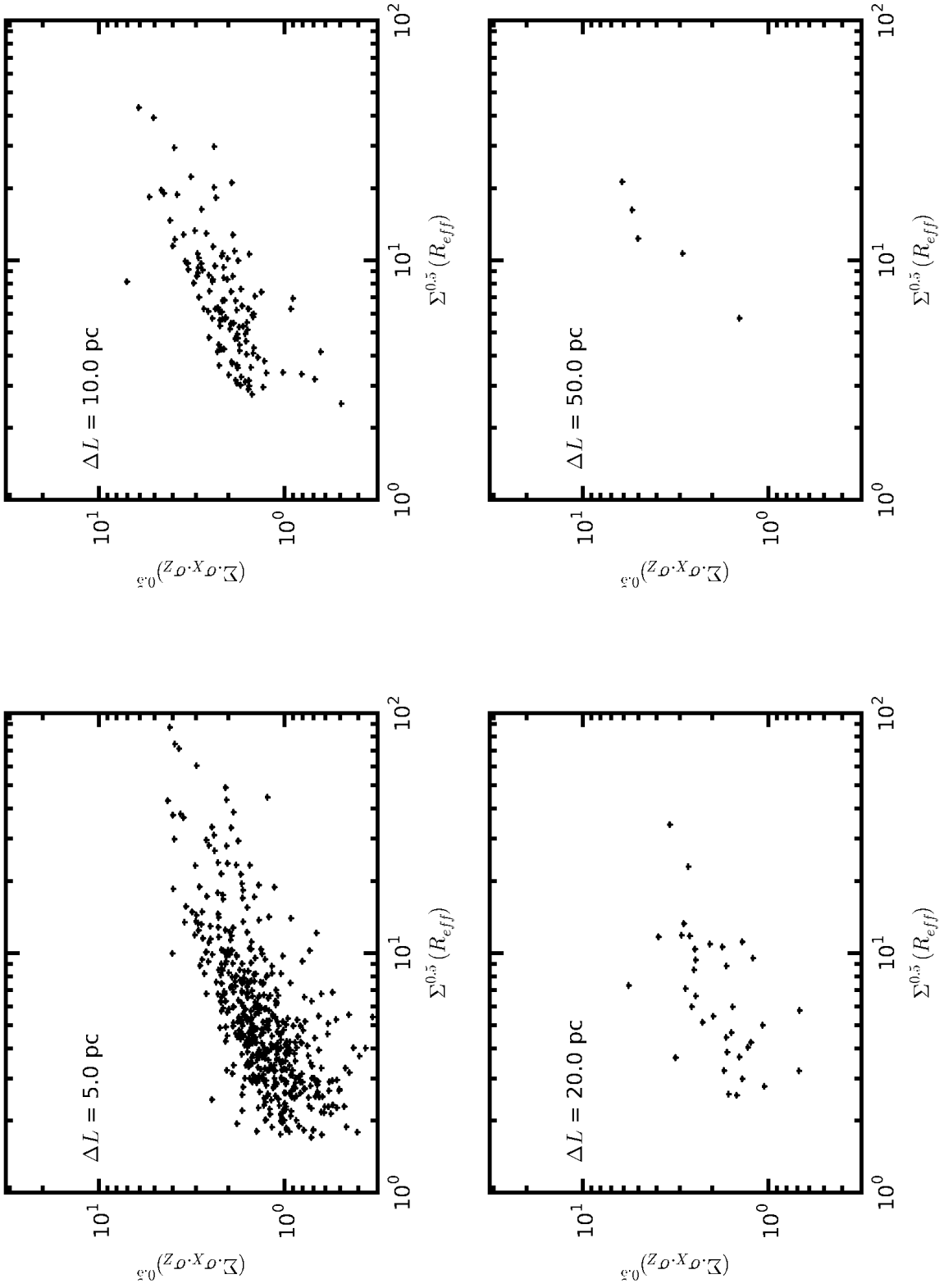

Figure 5.10: Comparison of the two surface density corrected cloud size parameters, R_{eff} and S_{87} for each resolution - the plots indicate the proportionality between the two size definitions.

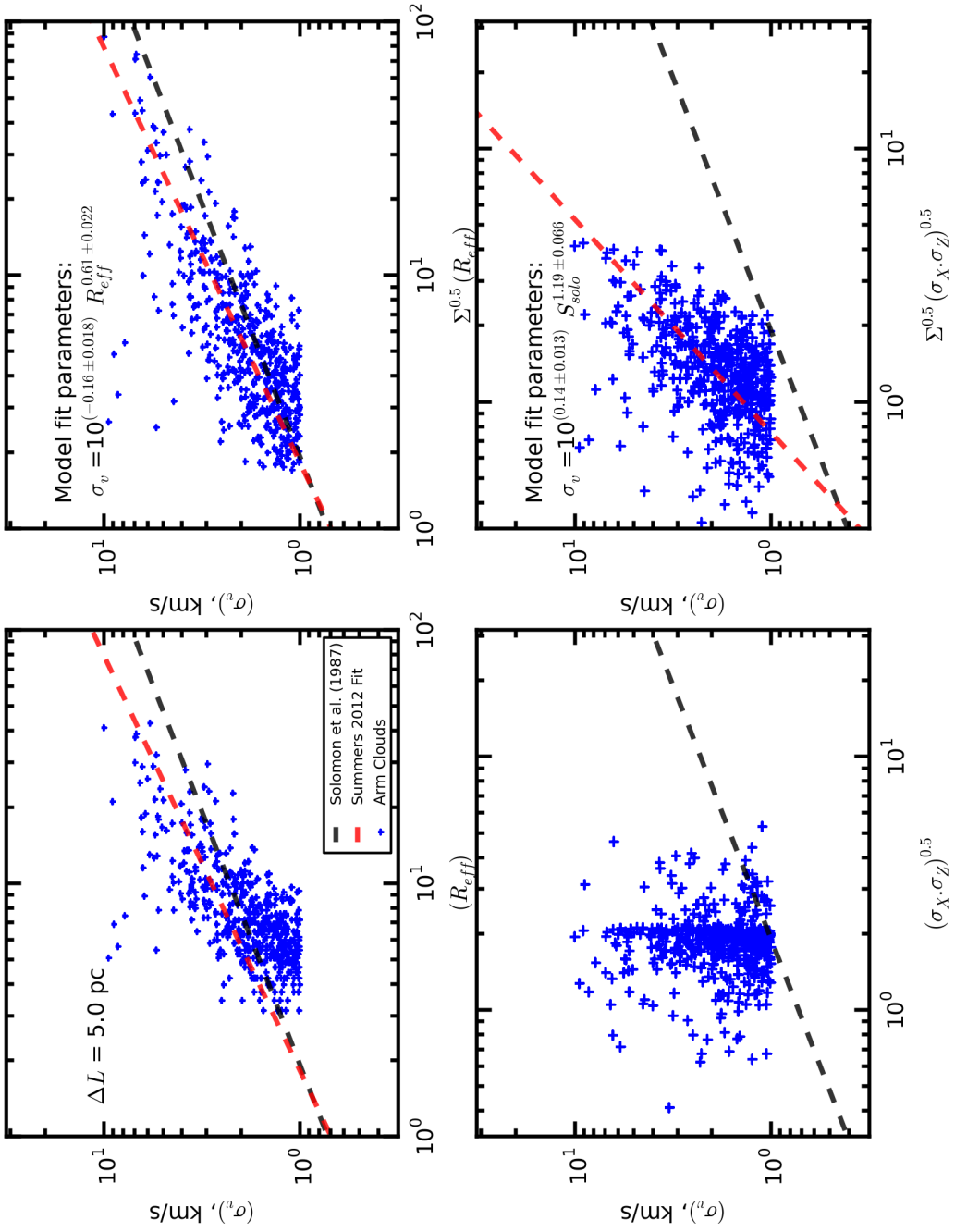

Figure 5.11: Size line-width relations for the R_{eff} and S_{87} size definitions for each resolution. Over plot on the axes are the relation defined by Solomon et al. (1987) and also the best fit to the data (Summers 2012). Though the R_{eff} distribution reflects the findings of the literature (Solomon et al. 1987) - the S_{87} relation does not appear to fit the trend.

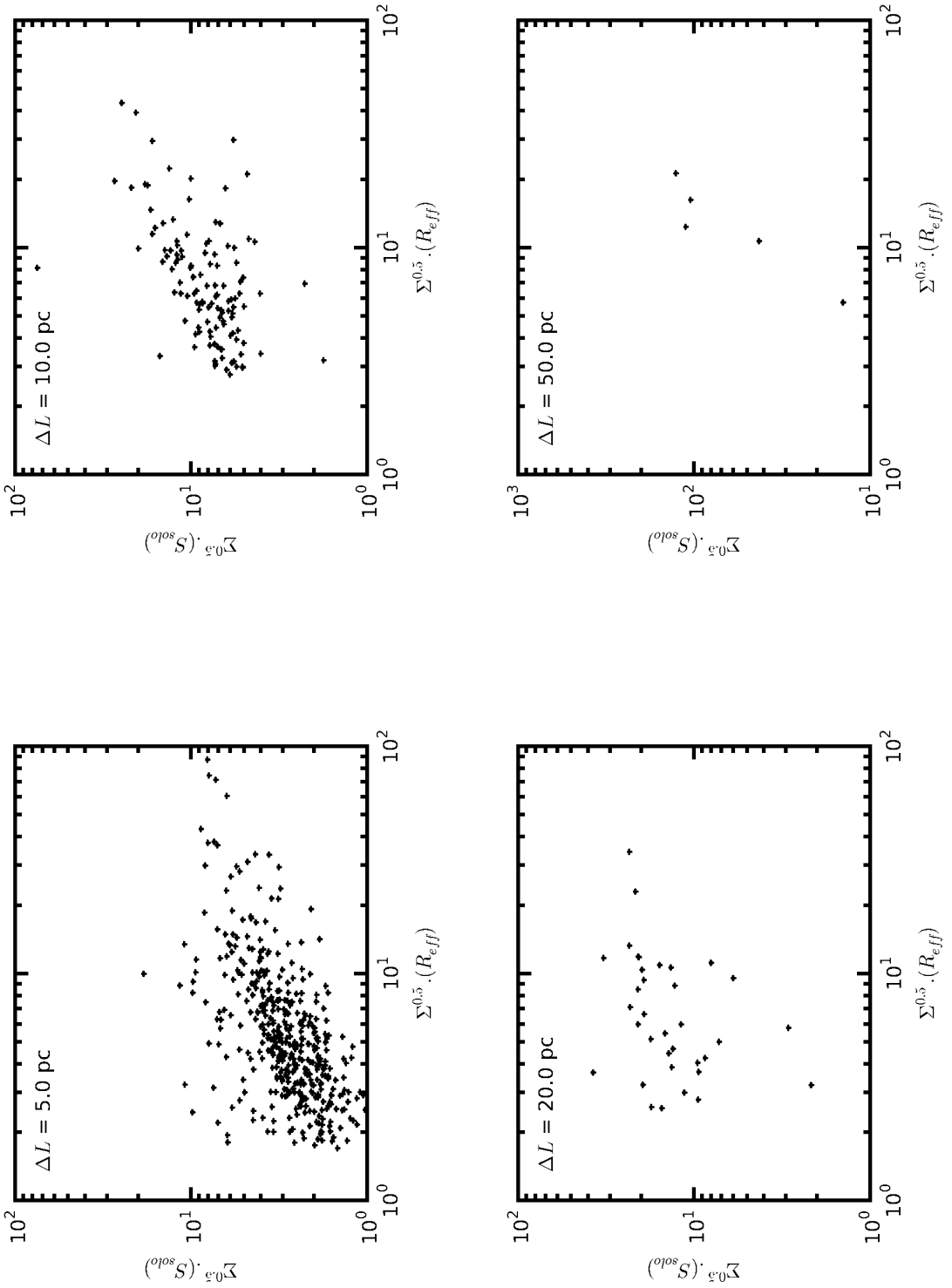

Figure 5.12: Comparison of the two surface density corrected cloud size parameters, R_{eff} and S_{solo} for each resolution. The R_{eff} and new S_{solo} size definitions are monotonically proportional making S_{solo} a viable replacement for S_{87}.

maxima dispersions in X and Z, whilst incorporating a constant scaling factor;

$$S_{solo} = \sqrt{\frac{\sigma_X^2 + \sigma_Z^2}{2}} \tag{5.6}$$

When expressing the size of a cloud in this manner, there is a tighter correlation between the two size parameters (see Figure 5.12) and also the scatter of the S_{solo} size is significantly reduced. - see Figure 5.13.

Heyer et al. (2008) found that the constant required to satisfy Larson's Scaling Laws (Larson 1981) varies as squared-root of the cloud's surface density, $\sqrt{\Sigma_{cloud}}$ dependence on the size-line width relation. The surface density, Σ, is calculated via;

$$\frac{\Sigma}{\mathrm{M}_\odot \mathrm{pc}^{-2}} = \left(\frac{\mathcal{M}_{cloud}}{\mathcal{A}_{cloud}} \right) \tag{5.7}$$

Where; $\mathcal{M}_{cloud}$ is the cloud's mass an - as above - $\mathcal{A}_{cloud}$ is the 2-dimensional projection of the cloud's area.

Figure 5.13 shows the R_{eff} and S_{solo} size line-width relations. Within the Figures, the effect of incorporating a surface density compensation factor has on *correcting* the size parameter is shown by plotting the raw and corrected sizes. The R_{eff}, surface density compensated, size parameter appears to follow the size line-width relation of Solomon et al. (1987); Heyer et al. (2008) for all resolutions, Figure 5.13. The effect of improving the resolution, however, appears to reduce the plausibility of the fit - in that it increases the spread of σ_v for sizes in the region of the resolution limit. This is because as one reduces the resolution, so too does the size of the minimum detectable object, very small objects can be subject to noise and so when corrected for surface density, the values are not effected.

Table 5.3: Perseus arm size line-width relation best fit parameters.

ΔL	R_{eff} Coefficient	R_{eff} Exponent	S_{solo} Coefficient	S_{solo} Exponent
5 pc	$10^{-0.16\pm0.02}$	0.61 ± 0.02	$10^{-0.15\pm0.03}$	0.92 ± 0.06
10 pc	$10^{-0.26\pm0.04}$	0.63 ± 0.05	$10^{-0.35\pm0.09}$	0.68 ± 0.09
20 pc	$10^{-0.38\pm0.10}$	0.83 ± 0.12	$10^{-0.26\pm0.15}$	0.46 ± 0.13
50 pc	$10^{-0.56\pm0.32}$	0.76 ± 0.30	$10^{-0.37\pm0.10}$	0.33 ± 0.06

The slope calculated from the R_{eff} size definition is consistently sleeper than the expected literature relation of $\sigma_v \propto size^{0.5\pm0.05}$, presented in Solomon et al. (1987). But is, however, of comparable value - for all the resolutions - to the relation presented to the extragalactic clouds, found in Bolatto et al. (2008), of $\sigma_v \propto size^{0.60\pm0.1}$. The S_{solo} size definition though is an improvement on the raw S_{87} definition from the beginning of this section, with the scatter significantly reduced for

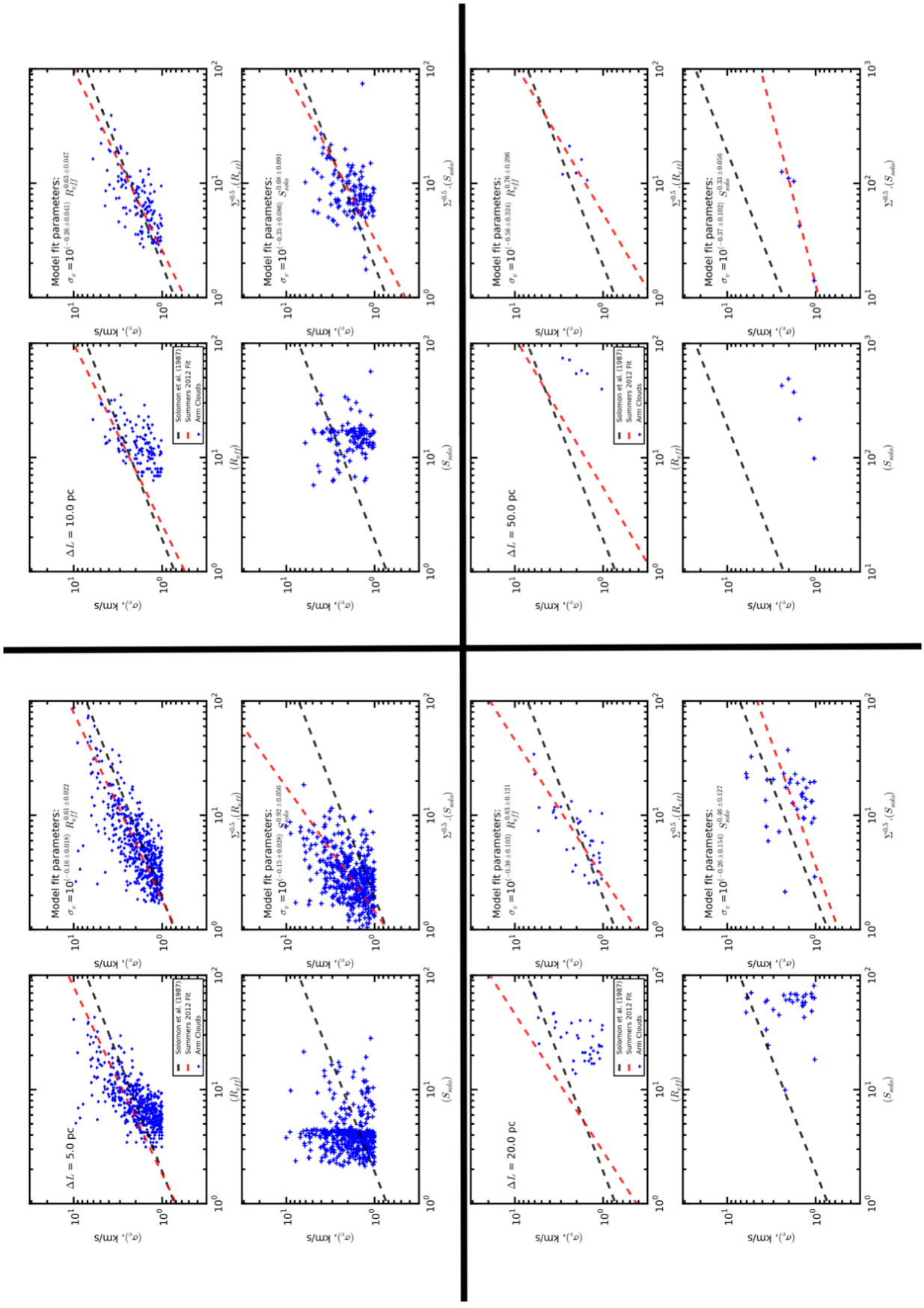

Figure 5.13: Perseus arm size line-width relations for the R_{eff} and S_{solo} size definitions for each resolution. Over plot on the axes are the relation defined by Solomon et al. (1987) and also the best fit to the data (Summers 2012).

the S_{solo} relation. Though it is obvious that the relation is improved with the incorporation of the surface density dependance on the size parameters in both cases. However, it is important to notice that the gradient of the relation for the S_{solo} size is dependant on resolution, see Section 5.4.5, this is more than likely that the lower resolution biases against smaller, highly turbulent clouds being included in the sample. I would indicate at this juncture that the ΔL has so few parent clouds within the sample, when compared to the other resolutions, that the validity of the slope for both the R_{eff} and S_{solo} definitions are probably unreliable at this point and do not reflect the true trend in the region - again highlighting the importance of clumping/splitting and the effective resolution. Resolution effects in clump finding algorithms is discussed in Section 5.4.5.

5.4.4 Luminosity-Size Relation

The last parameter plotted is the final Larson relation to be investigated, the luminosity-size relation. The literature luminosity-Size relations for molecular clouds, from Solomon et al. (1987) - Equation 5.8 - and Bolatto et al. (2008) - Equation 5.9 - are shown beow.

$$\mathrm{L_{CO}} = 25.\mathrm{R}^{2.5}\ (\mathrm{K\ kms^{-1}\ pc^2}) \tag{5.8}$$

$$\mathrm{L_{CO}} = 7.8^{+6.9}_{-3.7}.\mathrm{R}^{2.54\pm0.2}\ (\mathrm{K\ kms^{-1}\ pc^2}) \tag{5.9}$$

Table 5.4: Perseus arm Luminosity-Size relation best fit parameters.

ΔL	R_{eff} Coefficient	R_{eff} Exponent	S_{solo} Coefficient	S_{solo} Exponent
5 pc	$10^{1.0\pm0.02}$	3.25 ± 0.03	$10^{1.58\pm0.11}$	3.84 ± 0.06
10 pc	$10^{0.70\pm0.06}$	3.27 ± 0.07	$10^{0.74\pm0.47}$	2.94 ± 2.28
20 pc	$10^{0.80\pm0.10}$	3.26 ± 0.13	$10^{1.51\pm0.45}$	1.65 ± 1.35
50 pc	$10^{0.66\pm0.34}$	2.95 ± 0.31	$10^{1.1\pm0.25}$	1.51 ± 2.83

Figure 5.14 show the luminosity-size relation for the two difference size definitions with the best fit parameters summarised in Table 5.4. As with the size line width relations, the R_{eff} parameter is self consistent but has a steeper slope than that of the expected gradients from the literature. Also, as was seen in the size line-width relations, the S_{solo} size does appear to be resolution dependant with the gradient of the slope decreasing with resolution. I propose this being for the same reasons as for the size line width relation, in that the lower resolution makes the cloud more diffuse/extended and as such the range of masses - hence luminoisties - decreases and is biases towards larger sizes. As with most of the parameters derived here, the deviations from the 'expected' canonical values could be explained by samples on which they are based. The

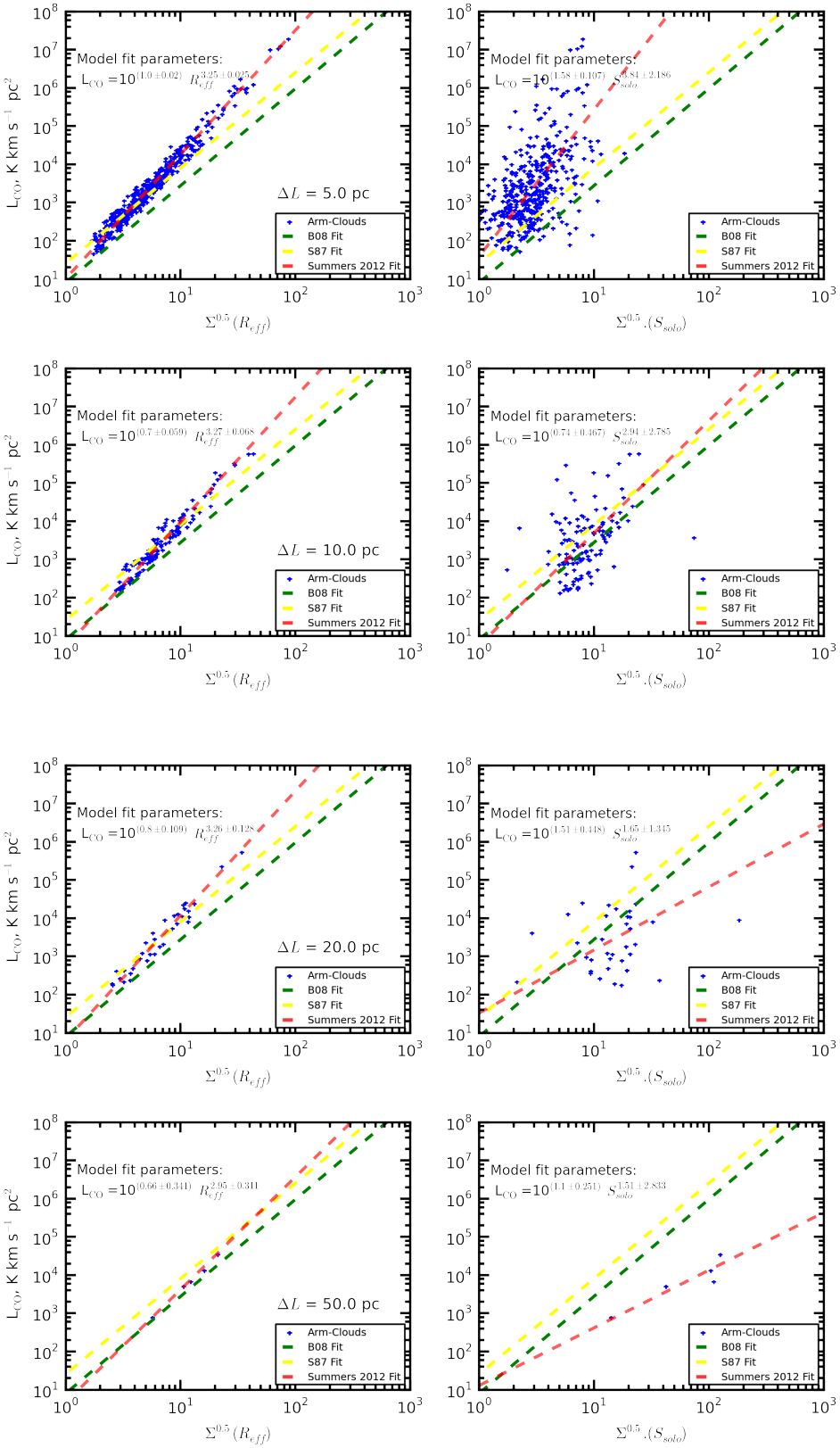

Figure 5.14: Luminosity-Size relation plots corresponding to the values in Table 5.4, for the two different definitions of a clouds' size - R_{eff} and S_{solo}. The errors in the parameters are based on the scatter of the data about the best calculated fit.

B08 relations are generated using extragalactic samples and as such are at a lower resolution that the best CRM maps here. This would force a more shallow gradient - as we have seen - meaning that the clouds are artificially extended in the region of the resolution limit and also the sample of clouds is going to be bias against clouds of a smaller size. On the Galactic scale, in terms of the angular observations of Solomon et al. (1987) - there is a possibility as was mentioned previously, that near-by small objects are being compared to distant large objects and there properties being treated as comparable. This could go some way to explaining the difference between the S_{solo} size and the expected relations for the S_{87} size, though there is a distance dependance on the dispersive size, there is still a possibility that the distance assigned to an individual cloud - within the Solomon sample - is not correct due to kinematic contamination.

5.4.5 The Apparent Resolution Dependence of Derived Parameters

Systematic Resolution Effects in Clump Finding Algorithms

Having completed the analysis, the apparent resolution dependance on the S_{solo} size definition is concerning and undesirable, though this is to be expected. There is precedent set in the recent literature, that there are systematic resolution effects introduced into cloud catalogues when using clump-finding algorithms (Schneider & Brooks 2004; Pineda et al. 2009; Curtis & Richer 2010; Reid et al. 2010). Discussing the literature chronologically, beginning with the work of Schneider & Brooks (2004), whilst conducting a large-scale ^{12}CO survey of the Carina molecular complex ($\approx$ 2.2 kpc , extended over 130 pc) produced a cloud decomposition and analysis using both `CLUMPFIND` and `GAUSSCLUMPS`. Schneider & Brooks (2004) found that the scaling relations determined from the decomposition, provided by each algorithm, were not consistent with literature values. They suggest that for observational data-sets with a limited spatial resolution, by either design or via sub-selection, the application of cloud-finding algorithms without an understanding on how the level of hierarchy and decomposition behaves within the routines can lead to a falsified interpretation of the physics and structure of the molecular clouds studied.

Further work by Pineda, Rosolowsky, & Goodman (2009) found that, when using `CLUMPFIND`, one should not *blindly* derive mass functions using the cloud definitions output by the algorithm. It was suggested that the ^{13}CO mass spectrum derived was dependant on the resolution of the observations due to the hierarchical nature of the host molecular cloud - i.e. the level of substructure to which the cloud is resolved during decomposition. Pineda et al. (2009) goes on to say that though there is a strong functional dependance of the resolution with the mass spectrum's slope, there is no dependance on the initial threshold selected. Interestingly, the ^{13}CO power-law exponent varies as deeper levels of sub-structure are probed - the implication being that it is unlikely that there is a single mass-function fully describing the decompositional structure of the parent molecular cloud. Pineda et al. (2009) finally hypotheses that the resolution dependance of the cloud sample can be eliminated by taking into account the hierarchy of the decomposition by presenting the data as dendrograms. An analysis of the star-forming core population in Perseus conducted by Curtis & Richer (2010) performed a clump decomposition and extraction on SCUBA 850 μm data using the `CLUMPFIND` and `GAUSSCLUMPS` algorithms. Like the Schneider & Brooks (2004) study of Carina,

Curtis & Richer (2010) found that CLUMPFIND found fewer clumps than GAUSSCLUMPS - 85 and 122 respectively - owing to the different methods by which emission is hierarchised. The parameters derived from the clump analysis were different depending on which clump sample was used to determine and fit the scaling relation. Unsurprisingly, Curtis & Richer (2010) also observed a resolution dependance on their break down of the core-like objects in the sample. They suggest the discrepancy between literature values and the values presented in their work is due to the fact that the cores could, conceivably, be broken up further by higher resolution observations. This implies, as with the previous works discussed, that there is not only a dependance on the algorithm used, but also in the resolvable limit of clouds within one's sample.

Lee J Summers

Image Copyrighted.
Original source image can be found:

Figure 5, Reid et al.(2010)

Third Party Copyright Marker

Figure 5.15: Adapted from Figure 5 Reid et al. (2010): Differential clump mass functions (black lines) with power-law fits (gray lines). Each mass function is fit with the best-fitting double power law or, where a double power law did not produce a good fit, a single power law. The number and text indicated in the upper right corner of each plot is the power-law index of either the single power law or the high-mass portion of the double power law, the qualitative noise level and the resolution.

To complete this section, there has also been work carried out using simulations of star-forming regions to observe and interpret the effects of resolution and decomposition techniques. Motivated by the clump mass function increasingly being used in determinations of star formation theories, Reid et al. (2010) used simulated images of star-forming regions to investigate the effects that resolution limits and the methods by which cloud definitions are acquired have on the derived mass function. They found that even in the situation where their images had been smoothed to a lower resolution and degraded by the addition of synthetic noise - to a degree where the clumps in the image no longer correspond to the definition of *cores* - the clump mass function that they were able to derive was still comparable to the literature relations. The conclusion they

draw over this worrying result is, the lower resolution and noise contributes to a perturbation of the individual clump masses such that the derived function is best described by a Salpeter power law. As such, this is merely a consequence of the central limit theorem - explaining why higher resolution observations, equivalent to probing deeper levels of substructure, do not appear to present a Salpeter slope. The plots in Figure 5.15 show the effect which Reid et al. (2010) describes with the slope varying with both resolution and noise level. The mass functions derived from the CRM data follow the same basic trend as with the Reid et al. (2010) data, with the coarse resolution images having a less negative slope than the data, at a comparable noise level, but at a finer resolution. The hypothesis suggested by Reid et al. (2010) - as I summarised earlier - is that a combination of effects, the coarse resolution, turbulence, temperature variations, radiative effects, uncertainties in the flux to mass conversion, idiosyncrasies in the clump-finding algorithms used, image noise, source blending, and spatial filtering may lead to a situation where clump mass functions always appear lognormal - and by inference yield a Salpeter slope.

The New Size Definition, S'_{solo}

To attempt to compensate for the resolution dependance of the S_{solo} definition, I decided to return to the original definition of the S_{87} size and considering the $\sigma_X\sigma_Z$ as an area and treating it as such. A new size based on the dispersions, S'_{solo} was calculated via;

$$S'_{solo} = \sqrt{\frac{\sigma_X\sigma_Z}{\pi}} \tag{5.10}$$

I re-plot the size line-width and also the Luminosity size relations for the new, S'_{solo}, size definition in an attempt to see if the resolution dependance can be compensated for. This - though still based on the dispersions - is a more comparable size definition to R_{eff}. Mainly due to the treatment of the combinations of these dispersions as an effective area rather than a length. To some extent, the resolution will still have an influence on what section of the possible cloud sample is being probed - in terms of its minimum size. But this new dispersive size will not be as susceptible to this bias - or at least be equally systematically affected as the R_{eff} size - as for the previous dispersive definition.

The size line-width and Luminosity-Size relations for the S'_{solo} size definition can be seen in Figures 5.16 and 5.17 respectively. It is apparent, from the plots, that the resolution dependence still exists - however with the relations' gradient converging on the expected value from the literature at higher resolutions. One could easily say that this new size treatment compensates for the resolution dependence at lower resolutions and as a result, this is the treatment which should be used. However, were I to be sceptical - this is only the case because there is an expected value to be reached, in the form for the B08 and S87 relations. It is possible that at higher linear resolutions, the expected relations do not hold and it is the spreading out of the clouds at lower resolutions in to more diffuse structures which gives the relations this expected value - as has been proven in the literature.

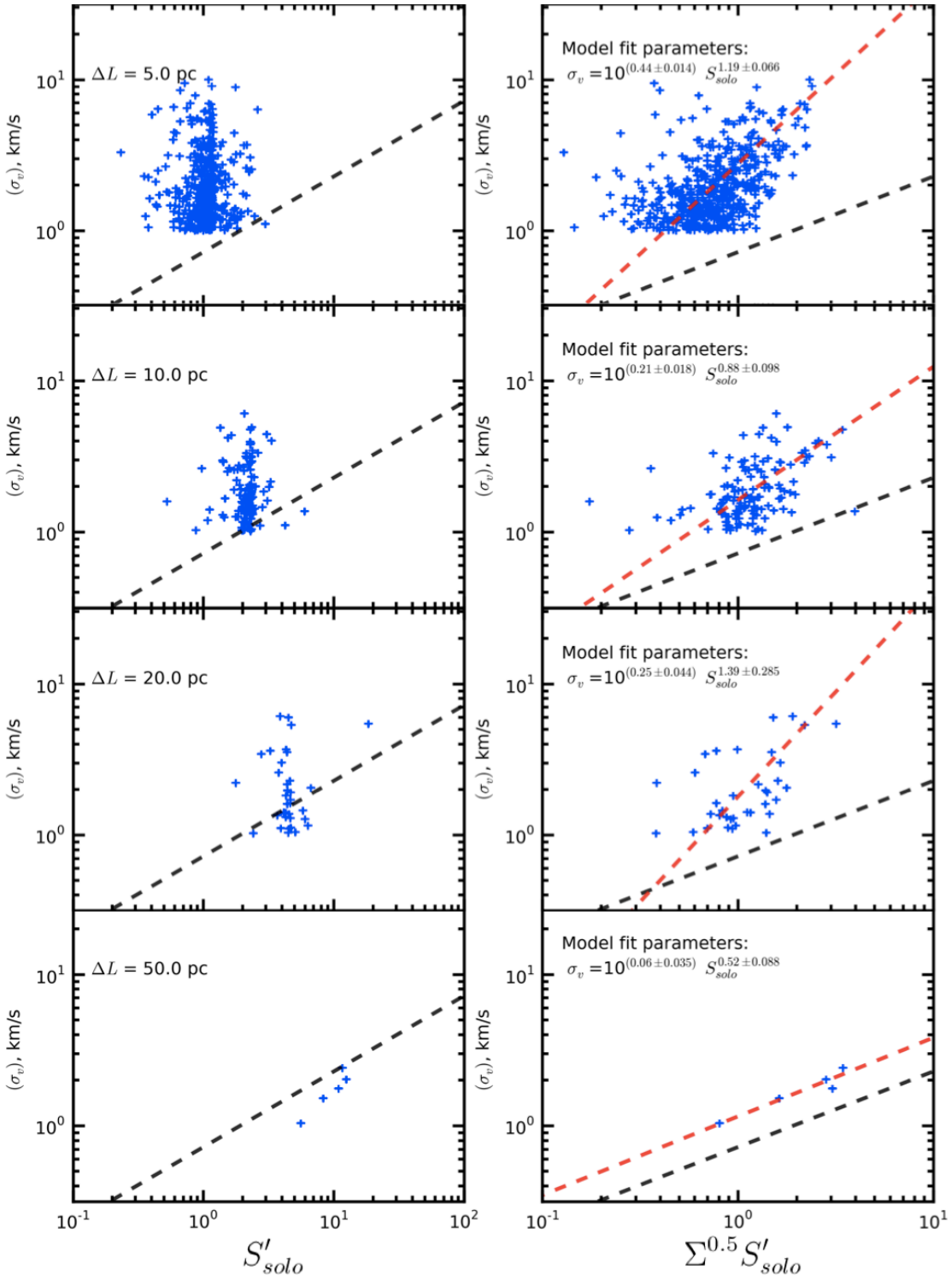

Figure 5.16: Perseus arm size line-width relation for the S'_{solo} size definition, fits derived via a bisector fit to the data. Resolution deceases from the top to bottom panels.

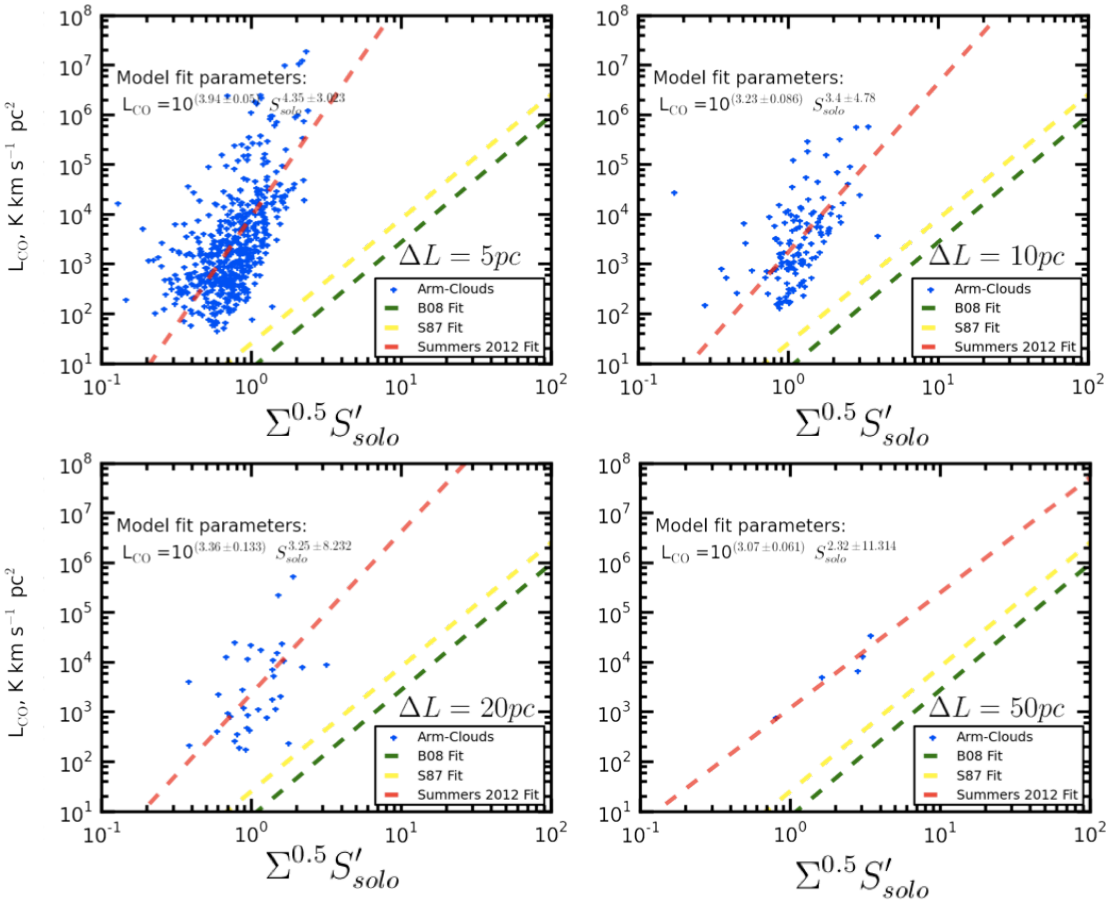

Figure 5.17: Perseus arm Luminosity-size relation for the S'_{solo} size definition. Resolution decreases from the top to bottom panels.

The N_{min} Anomalies

It is also noteworthy to mention the phenomena which occurs in some of the data and was not expected. Best exemplified by the S_{87} data in Figure 5.11 and also in the S'_{solo} data which has not be surface density corrected in Figure 5.16. The clumps which make up the vertical clump have a 2-dimensional (N_{pix}^{2D}) of approximately half the N_{min}, with the remainder of the pixels existing in the spectral axis. Hence the *spike* of vertical clumping with a common 2D size. A more thorough analysis of the cloud data and more post-processing would enable this effect to be reduced. Though, it is noteworthy to mention that the surface density compensation appears to reduce the effect and improves the fit - since the surface density is a spatial compensation and is not influenced by the velocity extent of an individual cloud.

5.4.6 The Outer Spiral Arm

I also conducted a brief analysis of the Outer spiral arm at a representative resolution - i.e. a resolution which is achievable over the full extent of the Ex-FCRAO survey - of ΔL=20pc. As with the Perseus arm, I use the same size parameters of R_{eff} and S_{solo} - but also introduce the

Table 5.5: Outer arm relation best fit parameters, ΔL=20 pc CRM data.

Relation	Coefficient	Exponent, m
Mass Spectrum	$10^{3.61\pm0.17}$	-1.70 ± 0.05
Luminosity-Size (R_{eff})	$10^{0.52\pm0.04}$	3.64 ± 0.04
Luminosity-Size (S_{solo})	$10^{2.42\pm0.24}$	1.47 ± 0.34
Luminosity-Size (S'_{solo})	$10^{3.99\pm0.07}$	2.40 ± 1.55
Size line width (R_{eff})	$10^{-0.42\pm0.04}$	0.71 ± 0.04
Size line width (S_{solo})	$10^{0.15\pm0.04}$	0.09 ± 0.02
Size line width (S'_{solo})	$10^{0.18\pm0.02}$	0.62 ± 0.06

S'_{solo} size - to present the mass spectrum, size line-width and Luminosity-Size relations for the Outer arm at ΔL=20pc. All the Outer arm parameters for the R_{eff} and S_{solo} size definitions can be seen in Figure 5.18, with the additional plots for the S'_{solo} size being presented in Figure 5.19. All the best fit parameters are summarised in Table 5.5.

As for the Perseus arm, the S'_{solo} size has the best fit parameters closest to the expected literature values, giving credence to this size definition as a better description of a Galactic cloud's linear size when comparing a sample to literature. It also suggests that the current canonical relations are only such due to the resolution limit which is achievable for a given observation and also the resolution effects and biases inherent with the clump-finding algorithms used - see earlier.

5.4.7 Clump Finding Summary

As was discussed previously in Section 5.4.5, the clump finding and analysis presented here replicated the resolution dependance of the derived relations which had already be been identified - and discussed - in the literature as being due to limitations of the clump finding algorithm used. The target values of ΔL - the smoothed linear resolution - were chosen based on the Ex-FCRAO ^{12}CO survey. The best resolution was selected to be 5 pc which is the maximum resolution achieved over the complete Ex-FCRAO region, the coarsest resolution was chosen to be ten times that value, since - in angular terms - Ex-FCARO survey is a factor ten improvement on the CfA composite survey of Dame et al. (2001). The linear resolutions - and by inference the equivalent angular resolution when comparing to Solomon et al. (1987); Heyer et al. (2008) - achieved are better, and more self consistent, than the extragalacitc Bolatto et al. (2008) sample, whom have cloud sample a series of resolutions ($\approx$ 10pc $\rightarrow\approx$120pc) due to their varying distances (Bolatto et al. 2008,

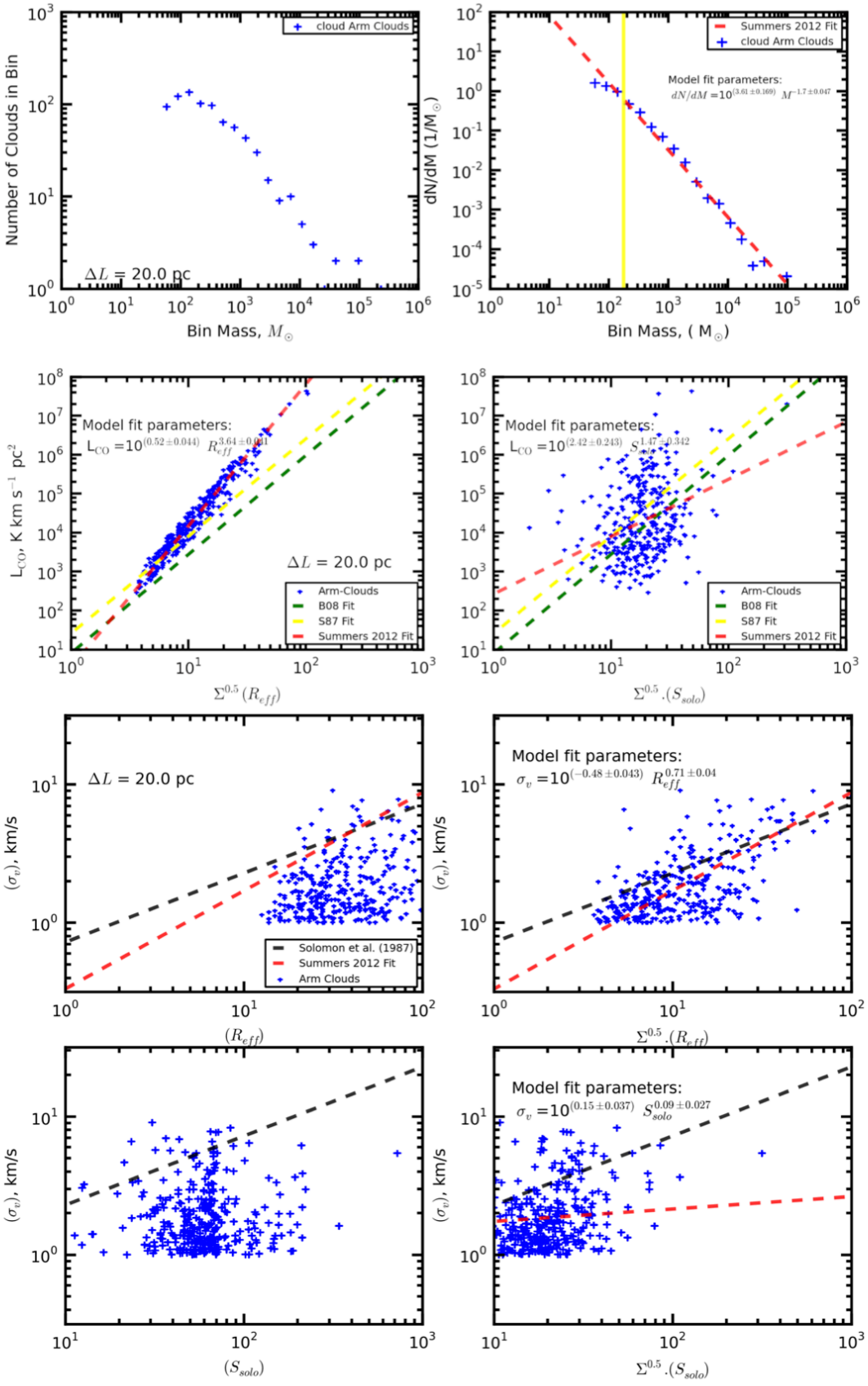

Figure 5.18: Outer spiral arm molecular content parameters. From top to bottom; Mass spectrum, Luminosity-Size relation, R_{eff}-line width relation, S_{solo}-line width relation.

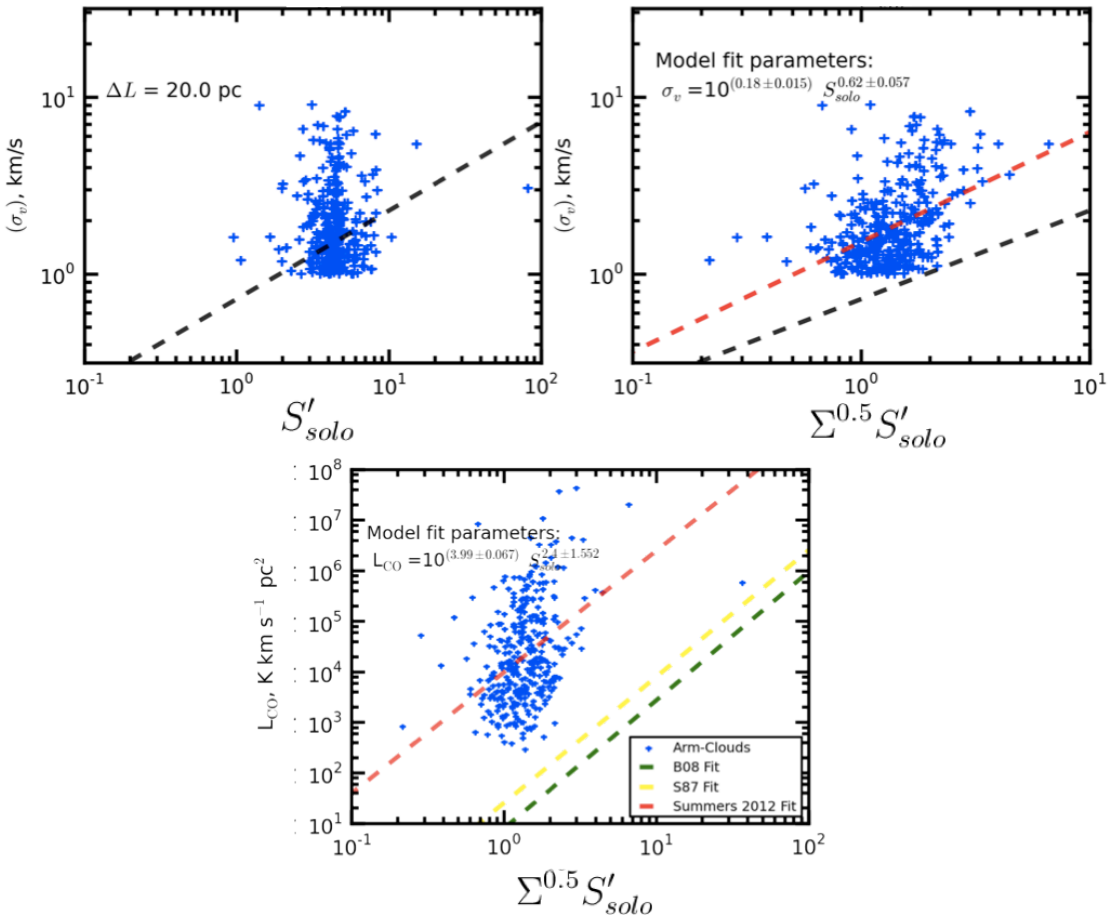

Figure 5.19: Outer arm size line-width and Luminosity-size relations for the S'_{solo} size definition, for ΔL=20pc.

Figure 7). This must be taken into account when evaluating the results presented here, since the clouds presented in this sample are all at a common distance and at a common resolution across the full extent of each arm.

As I have mentioned at various points within this Chapter, and also earlier in Chapter 1, the effective resolution dependance is representative of the level of clumping or splitting. The lower resolution effectively aggregates more material per 'clump' and the higher resolution allows one to probe more deeply the substructure of the ISM. The reasons for this were discussed in Section 5.4.5. The is also another consideration which must be taken into account when interpreting the results from the CRM data for the Perseus arm - and to a greater extent, the Outer arm - is that though the data are smoothed to a common resolution, the maps of the arm do span a series of Galactic radii. The clouds to be included within the sample to be analysed were limited to a subset of the each arm which is kinematically unconfused with back- and fore-ground emission. Even so, though the clouds within the arm are all defined to be within the arm, the section arm itself spans a range of R, and as a consequence, different Galactic environments.

Beginning with the mass functions derived for the Perseus arm. The best fit exponents for the data did reflected the resolution dependance of the parameters derived - as discussed in

Section 5.4.5 - and, as a consequence, do not reflect the relations presented in the literature. This was also reflected in the the size line-width relation - an expression of the equilibrate turbulent conditions within the ISM. Unlike the works of Solomon et al. (1987) and Bolatto et al. (2008) who found that the ratio $\frac{\sigma_v}{R^{0.5}}$ was constant for their respective molecular cloud samples, here it was found to vary. As in Heyer et al. (2008) there is a dependance of this relation of the square root of the surface density of the clouds within the sample. This suggesting that there is variation in the scale and presence of the turbulence within self-gravitating molecular clouds - as predicted by Mouschovias (1987). It is with the higher resolution of the Ex-FCRAO survey, of which the ogs region is subject, used in the Heyer et al. (2008) analysis which finds the variation of the $\frac{\sigma_v}{R^{0.5}}$ with surface density. This, again, lending credence to the resolution dependance of the derived relations and physics. Even the introduction of an alternative size definition of, S'_{solo}, in an attempt to nullify the resolution dependance of the cloud size, did not improve the derived relations. However, the lower resolutions for did appear to reflect the literature values more closely, again implying that the current canonical relations may be subject to change with the advent of new instrumentation and a reduction in the biases of the clump finding techniques.

The brief analysis of the ΔL=20 pc Outer arm CRM data cannot be subject to the resolution dependance investigation, as was completed with the Perseus arm, since there was only one resolution presented. The S'_{solo} size definition reflects the literature values more closely, this is probably is due to the level of sub-structure that the resolution probes to. Evidence of the beginnings of a turn-over at the lower mass end of the Outer arm mass function perhaps being indicative of this. Maybe, then, it is not the resolution of the observations alone which changes the parameters of the derived relations, but instead it is the the level to which the ISM is broken up - i.e. clumped or split. Therefore, the resolution dependant relation variance may be related to the depth to which the ISM is decomposed, rather than the influence of the improved resolution itself.

CHAPTER 6

Final Summaries & Conclusions

"In proving foresight may be vain:
The best-laid schemes o' mice an' men
Gang aft agley.'
Robert Burns, 1785

6.1 Summary of Work Presented

The work detailed within this thesis has presented the initial steps towards a coherent description of the spatial and kinematic structure of the Milky Way's spiral arms - which will be developed and built upon. There are two works presented here; the precursor and the model. Beginning with the precursory work, Appendix C, I investigated the relation between the age of stellar clusters and the mass of molecular material surrounding the cluster which is residual from its formation. The ^{12}CO data are taken from the Ex-FCRAO CO Survey of the Northern Galactic Plane (Brunt et al. in prep) with the stellar cluster catalogue being based on the WEBDA online catalogue and the catalogue described in Dias et al. (2010). It was found that the most of the material which was present for the clusters' formation has been dissipated - or at least not residual from formation - by $\approx 10^7$ years. It was found that the distance and age estimates of the clusters within these catalogues were not as reliable as first thought - which led to the introduction of errors when assigning velocities and whether the cluster resides within the arm. It was found that the models used to describe the kinematic and spatial structure of the Perseus arm were not representing the behaviour and structure within the high-resolution ^{12}CO data. This lead to the work in modelling the the Milky Way's spiral structure.

The model of spiral structure devised makes use of defining a spatial and kinematic description of each of the arm features. Initially, I planned to model on the Perseus arm, but as the work progressed I found that this model could also describe the Outer and outer Sct-Cen spiral arms too. The key results of each section of work are presented in the following Chapter with the limitations,

possible extensions and the future direction of this line of enquiry presented in section 6.6.

6.2 Spatial Fitting to Spiral Structure

The spatial structure of each arm were fit by a linear logarithmic spiral which were then constrained by known arm objects - with measured distances. For the Perseus spiral arm, the spatial structure was fit to methanol and water masers taken from Reid et al. (2009); Oh et al. (2010); Shiozaki et al. (2011); Niinuma et al. (2011). The Outer spiral arm is fit to various tracers with measured distances taken from various works - Maser emission (Hachisuka et al. 2009; Reid et al. 2009; Sanna et al. 2011), measurements of open stellar clusters (Pandey et al. 2006) and spectroscopic observations detections of early-type stars (Negueruela & Marco 2003, 2008). Unlike the Perseus and Outer arms, the outer Sct-Cen arm is not as constrained as the other two outer Galaxy spiral arms. I applied a kinematic distance correction for the molecular cloud complexes identified within Dame & Thaddeus (2011) - using these corrected kinematically estimated distances I fit the linear logarithmic spiral to these molecular complexes. From the linear fit, one is able to derive several parameters about each of the spiral arms.

An estimate as to the width of an arm is taken to be the dispersion about the best fit line to an arm's tracers - one may assume that the tracers observed span the full width of an observable arm and not solely the near or far side. An estimate as to the pitch angle of an arm is calculated via the arctangent of the differential - in the linear log case being the gradient - of the best spatial fit. The XY projection of the models for the Perseus, Outer and outer Sct-Cen arms over 2π radians of Galactocentric longitude can be seen in Figure 6.1 - the level of constraint as not been improved for this fit it is merely to show how the models behave. The main limitation of the linear fit to the spiral arms is that one must assume a constant pitch angle across the whole length of the arm. An extension for this work will be to fit more complex logarithmic forms to the data - see section 6.6.

Table 6.1: The Spatial parameters of the Shock-Motion-Model of Spiral Structure. $ln(R) = a_0 + a_1\theta$

Spiral Arm	a_1 (kpc)	a_0 (kpc)	ϕ_{pitch} (°)	Arm Width (kpc)
Perseus	0.270±0.06	1.898±0.09	15.1±3.3	0.45
Outer	0.237±0.03	2.220±0.04	13.3±1.4	1.51
outer Sct-Cen	0.235±0.04	2.537±0.03	13.2±2.3	1.06

6.3 The Kinematic Shocked-Motion-Model

Having fitted the spatial structure of an arm, it was then possible to fit and model the kinematic structure of each of the spiral features. There were three *iterations* investigated for the kinematic

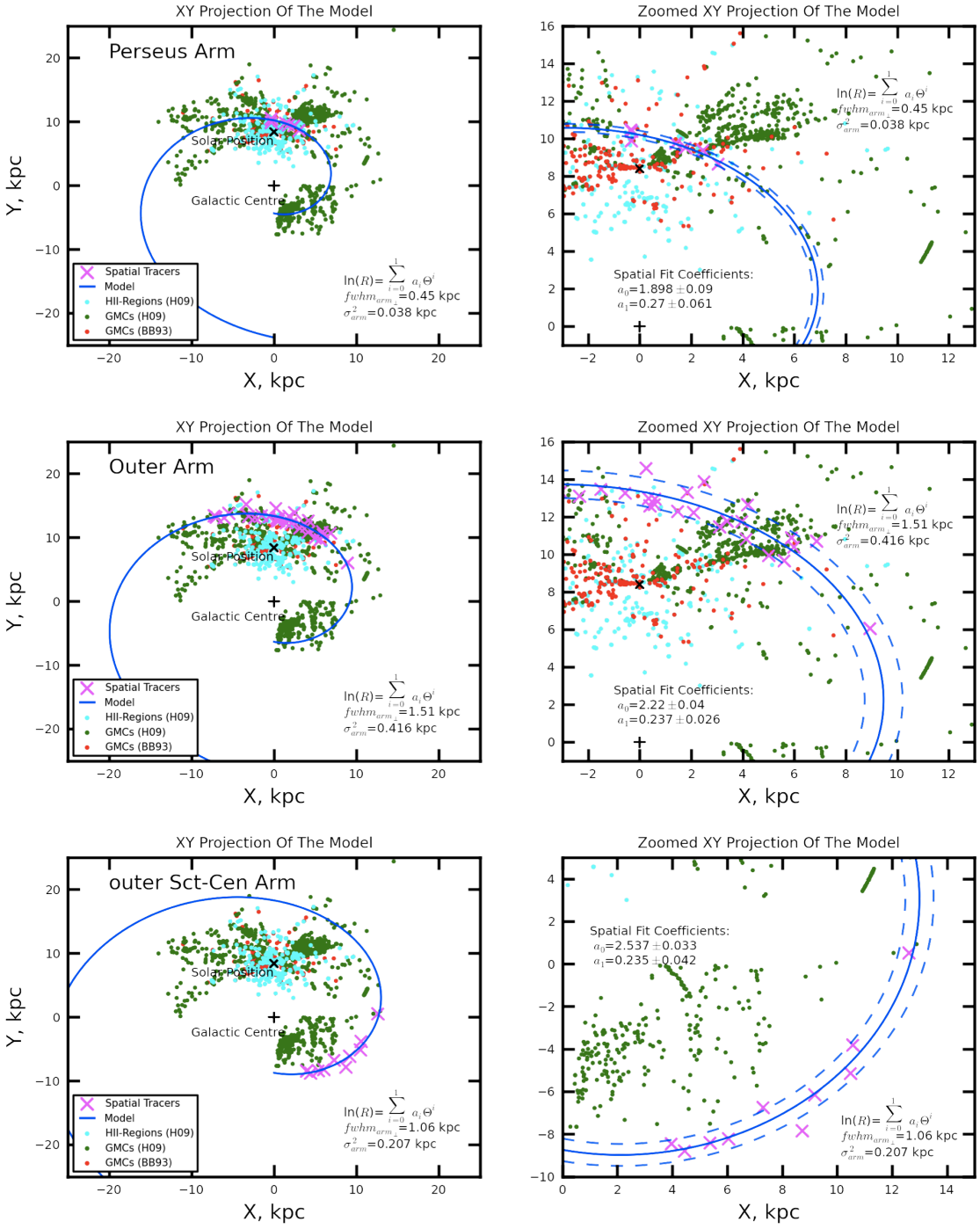

Figure 6.1: Galactic *XY* projection of the spatial model fits overplot with the tracers used to fit the models. Also plot are HII and GMC data Hou et al. (2009) (H09) and also GMC data from Brand & Blitz (1993) (BB93). Solid blue line shows the spatial-arm-centre with the dotted lines either side of the fit corresponding to the interpretation of the arm width being one $fwhm_{arm_\perp}$ as described by the spread of the arm tracers fit. The positioning of the GMCs and HII regions show the *fingers-of-god* effect and the inaccuracies which can be introduced by kinematically determined distances.

structure:

- **Constant Shock** with *Flat Rotation Curve*
- **Variable Shock** with *Flat Rotation Curve*
- **Constant Shock** with *Non-Flat Rotation Curve*

The kinematic models were initially best fit via a least-squares reduction to the velocities assigned to the spatial fitting tracers. This was used to define an initial kinematic locus, which would then be used to refine the model based on molecular cloud positions. The interpretation of the kinematic model is that as material enters a spiral potential it is subject to a scalar negative shift in velocity - a shock - which is vectorially dependant on a shock angle. It is possible to obtain an observed velocity for a point in a spiral arm, v_{obs}, via;

$$v_{obs} = \left((v_0 - v_{shock}).\sin\left(\arcsin\left(\frac{R_0}{R}\sin(\ell)\right) - \Delta\phi_{sp}\right)\right) - v_0\sin(\ell) \tag{6.1}$$

Table 6.2: The shock parameters of the constant Shock-Motion-Model of Spiral Structure.

Spiral Arm	v_{shock} (Tracers) (km s^{-1})	$\Delta\phi_{sp}$ (Tracers) (°)	v_{shock} (clouds) (km s^{-1})	$\Delta\phi_{sp}$ (clouds) (°)
Perseus	20.0±3.6	2.0	20.0±3.3	1.6
Outer	13.0±6.9	3.3	9.0±4.8	3.6

It was found that the first order approximation of a constant shock was found to be suitable for the relatively small span of Galactic radius in the Perseus arm. However, when fitted to the Outer arm, at lower longitudes, the fit was found to track too positive a velocity. It was deduced that the lower longitude values required a stronger shock, so a variable shock model was devised - see equation 6.2. This model was found to improve the fit of the Outer arm *and* enable the kinematic description of the outer Sct-Cen arm. the variable shock parameters for the Outer and out Sct-Cen arms is shown in Table 6.3.

$$v_{obs} = \left(\left(v_0 - \left(v_a - v_b.\left(\frac{R}{R_0} - 1\right)\right)\right).\sin\left(\arcsin\left(\frac{R_0}{R}\sin(\ell)\right) - \Delta\phi_{sp}\right)\right) - v_0\sin(\ell) \tag{6.2}$$

Using the kinematic model we were able to isolate the arm material from within the spectral line surveys suing Arm-Centric-Velocity Mapping. The regions kinematic designations, as defined by the model can be seen in Figure 6.2. It is important to be aware of the velocity compressed regions around +/-15° of the anti-centre (ℓ =180°). A conservative estimate of where the regions are kinematically distinct is between the longitude range of $50° < \ell < 150°$, i.e. in the first and second quadrants, beyond this range, the level of constraint is variable.

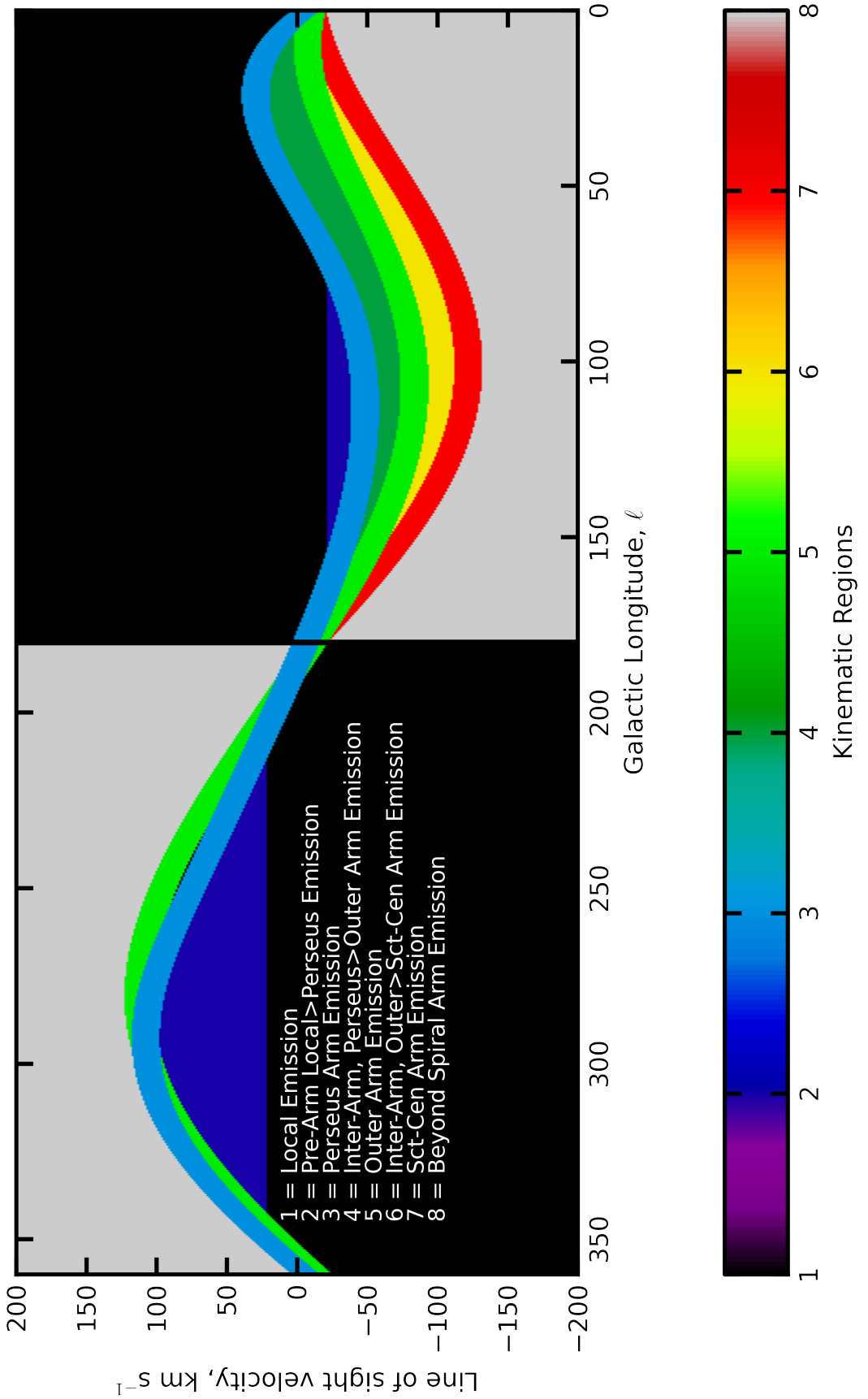

Figure 6.2: The above Figure shows the $\ell - v_{LSR}$ structure of the models and the various kinematically defined regions of the Galaxy as dictated by the model presented. The outer Sct-Cen arm is limited to ℓ <180°- due to this being the upper most ℓ of identified molecular cloud candidates and also that the outer Sct-Cen arm is only constrained to $\ell \simeq 58°$.

Table 6.3: The shock parameters of the variable Shock-Motion-Model of Spiral Structure.

Spiral Arm	Fit To Tracers v_a (km s^{-1})	Fit To Tracers v_b (km s^{-1})	Fit To Tracers $\Delta\phi_{sp}$ (°)	Fit to Clouds v_a (km s^{-1})	Fit to Clouds v_b (km s^{-1})	Fit to Clouds $\Delta\phi_{sp}$ (°)
Perseus	20.0	0.0	2.0	20.0	0.0	1.5
Outer	16.0	9.8	3.1	22.5	37.0	2.8
outer Sct-Cen	20.0	22.0	2.7	-	-	-

Table 6.4: Comparison of Oort's Constants A and B from literature and this work

Reference	A (km s^{-1} kpc^{-1})	B (km s^{-1} kpc^{-1})
Summers 2012 (Perseus)	14.0±2.8	-16.3±2.8
Summers 2012 (Outer)	13.3±2.6	-16.9±2.6
Kerr & Lynden-Bell (1986) (IAU Standard)	14.4±1.2	-12.0±2.8
Hanson (1987)	11.3±1.1	-13.9±0.9
Feast & Whitelock (1997)	14.8±0.8	-12.4±0.9
Gould & Ramirez (1998)	14.5±1.5	-12.5±2.0
Elias et al. (2006)	14.0±1.0	-18.0±1.0
Elias et al. (2006) (Gould Belt)	11.0±2.0	-20.0±1.0
Elias et al. (2006) (Local Galactic Disk)	16.0±2.0	-16.0±1.0
Bobylev & Bajkova (2010) (Galactic Masers)	17.8±0.8	-13.2±1.5
Shen & Zhang (2010) (Galactic Cepheids)	17.42±1.17	-10.85±6.83
Branham (2011) (G giants)	14.05±3.28	-9.30±2.87

The final kinematical analysis was investigate the effect of a constant shock combined with a non-flat rotation curve would have on the fits. It was found that the fit to both Perseus and Outer arms were well fitted by a rising rotation curve - with similar v_{shock} values for both arms. From the fit to the rising rotation curve, the values of Oort's constants were estimated for this simple rising curve. It was found that Oort's constant A was representative of the IAU standard and also of other determinations, but the B constant was found - even taking into account the error - to be inconsistent with other determinations of its value. Values of Oort's constant A and B - from this work and literature - are summarised in Table 6.4. It is important to mention that - in its current formulation - the variable shock model has the effect of exhibiting a rising rotation curve. Though, with the current level of constraint and current understanding it is not possible to distinguish between the two effects - i.e. rising curve or variable shock.

6.4 Spiral Arm Mapping Routines

Since the ACM maps are the basis for each subsequent mapping routine, the effects mentioned here, the errors and discrepancies described should be considered cascaded to the CRM and AMF data maps unless explicitly stated to the contrary. For both the Outer and Perseus spiral arms I am confident that their kinematic structures are well fit by the models presented within this thesis. However, it is important to understand that the models may be improved with the advent of more accurate measurements or by the identification of more arm-based tracers. This is especially true for Perseus - but also true for the Outer arm. With additional low ℓ, first quadrant, tracers and more third quadrant tracers, it will help constrain and improve the fit and shape of the kinematic model. More accurate - and measured - distances to the outer Sct-Cen arm, would help in identifying whether the outer Sct-Cen arm extends beyond ℓ=58°. Though, I have been able to present some potential molecular cloud candidates which exist within the **eogs** and **ogs** regions of the Ex-FCRAO survey. Other difficulties with the ACM data is the velocity compression in the centre and anti-centre region, meaning that material at a wide range of distances share a common velocity. Also, in the regular kinematic selection, outside the confused areas, there is a possibility that the material within the kinematic window is from many distances, for the reasons explained in Chapters 3 and 4, due to the multivalued velocity-distance mapping in both the inner- and outer-Galaxy.

For the CRM and AMF data maps, these data are no longer in angular - ℓ, b - coordinates and are instead in terms of - linear - X and Z. Because of this, the actual mapping from $(\ell, b) \rightarrow (X, Z)$ is dependent on the spatial fit to each of the spiral arms. So, with improving the spatial fit by incorporating new (or more accurate) arm-based tracers will have the effect of changing the effective mapping between the angular and linear coordinates. It was found, however, that the variation of the solar constants (v_0 and R_0) has very little effect on the overall spatial fit to the Perseus arm. Though the variation in these parameters had *more* of an effect on the kinematic model derived from the spatial fit. It is, therefore, important to understand that though this model describes the spatial and kinematic Perseus and Outer spiral arms at our current understanding - the parameters can be subject to change with more accurate measurements and better understanding of the Physics within them.

Finally, considering the fits to the outer Sct-Cen arm: This model is not that well described since the distances used to constrain the fit were kinematically determined - which are already subject to the inherent biases included within the rotation curve used to convert the measured velocity to a distance. The maximum longitude to where the model is 'constrained', by the data within Dame & Thaddeus (2011), is $\ell \approx 58°$- it is important to remember that the model beyond this ℓ is an extrapolation and requires further work to identify if the outer Sct-Cen extends beyond the first quadrant. It is noteworthy to mention here, and has been mentioned already in this section, that I have identified possible ^{12}CO clouds in the Ex-FCRAO survey, this could mean that the arm beyonds the initial first quadrant constraint.

6.5 Clouding and Clumpology

The decomposition present was by no means a comprehensive analysis of the clumpology of the spiral arm regions, but instead the general trends deduced from the maps were found to self-consistently follow Galactic and extra-galactic relations from Solomon et al. (1987) and Bolatto et al. (2008) respectively. There was found to be a slight resolution dependance on the size parameter when converted from the Solomon et al. (1987) treatment to this work, so this required a slight modification to be applicable to Galactic linear data. There was also a suggestion that the relations presented in the literature were true for the lower resolution cloud decompositions, whilst the higher resolution data were found to obey a different relation. Whether this is symptomatic of the smallest resolvable clouds in a sample allowing for more small-size clouds to be measured is unclear at this time and will require further investigation. The key findings were presented in Chapter 5, but I will discuss possible improvements to the clouding analysis to present a more complete picture. The first main improvement which would be to vary each of the clouding parameters and observe how the relations vary based on the actual level of sub-clumping - rather that the pseudo sub-clumping introduced by varying the resolution. This will allow more analysis of the low-mass turnover for small, low mass, clouds. Possibly another route which could be used to investigate systematic resolution effects in using different clump finding algorithms, e.g. `GAUSSCLUMPS` (Stutzki & Guesten 1990); `CLUMPFIND` (Williams et al. 1994); `CLOUDPROPS` (Rosolowsky & Leroy 2006) on the linear data. This will allow an understanding of whether the nature of the algorithm - be it a 'splitter' or a 'clumper' (Brunt et al. 2003) - has any effect of the lower most threshold cut of the data, in terms of the mass value of the turn over.

Considering the Perseus arm clouds, there does appear to be dependancy of the observed relation per quantity with resolution - as found in the literature. If anything, the increase of precision of the resolution increases the scatter of the points which may imply that using a coarse resolution limit in the higher resolution data could be the source of this scatter. An improvement on this may be to limit the N_{min} - in unit coordinates, not pixels - to be some multiple of the resolution being decomposed, causing N_{min} to vary for each resolution.

6.6 Future Work & Research

A possible future expansion of this dynamical modelling could be to see the effect of the degeneracy of the v_{shock} and $\Delta\phi_{sp}$ values within the models. By using a more complicated spatial description of the spiral arm one could have a varying pitch angle, $\phi_{pitch}(R)$, into the model by using a more complex logarithmic form. Therefore creating a varying $\Delta\phi_{sp}$. One additional feature of the model I would like to pursue is the incorporation of a 'height' term in the spatial fit to be able to track the position of the arm $\ell, b, R/v_{LSR}$. Though this is possible during post-processing, i.e. extract the mid-plane function from the data and use that to track the warp, I would prefer to be able to describe the arm as $R_{arm}(\theta, Z)$ and v_{arm} (θ, Z). From this, if one is able to describe the transverse velocity gradient of an arm, it may be possible to quantify the relative apparent *rolling motions* of HI in the outer Galaxy (Yuan & Wallace 1973; Feitzinger & Spicker 1985; Foster & Cooper 2010). With these additional features it will be possible to model the spiral features of the

Lee J Summers

Image Copyrighted.
Original source image can be found:

[Left]:
www.astro.ex.ac.uk/people/lsummers/SpiralStructure.html
[Right]:
Churchwell et al. (2009)

Third Party Copyright Marker

Figure 6.3: Left Panel: shows the three dynamically modelled spiral arms presented within this thesis, the Perseus, Outer and outer Scutm-Centaurus spiral arms. Right panel: shows a schematic view of the Milky Way derived from GLIMPSE observations, image credit: : R. Hurt (SSC), JPL-Caltech, NASA.

Milky Way - and other galaxies - with a constant or variable shock potential; a constant or variable pitch angle; a flat or non-flat rotation curve and with a 1 or 2 dimensional spatial fit too the spiral arms. Though the 2D fit to the spatial structure would only be valid within the Milky Way due to the lack of height information in extra-galactic samples.

One other consideration which would be an interesting avenue to pursue would be to see if the kinematic structure, or at least the variation of the velocity shift with R, is invariant with spiral arm. So instead of effectively having a v_{arm} (ℓ, d_{helio}) for each spiral structure - jut have a single v_{arm} (R), where R just the Galactocentric radius. That way, though for a single (ℓ, b) line of sight the values of R will be different for each arm identified, the value of "*the velocity shift* " at some value of R will be the same disregarding which arm one is in. Therefore all which will be needed is a spatial fit to an arm and the kinematics will be easily derived, resulting in a more complete analysis than that which was presented in Russeil et al. (2007).

The work presented within this thesis lays the groundwork by which we will be able to fully map, describe and classify the spiral structure and composition of the Milky Way, see Figure 6.3. Being within the Milky Way, Galactic astronomers have the unique point of view that we are within the object we are trying to classify - meaning we can obtain higher resolutions than in extragalactic samples and also we have information as to the height distribution of star formation and the potential thereof. With the next generation of instrumentation we able to map and to model both the inner- and outer- Galaxy spiral arms - see Figure 6.3 to unprecedented scales. Comparison of the modelling parameters not only between different arms, but also along the different

segments of the same arm - for example, the Norma-Outer arm and the inner- and outer Galactic parts of the Scutum-Centaurus arm, to see whether the non-circular component of velocity present within the spiral arms varies with extreme changes of Galactocentric radius will be important in identifying whether spiral waves are transient and whether their shocks vary temporally. Though we have found that the outer arms are best described by a varying shock, the goal would be to see whether the inner and outer parts of he arm can be described by the same model. This will provide invaluable insights into the dynamical processes and physics of these different environments and how they vary with Galactic position. Furthermore, this will provide a powerful tool to determine the kinematic distances for arm-based material and stellar objects with greater accuracy than previously has been able.

Development of the model to incorporate more complex functions to describe the arms more accurately, similar to Hou et al. (2009), to allow for a varying pitch angle across a spiral arm's length. This may be the key in describing *extended arms*, i.e. arms which traverse the inner- and outer- Galaxy, such as Norma-Outer and Sct-Cen more accurate in space. Preliminary results obtained suggest that the variation in pitch -angle - or at least the possibility that the pitch of an arm varies - is indeed R dependant, with the fit to Perseus not being improved by higher order logarithmic polynomials. Where as the outer arm appears to be better fit by a quadratic or cubic form. Coupling these more complex spatial forms with more descriptive rotation curves and with the variable-Shock-Motion-Model (Summers & Brunt, *in prep a*), this will allow for a more accurate description of the Milky Way's structure.

The models presented here can be used by the community to define various regions of the Milky Way as a basis to observe the different conditions within the Spiral arm/inter-arm/intra-arm regions. Thus enabling information as to the physics of different Galactic environments to be determined and compared to similarly defined regions in extragalactic observations. This may also give indications as to how the ISM in these different regions evolves over time in galaxies exhibiting varying degrees of spiral structure. Comparing the Milky Way observations to other galaxies may give information as to the true structure of the Milky Way itself. Using these comparisons, it will be possible to see how the gaseous and stellar content varies not only from region-to-region within the Milky Way, but also how the stellar content and ISM differ between the Milky Way, *local* galaxies and eventually those galaxies of higher redshift. These definitions will be of tremendous import to recent large-scale projects (e.g. GLIMPSE, Hi-GAL, SCUBA-2 and Planck surveys) being able to anchor distances to objects and emission. Such an improved map of Milky Way structure would be tested - and refined - in the local Galaxy using future projects (e.g. GAIA, Bessel) therefore strengthening the predictions of my models in less well surveyed regions of the Galaxy. Also, for projects using dust and stellar-extinction mapping (IPHAS, VPHAS+), they will provide a scheme by which to constrain the fore- and back-ground emission. The extracted emission will also be able to used in studies of how star formation varies with height out of the plane of the galaxy, since in extragalactic observations we have no information in the depth axis.

It will also be possible to apply the methods described to synthetic observations of simulated galaxies (a proof of concept for which has already been conducted). The recovery spiral structure from synthetic observations will give information and understanding as to where, and to

what extent, each of the biases contribute to the inaccurate map we derive will assist in correcting the uncertainties which are introduced using angular observations allowing compensation for these biases when observing the Milky Way.

Bibliography

Acharova, I. A., Mishurov, Y. N., & Rasulova, M. R. 2011, Monthly Notices of the Royal Astronomical Society: Letters, 415, L11

Allen, R. J. 2001, in Astronomical Society of the Pacific Conference Series, Vol. 240, Gas and Galaxy Evolution, ed. J. E. Hibbard, M. Rupen, & J. H. van Gorkom, 331

Aller, L. H. 1991, Atoms, Stars, and Nebulae, 3rd edn. (Cambridge University Press)

Andersson, B.-G., Wannier, P. G., & Morris, M. 1991, ApJ, 366, 464

Apianus, P. 1539, Cosmographia

Bacmann, A., Lefloch, B., Ceccarelli, C., et al. 2002, A&A, 389, L6

Bahcall, N. A., Soneira, R. M., & Burgett, W. S. 1986, ApJ, 311, 15

Bailey, M. E., Butler, C. J., & McFarland, J. 2005, Astronomy and Geophysics, 46, 2.26

Ballesteros-Paredes, J. 2006, MNRAS, 372, 443

Ballesteros-Paredes, J., Gómez, G. C., Pichardo, B., & Vázquez-Semadeni, E. 2008, ArXiv e-prints

Ballesteros-Paredes, J., Hartmann, L., & Vázquez-Semadeni, E. 1999, ApJ, 527, 285

Barnard, E. E. 1899, ApJ, 9, 157

Barnard, E. E. 1906, Popular Astronomy, 14, 579

Barnard, E. E. 1907, ApJ, 25, 218

Barnard, E. E. 1913, ApJ, 38, 496

Barnard, E. E. 1919a, ApJ, 49, 360

Barnard, E. E. 1919b, ApJ, 49, 1

Bate, M. R. 1997, MNRAS, 285, 16

Bate, M. R. 2009, MNRAS, 392, 590

Bate, M. R. 2011, MNRAS, 2080

Beals, C. S. & Blanchet, G. H. 1938, MNRAS, 98, 398

Benaglia, P. 2011, in Revista Mexicana de Astronomia y Astrofisica Conference Series, Vol. 40, Revista Mexicana de Astronomia y Astrofisica Conference Series, 211–216

Benjamin, R. A., Churchwell, E., Babler, B. L., et al. 2003, PASP, 115, 953

Benson, P. J. & Myers, P. C. 1989, ApJS, 71, 89

Bergin, E. A. & Tafalla, M. 2007, ARA&A, 45, 339

Beuther, H. 2011, Bulletin de la Societe Royale des Sciences de Liege, 80, 200

Binney, J. & Dehnen, W. 1997, MNRAS, 287, L5

Blitz, L. 1979, ApJL, 231, L115

Blitz, L. 1993, in Protostars and Planets III, ed. E. H. Levy & J. I. Lunine, 125–161

Blitz, L. 1997, in IAU Symposium, Vol. 170, IAU Symposium, ed. W. B. Latter, S. J. E. Radford, P. R. Jewell, J. G. Mangum, & J. Bally, 11–18

Blitz, L. & Shu, F. H. 1980, ApJ, 238, 148

Blitz, L. & Williams, J. P. 1999, ArXiv Astrophysics e-prints

Bobylev, V. V. & Bajkova, A. T. 2010, MNRAS, 408, 1788

Bok, B. J. 1938, The Scientific Monthly, 46, 397

Bok, B. J. 1959, The Observatory, 79, 58

Bok, B. J. 1977, PASP, 89, 597

Bok, B. J. & Reilly, E. F. 1947, ApJ, 105, 255

Bolatto, A. D., Leroy, A. K., Rosolowsky, E., Walter, F., & Blitz, L. 2008, ApJ, 686, 948

Bonnell, I. A. & Bate, M. R. 2006, MNRAS, 370, 488

Bonnell, I. A., Bate, M. R., Clarke, C. J., & Pringle, J. E. 1997, MNRAS, 285, 201

Bourke, T. L., Hyland, A. R., & Robinson, G. 1995a, MNRAS, 276, 1052

Bourke, T. L., Hyland, A. R., Robinson, G., James, S. D., & Wright, C. M. 1995b, MNRAS, 276, 1067

Brand, J. & Blitz, L. 1993, A&A, 275, 67

Branham, Jr., R. L. 2011, Revista Mexicana de Astronomia y Astrofisica, 47, 197

Braun, R. & Walterbos, R. A. M. 1992, ApJ, 386, 120

Bressert, E., Bastian, N., & Gutermuth, R. 2011, ArXiv e-prints

Brunt, C. M., Heyer, M. H., Mottram, J., Douglas, K., & Summers, L. J. in prep

Brunt, C. M., Kerton, C. R., Kothes, R., & Gibson, S. J. 2002, in Astronomical Society of the Pacific Conference Series, Vol. 276, Seeing Through the Dust: The Detection of HI and the Exploration of the ISM in Galaxies, ed. A. R. Taylor, T. L. Landecker, & A. G. Willis, 140–+

Brunt, C. M., Kerton, C. R., & Pomerleau, C. 2003, ApJS, 144, 47

Burgh, E. B., France, K., & McCandliss, S. R. 2007, ApJ, 658, 446

Burstein, P., Borken, R. J., Kraushaar, W. L., & Sanders, W. T. 1977, ApJ, 213, 405

Buta, R. J., Corwin, H. G., & Odewahn, S. C. 2007, The de Vaucouleurs Altlas of Galaxies, ed. Buta, R. J., Corwin, H. G., & Odewahn, S. C. (Cambridge University Press)

Cambrésy, L., Beichman, C. A., Jarrett, T. H., & Cutri, R. M. 2002, AJ, 123, 2559

Cappellari, M., Emsellem, E., Krajnovic, D., et al. 2011, ArXiv e-prints

Carey, S. J., Clark, F. O., Egan, M. P., et al. 1998, ApJ, 508, 721

Cazaux, S. & Tielens, A. G. G. M. 2004, ApJ, 604, 222

Cazaux, S. & Tielens, A. G. G. M. 2010, ApJ, 715, 698

Christiansen, W. N. & Hindman, J. V. 1952, The Observatory, 72, 149

Churchwell, E., Babler, B. L., Meade, M. R., et al. 2009, PASP, 121, 213

Clemens, D. P. 1985, ApJ, 295, 422

Clemens, D. P. & Barvainis, R. 1988, ApJS, 68, 257

Colless, M. 1999, in Large-Scale Structure in the Universe, ed. G. Efstathiou & et al., 105

Combes, F. 1991, ARA&A, 29, 195

Cox, D. P. 2005, ARA&A, 43, 337

Cox, D. P. & Smith, B. W. 1974, ApJL, 189, L105+

Crutcher, R. M. 1999, ApJ, 520, 706

Curtis, E. I. & Richer, J. S. 2010, MNRAS, 402, 603

Dame, T. M., Hartmann, D., & Thaddeus, P. 2001, ApJ, 547, 792

Dame, T. M. & Thaddeus, P. 2011, ApJL, 734, L24+

de Vaucouleurs, G. 1959, Handbuch der Physik, Vol. 53, 275

Dehnen, W. & Binney, J. 1998, MNRAS, 294, 429

D'Hendecourt, L. B., Allamandola, L. J., Baas, F., & Greenberg, J. M. 1982, A&A, 109, L12

Dias, W. S., Alessi, B. S., Moitinho, A., & Lépine, J. R. D. 2002, A&A, 389, 871

Dias, W. S., Alessi, B. S., Moitinho, A., & Lepine, J. R. D. 2007, VizieR Online Data Catalog, 1, 2022

Dias, W. S., Alessi, B. S., Moitinho, A., & Lepine, J. R. D. 2010, VizieR Online Data Catalog, 1, 2022

Dias, W. S. & Lépine, J. R. D. 2005, ApJ, 629, 825

Dickey, J. M. & Lockman, F. J. 1990, ARA&A, 28, 215

Dobbs, C. 2010, ArXiv e-prints

Dobbs, C. L., Bonnell, I. A., & Pringle, J. E. 2006, MNRAS, 371, 1663

Dobbs, C. L. & Pringle, J. E. 2010, MNRAS, 409, 396

Dobbs, C. L., Theis, C., Pringle, J. E., & Bate, M. R. 2010, MNRAS, 403, 625

Donn, B. 1968, ApJL, 152, L129+

Douglas, A. E. & Herzberg, G. 1941, ApJ, 94, 381

Dreyer, J. L. E. 1888, MmRAS, 49, 1

Driver, S. P. 2004, in Bulletin of the American Astronomical Society, Vol. 36, American Astronomical Society Meeting Abstracts 204, 781–+

Driver, S. P., Allen, P. D., Graham, A. W., et al. 2006, MNRAS, 368, 414

Du, F. & Yang, J. 2008, ApJ, 686, 384

Dunham, Jr., T. 1937, PASP, 49, 26

Eddington, A. S. 1926a, Royal Society of London Proceedings Series A, 111, 424

Eddington, A. S. 1926b, The Observatory, 49, 193

Eddington, A. S. 1937, The Observatory, 60, 99

Efremov, Y. N. 2011, Astronomy Reports, 55, 108

Egan, M. P., Shipman, R. F., Price, S. D., et al. 1998, ApJL, 494, L199

Egusa, F., Koda, J., & Scoville, N. Z. 2010, in Bulletin of the American Astronomical Society, Vol. 42, American Astronomical Society Meeting Abstracts 215, 354.03–+

Elias, F., Alfaro, E. J., & Cabrera-Caño, J. 2006, AJ, 132, 1052

Ellis, R. S. 1997, ARA&A, 35, 389

Elmegreen, B. G. 1990a, ApJ, 357, 125

Elmegreen, B. G. 1990b, ApJL, 361, L77

Elmegreen, B. G. 2000, ApJ, 530, 277

Elmegreen, B. G. 2011, in EAS Publications Series, Vol. 51, EAS Publications Series, ed. C. Charbonnel & T. Montmerle, 19–30

English, J., Taylor, A. R., Irwin, J. A., et al. 1998, PASA, 15, 56

Evans, A. S., Kim, D. C., Mazzarella, J. M., Scoville, N. Z., & Sanders, D. B. 1999, ApJL, 521, L107

Ewen, H. I. & Purcell, E. M. 1951, Nature, 168, 356

Feast, M. & Whitelock, P. 1997, MNRAS, 291, 683

Feitzinger, J. V. & Spicker, J. 1985, MNRAS, 214, 539

Feitzinger, J. V. & Stuewe, J. A. 1984, NASA Conference Publication, 2345, 239

Fernández, D., Figueras, F., & Torra, J. 2001, A&A, 372, 833

Ferrini, F. & Galli, D. 1988, A&A, 195, 27

Field, G. B., Goldsmith, D. W., & Habing, H. J. 1969, ApJL, 155, L149+

Fosbury, R. A. E., Villar-Martín, M., Humphrey, A., et al. 2003, ApJ, 596, 797

Foster, T. & Cooper, B. 2010, ArXiv e-prints

Foster, T. & MacWilliams, J. 2006, ApJ, 644, 214

Foster, T. & Routledge, D. 2003, ApJ, 598, 1005

Fukui, Y., Kawamura, A., Wong, T., et al. 2009, ApJ, 705, 144

Galazutdinov, G. A., Musaev, F. A., Krełowski, J., & Walker, G. A. H. 2000, PASP, 112, 648

Girichidis, P., Federrath, C., Banerjee, R., & Klessen, R. S. 2011, MNRAS, 413, 2741

Glover, S. C. O. & Clark, P. C. 2012, MNRAS, 421, 9

Glover, S. C. O. & Mac Low, M. 2010, ArXiv e-prints

Glover, S. C. O. & Mac Low, M. 2011, MNRAS, 412, 337

Glover, S. C. O. & Mac Low, M.-M. 2007, ApJ, 659, 1317

Goldsmith, P. F., Bergin, E. A., & Lis, D. C. 1997, ApJ, 491, 615

Gómez, G. C. 2006, AJ, 132, 2376

Gómez, G. C. & Cox, D. P. 2004, ApJ, 615, 758

Gould, A. & Ramirez, S. V. 1998, ApJ, 497, 713

Gould, R. J., Gold, T., & Salpeter, E. E. 1963, ApJ, 138, 408

Gould, R. J. & Salpeter, E. E. 1963, ApJ, 138, 393

Govers, T. R., Mattera, L., & Scoles, G. 1980, J. Chem. Phys., 72, 5446

Graham, A. W. & Guzmán, R. 2003, AJ, 125, 2936

Guzmán, R., Graham, A. W., Matković, A., et al. 2003, in Astronomical Society of the Pacific Conference Series, Vol. 297, Star Formation Through Time, ed. E. Perez, R. M. Gonzalez Delgado, & G. Tenorio-Tagle, 271–+

Gwinn, C. R., Moran, J. M., & Reid, M. J. 1992, ApJ, 393, 149

Hachisuka, K. et al. 2009

Hagen, J. P., Lilley, A. E., & McClain, E. F. 1955, ApJ, 122, 361

Hanson, R. B. 1987, AJ, 94, 409

Hartmann, J. 1904a, ApJ, 19, 268

Hartmann, J. 1904b, ApJ, 20, 338

Hawking, S. W. & Penrose, R. 1970, Royal Society of London Proceedings Series A, 314, 529

Heger, M. L. 1922, Lick Observatory Bulletin, 10, 141

Heitsch, F., Burkert, A., Hartmann, L. W., Slyz, A. D., & Devriendt, J. E. G. 2005, ApJL, 633, L113

Helfer, T. T., Thornley, M. D., Regan, M. W., et al. 2003, ApJS, 145, 259

Herbig, G. H. 1975, ApJ, 196, 129

Herbig, G. H. 1995, ARA&A, 33, 19

Herbst, E. & Klemperer, W. 1973, ApJ, 185, 505

Herschel, J. F. W. 1864, Royal Society of London Philosophical Transactions Series I, 154, 1

Heyer, M., Krawczyk, C., Duval, J., & Jackson, J. M. 2008, ArXiv e-prints

Heyer, M. H. 1996, in IAU Symposium, Vol. 170, CO: Twenty-Five Years of Millimeter-Wave Spectroscopy, ed. W. B. Latter, J. E. Radford Simon, P. R. Jewell, J. G. Mangum, & J. Bally, 36–+

Heyer, M. H., Brunt, C., Snell, R. L., et al. 1998, ApJS, 115, 241

Heyer, M. H., Carpenter, J. M., & Snell, R. L. 2001, ApJ, 551, 852

Hollenbach, D. & McKee, C. F. 1979, ApJS, 41, 555

Hollenbach, D. & Salpeter, E. E. 1971, ApJ, 163, 155

Honma, M. & Sofue, Y. 1997, PASJ, 49, 453

Hou, L. G., Han, J. L., & Shi, W. B. 2009, ArXiv e-prints

Huard, T. L., Sandell, G., & Weintraub, D. A. 1999, ApJ, 526, 833

Huard, T. L., Weintraub, D. A., & Sandell, G. 2000, A&A, 362, 635

Hubble, E. 1936, ApJ, 84, 158

Hubble, E. P. 1926, ApJ, 64, 321

Huchra, J., Davis, M., Latham, D., & Tonry, J. 1983, ApJS, 52, 89

Hur, H., Sung, H., & Bessell, M. S. 2012, AJ, 143, 41

Imara, N. & Blitz, L. 2011, ApJ, 732, 78

Ivanovskaya, V. V., Zobelli, A., Teillet-Billy, D., et al. 2010, Phys. Rev. B, 82, 245407

Jackson, J. M., Rathborne, J. M., Shah, R. Y., et al. 2006, ApJS, 163, 145

Janák, F. & Mayer, P. 1959, Bulletin of the Astronomical Institutes of Czechoslovakia, 10, 22

Jenkins, E. B. & Meloy, D. A. 1974, ApJL, 193, L121

Joshi, P. & Tarafdar, S. P. 1977, Ap&SS, 49, 199

Kaiser, N. 1987, MNRAS, 227, 1

Kalberla, P. M. & Kerp, J. 2009, Annual Review of Astronomy and Astrophysics, 47, 27

Kalberla, P. M. W. & Dedes, L. 2008, A&A, 487, 951

Kalberla, P. M. W., Dedes, L., Kerp, J., & Haud, U. 2007, A&A, 469, 511

Kaplan, S. A. 1966, Interstellar gas dynamics (Oxford: Pergamon Press)

Kaplan, S. A. 1977, in Early Stages of Stellar Evolution, ed. K. Kaerre & H. Lindkvist, 5–10

Kapteyn, J. C. 1909a, ApJ, 29, 46

Kapteyn, J. C. 1909b, ApJ, 30, 284

Kauffmann, J. & Pillai, T. 2010, ApJL, 723, L7

Kelvin, L., Driver, S., Robotham, A., Hill, D., & Cameron, E. 2010, in American Institute of Physics Conference Series, Vol. 1240, American Institute of Physics Conference Series, ed. V. P. Debattista & C. C. Popescu, 247–248

Kerr, F. J. & Lynden-Bell, D. 1986, MNRAS, 221, 1023

Keto, E., Ho, L. C., & Lo, K.-Y. 2005, ApJ, 635, 1062

Kimeswenger, S. & Weinberger, R. 1989, A&A, 209, 51

Klessen, R. S. 2011, in EAS Publications Series, Vol. 51, EAS Publications Series, ed. C. Charbonnel & T. Montmerle, 133–167

Klessen, R. S., Ballesteros-Paredes, J., Li, Y., & Mac Low, M.-M. 2004, in Astronomical Society of the Pacific Conference Series, Vol. 322, The Formation and Evolution of Massive Young Star Clusters, ed. H. J. G. L. M. Lamers, L. J. Smith, & A. Nota, 299–+

Kutner, M. L. & Ulich, B. L. 1981, ApJ, 250, 341

Larson, R. B. 1981, MNRAS, 194, 809

Launhardt, R., Sargent, A. I., Henning, T., Zylka, R., & Zinnecker, H. 2000, in IAU Symposium, Vol. 200, IAU Symposium, 103P

Ledoux, P. 1951, Annales d'Astrophysique, 14, 438

Leisawitz, D., Bash, F. N., & Thaddeus, P. 1989, ApJS, 70, 731

Lemaître, G. 1927, Annales de la Societe Scietifique de Bruxelles, 47, 49

Lemaître, G. 1931, MNRAS, 91, 483

Levine, E. S., Blitz, L., & Heiles, C. 2006, Science, 312, 1773

Lin, C. C., Yuan, C., & Shu, F. H. 1969, ApJ, 155, 721

Lindsay, E. M., Bok, B. J., & Shapley, H. 1937, Annals of Harvard College Observatory, 105, 255

Liszt, H. S. 1982, ApJ, 262, 198

Lockman, F. J. & Gehman, C. S. 1991, ApJ, 382, 182

Lynden-Bell, D. 1986, QJRAS, 27, 319

Lynds, B. T. 1962, ApJS, 7, 1

Mac Low, M.-M. & Glover, S. C. O. 2012, ApJ, 746, 135

McClure-Griffiths, N. M., Dickey, J. M., Gaensler, B. M., et al. 2005, ApJS, 158, 178

McKee, C. F. 1989, ApJ, 345, 782

McKee, C. F. 1990, in Astronomical Society of the Pacific Conference Series, Vol. 12, The Evolution of the Interstellar Medium, ed. L. Blitz, 3–29

McKee, C. F. & Ostriker, E. C. 2007, ARA&A, 45, 565

McKee, C. F. & Ostriker, J. P. 1977, ApJ, 218, 148

McKee, C. F. & Tan, J. C. 2002, Nature, 416, 59

McKee, C. F. & Tan, J. C. 2003, ApJ, 585, 850

McKellar, A. 1941, PASP, 53, 233

Mermilliod, J. C. 1988, Bulletin d'Information du Centre de Donnees Stellaires, 35, 77

Merrill, P. W. 1934, PASP, 46, 206

Merrill, P. W. & Humason, M. L. 1938, PASP, 50, 212

Mestel, L. & Paris, R. B. 1984, A&A, 136, 98

Mihalas, D. & Binney, J. 1981, Galactic astronomy: Structure and kinematics /2nd edition/, ed. D. Mihalas & J. Binney

Minchev, I. & Quillen, A. C. 2007, MNRAS, 377, 1163

Mishurov, Y. N. & Zenina, I. A. 1999, A&A, 341, 81

Moffat, A. F. J. & Vogt, N. 1973, A&AS, 11, 3

Monaco, P. 2002, in Astronomical Society of the Pacific Conference Series, Vol. 253, Chemical Enrichment of Intracluster and Intergalactic Medium, ed. R. Fusco-Femiano & F. Matteucci, 279–+

Monaco, P. 2003, in Revista Mexicana de Astronomia y Astrofisica, vol. 27, Vol. 17, Revista Mexicana de Astronomia y Astrofisica Conference Series, ed. V. Avila-Reese, C. Firmani, C. S. Frenk, & C. Allen, 71–72

Mouschovias, T. C. 1987, in NATO ASIC Proc. 210: Physical Processes in Interstellar Clouds, ed. G. E. Morfill & M. Scholer, 453–489

Muller, C. A. 1957, ApJ, 125, 830

Nakanishi, H. & Sofue, Y. 2003, PASJ, 55, 191

Negueruela, I. & Marco, A. 2003, A&A, 406, 119

Negueruela, I. & Marco, A. 2008, A&A, 492, 441

Neufeld, D. A., Wolfire, M. G., & Schilke, P. 2005, ApJ, 628, 260

Niinuma, K., Nagayama, T., Hirota, T., et al. 2011, PASJ, 63, 9

Normandeau, M., Taylor, A. R., & Dewdney, P. E. 1997, ApJS, 108, 279

Obreschkow, D., Klöckner, H.-R., Heywood, I., Levrier, F., & Rawlings, S. 2009, ApJ, 703, 1890

Obreschkow, D. & Rawlings, S. 2009, MNRAS

Oh, C. S., Kobayashi, H., Honma, M., et al. 2010, PASJ, 62, 101

Oort, J. H. 1927, Bull. Astron. Inst. Netherlands, 3, 275

Oort, J. H. 1928, Bull. Astron. Inst. Netherlands, 4, 269

Oort, J. H., Kerr, F. J., & Westerhout, G. 1958, MNRAS, 118, 379

Oppenheimer, M. & Dalgarno, A. 1975, ApJ, 200, 419

P. M. W. Kalberla, W. B. Burton, Dap Hartmann, et al. 2005, A&A, 440, 775

Pandey, A. K., Sharma, S., & Ogura, K. 2006, MNRAS, 373, 255

Parravano, A., Hollenbach, D. J., & McKee, C. F. 2003, ApJ, 584, 797

Pillai, T., Wyrowski, F., Menten, K. M., & Krügel, E. 2006, A&A, 447, 929

Pineda, J. E., Rosolowsky, E. W., & Goodman, A. A. 2009, ApJL, 699, L134

Pirronello, V., Biham, O., Liu, C., Shen, L., & Vidali, G. 1997a, ApJL, 483, L131+

Pirronello, V., Liu, C., Shen, L., & Vidali, G. 1997b, ApJL, 475, L69+

Pont, F., Queloz, D., Bratschi, P., & Mayor, M. 1997, A&A, 318, 416

Popova, M. É. 2006, Astronomy Letters, 32, 244

Popova, M. É. & Loktin, A. V. 2005, Astronomy Letters, 31, 663

Reid, M. A., Wadsley, J., Petitclerc, N., & Sills, A. 2010, ApJ, 719, 561

Reid, M. J., Menten, K. M., Zheng, X. W., et al. 2009, ApJ, 700, 137

Riess, A. G., Macri, L., Casertano, S., et al. 2011, ApJ, 730, 119

Roberts, M. S. 1967, in IAU Symposium, Vol. 31, Radio Astronomy and the Galactic System, ed. H. van Woerden, 189

Roberts, M. S. & Haynes, M. P. 1994, ARA&A, 32, 115

Roberts, Jr., W. W. 1972, ApJ, 173, 259

Rogerson, J. B., York, D. G., Drake, J. F., et al. 1973, ApJL, 181, L110+

Roman-Duval, J., Jackson, J. M., Heyer, M., Rathborne, J., & Simon, R. 2010, ApJ, 723, 492

Rosolowsky, E. & Leroy, A. 2006, PASP, 118, 590

Russeil, D. 2003, A&A, 397, 133

Russeil, D., Adami, C., & Georgelin, Y. M. 2007, A&A, 470, 161

Russell, H. N. 1935, MNRAS, Vol. 95, 610

Saha, M. N. 1937, Nature, 139, 840

Salama, F., Galazutdinov, G. A., Krełowski, J., Allamandola, L. J., & Musaev, F. A. 1999, ApJ, 526, 265

Salpeter, E. E. 1955, ApJ, 121, 161

Sandage, A. 1961, The Hubble atlas of galaxies, ed. Sandage, A.

Sandage, A. 1986, A&A, 161, 89

Sanna, A., Reid, M. J., Dame, T. M., et al. 2011, ArXiv e-prints

Sato, M., Hirota, T., Honma, M., et al. 2008, PASJ, 60, 975

Schmidt, M. 1965, in Galactic Structure, ed. A. Blaauw & M. Schmidt, 513

Schneider, N. & Brooks, K. 2004, PASA, 21, 290

Schneider, N., Simon, R., Bontemps, S., Comerón, F., & Motte, F. 2007, A&A, 474, 873

Seigar, M. S. & James, P. A. 1998, MNRAS, 299, 685

Shaw, H. K. 1914, The Observatory, 37, 98

Shen, M. & Zhang, H. 2010, Chinese Astronomy and Astrophysics, 34, 89

Shiozaki, S., Imai, H., Tafoya, D., et al. 2011, ArXiv e-prints

Shuter, W. L. H. & Verschuur, G. L. 1964, MNRAS, 127, 387

Simon, R., Jackson, J. M., Rathborne, J. M., & Chambers, E. T. 2006, ApJ, 639, 227

Skrutskie, M. F., Cutri, R. M., Stiening, R., et al. 2006, AJ, 131, 1163

Slipher, V. M. 1912, Lowell Observatory Bulletin, 2, 26

Snow, T. P. & McCall, B. J. 2006, Annual Review of Astronomy and Astrophysics, 44, 367

Solomon, P. M., Rivolo, A. R., Barrett, J., & Yahil, A. 1987, ApJ, 319, 730

Spitzer, L. 1968a, Diffuse matter in space, ed. Spitzer, L. (New York: Interscience Publication)

Spitzer, Jr., L. 1968b, Dynamics of Interstellar Matter and the Formation of Stars (the University of Chicago Press), 1–+

Spitzer, Jr., L. & Scott, E. H. 1969, ApJ, 158, 161

Stahler, S. & Palla, F. 2004, The Formation of Stars (Wiley)

Stark, A. A. & Brand, J. 1989, ApJ, 339, 763

Stark, A. A. & Lee, Y. 2006, ApJL, 641, L113

Sterzik, M. F., Durisen, R. H., & Zinnecker, H. 2003, A&A, 411, 91

Stil, J. M., Taylor, A. R., Dickey, J. M., et al. 2006, AJ, 132, 1158

Stone, M. E. 1970a, ApJ, 159, 277

Stone, M. E. 1970b, ApJ, 159, 293

Strasser, S. & Taylor, A. R. 2004, ApJ, 603, 560

Strasser, S. T., Dickey, J. M., Taylor, A. R., et al. 2007, AJ, 134, 2252

Stutzki, J. & Guesten, R. 1990, ApJ, 356, 513

Summers, L. J. 2008, Master's thesis, Univeristy of Bristol

Summers, L. J. 2010, in From Stars to Galaxies: Connecting our Understanding of Star and Galaxy Formation, University of Florida, Gainesville, Florida, USA, 7-10 April 2010. Online at http://conference.astro.ufl.edu/STARSTOGALAXIES, pg.100

Summers, L. J. 2011, in Royal Astronomical Society : National Astronomy Meeting, April 2011

Summers, L. J. & Brunt, C. M. in prep, in prep

Summers, L. J. & Brunt, C. M. submitted, MNRAS

Sung, H. & Bessell, M. S. 2004, AJ, 127, 1014

Swings, P. 1937, MNRAS, 97, 212

Swings, P. & Rosenfeld, L. 1937, ApJ, 86, 483

Tafalla, M. 2008, Ap&SS, 313, 123

Tarafdar, S. P. 1978, A&A, 68, 165

Tasker, E. J. & Tan, J. C. 2009, ApJ, 700, 358

Taylor, A. R., Gibson, S. J., Peracaula, M., et al. 2003, AJ, 125, 3145

Thrower, J. D., Nilsson, L., Jørgensen, B., et al. 2011, in EAS Publications Series, Vol. 46, EAS Publications Series, 453–460

Tulej, M., Kirkwood, D. A., Pachkov, M., & Maier, J. P. 1998, ApJL, 506, L69

Vallée, J. P. 2002, ApJ, 566, 261

Vallée, J. P. 2008, AJ, 135, 1301

van den Bergh, S. 1960a, ApJ, 131, 558

van den Bergh, S. 1960b, ApJ, 131, 215

van der Wiel, M. H. D. & Shipman, R. F. 2008, A&A, 490, 655

van Dishoeck, E. F. & Black, J. H. 1988, ApJ, 334, 771

van Dishoeck, E. F. & Visser, R. 2011, ArXiv e-prints

Vasyunina, T., Linz, H., Henning, T., et al. 2009, A&A, 499, 149

Vázquez-Semadeni, E., Banerjee, R., Gómez, G. C., et al. 2011, MNRAS, 414, 2511

Verschuur, G. L. 1973, A&A, 24, 193

Verschuur, G. L. 1988, Interstellar Matters (Springer-Verlog)

von Fraunhofer, J. 1814, Denkschriften (1814-1815), Academy of Sciences in Munich

Walsh, W., Beck, R., Thuma, G., et al. 2002, A&A, 388, 7

Weinreb, S., Barrett, A. H., Meeks, M. L., & Henry, J. C. 1963, Nature, 200, 829

Williams, J. P., de Geus, E. J., & Blitz, L. 1994, ApJ, 428, 693

Williamson, F. O., Sanders, W. T., Kraushaar, W. L., et al. 1974, ApJL, 193, L133

Wilson, C. D., Warren, B. E., Irwin, J., et al. 2011, MNRAS, 410, 1409

Wilson, R. W., Jefferts, K. B., & Penzias, A. A. 1970, ApJL, 161, L43+

Xu, Y., Reid, M. J., Zheng, X. W., & Menten, K. M. 2006, Science, 311, 54

Yorke, H. W. & Sonnhalter, C. 2002, ApJ, 569, 846

Yuan, L. & Wallace, C. 1973, ApJ, 185, 453

Zinnecker, H. & Yorke, H. W. 2007, ARA&A, 45, 481

Zwicky, F. 1937, ApJ, 86, 217

Appendix

A Proof of Formation time of Molecular Clouds

Taking the formalism from MacLow & Glover (2012),

$$\rho_{H_2} = \frac{2n_H}{n_{tot}}$$

where, $n_{tot} = n_H + 2n_{H_2}$, with the formation rate ($\mathbb{R}$) is proportional to the temperature via,

$$\mathbb{R} \propto T^{\frac{1}{2}}$$

Including a time dependant clumping factor, C(t).

$$n_H = 2n_{H_2}\left(\frac{1}{X_{H_2}} - 1\right)$$

where n_H grows as,

$$\dot{X} = C(t)\ \mathbb{R}(T)\ 2n_{H_2}\ \left(\frac{1}{X_{H_2}} - 1\right)$$

$$n_H = X_{H_2} n$$

$$\dot{X} = C(t)\ \mathbb{R}(T)\ X_{H_2}\ n\ \left(\frac{1}{X_{H_2}} - 1\right) = C(t)\ \mathbb{R}(T)\ n\ (1 - X_{H_2})$$

y=(1-X) and dy=-dx

$$\int \frac{-dy}{dt}.dt = \int C(t)\ \mathbb{R}(T)\ n\ y.dt$$

$$\int_{y(0)}^{t(t)} \frac{-dy}{y} = \int C(t)\ \mathbb{R}(T)\ n.dt$$

$$[\ln(y(t))]_0^t = -C(t)\,\mathbb{R}(T)\,n$$

at t=0, X=0, y=1, X=1-y

$$y(t) = \exp[-C(t)\,\mathbb{R}(T)\,n]$$

$$x(t) = 1 - \exp[-C(t)\,\mathbb{R}(T)\,n]$$

$$\tau_f = \frac{1}{C(t)\,\mathbb{R}(T)\,n}$$

$$x(t) = 1 - \exp\left(-\frac{1}{\tau_f}\right)$$

$$\tau_f = \frac{10^9 \mathrm{yr}}{n[\mathrm{cm}^{-3}]}$$

B Convolution of two one-dimensional Gaussian functions

$(f \otimes g)$ is the convolution of $f(x)$ and $g(x)$ which are both one-dimensional Gaussian functions.

$$f(x) = \frac{1}{\sqrt{2\pi\sigma_f}}.\exp\left[\frac{(x-\mu_f)^2}{2\sigma_f^2}\right]$$

F is the Fourier Transform,

$$F^{-1}[F(f(x))\ F(g(x))] \ = \ f(x) \otimes g(x)$$

$$F[f(x)] \ = \ \int_{-\infty}^{\infty} f(x).\exp[-2\pi\ i\ k\ x]\ .dx$$

with the inverse transform being,

$$F^{-1}[f(k)] \ = \ \int_{-\infty}^{\infty} f(k).\exp[2\pi\ i\ k\ x]\ .dk$$

using the substitution of x' = x-μ, which implies; dx'=dx

$$F[f(x)] = \int \frac{1}{\sqrt{2\pi\sigma_f}}.\exp\left[\frac{-x'^2}{2\sigma_f^2}\right]\ .\exp[-2\pi\ i\ k\ (x'-\mu)]\ .dx'$$

$$F[f(x)] \ = \ \frac{\exp[2\pi\ i\ k\ \mu]}{\sqrt{2\pi\sigma_f}} \ \int \ \exp\left[\frac{-x'^2}{2\sigma_f^2}\right]\ .\exp[-2\pi\ i\ k\ x'].dx'$$

From Euler's theorem; $e^{-i\theta} = \cos\theta + i\ \sin\theta$

$$F[f(x)] \ = \ \frac{\exp[2\pi\ i\ k\ \mu]}{\sqrt{2\pi\sigma_f}} \ \int \ \exp\left[\frac{-x'^2}{2\sigma_f^2}\right]\ (\cos(2\pi\ k\ x') - i\ \sin(2\pi\ k\ x')).dx'$$

Over all space, $\int \sin(x') = 0$,

$$F[f(x)] \ = \ \frac{\exp[2\pi\ i\ k\ \mu]}{\sqrt{2\pi\sigma_f}} \ \int \ \exp\left[\frac{-x'^2}{2\sigma_f^2}\right]\ \cos(2\pi\ k\ x').dx'$$

Using the standard integral,

$$\int_0^{\infty} e^{-at^2}.\cos(2xt)\ dt \ = \ \frac{1}{2}\ \sqrt{\frac{\pi}{a}}\ e^{-\frac{x^2}{a}}$$

$$F[f(x)] \ = \ \exp[-2\pi\ i\ k\ \mu_f].\exp[2\ \pi^2\ \sigma_f^2\ k^2]$$

$$F[f(x)]F[g(x)] \ = \ \exp[-2\pi\ i\ k\ \mu_f]\ \exp[2\ \pi^2\ \sigma_f^2\ k^2]\ \exp[-2\pi\ i\ k\ \mu_g]\ \exp[-2\ \pi^2\ \sigma_g^2\ k^2]$$

Amalgamating like terms,

$$F[f(x)]F[g(x)]\ \exp[-2\pi\ i\ k\ (\mu_f - \mu_g)]\ \exp[-2\ \pi^2\ (\sigma_f^2 - \sigma_g^2)\ k^2]$$

Comparing like terms from the original convolution and the components therein,

$$\mu_{f\otimes g}\ =\ (\mu_f + \mu_g)\ \text{and}\ \sigma_{f\otimes g}\ =\ \sqrt{\sigma_f^2 + \sigma_g^2}$$

Substituting this into the original transform;

$$P_{f\otimes g}(x)\ =\ F^{-1}(F[f(x)]F[g(x)])\ =\ \frac{1}{\sqrt{2\pi(\sigma_f^2 + \sigma_g^2)}}.\exp\left[\frac{(x - (\mu_f + \mu_g))^2}{2(\sigma_f^2 + \sigma_g^2)}\right]$$

C The Mass:Age Relation of Molecular Material to Young Stellar Clusters

This section details the initial ground work which lead to the work to investigate Galactic structure. Whilst this work was being completed it was realised the state of the field with regards to the spiral structure modelling had scope for improvement.

C.1 Molecular Clouds and Stellar Clusters

Molecular Clouds are the sites of all known star formation, hence is assumed wherever one observes an area where young stars reside, it is assumed one will also find Molecular Material (Blitz & Williams 1999). The mechanism by which star formation is thought to involve the gravitational condensation of matter into areas of, eventually, significantly higher density, Klessen, Ballesteros-Paredes, Li, & Mac Low (2004) - see also Chapter 1.

Local macroscopic over-densities within the cloud cause minor potential wells. These potential wells facilitate the flow of molecular material, increasing the local density gradient, which increases the potential and so on. It is thought that the OB associations, clusters of; young, hot, blue stars, see Figure i - which the clouds are likely to form - are the main source of the cloud's eventual dispersion. The stellar winds produced by the young stars, and the associated heating, causes the surrounding atomic and molecular gas to disperse. Many studies concentrate on individual spatial areas or clusters for observing the behaviour and interaction of Molecular Clouds with their local environment. Though one may extrapolate one's findings from the specific to include the general case, as explained in Leisawitz, Bash, & Thaddeus (1989), the initial conditions of individual regions can have great effect on how it evolves, thus introducing uncertainties which one is unable to compensate for. Providing a cluster's age is known, one may draw conclusions from the mass of associated material and the average lifetime of the clouds. Previous work conducted in this area by Leisawitz et al. (1989), found that the mass of molecular material is inversely proportional to the age of the cluster to which it is associated, the summary of their findings are presented in Figure ii.

However, in the 23 years since Leisawitz et al. (1989) completed their study, there have been significant improvements in detection techniques and the surveyed coverage of the Milky Way. Hence, the quality and quantity of the available data have increased. The main focus of this section of work is to study how, and over what timescale, molecular clouds progress and flow through the spiral arms - specifically the Perseus spiral arm - using the higher resolution data of the J=1→0 ^{12}CO rotational transition presenting an improvement on the original work by Leisawitz et al. (1989). These data are taken from the ExFCRAO ^{12}CO survey Brunt et al. (in prep) - presented in Chapter 2 of this thesis.

C.2 Condensation of Molecular Material

Though there is significant variety of both observable and detectable molecules within the clouds, see Tables 1.3. The main constituent, by fraction, of the mass is molecular H_2. Due to the ax-

Lee J Summers

Image Copyrighted.
Original source image can be found:

http://cococubed.asu.edu/images/hr_diagrams/hr_fancy.jpg

Third Party Copyright Marker

Figure i: Artistic representation of a Hertsprung-Russell Diagram. With reference to the main text, the **O** and **B** class stars are young, hot stars and are in the *blue* region of the colour scale in the plot. Original Image Credit: Julian Baum, Wildlife Art Ltd.

Lee J Summers

Image Copyrighted.
Original source image can be found:

Figure 47, Leisawitz et al. (1989)

Third Party Copyright Marker

Figure ii: Figure taken from (Leisawitz, Bash, & Thaddeus 1989, Figure 47 therein). Variation in mass of molecular material as a function of the age of the associated stellar cluster. Using a sample of 34 Open Stellar Clusters.

isymmetric nature of molecular Hydrogen, its lack of a dipole moment leads to its direct detection being very difficult - as was discussed in the Chapter 1.

Molecular clouds are essentially a compound structure which are created through the aggregation of smaller *clumps* of gas into a larger structure, similar to Galaxies leading to Groups which can lead to Clusters and so on. Having said that, it is better to think of the cloud as an area of continuous gas where the clumps are areas of relatively high density than when compared to the inter-clump medium, Evans et al. (1999); Snow & McCall (2006). Galaxy morphology plays an important role in governing active Galactic star formation, with the main sites of star formation occurring within the spiral arms of S-type galaxies. It is the flow of molecular material thorough shock-fronts within the arms which cause the perturbations in the cloud which facilitate its collapse into young stellar objects, Roberts (1972). Through the detection of CO lines, it is possible to deduce that some fraction of the Intra-Clump Medium is molecular, with the remainder being atomic in nature, detected through the 21-cm line. The atomic gas envelopes of the clouds, in linear size, are significantly larger than the complexes which they surround. On average, such a cloud envelope can extend for several times the linear size of the cloud, Weinreb et al. (1963).

C.3 Measuring Cloud Mass

As already discussed in Chapter 1, the lack of a dipole moment in H_2 makes it difficult to detect. CO forms in a similar way to that of molecular Hydrogen, through atomic self-shielding, thus making it an excellent tracer (Oppenheimer & Dalgarno 1975; van Dishoeck & Black 1988). CO molecules have a strong dipole moment which strongly emits in the radio band (2.6mm). It is the J=1→0 of the ^{12}CO which we observe to infer the presence of the H_2. However, CO is only a good tracer of low density environments, above the density limit, the photon emitted as a result of the decent of the electron from the 1 to 0 J-state is reabsorbed before it can be fully emitted, thus making the area optically thick. It is the low density limit which will be observed here, with the rotational levels of CO being progressively occupied with increasing density.

For the purposes of this work, the isotope of ^{12}CO will be used to measure the Hydrogen, and subsequently the cloud's, mass. The method used to equate the CO mass to that of Hydrogen is a simple conversion using X_{CO} and X_{HI}. Each of the clusters will have a position in parameter space of (l,b,V_{LSR}), centering the integration of material at this value of V_{LSR}. There will be a series of radii of integration up to 25pc, which is the upper limit at which material can be said to be probably associated to its parent cluster (Leisawitz et al. 1989). The radii will be incremented in 5pc steps from 5 to 25pc, there will also be a radius of size of o?rder of the cluster angular size on the sky. The procedure for converting the CO temperature into a brightness was presented in Section 1.3.7.

C.4 Galactic Structure and Kinematics

As material flows into the regions of the Galaxy where there are spiral arms, it is subject to a shock. Arguably, the most widely accepted interpretation of this is described via the Two-Arm-Spiral-Shock Model described in Roberts (1972). This shock manifests itself as a step in observed

Lee J Summers

Image Copyrighted.
Original source image can be found:

Figure 3, Brand & Blitz (1993)

Third Party Copyright Marker

Figure iii: The above Figure the Brand & Blitz (1993) Galactic rotation curve.

velocity which deviates from the assumed circular rotation curve of the Galaxy. Shocked material within the Perseus arm in the outer galaxy exhibits a $\Delta v_{LSR} \simeq$-10 km s^{-1} , i.e. it orbits approximately 10 km s^{-1} slower than non-arm material at the same R. Therefore it is imperative to have information as to the position of the spiral arms so one may ascertain whether a cluster is entering, exiting or traveling along a spiral arm. Gómez (2006) found that there are large errors when trying to determine spiral arm positions kinematically, Hou, Han, & Shi (2009) state that these difficulties will not be overcome until accurate distances to HII regions within the arms are determined, Xu et al. (2006).

Galactic Rotation Curves

There are two rotation curves considered for this work. The first assumes flat rotation; with rotational velocity, Θ_*, invariant with R (Galactocentric distance), i.e. that $\frac{d\Theta}{dR}$=constant. The second rotation curve, suggested by Brand & Blitz (1993) (from here on referred to as BB93), is given in equation 1.3.

$$\frac{\Theta_*}{\Theta_0} = a_1 \left(\frac{R}{R_0} \right)^{a_2} + a_3 \tag{1.3}$$

Where; R is Galactocentric radius, R_0 is the Solar-Galactic centre distance, Θ_0 is the speed of the solar motion and Θ_* is the orbital velocity of the emission about the Galactic centre.
The constants are; $a_1 = 1.00737$; $a_2 = 0.0394$; $a_3 = 0.00712$.

Both the flat and the BB93 rotation curves utilise the same solar constants of $\Theta_0 = 220$km/s and R=8.5kpc, the IAU standard. Figure iii shows the BB93 rotation curve and the Foster &

Cooper (2010) velocity anomaly. The BB93 curve is approximately flat with the outermost points implying a gentle increase with distance. Translating the circular rotation velocity to that of velocity with respect to the local standard of rest, V_{LSR}.

$$V_{LSR} = \left(\left(\frac{\Theta_* R_0}{R}\right) - \Theta_0\right)\sin(l)\cos(b) + \Delta V_{LSR}^{shock} \tag{1.4}$$

$$R = (d^2\cos^2(b) + R_0^2 - 2R_0 d\cos(b)\cos(l))^{\frac{1}{2}} \tag{1.5}$$

Equation 1.4 shows the form for the relations using BB93. Assuming flat rotation, the expression loses its dependance in Galactic latitude, b. In addition to the independence on b, one may also assume that $\Theta_* = \Theta_0$.

There is a more recent study by Reid et al. (2009), published after the completion of this body of work, of the velocity field of the Galaxy using the Very Long Baseline Array (VBLA). This was conducted by measuring the trigonometric parallaxes of masers in high-mass star-forming regions throughout the Milky Way. The Reid et al. (2009) measurements calculate the solar constants (hence forth referred to as the R09 standard) to be Θ_0=254km/s and R_0=8.4kpc, this is in difference to the IAU standard of Θ_0=220 km s^{-1} and R_0=8.5kpc. In Chapter 4, the IAU and R09 solar constants are compared when modelling the spiral structure of the Perseus arm via the Shocked-Motion-Model and how each set affect the modelled result, however, for this section of work the IAU standard solar constants are adopted.

Perseus Spiral Arm Spatial Structure - The Hou et al. 2009 Model

Within the Milky Way, HII regions and Giant Molecular Clouds are among the most prominent tracers of spiral structure. Despite this, the overall structure of our Galaxy is still mostly unknown (Hou et al. 2009). For this work, the polynomial form of a logarithmic spiral, as described in Hou et al. (2009), will be used to describe the position of the ith spiral arm through the cluster sample. The expression for the spiral form is shown below;

$$log(R_{arm}) = a_i + b_i\theta + c_i\theta^2 + d_i\theta^3 \tag{1.6}$$

$$\tan(\phi_{pitch_i}) = \frac{d}{d\theta}(log(R_{arm})) = b_i + 2c_i\theta + 3d_i\theta^2 \tag{1.7}$$

Where, (r,θ) are polar coordinates of the ith arm centred on the Galactic Centre, with θ increasing anti-clockwise from the ℓ =0°line of sight. The polynomial treatment of the Perseus arm's structure differs from the discrete linear logarithmic form - in that the polynomial expression takes into account the variation of pitch angle, ϕ_{pitch} along the arm. A linear logarithmic fit to the spiral arms assumes a constant pitch angle, i.e. the angle at which the spiral arm's locus bisects a locus of constant Galactocentric radius. Over the relatively small range of R which the Perseus arm spans, the variation in pitch angle - and its shock - have since been found that they can be assumed to be approximately constant Summers (2010, 2011); Summers & Brunt (in prep). However, at

Table i: Parameters describing the polynomial logarithmic spiral, Hou et al. (2009). Using the IAU standard solar constants of R_0=8.5kpc and Θ_0=220km/s.

Arm	a_i	b_i	c_i	d_i
(1) Norma	1.376	-0.07792	0.04309	0.0
(2) Scutum-Crux	7.330	-2.302	0.2849	-0.01059
(3) Sagittarius-Carina	10.403	-3.526	0.4620	-0.01895
(4) Perseus	1.978	-0.1181	0.02098	0.0
(5) Outer	2.297	0.09116	0.04273	0.0

the time of pursuing this work, it was felt a more complete treatment is the preferred option. Therefore, the variation of ϕ_{pitch} as a function of θ is given in equation 1.7, with the parameters for the polynomial logarithmic spiral model are given in Table i.

The best fit parameters where found by fitting the polynomial form to HII and GMC tracer data and then by minimising a likelihood function with the parameters. The tracers are weighted by their contribution to the overall structure of the arm, i.e. with brighter HII regions being judged to have contributed more to the shape of the spiral etc (Figure iv). The full methodology can be seen in Hou et al. (2009). Though it is important to consider the weaknesses in the spiral form suggested in Hou et al. (2009), in that it does not predict arm trajectory nor possible inter-arm connections outside known or mapped regions. However, for the purposes of this work, merely the functional form was required.

Perseus Spiral Arm Kinematic Structure - The Russeil et al. 2007 Model

The velocities of the material within the Perseus spiral arm are subject to a blueshift in velocity when compared to the assumption of circular motion, Brunt et al. (2002). The accepted model describing this blue-shifted velocity is the Two Armed Spiral Shock (TASS) model presented in Roberts (1972). This is exemplified in Figure v showing the difference in assumed circular motion and the TASS model's velocities. This model has since been modelled using hydrodynamical simulations (Dobbs & Pringle 2010, Figure 3) which are described in Chapter 4

Roberts (1972) state that "the [observations as a] group show a net negative motion of order 10km/s". The gas clouds at the shock boundary may be compressed, triggering gravitational collapse which facilitates the birth of young (optical) stellar objects. However, more recent studies by Russeil et al. (2007) show that the mean velocity deviation of a Perseus arm object is of the order -14.9±8.9km/s. In addition to the mean shock velocity, Russeil et al. (2007) also present a form of the shock velocity varying as, essentially, a function of Galactocentric radius, R. There is also inference to the co-rotation radius, the radius at where the orbital velocity of material is equal

Lee J Summers

Image Copyrighted.
Original source image can be found:

[adapted] Figure 3, Hou et al. (2009)

Third Party Copyright Marker

Figure iv: Taken from Hou et al. (2009) showing the tracer data of HII and GMC locations overlayed with the polynomial spiral for each of the 5 arms. Brightness is proportional to the contribution, by a mass-probability rating - see Hou et al. (2009), of the region to the overall spiral structure.

to the pattern speed of the spiral density wave. This is investigated further in Chapter 4.

The expression for the shock velocity was derived through the extrapolation of a linear regression treatment from Russeil et al. (2007). This was calculated for the Perseus and Outer (which they refer to as the Cygnus arm) by measuring and identifying the velocity difference of HII regions within each of these arms and were plotted against Galactic radius - a linear function was then fit to it.

$$\Delta V_{LSR}^{shock} = \left(8.74 \pm 1.10.\frac{R}{[\mathrm{kpc}]}\right) - (111.09 \pm 13.34) \tag{1.8}$$

Where ΔV_{LSR}^{shock} is the magitude of the shock in the spiral arm region, measured in km s^{-1} , of material at Galactocentric distance, R.

Perseus Spiral Arm Association

I used the value for the width of the Perseus arm presented in Russeil et al. (2007) - derived by plotting HII regions and fitting a spatial model to known Perseus arm locations - it being $\approx$ 700pc. This width is subject to a probability distribution, since one would expect a majority of Perseus arm objects to reside relatively close to the Perseus arm spatial centre. Each of the clusters in the catalogue will be assigned a Perseus arm probability statistic, which is derived from the assumption of a normally distributed PDF, $\varphi(x)$, assuming that the clusters designated to be Perseus arm would an arm statistic within some multiple of σ. However, as the work progressed

Lee J Summers

Image Copyrighted.
Original source image can be found:

[adapted] Figure 3, Roberts (1972)

Figure v: Figure taken from Roberts (1972). Schematic representation of the shocked motion of gas local to the Perseus arm over the Galactic Longitude range of $130^o < l < 140^o$. The hollow triangles show the location of OB associations and the black squares are HII regions. The solid black line represents the TASS model, other models are shown; (- - - - -) is the linear density model and the two dotted curves (.....) outline a dispersion band of ± 8 km s^{-1} corresponding to the Schmidt model (Schmidt 1965).

it was found that this variable parameter cut added nothing to the overall analysis of the clusters. Instead, the distances of the clusters were used and directly compared to the Perseus arm spatial centre - in conjunction with the arm-width (Russeil 2003; Russeil et al. 2007) - to decide whether the cluster is located within the Perseus arm. Therefore if a cluster is designated to be within the Perseus arm in terms of its distance, then it has the additional $\Delta V_{LSR}^{shock}(R)$ applied to its calculated v_{LSR} when compared to the data in the spectral surveys. This will compensate for the slowing of the cluster's orbital velocity as it resides within the arm.

C.5 Source Data Selection and Preparation

Source Catalogue

The clusters were initially, for the preliminary work, selected from the WEBDA[1] online cluster catalogue. All the clusters were selected residing within the second Galactic quadrant. Secondly, all clusters *without* ages nor observed distances were removed from the sample, leaving a final sample size of 112 clusters.

However, upon further inspection, the distances and ages were not consistent with other works. Because of this the catalogue as described in Dias et al. (2002, 2007) is used as a basis. There are three forms of this catalogue used;

- Stellar clusters with measured radial velocities. (54 clusters)
- Stellar clusters residing within the limits of the data-cubes. (153 clusters - D2)
- Stellar clusters cut in Age ($6.5 \leq \mathrm{Log}_{10}[\mathrm{Age(years)}] \leq 9.0$). (133 clusters - D3)

The clusters reside between the Solar locus and a Galactocentric radius of 16kpc and have an age less than 10Gyr. The physical positions of the clusters must reside within the CO data regions obtained from the Outer Galaxy (Heyer 1996) and Extended Outer Galaxy (Brunt et al. in prep) surveys , that is in the second galactic quadrant with a Galactic longitude $100^o < l < 180^o$. For each of the clusters, the v_{LSR} was calculated using the flat rotation curve ($\Theta_* = \Theta_0$). For objects exterior to the Perseus arm, ΔV_{LSR}^{shock}=0. For objects residing in the arm, the shock velocity difference is applied to V_{circ}. In addition to the positional information each of the clusters also has an angular diameter on the sky, in arc-minutes.

Data Maps

The CO and HI data used, described fully in Chapter 2. The series of annuli, centered at each of the clusters, at various radii are used to determine the extent of the CO content within. The fixed radii range from 5pc→25pc in increments of 5pc. The upper limit is selected as the extent at which detected material can be assumed, probabilistically speaking, to be associated to the central cluster (Leisawitz et al. 1989). To consolidate the methods before applying them to the complete data-set, a preliminary set of data were used:

[1] www.univie.ac.at/webda - Operated by the Institute for Astronomy of the University of Vienna

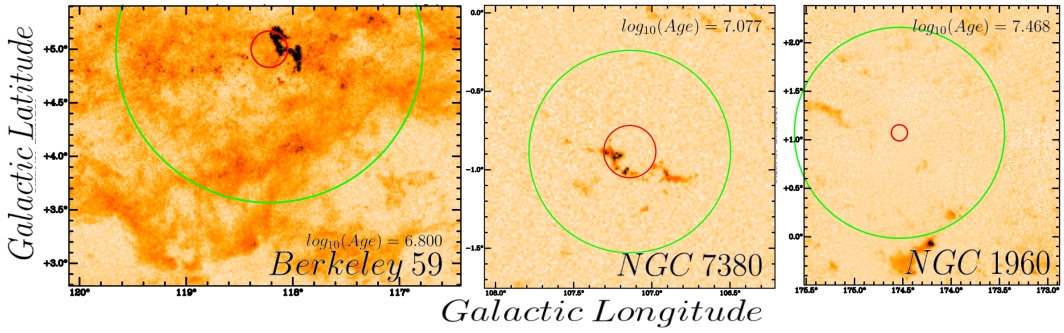

Figure vi: CO map of integrated T_A for three example clusters. The *Green* locus has a radius of 25pc centered on the host cluster. The *Red* locus is the radius of the cluster on the sky

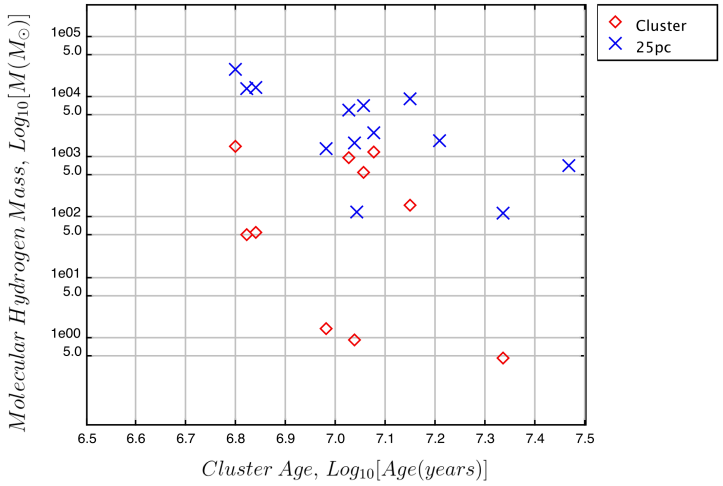

Figure vii: Preliminary results showing the variation in mass of associated molecular material with host cluster age. The *Blue* crosses show the mass interior to a 25pc locus and the *Red* diamonds show the mass interior to the cluster radius.

Using clusters within the sample with velocities which can be confirmed with observations in the Simbad[1] online catalogue and only two radii of association, that of the cluster radius and a fixed 25pc, the test CO maps can been seen in Figure vi. The plot in Figure vii shows the variation in mass of molecular material with host cluster age.

Though, at present, the number of samples do not show a clear trend in proportionality between mass and age. Though one can observe the beginnings of a trend between $\frac{dM}{d(age)}$ and the radius of the the integration area. The mass of molecular Hydrogen is then calculated via equation 4-6. To overcome this, the number of annuli were increased up to 200pc (See Figure viii) of the host cluster centre, again even over these large areas there is little variation of mass with age, see Figure ix - for each annulus selection the results show very little - if any - correlation between

[1] http://simbad.u-strasbg.fr/simbad/

mass and age.

The Cluster Sample

As has been mentioned previously, the WEBDA catalogue was not used for the actual analysis due to the large variation in the validity of the given parameters (more specifically distance and age). Therefore for the actual analysis of the data, the Dias 2007 versions (ii) and (iii) catalogue will be used from section C.5. In addition to a change in catalogue, the annuli used will not be fixed radii independent to the data (i.e. 5-25pc), instead the mean and median cluster size for the sample will be found and it will be multiples of these two root radius will be used. The multiples of the mean/median cluster radius will be 1.0-8.0 in increments of of 0.5. Hence, if one uses annuli related to the cluster radii within the sample it would give a more accurate representation of the CO distribution centred on each of the clusters. There are two candidate descriptors of cluster radius; the mean and median, 3.17pc and 2.07pc respectively. The Dias 2007 catalogue can be seen in the Appendix to this thesis.

C.6 Mass Results

The Age-Cut, D2, catalogue will be considered at each cluster radius regime. Figure xi shows the distribution of the clusters, in Size-Age space, of the complete Dias catalogue. The blue and green size cuts are the mean and median cluster sizes respectively, the magenta line denotes the upper age at which the bins have low occupancy.

Figure xii shows that there is no obvious correlation between the mass of associated molecular gas and the host cluster, this is because of the noise in the sample. Therefore, the mass will be binned using the mean and median cluster sizes for each age bin with the sample also being cut in age .

Mean Cluster Radius

Figure xiii shows the total enclosed mass of gas within a set annulus and how the mass of molecular Hydrogen, HI and the ratio of molecular to total gas mass varies with the age of the host stellar cluster.The HI distribution for all annuli is relatively flat with little variation of HI with age, which is as to be expected. The total mass of gas interior to to the 1.0-3.0x the mean cluster radius (CR) tails off over an order of magnitude from the youngest to the oldest clusters.For 3.0 to approximately 5.0 times the mean CR, these sizes the annuli generally encompass the whole of the cluster for most of the sample (looking at Figure xi for reference) thus giving a good representation of the mass association of these clusters. Progressing from 3.0-5.0 mean CR, the older end of the distribution tends to flatten whilst the younger clusters tend to have a mass drop from youngest to oldest (6.75-7.75 age bins respectively) of approximately an order of magnitude. Above 5.0 times the mean CR, the molecular Hydrogen mass distribution tends to flatten with largest annulus having a variation completely within far less than an order of magnitude. This is because at the largest annulus, not all the gas measured is physically associated to the host cluster rather it is merely spatially associated within the parameter space - see Figure viii for examples of this.

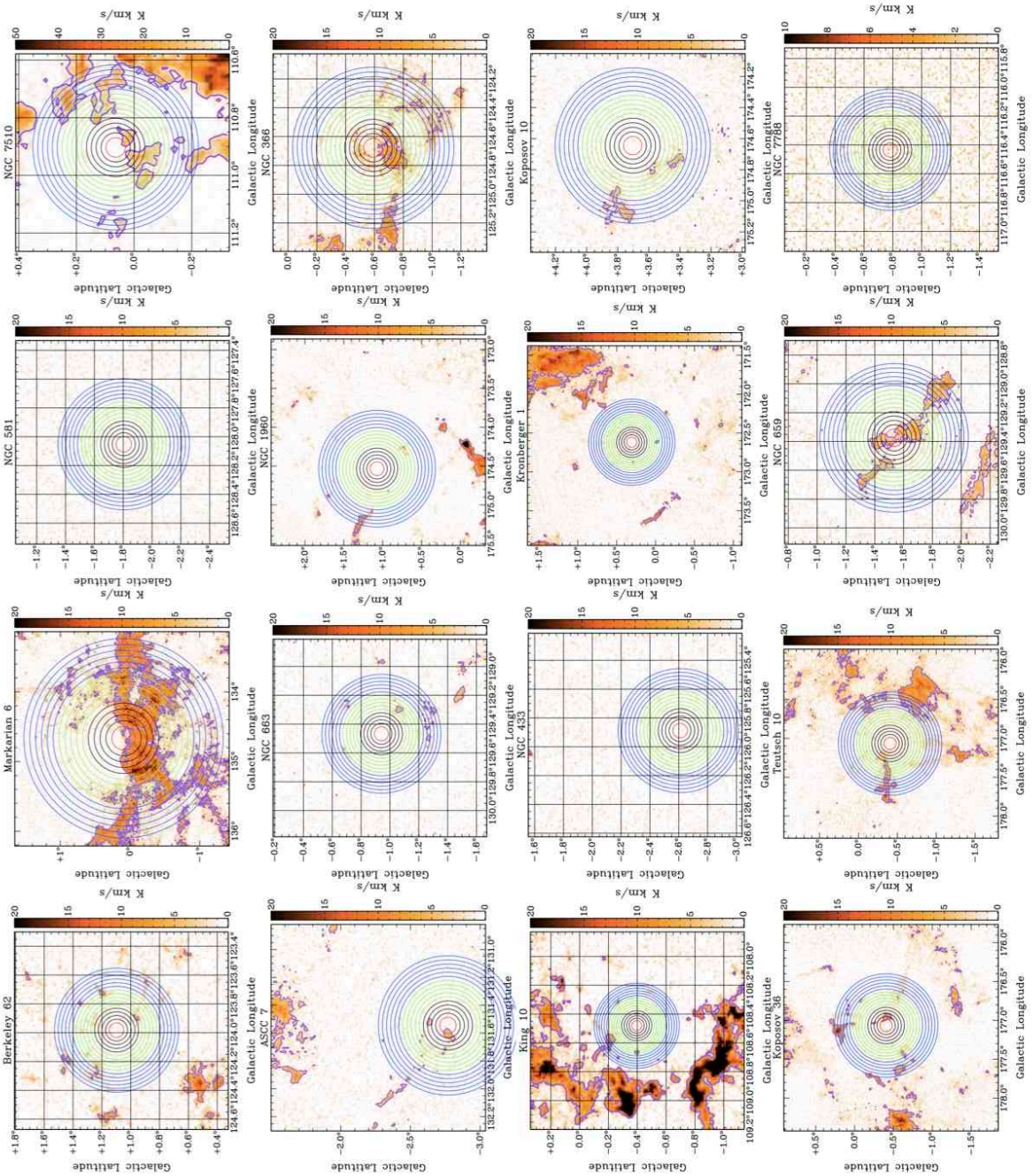

Figure viii: Figure showing the series of fixed annuli for a selection of clusters, with ^{12}CO emission integrated over ±10 km s^{-1} of each of the sample cluster's velocity centre.

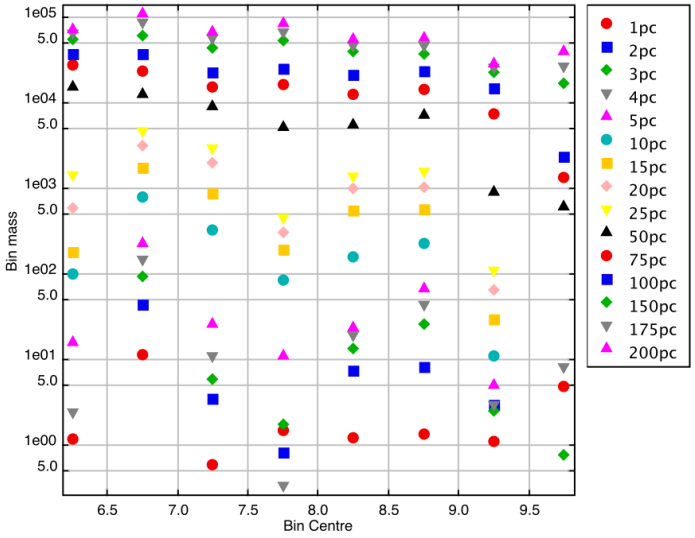

Figure ix: Preliminary results showing the variation in mass of associated molecular material with host cluster ages. Bin Centre is the age of the host stellar cluster, the bin mass is in solar masses.

Table ii: Equating the multiple of each CR to its linear size in parsec

Multiple of Cluster Radius	Linear Size Mean (3.17pc)	Linear Size Median (2.07pc)
1.0	3.17	2.07
1.5	4.76	3.11
2.0	6.34	4.14
2.5	7.93	5.18
3.0	9.51	6.21
3.5	11.10	7.25
4.0	12.68	8.28
4.5	14.27	9.32
5.0	15.85	10.35
5.5	17.44	11.39
6.0	19.02	12.42
6.5	20.61	13.46
7.0	22.19	14.49
7.5	23.78	15.53
8.0	25.36	16.56

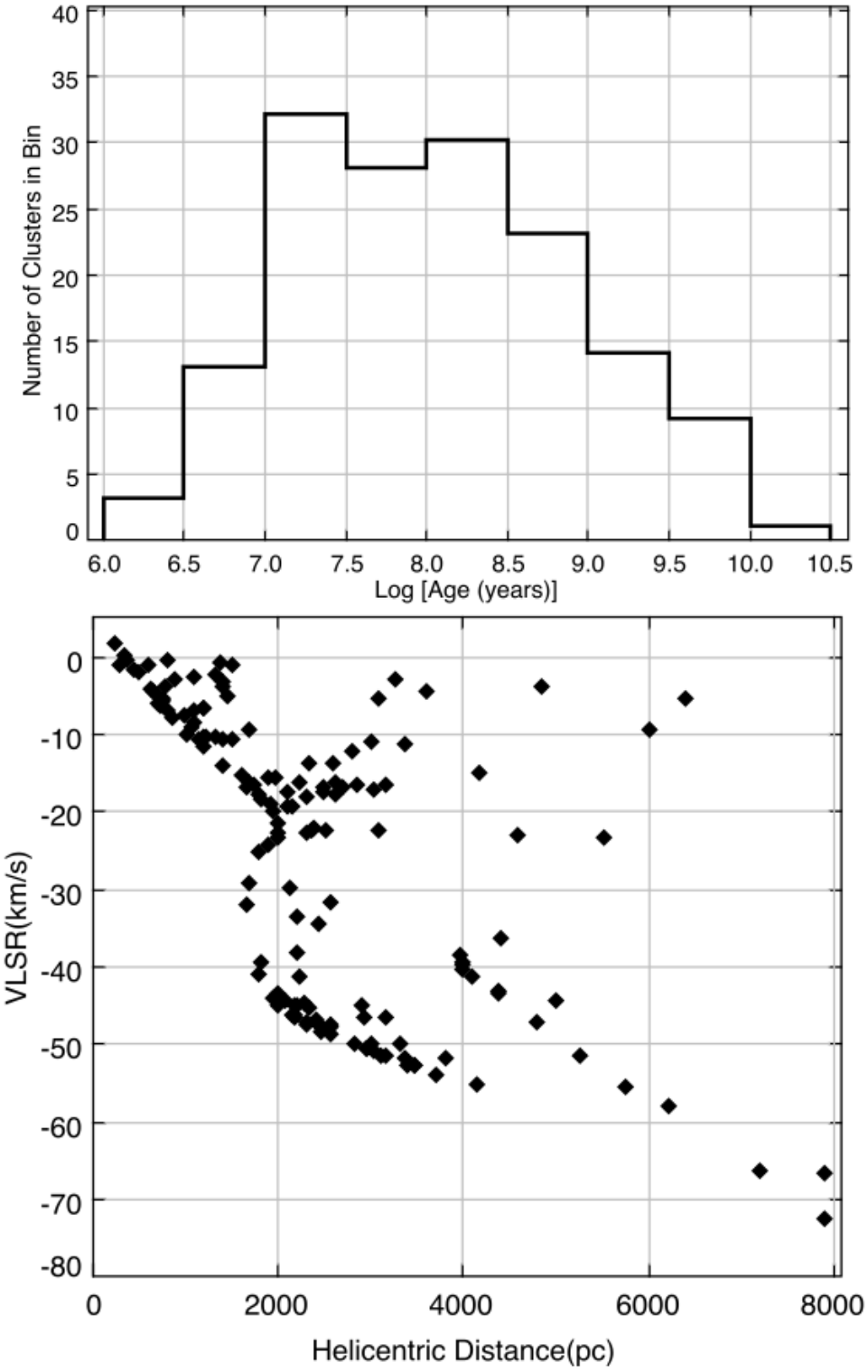

Figure x: The stellar cluster parameters in the catalogue, in terms of the age distribution and the corrected v_{LSR} -d_{helio} relation.

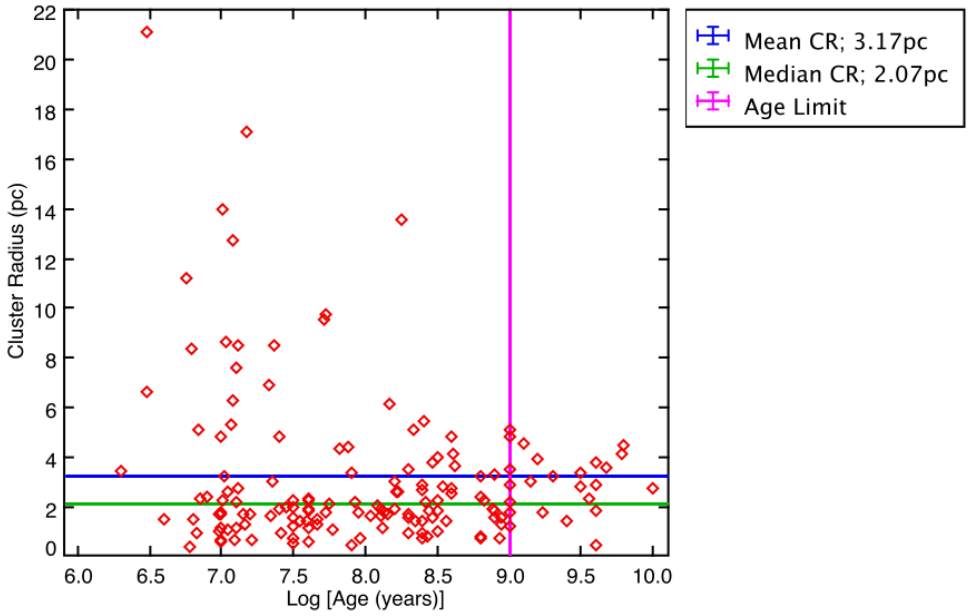

Figure xi: The Figure above shows the position in Size-Age space and the positions of he various cuts and parameters within that space.The significantly larger clusters appear to have increased the value of the mean since it is apparent that there are a number of clusters residing below the mean. The implication of this being that the median cluster radius is the better descriptor to use.

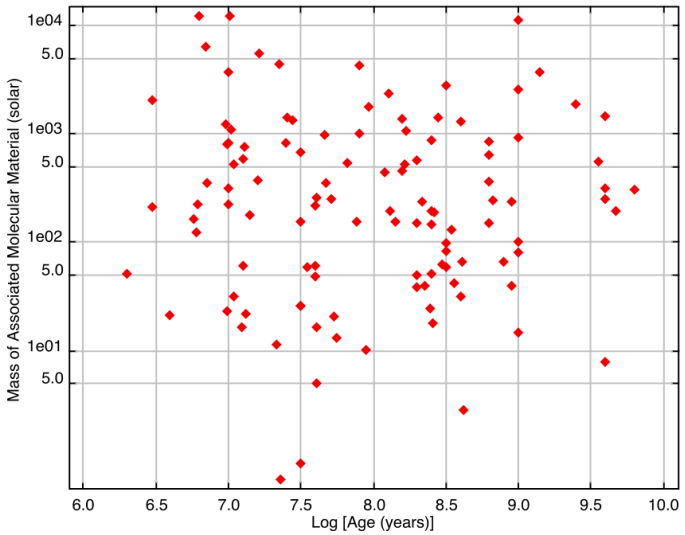

Figure xii: Variation of mass with age at five times the mean cluster radius. The amount of scatter makes it difficult to ascertain a mass:age relation leading to the need to bin the data in mass and age, as is discussed in the main text.

Figure xiii: Variation of Gas Mass and Molecular to total Gas ratio with age of the host stellar cluster for the multiples of the mean cluster radius (3.17pc), the points signify the uppermost edge of the age bin. The HI emission has a even distribution across all integration annuli due to the ubiquitous nature of Galactic HI . The molecular emission material drops off with age up to $10^{7.5}$ bin - after which the distributions flattens out in the older cluster bins.

Figure xiv: Variation of Gas Mass and Molecular to total Gas ratio with age of the host stellar cluster for the multiples of the median cluster radius (2.07pc), the points signify the uppermost edge of the age bin. As with the mean distributions in Figure xiii, the distribution o fHI is uniform across all annuli for all ages, whereas the molecular material drops off at $10^{7.5}$ age bin before flattening the distribution at the older age bins.

The third parameter variation with age of host cluster to be measured is the variation of the fraction of $\frac{Molecular}{Total}$ associated gas mass. Looking at the same mean CR divisions as for the molecular mass variation; the smallest multiples of the mean CR (1.5-2.5), excluding the actual mean CR since there is an incomplete sample, there is a variation of mass with age with the younger clusters having more associated mass than the older clusters. For annuli within the 3.0-5.0 mean CR, the older end of the distribution flattens, this suggests that clusters older than the 7.75 age bin, there is very little variation of mass with increasing annulus. Finally, for the largest annuli the general shape of the distribution remains constant with only its position in the mass-age space increasing in mass. This is because at these annuli all the physically associated mass has already been identified at smaller annulus sizes.

In addition to the three forms of mass measurement, there will be a second convention for the annulus used - multiples of the median cluster radius will be used.

Median Cluster Radius

As with the mean CR, the distribution of HI in Figure xiv remains fairly flat for all annuli but with the whole distribution shifting up, in mass, for larger annuli. From where the sample becomes complete (>1.5CR), the mass of physically associated Molecular material decreases over approximately an order of magnitude until the 4.0CR plot at which point the older end of the distribution flattens. This flattening of the oldest clusters is of a comparable linear size to that of the flattening of the mean CR distribution. Considering all the plots, it is shown that the mass decreases up until the $10^{7.75}$ age bin after which the distribution flattens.

Considering the ratio of the $\frac{Molecular}{Total}$ mass gas fraction, though over a significantly smaller mass range, it decreases with age over the complete range of median CR. This is because the maximum median CR is only equivalent to two thirds of the mean CR range, i.e. the annulus does not encompass enough area to completely flatten the oldest clusters mass distribution.

Modification To Velocity Assignment

In an attempt to improve the correlation of emission to the host cluster, i.e. removing the over saturation emission of the older cluster bins, the method by which the velocity for each cluster was selected. Instead of *clinically* assigning the velocity at which the material will be extracted from, using the intensity profiles (see Figure xv) of the ^{12}CO . Using the velocity which was determined previously as an initial *best guess* as to the velocity of the associated emission, the intensity profile is then used to observe the peaks in ^{12}CO emission, see Figure xv. If a cluster has a peak of emission within ± 10 km s^{-1} of its initially determined v_{LSR} , the cluster's v_{LSR} is then modified to be centred on the peak of the ^{12}CO . However, if there is no peak in ^{12}CO emission within ± 10 km s^{-1} , then the cluster is defined to have *no associated emission*.

The example of this can be seen in Figure xv, Trumpler 1 has an initial $v_{LSR} \approx 50$ km s^{-1} and there is no peak in ^{12}CO within ± 10 km s^{-1} of this and therefore is said to have no associated emission. Whereas Berkeley 15 has an initial $v_{LSR} \approx 7$ km s^{-1} is near a peak in ^{12}CO emission at $v_{LSR} \approx 2$ km s^{-1} , therefore the ^{12}CO is summed over each annulus but is centred, in v_{LSR} , on

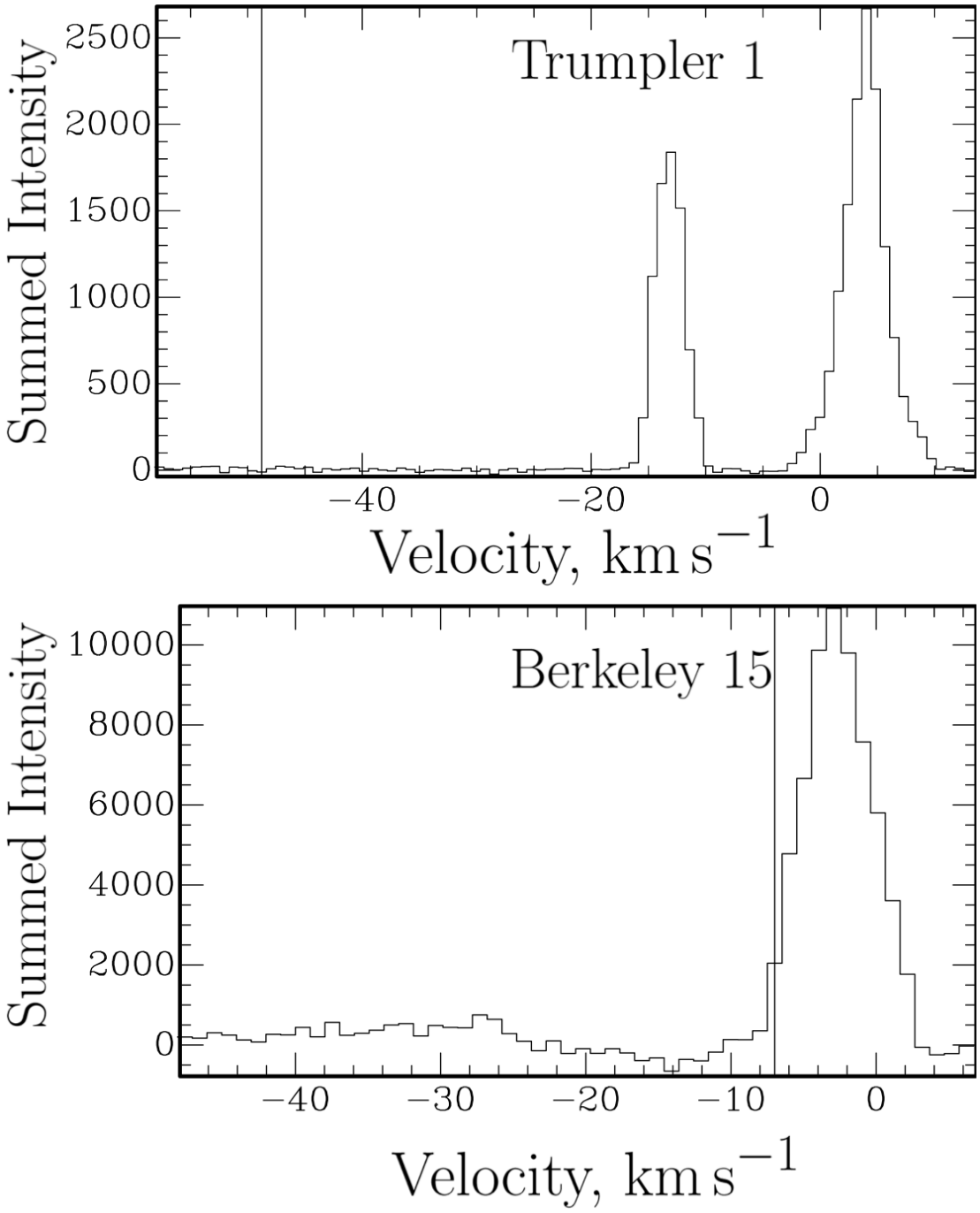

Figure xv: ^{12}CO Intensity profiles centred at the ℓ, b co-ordinates of each of the clusters labeled in the Figure. Trumpler 1 can be seen to have no enhanced emission in its vicinity where as Berkeley 15 can be seen to be near a peak in ^{12}CO at $v_{LSR} \simeq 2$ km s^{-1} .

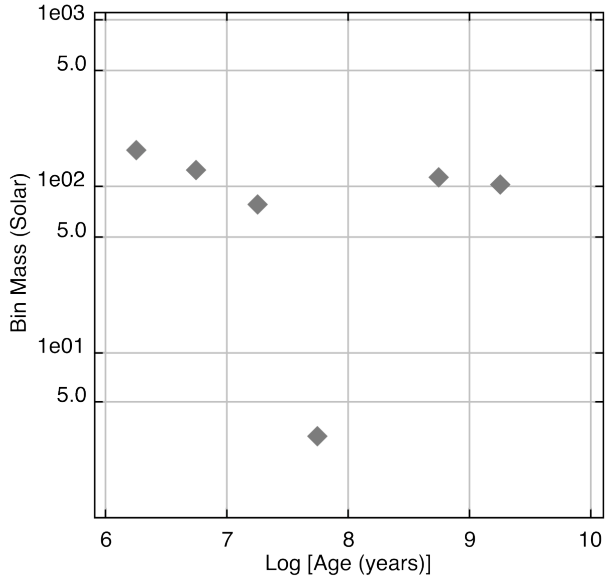

Figure xvi: Variation of host cluster age with associated molecular material within 5 times the median cluster radius, showing the drop off in associated molecular material by $10^{7.5}$ yrs -only to rise in the final two age bins. The points indicate the uppermost edge of the age bin with bin widths of 0.25 in Log space. This shows the older clusters have material kinematically associated with them which is not spatially coincident.

2 km s^{-1} rather than 7 km s^{-1} . Using this approach, the drop-off in molecular emission is more obvious around $10^{7.5}$ yrs, see Figure xvi, but there was still contamination of the older age bins. An example of this method, and the decrease in mass with age, for 5 times the median cluster radius annulus (10.35 pc) can be seen in Figure xvi. Again, as with the previous approach, the oldest age bins have artificially increased mass associated with them. This could be due to the older clusters, which are exterior to the Perseus arm, sharing an observed v_{LSR} with material within the Perseus arm - showing the difficulties with the kinematic uncertainy and degeneracy between arm-based shocked material sharing the same velocity as material at a much further distance.

C.7 Conclusions

As is to be expected, both the mean and median CR analyses show a uniform distribution of HI throughout all the plots with the whole trace moving up in mass as one encompasses more HI - reflecting the ubiquity of the HI distribution over the whole Galactic disc.

The mass of molecular material decreases with age, up until approximately 30Myr, beyond this age limit, the molecular mass distribution flattens. This flattening of the mass shows that the gas associated with the host cluster can be considered not to be associate with its formation, rather that is merely spatially associated rather than residual from the clusters' formation.

The gas fraction, though over a significantly reduced mass range, variation with age presents a similar distribution to that of the molecular material variation, but with less noise due to the nor-

malisation of the total mass. Though the findings of this work are similar to that of the work of Leisawitz et al. (1989), the large mass range and significant drop off in mass was not seen here. This could be due to the way in which the masses were determined; with the Leisawitz et al. (1989) work the mass of individual clouds surrounding the host clusters, i.e. if a cloud of mass X is 'near' a cluster of age 1 Myr, one is more likely to give positive association of cloud X with the cluster rather than if the same cloud was seen near a cluster of 10Myr, it is likely that the cloud would not be classified as being associated with the cluster. Here, there is no subjective element to the computation of the associated mass, hence the "older" clusters hence tend to have a higher mass than the "older" Leisawitz clouds - explaining why the older clusters have artificially higher masses. The modification to the emission assignment made the drop-off of emission with age more apparent - see Figure xvi - but the older cluster age bins are still contaminated with kinematically, but not spatially, associated emission.